

Ex nihilo nihil fit

University of Alberta

*Solid-State Nuclear Magnetic Resonance and Computational
Investigations of Exotic Nuclei*

by



Michelle Ambrosa Marie Forgeron

A thesis submitted to the Faculty of Graduate Studies and Research in partial fulfillment
of the requirements for the degree of Doctor of Philosophy

Department of Chemistry

Edmonton, Alberta

Fall 2006



Library and
Archives Canada

Bibliothèque et
Archives Canada

Published Heritage
Branch

Direction du
Patrimoine de l'édition

395 Wellington Street
Ottawa ON K1A 0N4
Canada

395, rue Wellington
Ottawa ON K1A 0N4
Canada

Your file *Votre référence*
ISBN: 978-0-494-23028-2
Our file *Notre référence*
ISBN: 978-0-494-23028-2

NOTICE:

The author has granted a non-exclusive license allowing Library and Archives Canada to reproduce, publish, archive, preserve, conserve, communicate to the public by telecommunication or on the Internet, loan, distribute and sell theses worldwide, for commercial or non-commercial purposes, in microform, paper, electronic and/or any other formats.

The author retains copyright ownership and moral rights in this thesis. Neither the thesis nor substantial extracts from it may be printed or otherwise reproduced without the author's permission.

AVIS:

L'auteur a accordé une licence non exclusive permettant à la Bibliothèque et Archives Canada de reproduire, publier, archiver, sauvegarder, conserver, transmettre au public par télécommunication ou par l'Internet, prêter, distribuer et vendre des thèses partout dans le monde, à des fins commerciales ou autres, sur support microforme, papier, électronique et/ou autres formats.

L'auteur conserve la propriété du droit d'auteur et des droits moraux qui protègent cette thèse. Ni la thèse ni des extraits substantiels de celle-ci ne doivent être imprimés ou autrement reproduits sans son autorisation.

In compliance with the Canadian Privacy Act some supporting forms may have been removed from this thesis.

Conformément à la loi canadienne sur la protection de la vie privée, quelques formulaires secondaires ont été enlevés de cette thèse.

While these forms may be included in the document page count, their removal does not represent any loss of content from the thesis.

Bien que ces formulaires aient inclus dans la pagination, il n'y aura aucun contenu manquant.


Canada

Abstract

Modern solid-state nuclear magnetic resonance (NMR) techniques have been employed to investigate several rarely studied nuclei, including ^{131}Xe , ^{95}Mo , and ^{53}Cr . These nuclei are considered experimentally challenging because of their low nuclear magnetic moments, significant quadrupolar moments, low natural abundance, or combinations thereof. By exploiting current resources, such as high magnetic field strengths and the quadrupolar Carr-Purcell Meiboom-Gill signal-to-noise enhancement technique, model compounds of high molecular symmetry have been investigated. In addition, ^{129}Xe ($I = 1/2$) has been probed to investigate XeF_2 and $\text{Na}_4\text{XeO}_6 \cdot x\text{H}_2\text{O}$ ($x = 0, 2$).

The primary goal of this research is to characterize the nuclear magnetic shielding (σ) and electric field gradient (EFG) tensors for the above-mentioned nuclei in several model compounds and to relate these NMR properties to the molecular and electronic structures. Zeroth-order density functional theory (ZORA DFT) and restricted Hartree-Fock (RHF) methods have been utilized to calculate σ and EFG tensors to corroborate experimental data and to provide insight into intriguing problems involving molecular and electronic structure.

Solid-state ^{129}Xe and ^{131}Xe NMR investigations of chemically bound Xe compounds demonstrate the sensitivity of the Xe σ and EFG interactions to changes in the local Xe environment. In addition, the importance of relativistic effects in determining nuclear magnetic shielding tensors for linear molecules is demonstrated through an experimental and computational study of XeF_2 . Solid-state ^{95}Mo NMR studies of monomolybdate, MoO_4^{2-} , and octacyanomolybdate, $\text{Mo}(\text{CN})_8^{4-}$, salts reveal that the Mo σ and quadrupolar interactions make substantial contributions to the observed

lineshapes of the central ^{95}Mo NMR transition. Significant is that ZORA DFT and RHF calculations indicate a substantial EFG at Mo for an isolated $\text{Mo}(\text{CN})_8^{4-}$ anion possessing ideal square antiprismatic symmetry, whereas the point-charge approximation predicts a zero EFG at Mo for this structure. Solid-state ^{53}Cr NMR investigations of chromate and dichromate salts demonstrate that the Cr quadrupolar interaction dominates the observed ^{53}Cr NMR lineshapes, while the anisotropic Cr shielding interaction is generally negligible.

Acknowledgements

First, I would like to thank my supervisor, Rod Wasylshen, for providing guidance and direction over the years. I will miss our many discussions on science, family, and running.

Second, I thank the current group members (in order of arrival): Kirk, Kris O., Kris H., Mat, Bryan, Fu, and Tom. Oftentimes, being part of this group has felt like being the only female in a large family of adolescent males. What can I say? It's been an interesting experience. I thank the group for scientific discussions, their feedback on manuscripts, and their general assistance over the years. I specifically thank Guy and Devin for readily answering many naive questions, for our daily morning coffee breaks, and always treating me with respect. Also thanks to Devin for computational help with the 'octacyanide project', to Mat for his efforts in synthesizing labelled octacyanide and for keeping our lab organized and up to par with the required safety standards. Thanks to Kirk and Harris for their help over the years with ADF. Finally, thanks to our temporary graduate student, Silvia, who joined our group for a short, but critical time. Thanks for brightening my days during a painful thesis-writing period and for your advice, support, and friendship. Un bacino!

I thank the former members of the solid-state NMR group, Myrlene and Dave, for hands-on training on the spectrometers and sharing with me your knowledge of NMR and computational chemistry. Thanks to Dave for keeping me updated on the latest music scene and to Myrlene for proofreading parts of this thesis. Lastly, I thank Renée, a former post-doc in our group, for sharing her expertise on Bruker software with me.

I thank Profs. Wolfgang Jäger, Alex Brown, Steve Bergens, Arthur Mar, Mark Freeman, and Chris Ratcliffe for serving on my Ph.D. committee and for reading through this thesis.

A large portion of the work presented in this thesis has been carried out at the Pacific Northwest National Laboratories (PNNL) in Richland, WA. Having the opportunity to conduct research at a state-of-the-art facility was a highlight of my graduate studies. The staff at PNNL: Nancy Isern, Jesse Sears, Andy Lipton, David Hoyt, Joe Ford and Paul Ellis, are thanked for their help, hospitality, and discussions on

research. I thank Nancy for having things organized, answering weekend "emergency" phone calls, and suggesting some excellent local wineries. Thanks to Jesse for fixing and tuning finicky probes and to Andy for introducing our lab to the QCPMG experiment, as well as sharing the ins-and-outs of experimental aspects of NMR with our group. Finally, thanks to my colleagues, Dave, Kirk, and Kris O., who accompanied me on several trips to PNNL and shared with me the stress and frustration of working on short timelines.

Within the chemistry department, I thank Prof. Steve Bergens for allowing me to use his glove box to pack air-sensitive samples for NMR studies, the electronic and machine shops for fixing probes, probe parts, and sample packing tools, and the secretaries for graciously reminding me of important deadlines, such as paying my tuition (thanks Ilona!); also, thanks, ladies, for the puppy visits and talks. Finally, I would like to thank Marty for his support during my studies and for adding life to the department.

Thanks to Michael Gerken (University of Lethbridge) for providing the perxenate samples, Raman spectra, and for helpful discussions on the perxenate project.

For generous financial support over the years, I thank the University of Alberta, NSERC, and Alberta Ingenuity.

The life of a graduate student is full of ups and downs and, as the song goes, you get by with a little help from your friends. Without the support of my wonderful family and friends, I'm not sure I would have survived. Thanks to my close friends: Paul, Pete, Holly, and Silvia; our evenings and weekends together kept me sane during some stressful and difficult times. Thanks for your much-appreciated advice and encouragement. To my far-away friend, Natasha, thanks for always believing in me!

Thanks to the following, who helped me in their own special way: Breton, Pat& Joanne, Cap&Anne, Sue&Blair, and Mike&Liz, and finally, to miscellaneous friends at the U of A whose friendships I hold dearly: the Burnds' day crew (Mike, Glenny, Sarah, D-Lo, Wiggy, Rob P., Ebbing, Bob, and Stevie-T), Chantel, Patrick, Vince, Steve Fletcher, and Ross.

Finally, I thank my family (Mom, Dad, Nicole, and Peter) for their unconditional love and support during my mysterious studies on enamar. I would especially like to thank my sister, Nicole, for providing private counseling sessions over the years.

To Mom and Dad

TABLE OF CONTENTS

List of Tables

List of Figures

List of Appendices

List of Symbols, Nomenclature, and Abbreviations

Chapter 1: Introduction and Objectives

| | |
|---|---|
| 1.1. Historical Overview..... | 1 |
| 1.2. Objectives and Thesis Outline..... | 5 |

Chapter 2: The Fundamentals of Nuclear Magnetic Resonance Spectroscopy

| | |
|--|----|
| 2.1. The NMR Hamiltonian..... | 8 |
| 2.2. Euler Angles..... | 9 |
| 2.3. Zeeman Interaction..... | 11 |
| 2.4. Nuclear Magnetic Shielding and the Chemical Shift..... | 13 |
| 2.5. Nuclear Electric Quadrupole Interaction..... | 18 |
| 2.5.1. <i>Quadrupolar Nuclei and Electric Field Gradients</i> | 18 |
| 2.5.2. <i>Quadrupolar Corrections to Zeeman Energy Levels</i> | 20 |
| 2.5.3. <i>Point-Charge Approximation</i> | 26 |
| 2.6. Nuclear Spin-Spin Coupling Interactions: Direct and Indirect..... | 29 |

Chapter 3: Experimental Techniques and Theoretical Methods

| | |
|--|----|
| 3.1. Standard Techniques used in Solid-State NMR Spectroscopy..... | 34 |
| 3.1.1. <i>Magic-Angle Spinning</i> | 34 |
| 3.1.2. <i>Abundant Spins: Pros and Cons</i> | 36 |
| 3.1.2.1. <i>Decoupling</i> | 37 |
| 3.1.2.2. <i>Cross-Polarization</i> | 38 |

| | |
|--|----|
| 3.2. Experimental Strategy and Practical Considerations for Solid-State NMR Studies of Low-Frequency Quadrupolar Nuclei..... | 39 |
| 3.2.1. <i>High Applied Magnetic Field Strengths</i> | 39 |
| 3.2.2. <i>Typical Pulse Sequences</i> | 41 |
| 3.2.2.1. <i>Spin-Echo</i> | 41 |
| 3.2.2.2. <i>Quadrupolar Carr-Purcell Meiboom-Gill</i> | 43 |
| 3.2.3. <i>Broad NMR Lineshapes</i> | 46 |
| 3.2.3.1. <i>Radiofrequency Pulses and Excitation Profiles</i> | 46 |
| 3.2.3.2. <i>Stepped-Frequency Technique</i> | 49 |
| 3.3. Manipulation and Interpretation of Data..... | 49 |
| 3.3.1. <i>Skyline Projection Method</i> | 49 |
| 3.3.2. <i>Spectral Simulations</i> | 51 |
| 3.3.2.1. <i>SIMPSON</i> | 52 |
| 3.3.2.2. <i>WSOLIDS</i> | 53 |
| 3.4. Theoretical Approach: Computation of NMR Parameters..... | 54 |
| Chapter 4: Solid-State NMR Investigations of Exotic Nuclei | |
| 4.1. Prologue..... | 57 |
| 4.2. Prelude to Xenon NMR Spectroscopy..... | 59 |
| 4.3. Solid-State ¹²⁹ Xe NMR Study of Xenon Difluoride..... | 62 |
| 4.3.1. <i>Introduction</i> | 62 |
| 4.3.2. <i>Nuclear Magnetic Shielding for Linear Molecules</i> | 64 |
| 4.3.3. <i>Experimental and Computational Details</i> | 65 |
| 4.3.3.1. <i>Solid-State ¹²⁹Xe NMR Spectroscopy</i> | 65 |
| 4.3.3.2. <i>Quantum Chemical Calculations</i> | 66 |
| 4.3.4. <i>Results and Discussion</i> | 67 |

| | |
|---|-----|
| 4.3.4.1. Solid-State ^{129}Xe NMR Spectroscopy..... | 67 |
| 4.3.4.2. Solid-State ^{19}F NMR Spectroscopy..... | 76 |
| 4.3.5. Conclusions..... | 78 |
| 4.4. Computational Investigation of Relativistic Effects on Magnetic Shielding Tensors for Linear Molecules..... | 79 |
| 4.5. Solid-State $^{129/131}\text{Xe}$ NMR Studies of Sodium Perxenates..... | 84 |
| 4.5.1. Introduction..... | 84 |
| 4.5.2. Experimental Details..... | 85 |
| 4.5.2.1. Synthesis and Structural Characterization of Sodium Perxenates..... | 85 |
| 4.5.2.2. Solid-State $^{129/131}\text{Xe}$ NMR Spectroscopy..... | 85 |
| 4.5.3. Results and Discussion..... | 88 |
| 4.5.3.1. $\text{Na}_4\text{XeO}_6 \cdot 2\text{H}_2\text{O}$ | 89 |
| 4.5.3.2. Na_4XeO_6 | 98 |
| 4.5.4. Conclusions..... | 103 |
| Chapter 5: Solid-State ^{95}Mo NMR Studies | |
| 5.1. Overview of ^{95}Mo NMR Studies..... | 105 |
| 5.2. Solid-State ^{95}Mo NMR Studies of A(I) and A(II) Molybdenum Oxide Salts..... | 107 |
| 5.2.1. Experimental Details..... | 108 |
| 5.2.2. Results and Discussion..... | 109 |
| 5.2.2.1. Structure of A(I) and A(II) Molybdate Salts..... | 109 |
| 5.2.2.2. Solid-State ^{95}Mo NMR Studies of Molybdate Salts..... | 110 |
| 5.2.2.3. Investigation of Anisotropic Mo Shielding in Molybdate Salts..... | 115 |
| 5.2.2.4. Assessing the Feasibility of Solid-State ^{95}Mo NMR Studies..... | 124 |
| 5.2.3. Conclusions..... | 125 |

| | |
|---|-----|
| 5.3. Solid-State ^{95}Mo NMR Study of Octacyanomolybdate(IV) Anions..... | 126 |
| 5.3.1. Introduction..... | 126 |
| 5.3.2. Experimental and Computational Details..... | 129 |
| 5.3.2.1. Solid-State ^{95}Mo NMR Spectroscopy..... | 129 |
| 5.3.2.2. Quantum Chemical Calculations..... | 131 |
| 5.3.3. Results and Discussion..... | 133 |
| 5.3.3.1. $\text{K}_4\text{Mo}(\text{CN})_8 \cdot 2\text{H}_2\text{O}$: Approximate Dodecahedral Symmetry..... | 133 |
| 5.3.3.2. $\text{Ti}_4\text{Mo}(\text{CN})_8$: Approximate Square Antiprismatic Symmetry..... | 139 |
| 5.3.3.3. Quantum Chemical Investigation of the PCA for D_{4d} Symmetry..... | 146 |
| 5.3.4. Conclusions..... | 151 |
| Chapter 6: Solid-State ^{53}Cr NMR Studies of Chromate and Dichromate Salts | |
| 6.1. Introduction..... | 153 |
| 6.2. Experimental Details..... | 155 |
| 6.2.1. Solid-State ^{53}Cr NMR Spectroscopy..... | 156 |
| 6.2.2. Quantum Chemical Calculations..... | 157 |
| 6.3. Results and Discussion..... | 157 |
| 6.3.1. Structure of A(I) and A(II) Chromate Salts..... | 157 |
| 6.3.2. Solid-State ^{53}Cr NMR Studies of Chromate Salts..... | 158 |
| 6.3.3. Relating Cr NMR Parameters to Structure..... | 166 |
| 6.3.4. Comparison of NMR Results for the Chromate and Molybdate Salts..... | 170 |
| 6.3.5. Solid-State ^{53}Cr NMR Studies of Dichromate Salts..... | 172 |
| 6.4. Conclusions..... | 176 |

| | |
|--|-----|
| Chapter 7: Concluding Remarks | 179 |
| Appendices | 182 |
| References and Notes | 196 |

List of Tables

| | | |
|-----------|---|----|
| Table 2.1 | Summary of Internal NMR Interactions; see Equations (2.1) and (2.2). | 8 |
| Table 2.2 | Non-Vanishing Components of the Nuclear Magnetic Shielding Tensor, σ , for Selected Nuclear Site Symmetries. | 14 |
| Table 2.3 | Relative Values of V_{ZZ} at Nucleus "M" Calculated Using the PCA for Selected Complexes. | 27 |
| Table 4.1 | Relevant Nuclear Properties and Relative Receptivities for Selected Nuclei. | 58 |
| Table 4.2 | Calculated Magnetic Shielding Parameters for the Xenon Atom and Isolated XeF_2 , XeF_4 and KrF_2 Molecules. | 70 |
| Table 4.3 | Xenon Magnetic Shielding and Indirect Nuclear ^{129}Xe , ^{19}F Spin-Spin Coupling Values for XeF_2 from this Study and the Literature. | 72 |
| Table 4.4 | Xenon Magnetic Shielding and Spin-Rotation Data for XeF_2 . | 73 |
| Table 4.5 | Calculated ng Magnetic Shielding Tensors for $ng\text{F}_2$, XeF^+ and $\text{XeF}_2\text{-AsF}_5$ and Experimentally-Determined Xe Chemical Shift Tensors for XeF_2 and $\text{XeF}_2\text{-AsF}_5$. | 81 |
| Table 4.6 | Experimentally-Deduced and Calculated Spans for Palladium and Platinum in the Linear Triatomic Molecules: <u>Pd</u> CO and <u>Pt</u> CO. | 83 |

| | | |
|-----------|---|-----|
| Table 4.7 | Useful Absolute Frequencies of Suggested Reference Samples for Xe NMR Studies. | 86 |
| Table 4.8 | Experimental Xe EFG and Shielding Parameters for $\text{Na}_4\text{XeO}_6 \cdot 2\text{H}_2\text{O}$ and Two Xe Polymorphs. | 91 |
| Table 4.9 | Calculated and Experimental ^{131}Xe Nuclear Quadrupolar Coupling Constants. | 102 |
| Table 5.1 | Summary of Structural Data for Molybdate Salts. | 110 |
| Table 5.2 | Isotropic Chemical Shifts and Mo Quadrupolar Parameters for A(I) and A(II) Molybdate Salts. | 112 |
| Table 5.3 | Anisotropic Mo Shielding Parameters and Euler Angles for A(I) and A(II) Molybdate Salts. | 118 |
| Table 5.4 | Experimental and Calculated Mo σ and EFG Parameters for $\text{K}_4\text{Mo}(\text{CN})_8 \cdot 2\text{H}_2\text{O}$. | 134 |
| Table 5.5 | Experimental and Calculated Mo σ and EFG Parameters for $\text{Tl}_4\text{Mo}(\text{CN})_8$. | 141 |
| Table 5.6 | Calculated NMR Parameters for Isolated, Idealized Model Compounds of High Symmetry and Experimental Mo Chemical Shift Values. | 147 |
| Table 6.1 | Summary of Structural Data for Chromate Salts. | 158 |

| | | |
|------------------|--|------------|
| Table 6.2 | Experimentally-Determined Cr Quadrupolar and Shielding Parameters for A(I) and A(II) Chromate and A(I) Dichromate Salts. | 161 |
| Table 6.3 | Comparison of Cr and Mo Quadrupolar and Shielding Parameters for Isomorphous Cs_2MoO_4 and Cs_2CrO_4. | 170 |

List of Figures

| | | |
|------------|---|----|
| Figure 2.1 | Typical solid-state NMR lineshapes and magnitudes for the (L-R): Zeeman, quadrupolar (showing <i>only</i> the central, $m_1 = +1/2 \leftrightarrow -1/2$, transition for a spin- $n/2$ nucleus), anisotropic magnetic shielding, direct spin-spin coupling, and indirect spin-spin coupling interactions. | 9 |
| Figure 2.2 | Schematic representation of the Euler angles (α, β, γ) which describe the relative orientations of coordinate systems (x_1, y_1, z_1) and (x_4, y_4, z_4); see text for further description. | 10 |
| Figure 2.3 | Zeeman energy level diagram for a spin-1/2 nucleus demonstrating the separation of nuclear spin states, $ I, m\rangle$, as a function of B_0 . | 12 |
| Figure 2.4 | Typical solid-state NMR chemical shift powder patterns observed for isolated spin-1/2 nuclei: (a, c) axially-symmetric and (b) non-axially symmetric chemical shift tensors. The principal components, $\delta_{11}, \delta_{22}, \delta_{33}$, are indicated, along with $\delta_{\text{iso}}, \Omega$ and κ (see Eqs. (2.9) to (2.12)). | 16 |
| Figure 2.5 | Depiction of nuclear charge distribution with respect to the nuclear spin-axis for (a,c) prolate and oblate quadrupolar nuclei, respectively, and (b) a spin-1/2 nucleus. | 18 |
| Figure 2.6 | NMR Periodic Table indicating elements with only $I = 1/2$ isotopes, ■, those with at least one isotope with $I > 1/2$, □, and those with no spin-active isotopes, $I = 0$, ▨. | 19 |

- Figure 2.7 (a) Schematic nuclear spin energy level diagram for a spin-3/2 nucleus indicating the $(2I + 1)$ Zeeman energy states and the first-order quadrupolar corrections to these states; below are the expected NMR spectra for a single crystal sample. (b) A characteristic axially-symmetric quadrupolar powder pattern for a stationary sample of a spin-3/2 nucleus. The central transition, $m_I = +1/2 \leftrightarrow -1/2$, corresponds to the sharp, intense peak at ν_L and the satellite transitions, $m_I = +3/2 \leftrightarrow +1/2$ (■) and $m_I = -3/2 \leftrightarrow -1/2$ (□), correspond to the broad, shaded areas. The sum of the two satellite transitions to the overall spectrum (■) is also shown. The indicated angles, $\theta = 0^\circ$ and $\theta = 90^\circ$, signify that V_{ZZ} is parallel and perpendicular to B_0 , respectively. 21
- Figure 2.8 Projection of V_{ZZ} in the lab frame, indicating polar angles, θ and ϕ . 22
- Figure 2.9 Nuclear spin energy level diagram and corresponding NMR lineshapes for the central transition of an $n/2$ -spin nucleus indicating first- and second-order quadrupolar corrections to the Zeeman energy levels. The inset corresponding to $\hat{H}_Q^{(2)}$ shows a typical second-order quadrupolar lineshape for $\eta_Q = 0$; the noted values represent the angle between V_{ZZ} and B_0 (*i.e.*, θ in Figure 2.8) and demonstrate the discontinuity of the second-order quadrupolar interaction. 24
- Figure 2.10 Typical central transition NMR lineshapes for $n/2$ quadrupolar nuclei for stationary (□) and MAS (▣) samples; (a-c) $\eta_Q = 1.0, 0.5, 0.0$, respectively. The scale is inversely proportional to both I and ν_Q^2 . 25

| | | |
|-------------|--|----|
| Figure 2.11 | Dependence of C_Q on Larmor frequency for several $n/2$ -spin quadrupolar nuclei. The results were constructed using Eq. 2.25 and assuming $\Delta v_{(+\frac{1}{2} \leftrightarrow -\frac{1}{2})}^{\text{Stationary}} = 100$ kHz and $\eta_Q = 0.0$. | 26 |
| Figure 2.12 | (a) The coordinate system for an isolated spin pair defining the orientation of $r_{NN'}$ with respect to B_0 . (b) Typical Pake doublet pattern for an isolated pair of <i>homonuclear</i> spin-1/2 nuclei. The angles $\theta_D = 0$ and 90° denote the orientation of $r_{NN'}$ with respect to B_0 ; the separation between "horns" or "shoulders" allows R_{DD} to be determined. Note, for a <i>heteronuclear</i> spin-pair, the separation between the horns and shoulders is R_{DD} and $2R_{DD}$, respectively. | 30 |
| Figure 2.13 | Schematic diagram of the indirect spin-spin coupling interaction, \mathbf{J} , showing an energetically-favourable configuration for nuclear spins, I_N and $I_{N'}$, and their respective electron spins, $S_{Z,N}$ and $S_{Z,N'}$, assuming $J(N,N')_{\text{iso}} > 0$. | 30 |
| Figure 3.1 | Solid-state $^{129}\text{Xe}\{^1\text{H}\}$ NMR spectra of MAS samples of $\text{Na}_4\text{XeO}_6 \cdot 2\text{H}_2\text{O}$ at variable spinning speeds. The isotropic chemical shift, $\delta_{\text{iso}} = -725.6$ ppm, is indicated in (a) and (b) with asterisks; $B_0 = 11.75$ T. | 35 |
| Figure 3.2 | Simulations of central transition ^{53}Cr NMR spectra for $\nu_L(^{53}\text{Cr}) = 28.179$ MHz, $C_Q(^{53}\text{Cr}) = 4.64$ MHz and $\eta_Q = 0.0$, which corresponds to $\Delta v_{(+\frac{1}{2} \leftrightarrow -\frac{1}{2})}^{\text{Stationary}} \sim 100$ kHz. The spectra have been calculated using different spinning rates, ν_{rot} , to illustrate the dependence of the second-order quadrupolar lineshape on ν_{rot} . | 36 |

| | | |
|------------|--|----|
| Figure 3.3 | Pulse sequence for cross-polarization; CT is the contact time, T_D the dead time, AT the acquisition time, and PD the pulse delay. | 38 |
| Figure 3.4 | Simulated (top) and experimental (bottom) central transition ^{11}B NMR spectra of solid hexamethylborazine at three applied magnetic field strengths, as indicated in the figure. The spectra shown in (a-c) were acquired using MAS rates of 8.1 kHz, 25.0 kHz, and 13.0 kHz, respectively. The vertical line indicates the isotropic frequency at each applied magnetic field. See Ref. 87. | 40 |
| Figure 3.5 | (a) Spin-echo experiment. (b) Depiction of spin dynamics in various stages of the spin-echo experiment: (i) application of the $(\pi/2)_x$ pulse forces magnetization along y -axis; (ii) during time period, τ , the individual spin vectors fan-out in xy -plane; (iii) application of π_y pulse effectively reflects the spin vectors in yz -plane; (iv) spin vectors refocus during the second τ period and at the end of τ , (v) magnetization is aligned along y -axis and described by: $M_0 \exp(-t/T_2)$. | 42 |
| Figure 3.6 | The quadrupolar Carr-Purcell Meiboom-Gill (QCPMG) pulse sequence: the first segment is identical to the spin echo experiment, the second involves the train of refocusing π pulses, and the third shows the extended sampling period to ensure the FID is fully decayed. The spacing between spikelets, ν_{QCPMG} , is equal to τ_a^{-1} . | 44 |
| Figure 3.7 | (a) ^{53}Cr QCPMG FID of a stationary sample of K_2CrO_4 acquired using $\tau_a = 2.0$ ms; (b) solid-state ^{53}Cr QCPMG NMR spectrum of an MAS sample of Cs_2CrO_4 with $\nu_{\text{QCPMG}} = 120$ Hz and $\nu_{\text{rot}} = 6000$ Hz; (c) conventional spin-echo ^{53}Cr NMR | 45 |

spectrum of an MAS sample of Cs_2CrO_4 with $\nu_{\text{rot}} = 6000$ Hz;
(a-c) $B_0 = 11.75$ T.

- Figure 3.8 Relationship between the "square pulse" applied for duration T_p 47
in the time domain and its frequency counterpart, the
 $\text{sinc}[\pi(\nu - \nu_c)T_p]$ function. The nutation behavior of the
 $\text{sinc}[\pi(\nu - \nu_c)T_p]$ function illustrates the non-uniform excitation
profile of the square pulse.
- Figure 3.9 Dependence of the signal intensity of the central transition, 48
 $S(T_p)$, on the nominal pulse angle for a selective (- - -) and non-
selective (—) pulse for (a) $I = 3/2$ and (b) $I = 5/2$; see Ref. 96.
- Figure 3.10 Solid-state ^{53}Cr QCPMG spectrum of $\text{Cs}_2\text{Cr}_2\text{O}_7$ acquired in a 48
single experiment; $B_0 = 18.8$ T, $\nu_{\text{QCPMG}} = 2$ kHz; total
experiment time = 15.5 hr.
- Figure 3.11 Solid-state ^{53}Cr QCPMG spectra of Ag_2CrO_4 acquired at 18.8 T 49
using the stepped-frequency method and processed using the
skyline projection technique. The spectrum shown in (a) is
composed of three sub-spectra and demonstrates incorrect
placement of ν_c , while the spectrum shown in (b) is composed
of two sub-spectra and shows correct placement of ν_c .
- Figure 3.12 (a) The individual ^{53}Cr QCPMG sub-spectra of $\text{Cs}_2\text{Cr}_2\text{O}_7$ 50
acquired using the stepped-frequency technique at 18.8 T. The
total spectra shown in have been processed using (b) VOCS and
the (c) skyline projection techniques, respectively.
- Figure 3.13 Stepped-frequency ^{55}Mn QCPMG spectrum of a stationary 51
sample of an unidentified decomposition product of $\text{Mn}_2(\text{CO})_{10}$;

$B_0 = 17.63$ T; $\nu(^{55}\text{Mn}) = 185.9$ MHz; the inset shows a single sub-spectrum. The total spectrum is the skyline projection of 16 sub-spectra with $\nu_{\text{QCPMG}} = 2.0$ kHz; each spectrum was acquired using a 1 s pulse delay and is the sum of 156. The entire spectrum is approximately 600 kHz broad and was obtained in 2 hours; $C_{\text{Q}}(^{55}\text{Mn}) = 60 \pm 1$ MHz and $\eta_{\text{Q}} = 0.0 \pm 0.02$.

- Figure 4.1 Xe chemical shift range, referenced with respect to the primary Xe chemical shift reference, XeOF_4 (neat liquid, 24 °C), indicating the most shielded, $\text{Re}(\text{}^i\text{PrCp})(\text{CO})(\text{PF}_3)\text{Xe}$, and least shielded, XeO_2F^+ , Xe compounds, along with other selected Xe systems; note, XeF_2 and XeO_6^{4-} are investigated in this *Thesis*. The Xe chemical shift range is often discussed in terms of the formal oxidation state of Xe, with Xe(0) being most shielded and Xe(VIII) being least shielded; however, from this Figure, the agreement is poor. Redrawn from Ref. 135. 60
- Figure 4.2 Experimental (a, c) and calculated (b, d) $^{129}\text{Xe}\{^{19}\text{F}\}$ NMR spectra of an MAS sample of XeF_2 acquired with TPPM ^{19}F decoupling. The half-height linewidth of the spinning sidebands, $\Delta\nu_{1/2}$, is 300 ± 50 Hz. $\delta(^{129}\text{Xe})_{\text{iso}}$ is indicated by an asterisk in (a) and (c). 67
- Figure 4.3 Unit cell of solid XeF_2 from Ref. 160; \bullet = xenon, \circ = fluorine. 68
- Figure 4.4 (a) Spin-orbit relativistic and (b) non-relativistic ZORA DFT calculations of $\Omega(\text{Xe})$ in XeF_2 , assuming $\delta(^{129}\text{Xe})_{\text{iso}} = -1603$ ppm. The isotropic ^{129}Xe chemical shift of the free Xe atom is shown with respect to $\delta(\text{XeF}_2)_{\parallel}$, calculated using $\sigma(\text{Xe}(\text{free atom}))_{\parallel} - \sigma(\text{XeF}_2)_{\parallel}$ from Table 4.2. (c) Experimentally- 69

determined $\Omega(\text{Xe})$ in XeF_2 and isotropic chemical shifts of selected xenon compounds plotted on the known xenon chemical shift scale.

- Figure 4.5 Expansions of ^{129}Xe NMR spectra of an MAS sample of XeF_2 acquired without ^{19}F decoupling at spinning frequencies of (a) 14.000 kHz and (b) 8.000 kHz. 74
- Figure 4.6 Experimental (a, c) and calculated (b, d) ^{19}F NMR spectra of an MAS sample of XeF_2 . The isotropic ^{19}F chemical shifts for XeF_2 and the teflon inserts of the rotor are indicated by * and #, respectively. The simulated ^{19}F NMR spectra do not include ^{19}F - ^{19}F dipolar coupling, which contribute $\sim 10\%$ to the relative intensities of the spinning sidebands in the observed ^{19}F NMR spectra (see text). 77
- Figure 4.7 Selected plots of $[\sigma(\text{free atom}) - \sigma_{\parallel}]$, calculated using non-relativistic (■) and spin-orbit relativistic (■) ZORA DFT calculations and TZ2P basis sets, for a series of linear molecules. The nucleus for which σ has been calculated is underlined. 82
- Figure 4.8 Simulated (top) and experimental (bottom) solid-state $^{129}\text{Xe}\{^1\text{H}\}$ NMR spectra of $\text{Na}_4\text{XeO}_6 \cdot 2\text{H}_2\text{O}$ acquired at 11.75 T using various spinning speeds; the spectrum shown in (a) was acquired using CP/TPPM with a pulse delay of 2 s and is the sum of 4096 scans; the spectra shown in (b, c) were acquired using a one-pulse experiment with a 30 s pulse delay and are the sum of 1916 and 6516 scans, respectively. Processing parameters for (a), (b) and (c) include linebroadening (15 Hz, 150 Hz, and 300 Hz, respectively) and zero-filling (16 384, 90

4096, and 8192, respectively). Simulations of $^{129}\text{Xe}\{^1\text{H}\}$ NMR spectra yield the following Xe shielding parameters: $\delta_{\text{iso}} = -725.6 \pm 0.1$ ppm, $\Omega = 94.5 \pm 5$ ppm, $0.70 \leq \kappa \leq +1.00$.

- Figure 4.9 Summary of $^{129}\text{Xe}\{^1\text{H}\}$ CP/TPPM experiments for MAS samples of $\text{Na}_4\text{XeO}_6 \cdot 2\text{H}_2\text{O}$ ($B_0 = 11.75$ T, $\nu_{\text{rot}} = 6.000$ kHz). The plotted points represent the normalized ^{129}Xe NMR signal intensity as a function of ^{129}Xe , ^1H contact time and have been fitted to Equation 4.12 to determine the cross-polarization parameters, T_{IS} and $T_{1\rho}(^1\text{H})$. 93
- Figure 4.10 Solid-state $^{129}\text{Xe}\{^1\text{H}\}$ NMR spectrum of $\text{Na}_4\text{XeO}_6 \cdot 2\text{H}_2\text{O}$ acquired at 11.75 T ($\nu(^{129}\text{Xe}) = 139.132$ MHz) using a one-pulse experiment. Labeled in the spectrum are the spinning sidebands (*ssb*) from $\text{Na}_4\text{XeO}_6 \cdot 2\text{H}_2\text{O}$ and two polymorphs at -743 ppm (*) and -700 ppm (#). The inset is an expansion about the isotropic ^{129}Xe NMR signal for $\text{Na}_4\text{XeO}_6 \cdot 2\text{H}_2\text{O}$ showing more clearly the signals attributed to the two polymorphs (#, *). The spectrum was acquired using a pulse delay of 600 s, an MAS rate of 6.000 kHz, and is the sum of 300 scans. 95
- Figure 4.11 (a) Selected stepped-frequency ^{131}Xe NMR spectra of a stationary sample of $\text{Na}_4\text{XeO}_6 \cdot 2\text{H}_2\text{O}$ acquired using the stepped-frequency technique at 11.75 T ($\nu(^{131}\text{Xe}) = 41.244$ MHz); a total of fifteen sub-spectra comprise the (b) skyline projection ^{131}Xe NMR spectrum. Each spectrum is the sum of 142,848 scans and was acquired using a 1 s pulse delay and $\nu_{\text{QCPMG}} = 6055$ Hz. 96
- Figure 4.12 Simulated (top) and experimental (bottom) ^{131}Xe NMR spectra of $\text{Na}_4\text{XeO}_6 \cdot 2\text{H}_2\text{O}$ at 11.75 T ($\nu(^{131}\text{Xe}) = 41.244$ MHz). The 97

broad ^{131}Xe NMR signal is attributed to $\text{Na}_4\text{XeO}_6 \cdot 2\text{H}_2\text{O}$ and the narrow, central component is the sum of two sites attributed to two Xe polymorphs of the main sample, $\text{Na}_4\text{XeO}_6 \cdot 2\text{H}_2\text{O}$. The best-fit shielding and quadrupolar parameters for $\text{Na}_4\text{XeO}_6 \cdot 2\text{H}_2\text{O}$ and the two polymorphs are listed in Table 4.8.

- Figure 4.13 Simulated (top) and experimental (bottom) solid-state ^{129}Xe NMR spectra of a stationary sample of Na_4XeO_6 acquired at 139.132 MHz using a spin-echo sequence, a pulse delay of 2 s and 1600 scans. A Lorentzian linebroadening function of 3700 Hz was applied to the simulated spectrum. 98
- Figure 4.14 ^{129}Xe NMR spectra of anhydrous Na_4XeO_6 acquired using the progressive saturation method for the determination of $T_1(^{129}\text{Xe})$. 99
- Figure 4.15 Solid-state ^{131}Xe NMR spectra of stationary samples of anhydrous sodium perxenate acquired at 41.244 MHz using (a) spin-echo (52,432 scans) and (b) QCPMG (53,024 scans, $v_{\text{QCPMG}} = 200$ Hz) experiments. Also shown in (a) is a simulated spectrum (top) to which a Lorentzian linebroadening function of 1200 Hz has been applied. The slight discrepancy in the linewidths between the experimental and simulated spectra shown in (a) results because a Lorentzian/Gaussian apodization function of 100 Hz was applied to the experimental spectrum upon Fourier transform. 101
- Figure 5.1 Experimental (top) and simulated (bottom) ^{95}Mo NMR spectra of MAS samples of alkali molybdate salts acquired using a one-pulse experiment at 11.75 T. The spectra are the sum of 6471, 2665, 2051, 4930 scans, respectively, and were acquired at 111

spinning rates of (a-c) $\nu_{\text{rot}} = 6$ kHz and (d) $\nu_{\text{rot}} = 3$ kHz using pulse delays of 10 s. Gaussian linebroadening functions of (a-d) 50 Hz, 25 Hz, 20 Hz, and 20 Hz; respectively, were applied to the FIDs prior to Fourier transformation.

- Figure 5.2 Simulated (top) and experimental (bottom) ^{95}Mo NMR spectra of MAS samples of (a-d) Bi_2MoO_6 , SrMoO_4 , BaMoO_4 , and CdMoO_4 . The spectra were acquired using a one-pulse experiment at $B_0 = 11.75$ T and $\nu_{\text{rot}} = 6$ kHz and are the sum of (a-d) 64014, 7724, 2319, and 2067 scans, respectively. Pulse delays of (a-d) 20 s, 20 s, 10 s, and 30s, respectively, were used and Gaussian functions of (a-d) 60 Hz, 50 Hz, 20 Hz, and 50 Hz; respectively, were applied to the FIDs prior to Fourier transformation. 114
- Figure 5.3 Experimental (a) and simulated (b, c) solid-state ^{95}Mo NMR spectra of stationary samples of (i) K_2MoO_4 and (ii) Rb_2MoO_4 acquired at 11.75 T (left) and 17.63 T (right). The spectra shown (b) represent the best-fit simulated spectra and the corresponding parameters are given in Tables 5.2 and 5.3; the spectra in (c) neglect contributions from the anisotropic Mo shielding interaction. The inset (top, center) shows the relative orientation of the principal components of the Mo shielding and EFG tensors for both K_2MoO_4 and Rb_2MoO_4 . Acquisition parameters for the experimental spectra are given in *Appendix 5.2*. 117
- Figure 5.4 Experimental (a) and simulated (b, c) ^{95}Mo NMR spectra of stationary samples of (i) Cs_2MoO_4 (left) and (ii) Li_2MoO_4 (right) acquired using a one-pulse experiment at 11.75 T. The inset shows the relative orientation of the principal components 119

of the Mo shielding and EFG tensors for Cs_2MoO_4 , corresponding to $\alpha, \beta, \gamma = 0, 90, 0^\circ$. The parameters for the best-fit calculated spectra for Cs_2MoO_4 and Li_2MoO_4 , shown in (b), are given in Tables 5.2 and 5.3; the simulated spectra shown in (c) neglect anisotropic Mo shielding. Acquisition parameters are given in *Appendix 5.2*.

- Figure 5.5 Simulated (top) and experimental (bottom) solid-state ^{95}Mo NMR spectra of stationary samples of (i) BaMoO_4 and (ii) SrMoO_4 , acquired at 11.75 T (left) and 17.63 T (right), and (iii) CdMoO_4 , (iv) PbMoO_4 , and (v) CaMoO_4 , acquired at 11.75 T. The parameters used to calculate the best-fit simulated spectra (top) are given in Tables 5.2 and 5.3. Acquisition parameters for the experimental spectra are given in *Appendix 5.2*. 121
- Figure 5.6 Experimental ^{95}Mo NMR spectra of isomorphous (a-e) Ba, Sr, Ca, Pb, and Cd molybdate acquired using a one-pulse experiment at 11.75 T. See Figure 5.5 for simulated spectra and Tables 5.2 and 5.3 for best-fit parameters. 123
- Figure 5.7 Simulated ^{95}Mo NMR spectra of SrMoO_4 showing the individual (a) EFG and (b) shielding interactions and (c) the sum of their contributions at $B_0 = 11.75$ T. The relative orientation of the principal components of the Mo EFG and shielding tensors is shown on the right for $\alpha, \beta, \gamma = 0, 90, 0^\circ$. 124
- Figure 5.8 Idealized structural forms of the dodecahedral (a) and square antiprismatic (b) diamagnetic $\text{Mo}(\text{CN})_8^{4-}$ anions. For dodecahedral symmetry, the two types of cyanide ligands are labeled A and B, and for square antiprismatic symmetry, all cyanide ligands are equivalent due to the molecular symmetry. 127

Partial electronic energy level diagrams for the $\text{Mo}(\text{CN})_8^{4-}$ anions possessing ideal D_{2d} and D_{4d} symmetry are also shown. The ordering of molecular orbitals (MOs) corresponds to the orientation of the $\text{Mo}(\text{CN})_8^{4-}$ anions in the indicated coordinate system and the MO labels specify the dominant atomic orbital contributions localized on Mo.

- Figure 5.9 Experimental (a) and best-fit simulated (b) QCPMG ^{95}Mo central transition NMR spectra of a solid stationary sample of $\text{K}_4\text{Mo}(\text{CN})_8 \cdot 2\text{H}_2\text{O}$ acquired at 11.75 T (left) and 17.63 T (right). The parameters used to calculate the simulated spectra are given in Table 5.4. A total of 24 682 and 4 480 transients were summed for spectra acquired at 11.75 T at 17.63 T, respectively. 133
- Figure 5.10 Simulations of central transition ^{95}Mo NMR spectra of solid, stationary $\text{K}_4\text{Mo}(\text{CN})_8 \cdot 2\text{H}_2\text{O}$ to show the individual contributions from the EFG (a) and σ (b) interactions. The sum of these interactions is shown in (c, d) using two possible relative orientations of the EFG and σ tensors. Simulations which best match the experimental spectra are shown in (a) and the corresponding best-fit simulation parameters are given in Table 5.4. 136
- Figure 5.11 Origin of the paramagnetic shielding contribution to the principal components of the Mo magnetic shielding tensor, $\sigma_{ii}^{\text{para}}$, for D_{2d} $\text{Mo}(\text{CN})_8^{4-}$, as determined by our DFT calculations. Symmetry-allowed mixing between occupied and virtual Mo d -dominated molecular orbitals via the orbital angular momentum operators, \hat{L}_x , \hat{L}_y , and \hat{L}_z give rise to $\sigma_{ii}^{\text{para}}$. The relative orientation of the Mo σ and EFG tensors in 138

the molecular frame (*i.e.*, V_{XX} , V_{YY} and V_{ZZ} are coincident with the x , y , z -axes), along with the Mo σ powder pattern, is shown to help visualize and rationalize the mixing of orbitals.

- Figure 5.12 Experimental (a) and best-fit simulated (b) ^{95}Mo central transition NMR spectra of a solid stationary sample of $\text{Tl}_4\text{Mo}(\text{CN})_8$ acquired using the QCPMG pulse sequence at 11.75 T (left) and the DFS/QCPMG pulse sequence at 21.15 T (right). The parameters used to calculate the simulated spectra are given in Table 5.5. A total of 31 760 transients were summed for $\text{Tl}_4\text{Mo}(\text{CN})_8$ at 11.75 T and 8 192 at 21.15 T. 140
- Figure 5.13 Simulations of central transition ^{95}Mo NMR spectra of solid, stationary $\text{Tl}_4\text{Mo}(\text{CN})_8$ to show the contributions from the EFG (a) and σ (b) interactions. The sum of these interactions is shown (c, d) using two possible relative orientations of the EFG and σ tensors. The simulations which best match the experimental spectra are shown in (d) and the simulation parameters are given in Table 5.5. 143
- Figure 5.14 Origin of the paramagnetic shielding contribution to the principal components of the Mo magnetic shielding tensor, $\sigma_{ii}^{\text{para}}$, for D_{4d} $\text{Mo}(\text{CN})_8^{4-}$. Symmetry-allowed mixing between occupied and virtual Mo d -dominated molecular orbitals via the angular momentum operators, \hat{L}_x , \hat{L}_y , and \hat{L}_z give rise to $\sigma_{ii}^{\text{para}}$. The relative orientation of the Mo σ and EFG tensors in the molecular frame (*i.e.*, V_{XX} , V_{YY} and V_{ZZ} are coincident with the x , y , z -axes), along with the Mo σ powder pattern, are shown to help visualize and rationalize the mixing of d -orbitals. 145

- Figure 5.15 (a) Non-relativistic $C_Q(^{95}\text{Mo})$ values for $\text{Mo}(\text{CN})_8^{4-}$ rotamers as a function of deviation from cubic symmetry. Using the PCA, a zero EFG at Mo results for all rotamers. ZORA DFT calculations, \blacklozenge , and RHF, \blacksquare , calculations. (b) Total energy, calculated at the RHF level, for $\text{Mo}(\text{CN})_8^{4-}$ rotamers as a function of deviation from cubic symmetry. 149
- Figure 5.16 Components of the axially-symmetric Mo shielding tensor, $\sigma_{11} = \sigma_{22}$ \blacksquare , $\sigma_{33} = \blacktriangle$, and span = ----, for $\text{Mo}(\text{CN})_8^{4-}$ rotamers as a function of deviation from ideal cubic symmetry, calculated using non-relativistic ZORA DFT. 150
- Figure 6.1 Selected view of the Cr and Mo NMR chemical shift scales, showing typical NMR reference compounds, along with relevant ^{53}Cr and ^{95}Mo nuclear properties. The primary reference for $^{95/97}\text{Mo}$ NMR studies is a 2.0 M aqueous solution of Na_2MoO_4 , while that for chromium is $\text{Cr}(\text{CO})_6$ dissolved in chloroform; however, a preferred, secondary reference for ^{53}Cr NMR studies is a saturated aqueous solution of Cs_2CrO_4 with $\delta_{\text{iso}} = 1798.0$ ppm; Ref. 37. 153
- Figure 6.2 Solid-state ^{53}Cr NMR spectra of MAS samples of Cs_2CrO_4 acquired under identical experimental conditions at 11.75 T using a spinning rate of 6.000 kHz with a rotor-synchronized (a) spin-echo and (b) QCPMG pulse sequence, respectively. The vertical scale of the spectrum shown in (a) has been scaled by a factor of 20 to match that shown in (b). 159
- Figure 6.3 Simulated (top) and experimental (bottom) QCPMG ^{53}Cr NMR spectra of stationary samples of (a) Cs_2CrO_4 , (b) Rb_2CrO_4 , (c) K_2CrO_4 , and (d) Ag_2CrO_4 acquired at 11.75 T (left) and 18.8 T 160

| | | |
|------------|--|-----|
| | (right); the best-fit parameters are given in Table 6.2. | |
| Figure 6.4 | Simulated (top) and experimental (bottom) QCPMG ^{53}Cr NMR spectra of stationary samples of (a) $\text{Li}_2\text{CrO}_4 \cdot 2\text{H}_2\text{O}$ and (b) $\text{MgCrO}_4 \cdot 2\text{H}_2\text{O}$ acquired at 11.75 T (left) and 18.8 T (right); the best-fit parameters are given in Table 6.2. | 163 |
| Figure 6.5 | Simulated (top) and experimental (bottom) QCPMG ^{53}Cr NMR spectra of stationary samples of (a) CaCrO_4 , (b) SrCrO_4 , (c) BaCrO_4 , and (d) PbCrO_4 acquired at 11.75 T (left) and 18.8 T (right); the best-fit parameters are given in Table 6.2. | 165 |
| Figure 6.6 | Dependence of experimentally-determined δ_{iso} and $C_Q(^{53}\text{Cr})$ values on structural parameters, Δr and σ^2 , respectively, for the A(I) and A(II) chromates. Structural parameters, Δr and σ^2 , were calculated using Equations 6.1 and 6.2, respectively, and available crystal data; these values are tabulated in <i>Appendix 6.2</i> . | 167 |
| Figure 6.7 | ZORA DFT results of the effects of (a) $\angle(\text{O}, \text{Cr}, \text{O})$ and (b) $r(\text{Cr}, \text{O})$ on $C_Q(^{53}\text{Cr})$ and (c) $\angle(\text{O}, \text{Cr}, \text{O})$ on the Cr shielding anisotropy, Ω , for the chromate anion, CrO_4^{2-} . | 169 |
| Figure 6.8 | Survey of experimentally-determined ^{53}Cr and ^{95}Mo quadrupolar coupling constants for selected A(I) and A(II) chromate and molybdate salts. | 172 |
| Figure 6.9 | Simulated (top) and experimental (bottom) solid-state ^{53}Cr NMR spectra of stationary samples of (a) $\text{Cs}_2\text{Cr}_2\text{O}_7$ and (b) $\alpha\text{-K}_2\text{Cr}_2\text{O}_7$ acquired using the stepped-frequency QCPMG experiment with $\nu_{\text{QCPMG}} = 5 \text{ kHz}$ and $B_0 = 18.8 \text{ T}$. The best-fit | 174 |

simulated parameters are given in the text and in Table 6.2.

- Figure 6.10 ZORA DFT results for Cr EFG and shielding tensors for the dichromate anion, summarizing the effects of $\angle(\text{Cr}, \text{O}_{\text{bridge}}, \text{Cr})$ on: (a) $C_Q(^{53}\text{Cr})$ and η_Q , and (b) the Cr shielding anisotropy, Ω . Note the dual y-axes in (a), which correspond to $C_Q(^{53}\text{Cr})$ (left) and η_Q (right). 176
- Figure A4.1 Plot of calculated isotropic magnetic shielding constants, σ_{iso} , as a function of atomic number, Z . Calculations were carried out for isolated, closed-shell atoms using non-relativistic (NR) and spin-orbit relativistic (SO) ZORA DFT. The data were fit to polynomial functions (given below), allowing σ_{iso} values for open-shell atoms to be determined through interpolation. 184

List of Appendices

| | | |
|--------------|--|-----|
| Appendix 3.1 | Sample input file for calculation of QCPMG NMR spectrum using SIMPSON. | 182 |
| Appendix 4.1 | Non-Relativistic and Spin-Orbit Relativistic ZORA DFT Plots of σ_{iso} for free atoms; TZ2P basis sets were employed. | 184 |
| Appendix 4.2 | X-Ray Diffraction Patterns of Various Hydrates of Sodium Perxenate: (a) $\text{Na}_4\text{XeO}_6 \cdot x\text{H}_2\text{O}$ (experimental; this work), (b) $\text{Na}_4\text{XeO}_6 \cdot 6\text{H}_2\text{O}$ (calculated from known cell parameters given in Ref. 206), (c) $\text{Na}_4\text{XeO}_6 \cdot 8\text{H}_2\text{O}$ (calculated from known cell parameters given in Ref. 207). | 185 |
| Appendix 4.3 | Raman Spectrum of Solid $\text{Na}_4\text{XeO}_6 \cdot 2\text{H}_2\text{O}$. | 186 |
| Appendix 4.4 | Raman Spectrum of Solid Na_4XeO_6 . | 187 |
| Appendix 4.5 | NMR Referencing by Absolute Frequency Method. | 188 |
| Appendix 5.1 | Structures of (a) K_2MoO_4 and Rb_2MoO_4 , (b) Li_2MoO_4 , (c) Cs_2MoO_4 , and (d) CaMoO_4 , SrMoO_4 , CdMoO_4 , BaMoO_4 , and PbMoO_4 , with views along the indicated crystallographic axes. Mo is yellow, O is red, and A(I) and A(II) cations are other. | 190 |
| Appendix 5.2 | Acquisition Parameters for Solid-State ^{95}Mo NMR Spectra of Stationary Samples of A(I) and A(II) Molybdate Salts. | 191 |
| Appendix 5.3 | Cartesian Coordinates (\AA) Employed for RHF and ZORA/DFT Electric Field Gradient Calculations of D_{2d} , D_{4d} and O_h $\text{Mo}(\text{CN})_8^{4-}$ and of the Hypothetical $\text{Zr}(\text{CN})_8^{4-}$ and MoF_8^{4-} Square | 192 |

Antiprismatic Anions.

- Appendix 6.1** Summary of Stepped-Frequency ^{53}Cr QCPMG Experiments for A(I) and A(II) Chromate and A(I) Dichromate Salts. 194
- Appendix 6.2** Summary of Structural Parameters, Δr and σ^2 , and NMR Parameters, δ_{iso} , $C_Q(^{53}\text{Cr})$, and η_Q , for A(I) and A(II) Chromate and A(I) Dichromate Salts; see Equations 6.1 and 6.2 for Δr and σ^2 . 195

List of Symbols, Nomenclature and Abbreviations

| | |
|------|------------------------------------|
| ADF | Amsterdam Density Functional |
| AT | Acquisition time |
| CP | Cross-polarization |
| CT | Contact time |
| CW | Continuous wave |
| DAS | Dynamic-angle spinning |
| DFS | Double-frequency sweep |
| DFT | Density functional theory |
| DOR | Double rotation |
| DSO | Diamagnetic spin-orbit |
| DZ | Double-zeta |
| EF | Electric field |
| EFG | Electric field gradient |
| FC | Fermi contact mechanism |
| FID | Free-induction decay |
| FT | Fourier transform |
| GGA | Generalized gradient approximation |
| HOMO | Highest occupied molecular orbital |
| IR | Infrared |

| | |
|---------|--|
| LB | Line broadening |
| LCAO | Linear combination of atomic orbitals |
| LUMO | Lowest unoccupied molecular orbital |
| MAS | Magic-angle spinning; $\theta = \arccos(1/\sqrt{3}) \approx 54.7356^\circ$ |
| MO | Molecular orbital |
| MQMAS | Multiple quantum MAS |
| MR | Magnetic resonance |
| MRI | Magnetic resonance imaging |
| NMR | Nuclear magnetic resonance |
| NQR | Nuclear quadrupole resonance |
| o.d. | Outer diameter |
| PAS | Principal axis system |
| PASS | Phase-altered spinning sidebands |
| PCA | Point-charge approximation |
| PD | Pulse delay |
| PSO | Paramagnetic spin-orbit mechanism |
| (Q)CPMG | (Quadrupolar) Carr-Purcell Meiboom-Gill |
| QE | Quadrupolar echo |
| Q-PASS | Quadrupolar PASS |
| QZ4P | Quadruple-zeta quadruply-polarized |

| | |
|-------------------------|---|
| RHF | Restricted Hartree-Fock |
| SD | Spin dipolar |
| SIMPSON | Simulation of solid-state NMR spectra (simulation program) |
| TGA | Thermal gravimetric analysis |
| TOSS | Total suppression of spinning sidebands |
| TPPM | Two-pulse phase-modulated |
| TZ2P | Triple-zeta doubly-polarized |
| VACP | Variable amplitude CP |
| VOCS | Variable offset cumulative spectra |
| VWN | Vosko-Wilk-Nusair |
| XRD | X-ray diffraction |
| ZORA | Zeroth-order regular approximation |
| α, β, γ | Euler angles defining the relative orientation of two tensors |
| δ | Chemical shift tensor |
| Δr | Bond length distortion |
| δ_{aniso} | Reduced shielding anisotropy |
| ΔE | Energy difference, $E_n - E_0$ |
| δ_{ii} | Principal components of δ , where $i = 1, 2, 3$, iso |
| ΔJ | Anisotropy in J |

| | |
|--|--|
| $\Delta \nu_{+\frac{1}{2} \leftrightarrow -\frac{1}{2}}^{\text{MAS}}$ | Breadth of the central transition for an MAS sample |
| $\Delta \nu_{+\frac{1}{2} \leftrightarrow -\frac{1}{2}}^{\text{Stationary}}$ | Breadth of the central transition for a stationary sample |
| $\Delta \nu_{1/2}$ | Linewidth at half-height |
| Δp | Population difference between two nuclear spin states |
| $\Delta \sigma$ | Shielding anisotropy |
| γ_N | Magnetogyric ratio |
| η_{CS} | Chemical shift asymmetry parameter |
| η_{J} | Indirect spin-spin coupling asymmetry parameter |
| η_{Q} | Nuclear quadrupole asymmetry parameter |
| κ | Skew of magnetic shielding tensor |
| μ_0 | Vacuum permeability |
| μ_N | Nuclear magnetic moment |
| ν_L | Larmor frequency |
| $\nu_{m,m-1}^{\text{CG}} - \nu_{\text{iso}}$ | Second-order quadrupolar shift of the center of gravity of the $m \leftrightarrow m-1$ transition relative to isotropic chemical shift |
| ν_{Q} | Quadrupolar frequency |
| ν_{QCPMG} | Spacing between spikelets (in Hz) in QCPMG NMR spectra |
| ν_{rot} | Sample spinning rate |
| θ and ϕ | Polar angles describing the orientation of \mathbf{V} with respect to B_0 |

| | |
|----------------------------|---|
| $(\pi/2)_x$ | 90° <i>rf</i> pulse with phase "x" |
| $\rho(t)$ | Reduced density matrix describing the spin system |
| $\rho_n(\mathbf{r})$ | Nuclear charge density |
| σ | Nuclear magnetic shielding tensor |
| $\sigma(\text{free atom})$ | Nuclear magnetic shielding for a free atom |
| σ^2 | Bond angle variance |
| σ^{dia} | Diamagnetic component of σ |
| σ^{para} | Paramagnetic component of σ |
| σ_{ii} | Principal components of σ , where $i = 1, 2, 3$, iso |
| τ | Time delay between $(\pi/2)$ and π pulses in QE and QCPMG experiments |
| τ_c | Correlation time |
| Ω | Span of σ or shielding anisotropy |
| ϵ_0 | Vacuum permittivity |
| $\tilde{\nu}$ | Absolute frequency |
| Φ | Electric potential |
| Ψ_0 | Nuclear wavefunction of ground state |
| Ψ_n | Wavefunction of n th excited state |
| A(I) | Cation with +1 charge |
| A(II) | Cation with +2 charge |

| | |
|------------------------|---|
| B_0 | External applied magnetic field |
| B_1 | External magnetic field of <i>rf</i> pulse |
| BW | Bandwidth of the <i>rf</i> pulse |
| C_I | Nuclear spin-rotation constant |
| C_n | Principal rotation axis of <i>n</i> -fold symmetry |
| C_Q | Nuclear quadrupolar coupling constant |
| $C_x(\tau)$ | Time-dependent auto-correlation function |
| D | Direct spin-spin coupling tensor |
| D | Nuclear receptivity |
| D_{2d} | Dodecahedral symmetry |
| D_{4d} | Square antiprismatic symmetry |
| D_{4h} | Square prismatic symmetry |
| e | Charge of an electron |
| E_0 | Electronic energy of the ground state |
| E_n | Electronic energy of the n^{th} excited state |
| $G_D(t)$ | FID response function due to the dipolar interaction |
| Gr(VI) | Group 6 (transition metals: Cr, Mo, W) |
| $G_{S/N}$ | Gain in signal-to-noise |
| \hbar | Reduced Plank's constant, $h/2\pi$ |
| $\hat{\mathcal{H}}(t)$ | Time-dependent Hamiltonian describing the relevant interactions |

| | |
|----------------------------------|--|
| \hat{H}_D | Direct spin-spin coupling Hamiltonian |
| \hat{H}_J | Indirect spin-spin coupling Hamiltonian |
| \hat{H}_Q | Quadrupolar Hamiltonian |
| \hat{H}_S | Nuclear magnetic shielding Hamiltonian |
| \hat{H}_{total} | Total NMR Hamiltonian |
| \hat{H}_Z | Zeeman Hamiltonian |
| I | Nuclear spin quantum number |
| I_Z | z-component of the nuclear spin angular momentum operator |
| \hat{I}_z^2 and \hat{I}^2 | Azimuthal and total spin angular momentum operators |
| \hat{I}_+ and \hat{I}_- | Raising and lowering operators, respectively |
| \mathbf{J} | Indirect spin-spin coupling tensor |
| $J_x(\Delta\omega_{\text{eff}})$ | Frequency-dependent spectral density function |
| k | Boltzmann constant |
| $\mathbf{K}(N, N')$ | Reduced indirect spin-spin coupling tensor |
| LF | Linewidth factor |
| l_k | Electron angular momentum operator with respect to the gauge origin |
| l_{kn} | Electron angular momentum operator with respect to the observe nucleus |
| L_i | Nuclear spin orbital angular momentum operator ($i = x, y, z$) |

| | |
|-----------|--|
| M | Number of loops of π pulses in the QCPMG experiment |
| M_2 | Second moment |
| m_e | Mass of an electron |
| m_p | Mass of a proton |
| M_z | Equilibrium magnetization aligned along the z-axis |
| N.A. | Isotopic natural abundance |
| ν_c | Transmitter or carrier frequency |
| nr | Non-relativistic |
| O_h | Octahedral symmetry |
| p | Population of nuclear spin state |
| Q | Nuclear quadrupole moment |
| R_1 | Spin-lattice relaxation rate, T_1^{-1} |
| $r_{NN'}$ | Internuclear separation between nuclei, N and N' |
| r_{cat} | Cationic radius |
| R_{DD} | Direct dipolar coupling constant |
| R_{eff} | Effective dipolar coupling constant |
| rf | Radiofrequency |
| r_k | Position vector of electron, k , to the chosen origin |
| r_{kn} | Position vector of electron, k , to the observe nucleus, n |
| S/N | Signal-to-noise |

| | |
|----------------|--|
| $\text{sinc}x$ | $(\sin x)/x$ |
| so | Spin-orbit |
| ssb | Spinning sideband |
| S | Electron spin quantum number |
| T | Temperature |
| T | General second-rank tensor |
| T_1 | Spin-lattice relaxation time |
| $T_{1\rho}$ | Relaxation time in the rotating frame |
| T_2 | Spin-spin relaxation time |
| T_2' | Effective T_2 value for the individual spikelets in a QCPMG spectrum |
| T_d | Tetrahedral symmetry |
| T_D | Dead time |
| T_{IS} | Cross-relaxation rate |
| T_{iso} | Isotropic or scalar value for T |
| TOF | Transmitter offset |
| T_p | Duration of the <i>rf</i> pulse |
| V | Electric field gradient tensor |
| V_{ii} | Principal components of V , where $i = X, Y, Z$; also written as eq_{ii} |
| V_{ZZ} | Largest component of the EFG tensor, V |
| x, y, z | Cartesian coordinates |

Z Atomic number

zcw Class of crystal file used in SIMPSON simulations

Chapter 1: Introduction and Objectives

1.1. Historical Overview

In contrast to many of the world's greatest scientific discoveries, the nuclear magnetic resonance (NMR) phenomenon is one that was predicted before it was observed. The early history of NMR¹ is somewhat obscure and no single person or event deserves credit for the discovery. Instead, a series of theoretical and experimental findings of extraordinary scientists eventually unveiled the NMR experiment.

The origin of NMR arguably lies in the discovery of electron and nuclear "spin" in quantum mechanics in 1927² and 1933,³ respectively. Subsequently, in 1936, a leading Dutch physicist, C. J. Gorter, attempted to measure "nuclear paramagnetism" in bulk matter using a resonance method. Gorter recognized that when a bulk sample is placed in a magnetic field, B_0 , a nuclear spin transition should occur at the Larmor⁴ frequency when an oscillating radiofrequency (*rf*) field, B_1 , is applied perpendicular to B_0 ; his objective was to measure the heat absorbed during this process using a sensitive calorimetric method. Gorter's attempts included measuring the ^1H and ^7Li resonances in $\text{KAl}(\text{SO}_4)_2 \cdot 12\text{H}_2\text{O}$ and LiF , respectively, at a temperature range of 14-20 K. The experiments were not successful; nevertheless, Gorter published his results.⁵ The negative results were later attributed to long spin-lattice relaxation (T_1) times — a problem that was amplified by working with "pure" samples and at low temperatures. Although unsuccessful, the potential of the resonance method was recognized by Gorter, who encouraged others to exploit the experiment. One researcher who was influenced by Gorter was Isidor I. Rabi - an expert in atomic and molecular beam experiments responsible for the first measurements of ^1H and ^2H magnetic moments, μ_N . Rabi's goal was to devise a method to obtain more precise measurements for $\mu_N(^1\text{H})$ and $\mu_N(^2\text{H})$. After Gorter suggested that Rabi employ the resonance experiment, Rabi and his colleagues were successful in observing the first nuclear magnetic resonance (NMR) signal in a molecular beam of LiCl in 1938. The results were published in a paper entitled, "A New Method of Measuring Nuclear Magnetic Moments".⁶ While this work earned Rabi the Nobel Prize in Physics in 1944, Gorter's contribution to the NMR

experiment often goes unrecognized, apart from an acknowledgement in Rabi's manuscript.*

With the outbreak of World War II, the next milestone discoveries related to NMR were forcibly delayed; however, in 1945, the first NMR signals in bulk materials were observed simultaneously and independently by two research groups. At Harvard University, Pound, Torrey and Purcell⁷ observed the ¹H NMR signal of a bulk sample of solid paraffin wax and at Stanford University, Bloch, Hansen, and Packard⁸ observed the ¹H NMR signal of liquid water. Although the first NMR experiments of solids and liquids occurred essentially simultaneously, their respective fields progressed at different rates. Initial NMR studies were conducted on solid samples and focused on measuring nuclear magnetic moments; peripheral research interests involved relaxation,⁹ molecular motion and the determination of molecular structure.¹⁰ While the physics community was elated by these observations, others were skeptical and questioned the diversity and utility of a technique whose main application was to measure nuclear magnetic moments.

A major breakthrough in NMR transpired in 1950 with the observation that nuclei in different chemical environments give rise to slightly different resonance frequencies, termed "chemical shifts".^{11,†} With this discovery, the potential of NMR as a characterization tool for molecular structure was realized and NMR spectroscopy would soon become a technique widely used by scientists of all disciplines, particularly chemistry, physics and medicine. The discovery of the chemical shift, together with the improved resolution of NMR spectrometers, sparked new interest in NMR studies of liquid samples. In contrast to the characteristic broad lines produced in solids, NMR of liquids produced highly-resolved spectra, enabling straightforward and efficient acquisition and facile spectral assignments. Consequently, the popularity of solid-state NMR for chemists declined until the development of two ingenious techniques: magic-angle spinning (MAS)¹² and cross-polarization (CP).¹³ The rapid spinning of solid

* In response to Rabi's publication, Gorter replied, "I cannot deny that I felt some pride, mixed with the feeling that my contribution was somewhat undervalued though my advice was acknowledged in the Letter."

† The phenomenon of a "nuclear magnetic resonance shift" was first observed in a series of metals and was reported the previous year by W. D. Knight, but, in the study of metals, the term "Knight shift" is generally used; see: Knight, W. D. *Phys. Rev.* **1949**, *76*, 1259-1260.

samples resulted in high-resolution NMR spectra which emulated those obtained from solutions, while CP allowed significant signal enhancements. With the discovery of MAS and CP, interest in solid-state NMR was rejuvenated.

Other important highlights in the history of NMR include the development of pulse techniques, such as the spin-echo experiment (1950),¹⁴ the discovery of field-independent frequency modulation, termed “scalar” or “spin-spin couplings” (1951),¹⁵ and pulsed Fourier¹⁶ transform (FT) detection (1966),¹⁷ the latter of which enhanced the sensitivity and efficacy of the MR technique by enabling simultaneous excitation and detection, rather than the traditional continuous wave method. Although paramount, the impact of FT on the field of NMR and other types of spectroscopy was, like many milestone discoveries, not realized *a priori*.*

During the 1970s, MR imaging (MRI) was introduced and the first MR experiments on tissues in test tubes were demonstrated, and, soon after, whole-body samples were investigated. In the 1980s, the development of sophisticated and elegant multiple-dimensional pulse sequences emerged, opening new avenues of research, such as the study of complex biological systems in solution. Other landmarks include many significant technological improvements and advances, ranging from the design and construction of multi-channeled probes to the production of homogeneous and stable superconducting magnets with "ever-increasing" field strength.

Together, these discoveries and developments have revolutionized the field of nuclear magnetic resonance spectroscopy, creating a powerful technique that has become an indispensable tool for many scientists. The success of NMR spectroscopy is evidenced by the five Nobel prizes awarded to renowned and respected pioneers in the field: Isaac I. Rabi (Physics, 1944); Felix Bloch and Edward M. Purcell (Physics, 1952); Richard R. Ernst (Chemistry, 1991); Kurt Wüthrich (Chemistry, 2002); Paul C. Lauterbur and Sir Peter Mansfield (Medicine, 2003). In a matter of decades, NMR has grown from

* Ironically, Ernst's paper describing the FT achievements was rejected twice by the *Journal of Chemical Physics*, but was eventually accepted and published in the *Review of Scientific Instruments*.¹⁷ In Ernst's autobiography, he wrote, "It took many years before in the competitive company Bruker Analytische Messtechnik...demonstrated in 1969 for the first time a commercial FT NMR spectrometer to the great amazement of Varian that had the patent rights on the invention." Quote from *Les Prix Nobel. The Nobel Prizes 1991*, Tore Frängsmyr, Ed. Nobel Foundation, Stockholm, 1992.

a postulated phenomenon to an rapidly expanding and multi-faceted field, and today, is deemed by many to be the most important and powerful characterization tool available.

Modern-day NMR spectroscopy is continuously expanding, supporting the claim that NMR is an evergreen. Although NMR of any state of matter, whether gas, liquid, liquid-crystal, or solid, is linked by the intricacies of the fundamental theories, research for each has grown into its own established and distinct field, each with many subdivisions. For many scientists, chemists included, the differences between NMR of solids and liquids are not well known; hence, the advantages of one technique over the other are not fully understood. In general, NMR interactions have an anisotropic nature and are properly described by second-rank tensors; *i.e.*, by their magnitude and direction.¹⁸ In isotropic fluids, the molecules tumble rapidly and randomly, resulting in an averaging of the NMR interactions to their isotropic, or scalar, values. While this simplifies NMR spectra and results in highly-resolved signals, a great deal of information is lost through the averaging process. In solids, however, the molecules are relatively rigid so that information involving the various NMR interactions is preserved in their "full forms"; hence, rather than scalar values, solid-state NMR offers the second-rank NMR interaction tensors. By characterizing these tensors and learning about the orientation dependence of these interactions, a more complete understanding of the system is obtained, which is not available from a solution NMR study.

There are several practical benefits of employing solid-state over solution NMR: first, samples are often insoluble or air- or moisture-sensitive and thus require special handling procedures and sample-holders; dealing with such samples is generally more straightforward in the solid state. Second, many compounds do not maintain their solid-state structure or are unstable when dissolved in solvent; hence, the desired structural information is unavailable from solution NMR. Third, the dynamics observed in solution NMR are often obscured by interactions with the solvent and cannot always be interpreted as the true dynamics of the system. Solid-state NMR may therefore be the technique of choice, in many cases, allowing both molecular and electronic structural information to be obtained through the analysis of the full NMR interactions.

1.2. Objectives and Thesis Outline

This *Thesis* focuses on solid-state NMR investigations of a class of nuclei that are rarely examined by NMR because of the experimental challenges they present due to their unfavorable nuclear properties; namely, their low resonance frequency, moderate to large nuclear quadrupole moment, low natural abundance, or combinations thereof. The Group VI transition metal elements, ^{53}Cr and ^{95}Mo , and the noble gas nuclide, ^{131}Xe , are a large focus of the research presented herein. A second magnetically-active isotope of xenon that is examined is ^{129}Xe , a spin-1/2 nucleus that has comparatively favourable NMR properties, yet few solid-state ^{129}Xe NMR studies of Xe compounds have been reported.

Specifically, this *Thesis* involves the experimental determination and theoretical interpretation of the nuclear magnetic shielding, σ , electric field gradient, EFG, and indirect nuclear spin-spin coupling, J , tensors for the aforementioned nuclei: $^{129/131}\text{Xe}$, ^{95}Mo and ^{53}Cr . To achieve this, the experimental obstacles presented by these nuclei must be circumvented. The research presented herein demonstrates that by employing alternative experimental methods and modern technology, the study of "challenging nuclei" by solid-state NMR is possible. For example, conducting experiments at the highest possible magnetic field strengths, employing available sensitivity-enhancement techniques and examining a select group of compounds of appropriately high molecular symmetry has allowed solid-state NMR studies to be successfully executed.

In addition to multi-nuclear solid-state magnetic resonance investigations, a second component of this *Thesis* is dedicated to computational studies using, principally, the zeroth-order regular approximation density functional theory (ZORA DFT) method. Computational chemistry has proven to be an essential tool in the research presented herein by complementing experimental data and providing key information concerning the molecular and electronic structure, which is critical in solving experimental problems.

This *Thesis* is partitioned as follows: the basic principles of NMR are discussed in *Chapter 2* to provide a foundation for the research presented herein. The theory describing the relevant nuclear spin interactions is discussed, as well as the influence of the interactions on NMR lineshapes. *Chapter 3* deals with the experimental and computational methods utilized in this work. The standard techniques employed in solid-

state NMR, as well as a proposed experimental strategy for observing low-frequency quadrupolar nuclei, are discussed. A summary of data processing and interpretation is provided and the chapter concludes with a discussion of high-level quantum computations of NMR parameters. In *Chapters 4, 5, and 6*, results from solid-state $^{129/131}\text{Xe}$, ^{95}Mo , and ^{53}Cr NMR studies of model compounds are presented, as outlined below.

Solid-state Xe NMR studies of xenon difluoride and sodium perxenates are the focus of *Chapter 4*. The spin-1/2 isotope, ^{129}Xe , is examined to measure the Xe shielding tensor and the ^{129}Xe , ^{19}F indirect spin-spin coupling tensor, $^1J(^{129}\text{Xe}, ^{19}\text{F})$ for XeF_2 . The Xe shielding tensor is characterized experimentally and theoretically and the role of relativistic effects in determining magnetic shielding tensors for heavy atoms is investigated. Following this study, the two magnetically active Xe isotopes, $^{129/131}\text{Xe}$, are exploited to examine two forms of sodium perxenate, $\text{Na}_4\text{XeO}_6 \cdot x\text{H}_2\text{O}$, ($x = 0, 2$), which possess octahedral and distorted-octahedral symmetry, respectively. Solid-state ^{129}Xe and ^{131}Xe NMR studies allow the Xe shielding and EFG tensors to be effectively separated and independently characterized. These results provide insight towards the local Xe environment in $\text{Na}_4\text{XeO}_6 \cdot x\text{H}_2\text{O}$ ($x = 0, 2$) and demonstrate the acute sensitivity of the Xe quadrupolar interaction to small structural changes.

Chapter 5 presents solid-state ^{95}Mo NMR studies of a series of approximately tetrahedral molybdate ions, MoO_4^{2-} , followed by an experimental and computational investigation of two forms of octacyanomolybdate(IV) anions, $\text{Mo}(\text{CN})_8^{4-}$, which possess approximately dodecahedral, D_{2d} , and square antiprismatic, D_{4d} , symmetry. In the former study, the relative importance of the Mo shielding anisotropy and quadrupolar interactions is investigated and, in the latter, the accuracy of the "Point-Charge Approximation" in predicting EFGs is assessed through an experimental and elaborate computational investigation.

Chapter 6 involves solid-state ^{53}Cr NMR studies of a series of chromate, CrO_4^{2-} , and dichromate, $\text{Cr}_2\text{O}_7^{2-}$ salts, as well as computational investigations of the dependence of the Cr shielding and EFG tensors on distortions of the chromate and dichromate anions.

The highlights and limitations of the research presented in this *Thesis* are summarized in the concluding chapter, *Chapter 7*. In addition, the prospects of continued studies in this area are critically evaluated.

Chapter 2: The Fundamentals of Nuclear Magnetic Resonance Spectroscopy

2.1. The NMR Hamiltonian

In this Chapter, the fundamental internal and external NMR interactions that are important in the study of solid samples are discussed. The differences between solution and solid-state NMR are highlighted and some practical considerations for investigating solid samples are outlined.

For a given nucleus in a solid, the total NMR Hamiltonian is given by:

$$\hat{H}_{\text{total}} = \hat{H}_Z + \hat{H}_S + \hat{H}_Q + \hat{H}_J + \hat{H}_D, \quad (2.1)$$

where \hat{H}_Z denotes the Zeeman¹⁹ interaction, \hat{H}_S , the magnetic shielding interaction, \hat{H}_Q , the quadrupolar interaction, and \hat{H}_J and \hat{H}_D , the indirect and direct spin-spin coupling interactions, respectively. A common characteristic of all internal NMR interactions is that their Hamiltonian may be expressed in the following general form:²⁰

$$\hat{H}_{\text{NMR}} = I_N \cdot \mathbf{T} \cdot X = \begin{bmatrix} I_{N,x} & I_{N,y} & I_{N,z} \end{bmatrix} \cdot \begin{bmatrix} T_{xx} & T_{xy} & T_{xz} \\ T_{yx} & T_{yy} & T_{yz} \\ T_{zx} & T_{zy} & T_{zz} \end{bmatrix} \cdot \begin{bmatrix} X_x \\ X_y \\ X_z \end{bmatrix}, \quad (2.2)$$

where I_N and X are first-rank tensors, or vectors: I_N is the spin vector for nucleus N, X depends on the specific NMR interaction and may be an internal-spin or external vector, and \mathbf{T} is a second-rank tensor describing the NMR interaction of interest; see Table 2.1. It is evident from Eq. (2.2) that all NMR interactions have both magnitude and direction. The main difference between NMR of isotropic liquids and solids is the amount of

Table 2.1: Summary of Internal NMR Interactions; see Equations (2.1) and (2.2).

| NMR Interaction | \mathbf{T} | X | T_{iso} |
|------------------------------------|--------------|----------|-----------------------|
| <i>Magnetic Shielding</i> | σ | B_0 | σ_{iso} |
| <i>Quadrupolar</i> | \mathbf{V} | I_N | 0 |
| <i>Direct Spin-Spin Coupling</i> | \mathbf{D} | $I_{N'}$ | 0 |
| <i>Indirect Spin-Spin Coupling</i> | \mathbf{J} | $I_{N'}$ | J_{iso} |

information that is available from the NMR spectra. In solution, the molecules are tumbling randomly and rapidly, resulting in an averaging of the interactions to their isotropic values, T_{iso} . Depending on the specific interaction, T_{iso} may be zero (Table 2.1). In the solid state, however, the orientation of molecules relative to the external, applied magnetic field, B_0 , is fixed, allowing the NMR interactions to be observed in their tensorial form and, thus, their magnitudes and orientations to be characterized. Typical magnitudes and lineshapes for the following interactions, V , σ , D , and J , are shown in Figure 2.1. When several NMR interactions are present, complex NMR lineshapes often result, making spectral analyses challenging.

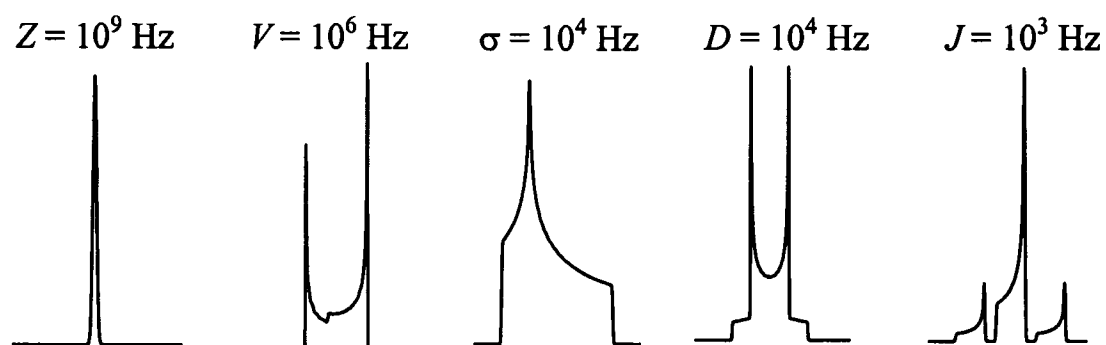


Figure 2.1: Typical solid-state NMR lineshapes and magnitudes for the (L-R): Zeeman, quadrupolar (showing *only* the central, $m_1 = +1/2 \leftrightarrow -1/2$, transition for a spin- $n/2$ nucleus), anisotropic magnetic shielding, direct spin-spin coupling, and indirect spin-spin coupling interactions.

2.2. Euler Angles

If two or more NMR interactions contribute to a given NMR spectrum, their respective magnitudes and orientations must be determined; in addition, the relative orientation of the two, or more, tensors must be considered since their coordinate systems are not necessarily coincident. To describe the relative orientations of two three-dimensional coordinate systems that share a common origin, a series of rotations, defined by the so-called Euler angles, α , β , and γ , is employed. The possibility of non-coincident coordinate systems in NMR was first recognized in 1990 at a time when NMR of solids was relatively mature.²¹ It was found that, for sites of low-symmetry, the coordinate systems of NMR tensors often deviate from coincidence and, hence, the Euler angles are

necessary to describe the relative orientation of the tensors. Determining the Euler angles was both an experimental problem and computational challenge which required newly developed and time-intensive software to solve; luckily, the implementation of fast algorithms greatly reduced computational time for spectral simulations.

Unfortunately the definition of Euler angles is not universal, and several conventions exist. That which will be used herein is the convention of Rose,²² referred to as *passive rotations* by Duer,²³ whereby a right-handed, mathematically-positive sense of rotations, occurring in a counter-clockwise fashion, is employed. The progression of rotations, (α, β, γ) , is shown in Figure 2.2, where the original coordinate system is defined by (x_1, y_1, z_1) . The first rotation, α , occurs about the original z_1 -axis to give a new coordinate system, (x_2, y_2, z_2) . The second rotation, β , involves a counter clock-wise rotation about y_2 to yield (x_3, y_3, z_3) and the third rotation, γ , takes place about z_3 , yielding

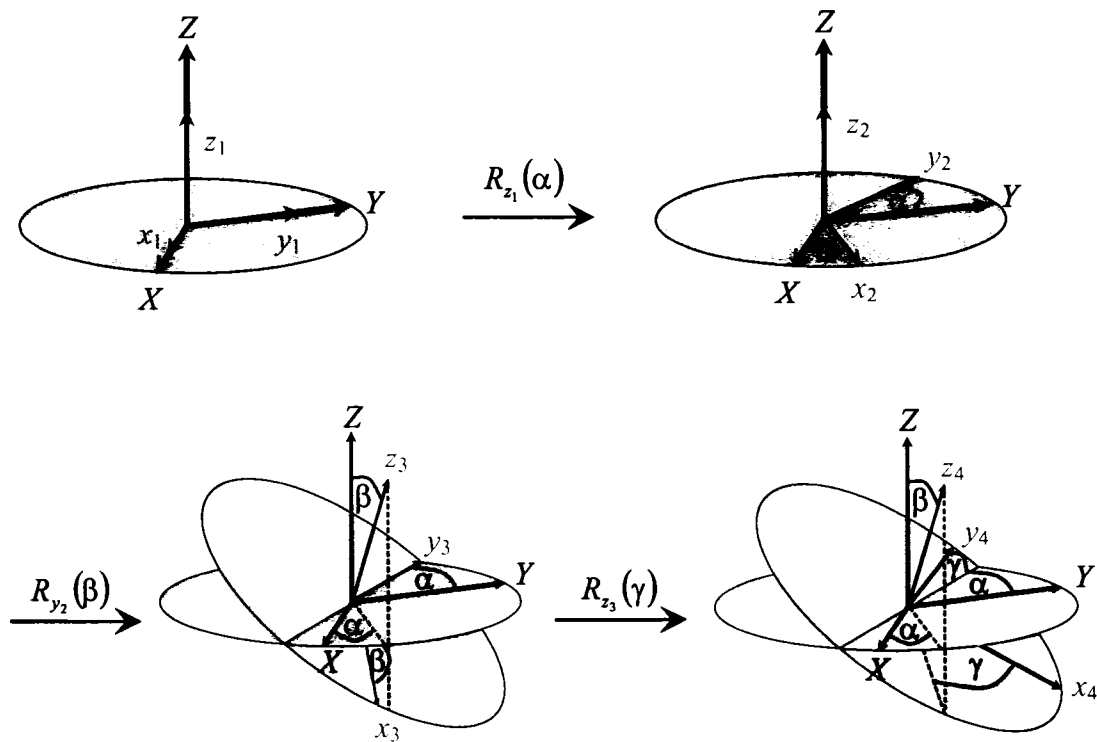


Figure 2.2: Schematic representation of the Euler angles (α, β, γ) which describe the relative orientations of coordinate systems (x_1, y_1, z_1) and (x_4, y_4, z_4) ; see text for further description.

the final coordinate system, (x_4, y_4, z_4) . Together, these angles allow the coordinate system (x_1, y_1, z_1) to be mapped onto that for (x_4, y_4, z_4) .

The relative orientation of NMR tensors may dramatically affect solid-state NMR lineshapes and are generally determined using computer simulations. The ranges for the Euler angles are: $0 \leq \alpha, \gamma \leq 360^\circ$ and $0 \leq \beta \leq 180^\circ$; however, restrictions are often placed on the Euler angles, depending strictly on the site symmetry of the nucleus in the crystal lattice. Consider an example where the observe nucleus is positioned on a mirror plane and two NMR interactions, \mathbf{T}_A and \mathbf{T}_B , are present. To describe the relative orientation of \mathbf{T}_A and \mathbf{T}_B , the site symmetry of the observe nucleus is first considered. The presence of a mirror plane requires that one principal component of \mathbf{T}_A and one principal component of \mathbf{T}_B must be perpendicular to the mirror plane. The remaining two principal components from \mathbf{T}_A and \mathbf{T}_B must lie in the plane of the mirror, but are not necessarily coincident, so the remaining Euler angles are not restricted. Another common symmetry element that dictates the relative orientation of \mathbf{T}_A and \mathbf{T}_B is a C_n -axis. If the observe nucleus is positioned on a C_n -axis, then one principal component of \mathbf{T}_A and \mathbf{T}_B must be collinear with the C_n -axis and the remaining components are perpendicular to the C_n -axis, but are not necessarily coincident. These examples demonstrate that symmetry aids in the determination of Euler angles by significantly reducing the number of possible values for α , β , and γ . When symmetry does not dictate the relative orientation of two tensors, the Euler angles are determined by manual iteration and visual inspection of the calculated (simulated) spectrum compared to experiment. In these circumstances, the accuracy of the solution is increased by performing experiments at two or more applied magnetic fields.

2.3. Zeeman Interaction

The fundamental interaction responsible for the nuclear magnetic resonance phenomenon is the Zeeman interaction, $\hat{\mathcal{H}}_Z$, which involves the interaction of a nuclear magnetic moment, μ_N , and B_0 . By convention, the direction of B_0 is taken as the z -direction and the Zeeman Hamiltonian is given by:

$$\hat{\mathcal{H}}_Z = -\mu_N \cdot B_0 = -\gamma_N \hbar B_0 \hat{I}_Z, \quad (2.3)$$

where γ_N is the magnetogyric ratio of nucleus, N , \hat{I}_z is the azimuthal spin angular momentum operator in the z -direction, with eigenvalue m_I , which can take on $(2I + 1)$ values from $-I$ to $+I$, and \hbar is the reduced Planck's constant, $h/2\pi$. The Zeeman energy level diagram for an isolated spin-1/2 nucleus is shown as a function of B_0 in Figure 2.3. The eigenfunctions, $|I, m\rangle$, associated with \hat{H}_z describe the possible nuclear spin states of a particular spin system in an applied magnetic field and the eigenvalues are the nuclear spin energy levels corresponding to these states,

$$E_{m_I} = -\gamma_N \hbar B_0 m_I. \quad (2.4)$$

The nuclear spin energy levels, $m_I = +1/2$ and $m_I = -1/2$, are quantized and allowed transitions must satisfy the selection rule, $\Delta m_I = \pm 1$, hence:

$$\Delta E = h \nu_L = \gamma_N \hbar B_0, \quad (2.5)$$

where ν_L is the Larmor frequency of nucleus, N . Figure 2.3 and Eq. 2.5 explicitly demonstrate that ΔE is directly proportional to B_0 .

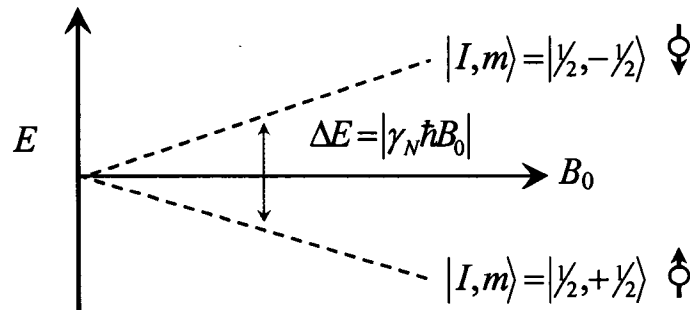


Figure 2.3: Zeeman energy level diagram for a spin-1/2 nucleus demonstrating the separation of nuclear spin states, $|I, m\rangle$, as a function of B_0 .

The nuclear spin energy level diagram depicted in Figure 2.3 represents the simplest system in NMR, *i.e.*, that describing non-interacting spin-1/2 nuclei in a uniform, external magnetic field. At thermal equilibrium there exists a Boltzmann distribution of nuclear spins over the two possible states, $m_I = +1/2$ and $m_I = -1/2$, and the relative population, p , of these two states is given by:

$$\frac{p_{+1/2}}{p_{-1/2}} = \exp\left(\frac{\Delta E}{kT}\right) = \exp\left(\frac{\gamma_N \hbar B_0}{kT}\right). \quad (2.6)$$

One can calculate the population difference, Δp , for a particular spin-1/2 isotope at a given B_0 and T . Consider ^1H at 18.8 T and at room temperature, 298 K. Assuming a total of 10^6 protons, Δp is only 64! From equation 2.6, one can see that it is preferable to employ the highest possible applied magnetic field strengths and the lowest temperatures since this amplifies the population difference and leads to a stronger NMR signal. Currently, the strongest superconducting magnets are approaching 1.0 GHz; *i.e.*, $B_0 \sim 23.5$ T.

The remaining NMR interactions, listed in Table 2.1, are perturbations to \hat{H}_z ; the presence, magnitudes, and orientations of these interactions (Figure 2.1) can be determined upon analysis of the observed NMR lineshapes. Each interaction provides unique and complementary information about the local molecular and electronic structure.

2.4. Nuclear Magnetic Shielding and the Chemical Shift^{24,25,26}

If it were not for the nuclear magnetic shielding interaction, σ , the resonance frequency of a particular isotope would be independent of its chemical surroundings and NMR would be of little use to chemists. Fortunately, σ acts as a discrete sensor of the local nuclear environment for NMR-active nuclei; for this reason, σ is deemed to be the most important fundamental interaction in NMR spectroscopy. The σ Hamiltonian, given in units of energy, is:

$$\hat{H}_s = -\gamma_N \hbar I_z \cdot \sigma \cdot B_0, \quad (2.7)$$

where σ is the nuclear magnetic shielding tensor. The origin of the shielding interaction lies in the small, secondary magnetic fields (B') that are created at a nucleus due to the circulation of electrons in a molecule placed in an external magnetic field. These secondary fields oppose the applied magnetic field and change the resonance condition of the nucleus, thereby allowing different nuclear sites to be distinguished based on their signature shielding values (or, equivalently, chemical shift values; *vide infra*).

The magnetic shielding interaction may be described by a general second-rank tensor with up to nine unique components, $\sigma_{\alpha\beta}$:

$$\sigma = \begin{bmatrix} \sigma_{xx} & \sigma_{xy} & \sigma_{xz} \\ \sigma_{yx} & \sigma_{yy} & \sigma_{yz} \\ \sigma_{zx} & \sigma_{zy} & \sigma_{zz} \end{bmatrix}, \quad (2.8)$$

which may be decomposed into symmetric (σ_{sym}) and antisymmetric (σ_{antisym})^{24b} components; however, the discussion herein is limited to the symmetric components, since σ_{antisym} does not affect NMR spectra to first order.^{24,27} To characterize σ , an axis system, called the principal axis system, PAS, is defined such that σ_{sym} is diagonal; *i.e.*, the off-diagonal components are equal to zero and the diagonal entries are the *principal components*: σ_{11} , σ_{22} , and σ_{33} , with the convention that: $\sigma_{33} \geq \sigma_{22} \geq \sigma_{11}$.²⁸ If the molecule possesses sufficiently high nuclear site symmetry, then the number of elements

Table 2.2: Non-Vanishing Components of the Nuclear Magnetic Shielding Tensor, σ , for Selected Nuclear Site Symmetries.²⁸

| <i>Nuclear Site Symmetry</i> | <i>Number of Non-vanishing Components</i> | | <i>Non-vanishing Components</i> |
|---|---|--------------------|---|
| | <i>Total</i> | <i>Independent</i> | |
| C_1, C_i | 9 | 9 | $\sigma_{11}, \sigma_{12}, \sigma_{13}, \sigma_{21}, \sigma_{22}, \sigma_{23}, \sigma_{31}, \sigma_{32}, \sigma_{33}$ |
| C_2, C_s, C_{2h} | 5 | 5 | $\sigma_{11}, \sigma_{12}, \sigma_{21}, \sigma_{22}, \sigma_{33}$ |
| $C_3, C_{3h}, C_4, C_{4v}, C_6, C_{6h}, S_4, S_6$ | 5 | 3 | $\sigma_{11} = \sigma_{22}, \sigma_{12} = -\sigma_{21}, \sigma_{33}$ |
| C_{2v}, D_2, D_{2h} | 3 | 3 | $\sigma_{11}, \sigma_{22}, \sigma_{33}$ |
| $C_{3v}, C_{4v}, C_{6v}, C_{\infty v}, D_{2d}$ | 3 | 2 | $\sigma_{11} = \sigma_{22}, \sigma_{33}$ |
| $D_3, D_{3d}, D_{3h}, D_4, D_{4h}, D_6, D_{6h}, D_{\infty h}$ | 3 | 1 | $\sigma_{11} = \sigma_{22} = \sigma_{33}$ |

* The non-vanishing components are shown for one specific orientation of the shielding tensor, where $\sigma_{11} = \sigma_{22} < \sigma_{33}$, which is not a unique solution since $\sigma_{11} < \sigma_{22} = \sigma_{33}$ is possible; the latter orientation of the magnetic shielding tensor generates a new set of non-vanishing components that gives rise to the same number of independent components as the former.

required to characterize the shielding tensor may be reduced (Table 2.2). For example, a centrosymmetric linear molecule is described by the $D_{\infty h}$ point group and requires two non-vanishing components to characterize σ : σ_{\perp} and σ_{\parallel} , which describe the shielding when the molecule is aligned perpendicular and parallel to B_0 , respectively. On the other hand, a molecule possessing tetrahedral, T_d , symmetry requires only one non-vanishing component, since the shielding is independent of the molecular orientation with respect to B_0 ; as a result, the shielding is isotropic; *i.e.*, the same in all directions.

In isotropic liquids, rapid molecular tumbling averages σ and only the trace of the shielding tensor, σ_{iso} , is observed,

$$\sigma_{\text{iso}} = (\sigma_{11} + \sigma_{22} + \sigma_{33})/3. \quad (2.9)$$

This shielding value represents the average magnetic shielding at a nucleus with respect to the bare nucleus and is referred to as the *absolute shielding*. Absolute shielding values are difficult to calculate and are known for only a select number of light nuclei;²⁹ hence, experimentally one gauges the shielding at a nucleus in relative terms, described by the chemical shift, δ :

$$\delta_{\text{iso}} = \frac{\nu(\text{sample})_{\text{iso}} - \nu(\text{ref})_{\text{iso}}}{\nu(\text{ref})_{\text{iso}}} \times 10^6. \quad (2.10)$$

For solid samples, however, the orientation of molecules is generally fixed with respect to B_0 . The random orientation of crystallites in a powder sample causes nuclei in different molecules to experience different effective magnetic fields, giving rise to a distribution of chemical shift (shielding) values. The envelope of chemical shift values has a distinct lineshape and breadth, from which the principal components can, in principle, be determined: δ_{11} , δ_{22} , and δ_{33} , where $\delta_{11} \geq \delta_{22} \geq \delta_{33}$. To describe the chemical shift interaction, the convention of Mason³⁰ is employed where the breadth of the spectrum due to anisotropic magnetic shielding is expressed in terms of the *span*, Ω :

$$\Omega = \sigma_{33} - \sigma_{11} = \delta_{11} - \delta_{33}, \quad (2.11)$$

and the lineshape by the *skew*, κ ,

$$\kappa = \frac{3(\sigma_{\text{iso}} - \sigma_{22})}{\Omega} = \frac{3(\delta_{22} - \delta_{\text{iso}})}{\Omega}, \quad (2.12)$$

which can take on values of -1 to +1, inclusive.^{30,31} Typical solid-state NMR chemical shift powder patterns are shown in Figure 2.4 and the relevant shielding (chemical shift) parameters (δ_{ii} , δ_{iso} , Ω , κ) are indicated. The simulated NMR spectra shown in Figures 2.4(a, c) are said to have axially-symmetric shielding tensors since only two principal components are required to characterize σ , while the spectrum shown in Figure 2.4(b) has a non-axially symmetric shielding tensor which requires three independent δ_{ii} (σ_{ii}) values to describe σ .

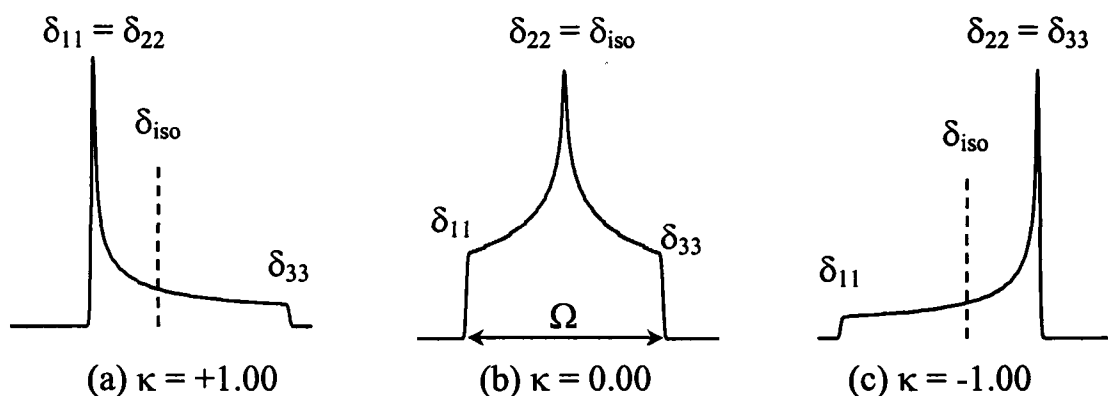


Figure 2.4: Typical solid-state NMR chemical shift powder patterns observed for isolated spin-1/2 nuclei: (a, c) axially-symmetric and (b) non-axially symmetric chemical shift tensors. The principal components, δ_{11} , δ_{22} , δ_{33} , are indicated, along with δ_{iso} , Ω and κ (see Eqs. (2.9) to (2.12)).

The convention of Haeberlen,^{24a} Mehring,¹⁸ and Spiess³² is an alternate and more cumbersome approach of describing the chemical shift interaction, where, the principal components are labelled and ordered according to: $|\delta_{ZZ} - \delta_{\text{iso}}| \geq |\delta_{YY} - \delta_{\text{iso}}| \geq |\delta_{XX} - \delta_{\text{iso}}|$. The isotropic value describes the center of gravity of the shielding tensor powder pattern and is given by, $\delta_{\text{iso}} = (\delta_{XX} + \delta_{YY} + \delta_{ZZ})/3$; the reduced anisotropy, $\delta_{\text{aniso}} = \delta_{ZZ} - \delta_{\text{iso}}$, and anisotropy, $\Delta\sigma = \delta_{ZZ} - (\delta_{XX} + \delta_{YY})/2 = 3\delta_{\text{aniso}}/2$, are used to describe the largest separation from the isotropic value and the sign of the anisotropy indicates whether the largest separation is to high or low frequency of δ_{iso} . Lastly, the asymmetry parameter, $\eta_{\text{CS}} = (\delta_{YY} - \delta_{XX})/\delta_{\text{aniso}}$, indicates the extent of deviation from axial symmetry and can take on values of 0 to 1, inclusive.

As mentioned in the *Introduction (Section 1.1)*, the chemical shift phenomenon was first observed in 1950.¹¹ Several years later, Norman Ramsey formalized the theory

of nuclear magnetic shielding.³³ This theory remains exact in the non-relativistic limit and, today, is regarded as being among the most influential in 20th century quantum chemistry.³⁴ According to Ramsey's formalism, σ may be partitioned into diamagnetic, $\sigma_{\alpha\beta}^{\text{dia}}$, and paramagnetic, $\sigma_{\alpha\beta}^{\text{para}}$, components, which depend on the electronic ground state, Ψ_0 , and n^{th} -excited electronic states, Ψ_n , respectively, of the molecule.^{28,35}

$$\sigma_{\alpha\beta} = \sigma_{\alpha\beta}^{\text{dia}} + \sigma_{\alpha\beta}^{\text{para}}, \quad (2.13)$$

where:

$$\sigma_{\alpha\beta}^{\text{dia}} = \frac{\mu_0}{4\pi} \frac{e^2}{2m} \left\langle \Psi_0 \left| \sum_k \frac{(\mathbf{r}_k \cdot \mathbf{r}_{kN} \mathbf{1} - \mathbf{r}_k \cdot \mathbf{r}_{kN})}{r_{kN}^3} \right| \Psi_0 \right\rangle \quad (2.14)$$

and

$$\sigma_{\alpha\beta}^{\text{para}} = -\frac{\mu_0}{4\pi} \frac{e^2}{2m^2} \sum_{n>0} \frac{1}{E_n - E_0} \left[\left\langle \Psi_0 \left| \sum_k \frac{l_{kN}}{r_{kN}^3} \right| \Psi_n \right\rangle \left\langle \Psi_n \left| \sum_k l_k \right| \Psi_0 \right\rangle + \left\langle \Psi_0 \left| \sum_k l_k \right| \Psi_n \right\rangle \left\langle \Psi_n \left| \sum_k \frac{l_{kN}}{r_{kN}^3} \right| \Psi_0 \right\rangle \right]; \quad (2.15)$$

here, μ_0 is the vacuum permittivity, e and m are the charge and rest mass of an electron, respectively, E_0 and E_n are the electronic energies for the ground state and the n^{th} excited electronic state, respectively, \mathbf{r}_k and \mathbf{r}_{kN} are the position vectors for electron k to the chosen origin (*i.e.*, the gauge origin) and to the observe nucleus, respectively, and l_k and l_{kN} are the electron angular momentum operators with respect to the gauge origin and observe nucleus, respectively. Equations (2.14) and (2.15) can be used to calculate all nine components of the shielding tensor in Eq. (2.8) by using the appropriate choice of indices, α and β , as well as \mathbf{r} and l . The diamagnetic term, $\sigma_{\alpha\beta}^{\text{dia}}$, is positive and exhibits small variations for any given element, while the paramagnetic term, $\sigma_{\alpha\beta}^{\text{para}}$, is usually negative and governs the shielding for any multi-electron molecular system. As evident from Equation 2.15, the paramagnetic term is governed by symmetry-allowed mixing of occupied and virtual orbitals that are centred on the nucleus of interest and the inverse of the energy difference between these states, $(E_n - E_0)^{-1}$. Thus, smaller ΔE values and greater overlap of molecular orbitals lead to a larger deshielding with respect to the bare nucleus.

2.5. Nuclear Electric Quadrupole Interaction^{23,36}

2.5.1. Quadrupolar Nuclei and Electric Field Gradients

Quadrupolar nuclei, $I > \frac{1}{2}$, possess an electrical quadrupole moment, Q , which arises from the anisotropic charge distribution about the nucleus. The quadrupole moment is often expressed as eQ , in which case the units are $C\ m^2$, given by:

$$eQ = \int \rho_n(\mathbf{r})(3z^2 - r^2) d\mathbf{r}, \quad (2.16)$$

where $\rho_n(\mathbf{r})$ is the nuclear charge density and the z -direction is parallel to the nuclear spin axis. Three different distributions of nuclear charge are depicted in Figure 2.5. For spin- $\frac{1}{2}$ nuclei, $\rho_n(\mathbf{r})$ is spherically symmetric, or isotropic, hence, $eQ = 0$ (Figure 2.5(b)); however, $\rho_n(\mathbf{r})$ may be distorted from the shape of a sphere to that of a football ($\rho_n(\mathbf{r})$ elongated along the spin-axis); these nuclei are termed “prolate” and, by convention, have $eQ > 0$ (Figure 2.5(a)). Nuclei with charge distributed in a disc shape ($\rho_n(\mathbf{r})$ contracted along the spin-axis) are termed “oblate” and have $eQ < 0$ (Figure 2.5(c)). Detailed descriptions of the internal structure of the nucleus consisting of protons and neutrons are generally not discussed in chemistry texts.

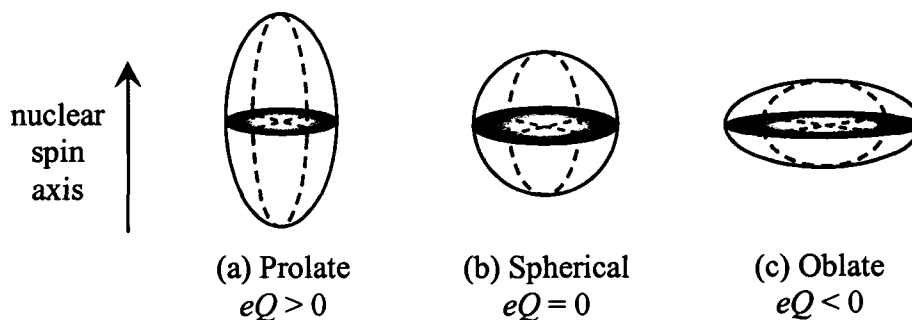


Figure 2.5: Depiction of nuclear charge distribution with respect to the nuclear spin-axis for (a,c) prolate and oblate quadrupolar nuclei, respectively, and (b) a spin- $\frac{1}{2}$ nucleus.

For quadrupolar nuclei, there is an interaction between the nuclear quadrupole moment, eQ , and the electric field gradient, EFG, at the quadrupolar nucleus referred to as the quadrupolar interaction. Approximately 85 % of the elements in the Periodic Table have at least one isotope that is quadrupolar, as indicated in Figure 2.6. Quadrupole moments are known to varying degrees of accuracy and are measured in

and must satisfy the condition: $V_{XX} + V_{YY} + V_{ZZ} = 0$; hence, V_{ZZ} may be positive or negative and $0 \leq \eta_Q \leq 1$.

A convenient measure of the EFG is the nuclear quadrupolar coupling constant, C_Q , which is generally expressed in frequency units, given by:

$$C_Q = \frac{eQV_{zz}}{h}; \quad (2.21)$$

Alternatively, the quadrupole frequency, $\nu_Q = 3C_Q/[2I(2I - 1)]$,³⁶ is used. The strength of the quadrupolar interaction is governed by both the quadrupolar moment, which is an intrinsic nuclear property, and the EFG, which is strictly dependent upon the chemical environment of the nucleus. There are special cases where the EFG at a nucleus in a molecule is necessarily zero; this will be discussed in *Section 2.5.3*. Quadrupolar coupling constants can be directly measured using solid-state NMR, nuclear quadrupole resonance (NQR), and microwave spectroscopy; as well, C_Q can be estimated using solution NMR and calculated using either the point-charge approximation (*Section 2.5.3*) or high-level quantum chemical computations (*Section 3.4*).

2.5.2. Quadrupolar Corrections to Zeeman Energy Levels

The quadrupolar interaction has important consequences in NMR spectra of quadrupolar nuclei, especially in the solid state. The Zeeman interaction splits the m_I energy levels into $(2I + 1)$ non-degenerate levels which are equally separated by the Larmor frequency of the observe nucleus; however, if the quadrupolar interaction is considered, the nuclear spin energy levels are perturbed, resulting in $2I$ single quantum transitions.

The nuclear spin energy level diagram for an $I = 3/2$ quadrupolar nucleus is shown in Figure 2.7, indicating the first-order quadrupolar corrections to the Zeeman energy levels; to determine these corrections, perturbation theory is applied. The resulting equations are valid in the high-field approximation, where the Zeeman interaction is much stronger than the quadrupolar interaction. The first-order quadrupolar Hamiltonian is given by:²³

$$h^{-1}\mathcal{H}_Q^{(1)} = \frac{C_Q}{8I(2I-1)} \left(3\hat{I}_z^2 - \hat{I}^2 \right) \left(3\cos^2\theta - 1 + \eta_Q \sin^2\theta \cos 2\phi \right), \quad (2.22)$$

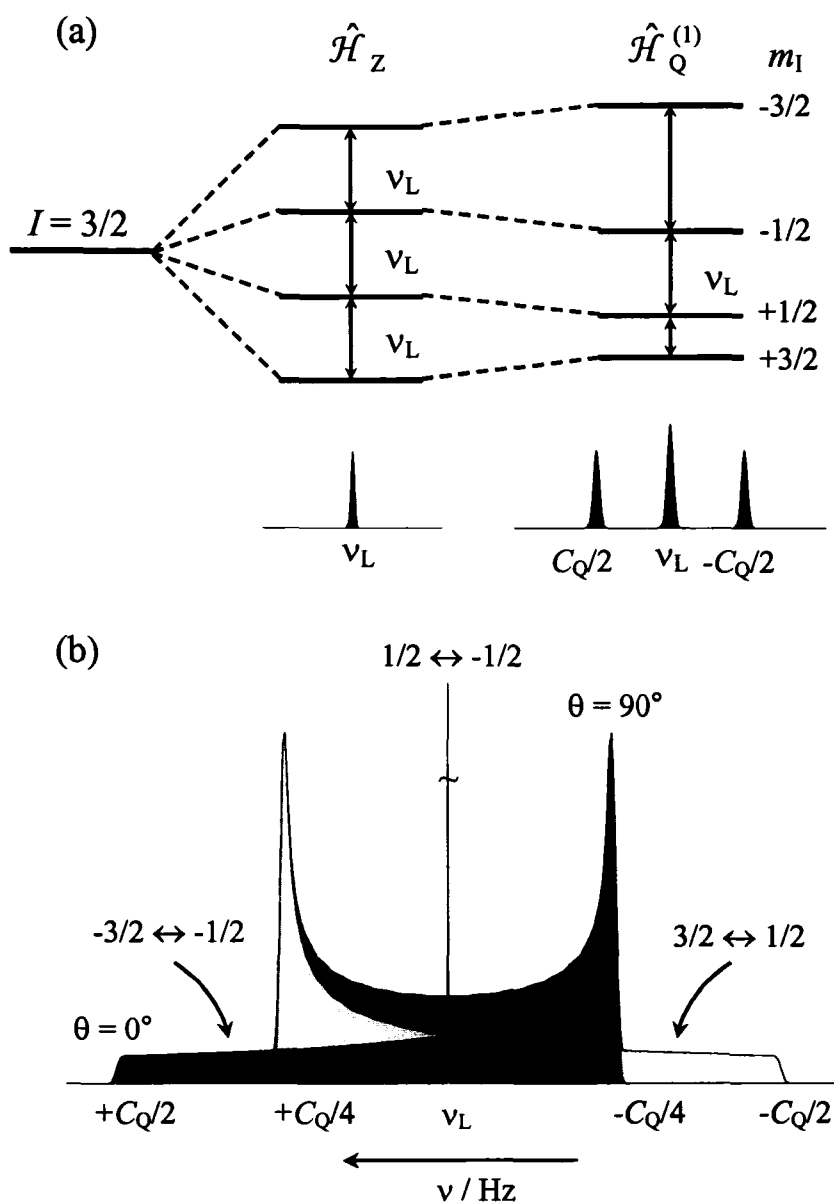


Figure 2.7: (a) Schematic nuclear spin energy level diagram for a spin-3/2 nucleus indicating the $(2I + 1)$ Zeeman energy states and the first-order quadrupolar corrections to these states; below are the expected NMR spectra for a single crystal sample. (b) A characteristic axially-symmetric quadrupolar powder pattern for a stationary sample of a spin-3/2 nucleus. The central transition, $m_I = +1/2 \leftrightarrow -1/2$, corresponds to the sharp, intense peak at ν_L and the satellite transitions, $m_I = +3/2 \leftrightarrow +1/2$ (\blacksquare) and $m_I = -3/2 \leftrightarrow -1/2$ (\blacktriangleleft), correspond to the broad, shaded areas. The sum of the satellite transitions to the overall spectrum (\blacksquare) is also shown. The indicated polar angles, $\theta = 0^\circ$ and $\theta = 90^\circ$, signify that V_{ZZ} is parallel and perpendicular to B_0 , respectively.

where \hat{I}_z^2 and \hat{I}^2 are the azimuthal and total spin angular momentum operators and θ and ϕ are the polar angles describing the orientation of the EFG tensor with respect to B_0 , as illustrated in Figure 2.8. In this discussion, an axially-symmetric EFG tensor is considered; *i.e.*, $\eta_Q = 0.0$, which simplifies Eq. (2.22) considerably. Replacing the nuclear spin angular momentum operators, \hat{I}_z^2 and \hat{I}^2 , in Eq. (2.22) with their corresponding eigenvalues, m_I^2 and $I(I + 1)$, it is obvious that the central transition is not perturbed by the quadrupolar interaction to first order. As depicted in Figure 2.7(a), both $m_I = +1/2$ and $-1/2$ are lowered in energy by the same extent and the corresponding transition frequency, ν_L , remains unchanged, whereas the $+3/2 \leftrightarrow +1/2$ and $-3/2 \leftrightarrow -1/2$ transitions, known as the satellite transitions, are perturbed.³⁶

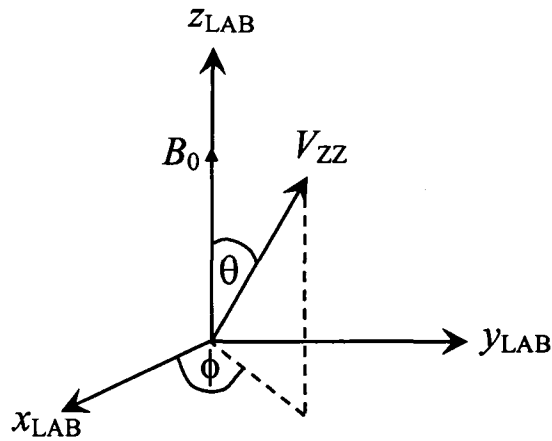


Figure 2.8: Projection of V_{ZZ} in the laboratory frame, indicating polar angles, θ and ϕ .

The resulting NMR spectrum of an $I = 3/2$ nucleus for a single crystal sample is shown in Figure 2.7(a) for a single orientation with respect to B_0 ($\theta = 0^\circ$). The spectrum consists of three peaks at ν_L and $\nu_L \pm C_Q/2$, which correspond to the central and satellite transitions, respectively. The NMR spectrum for the analogous powdered sample is shown in Figure 2.7(b); the broad, distinct lineshape is characteristic of an axially-symmetric EFG tensor for an $I = 3/2$ nucleus. In a powdered sample, the crystallites are randomly oriented with respect to B_0 and take on all possible values of θ and ϕ (Figure 2.8; Eq. 2.22), giving rise to a distribution of frequencies and resulting in a broad signal with a characteristic shape, often referred to as a "powder pattern". The intense,

featureless peak at ν_L represents the central transition and demonstrates the orientation-independence of this transition. The two satellite transitions are shaded in Figure 2.7(b) to illustrate their contributions to the overall spectrum, which is shaded in black. The inner and outer discontinuities of the satellite transitions, referred to as the “horns” and “shoulders”, represent orientations where crystallites are perpendicular, $\theta = 90^\circ$, and parallel, $\theta = 0^\circ$, to B_0 , and are indicated in Figure 2.7(b). Interestingly, for a quadrupolar lineshape with $\eta_Q = 1$, the frequency corresponding to $\theta = 90^\circ$ is coincident for the satellite transitions and equal to the center of gravity of the spectrum.

As a rule of thumb, first-order perturbation theory is adequate to describe the quadrupolar interaction when the quadrupole frequency, ν_Q , is much less than the Larmor frequency, ν_L . For cases where ν_Q is approximately one-tenth of ν_L , second-order, or higher-order,⁴⁰ perturbation theory must be applied. Second-order energy corrections to the Zeeman energy levels are:³⁶

$$E_{m_I}^{(2)} = -\left(\frac{\nu_Q^2}{12\nu_L}\right) m_I \left[\frac{3}{2} \mu^2 (1 - \mu^2) (8m_I^2 - 4a + 1) + \frac{3}{8} (1 - \mu^2)^2 (-2m_I^2 + 2a - 1) \right], \quad (2.23)$$

where $a = I(I + 1)$ and $\mu = \cos \theta$. The energy level diagram indicating first- and second-order corrections to the Zeeman energy levels for the central transition of an $I = 3/2$ nucleus is shown in Figure 2.9; also shown are typical NMR lineshapes obtained for a system described by \hat{H}_Z , $\hat{H}_Q^{(1)}$, and $\hat{H}_Q^{(2)}$.

Second-order quadrupolar effects are manifested in the central transition of a half-integer spin quadrupolar nucleus as a broadened peak with a distinct lineshape, as illustrated in Figure 2.9 for $\eta_Q = 0.0$. The breadth of the central transition for a stationary powder sample is given by:⁴¹

$$\Delta \nu_{(+\frac{1}{2} \leftrightarrow -\frac{1}{2})}^{\text{Stationary}} = \left(\frac{25 + 22\eta_Q + \eta_Q^2}{144} \right) \left(\frac{3C_Q}{2I(2I - 1)} \right)^2 \left(\frac{I(I + 1) - \frac{3}{4}}{\nu_L} \right). \quad (2.24)$$

Although the breadth of the $+m_I \leftrightarrow -m_I$ satellite transitions is similarly affected by the second-order quadrupolar interaction, one generally detects only the central transition since the satellite transitions are generally too broad for detection (on the order of ν_Q). In addition to the second-order quadrupolar broadening, there is a second-order quadrupolar

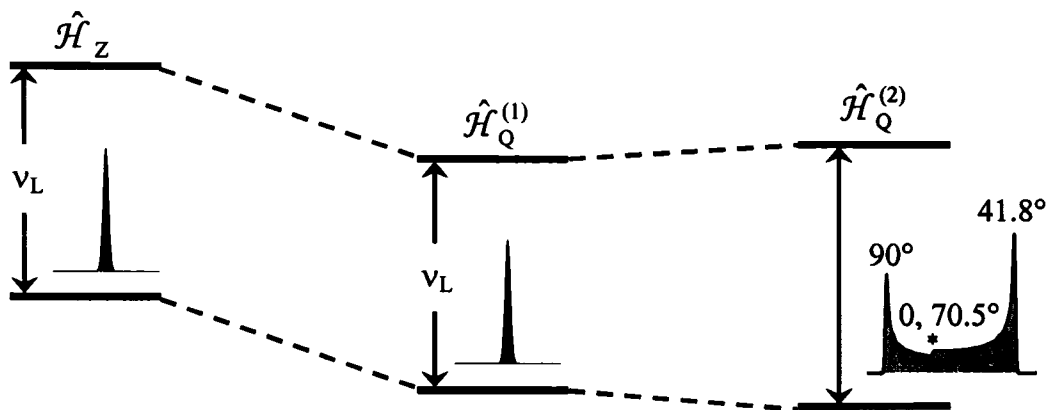


Figure 2.9: Nuclear spin energy level diagram and corresponding NMR lineshapes for the central transition of an $n/2$ -spin nucleus indicating first- and second-order quadrupolar corrections to the Zeeman energy levels. The inset corresponding to $\hat{H}_Q^{(2)}$ shows a typical second-order quadrupolar lineshape for $\eta_Q = 0$; the noted values represent the angle between V_{ZZ} and B_0 (*i.e.*, θ in Figure 2.8) and demonstrate the discontinuity of the second-order quadrupolar interaction.

shift, which shifts the center of gravity of the $m \leftrightarrow m-1$ transition, $\nu_{m,m-1}^{\text{CG}}$, relative to the isotropic chemical shift by:^{41,42}

$$\nu_{m,m-1}^{\text{CG}} - \nu_{\text{iso}} = -\frac{3}{40} \left(\frac{C_Q^2}{\nu_L} \right) \left\{ \frac{I(I+1) - 9m(m-1) - 3}{I^2(2I-1)^2} \right\} \left(1 + \frac{\eta_Q^2}{3} \right). \quad (2.25)$$

Upon analysis of the central transition NMR lineshape, δ_{iso} and the quadrupolar parameters, C_Q and η_Q , may be extracted. To aid in the determination of these parameters, samples are often oriented at $\sim 54.74^\circ$ with respect to B_0 , known as the "magic angle", and spun rapidly (on the order of kHz) (*vide infra*; Section 3.1.1). Rapid magic-angle spinning (MAS) does not completely average the quadrupolar interaction*

* Several methods have thus been devised to overcome this problem: double rotation (DOR), dynamic-angle spinning (DAS), and multiple-quantum magic-angle spinning (MQMAS). DOR works via simultaneous sample spinning about two rotation axes, while DAS involves two spinning axes, about which a sample is spun sequentially rather than simultaneously. Both methods work well in theory, but their implementation, in practice, requires specialized hardware and good fortune; hence, while elegant in theory, these techniques are simply impractical and have had little success. MQMAS, on the other hand, has received attention for its straightforward implementation as well as its efficacy; this two-dimensional method relies on quantum mechanical, rather than manual, manipulation, thereby allowing conventional MAS probes to be employed.

due to the presence of higher-order angular terms in Equation 2.23, but it does considerably reduce the linewidth, $\Delta \nu_{(+\frac{1}{2} \leftrightarrow -\frac{1}{2})}^{\text{MAS}}$, relative to $\Delta \nu_{(+\frac{1}{2} \leftrightarrow -\frac{1}{2})}^{\text{Stationary}}$.⁴¹

$$\Delta \nu_{(+\frac{1}{2} \leftrightarrow -\frac{1}{2})}^{\text{MAS}} = \left(\frac{(6 + \eta_Q)^2}{504} \right) \left(\frac{3C_Q}{2I(2I-1)} \right)^2 \left(\frac{I(I+1) - \frac{3}{4}}{\nu_L} \right). \quad (2.26)$$

Hence, in principle, MAS allows values of C_Q , η_Q , and δ_{iso} to be extracted with the use of computer simulations. Some drawbacks to MAS for the study of quadrupolar nuclei will be discussed in *Section 3.1.1*.

Typical central transition NMR lineshapes of static and MAS samples for spin- $n/2$ quadrupolar nuclei are shown in Figure 2.10 to illustrate the significant reduction in breadth upon employing MAS; the awkward units in the scale have been chosen to show the linear dependence of the breadth of the central transition on ν_L and the inverse dependence on ν_Q and I . Note, since ν_L is proportional to B_0 , second-order quadrupolar broadening is proportional to B_0^{-2} (in ppm) and B_0^{-1} (in Hz).

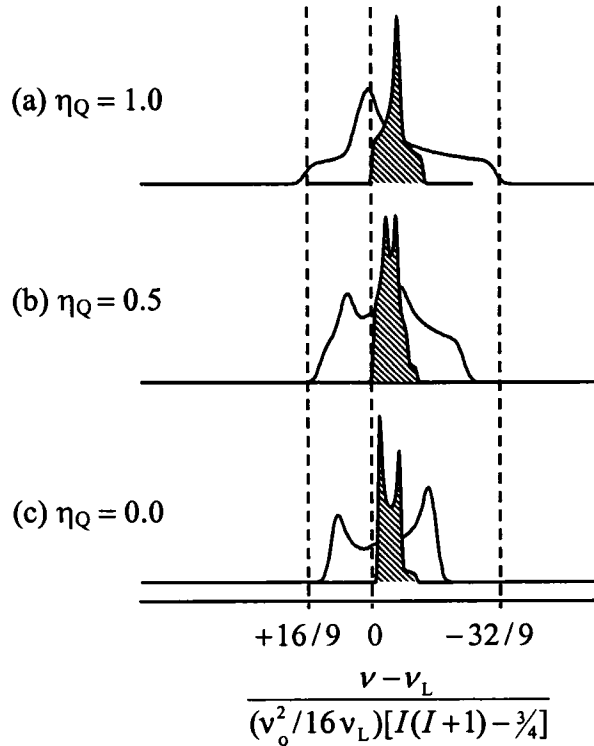


Figure 2.10: Typical central transition NMR lineshapes for $n/2$ quadrupolar nuclei for stationary (\square) and MAS (▨) samples; (a-c) $\eta_Q = 1.0, 0.5, 0.0$, respectively. The scale is inversely proportional to both I and ν_Q^2 .

From Eqs. (2.24) and (2.26), the nuclear spin quantum number, I , of the observe nucleus is another factor that determines the breadth of an NMR lineshape and thus, may limit the values of C_Q that can be successfully observed. Shown in Figure 2.11 is a plot of C_Q as a function of Larmor frequency for $n/2$ -spin quadrupolar nuclei with $n = 3, 5, 7$ and 9. The plot demonstrates that larger C_Q values can be measured for higher spin quantum numbers. Assuming $\nu_L = 25$ MHz and restricting $\Delta v_{(+1/2 \leftrightarrow -1/2)}^{\text{Stationary}}$ to 100 kHz results in measurable C_Q values ranging from approximately 5 MHz for $I = 3/2$ to 18 MHz for $I = 9/2$. Similarly, for $\nu_L = 200$ MHz, C_Q values of approximately 50 MHz and 10 MHz can be measured for $I = 9/2$ and $3/2$ nuclei, respectively.

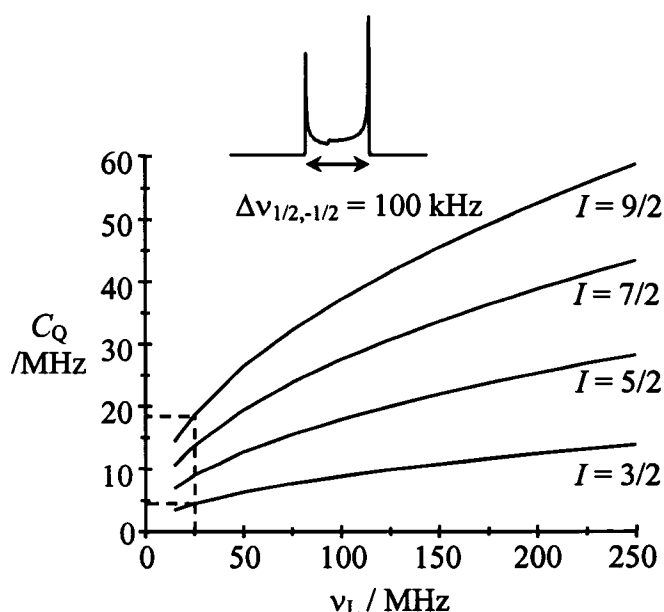


Figure 2.11: Dependence of C_Q on Larmor frequency for several $n/2$ -spin quadrupolar nuclei. The results were constructed using Eq. 2.25 and assuming $\Delta v_{(+1/2 \leftrightarrow -1/2)}^{\text{Stationary}} = 100$ kHz and $\eta_Q = 0.0$.

2.5.3. Point-Charge Approximation

As previously stated, certain molecular symmetries give rise to a zero EFG at a nucleus. The magnitude of the EFG can be estimated using a rudimentary method called the point-charge approximation (PCA). This involves a simple electrostatic modeling of ligands about a nucleus which provides a straightforward approach for estimating the

EFG at a nucleus. Each ligand is assigned a point charge and the principal components of the EFG tensor are subsequently calculated based on the atomic coordinates and the charge of ligands in the first coordination sphere. For example, in terms of spherical coordinates, the largest component of the EFG tensor, V_{ZZ} , may be calculated using:⁴³

$$V_{ZZ} = \sum_i \frac{e_i}{4\pi\epsilon_0} \frac{(3\cos^2\theta_i - 1)}{r_i^3}, \quad (2.27)$$

where e_i is the i^{th} charge at point (x_i, y_i, z_i) , r_i is the distance from charge i to the origin (x_0, y_0, z_0) , θ_i is the angle between vector r_i and the z -axis, and ϵ_0 is the vacuum permittivity; the remaining principal components, V_{XX} and V_{YY} , can be calculated in a similar manner. Using equation (2.27), it is straightforward to show that molecules possessing tetrahedral (T_d), octahedral (O_h), square prismatic (D_{4h}), and square

Table 2.3: Relative Values of V_{ZZ} at Nucleus "M" Calculated Using the PCA for Selected Complexes

| Complex | Nuclear Site Symmetry | Relative V_{ZZ} Values |
|--|-----------------------|--------------------------|
| Four Coordinate | | |
| MX_4 | T_d | 0 |
| MX_3Y | C_{3v} | 2 |
| MX_2Y_2 | C_{2v} | 2 |
| Six Coordinate | | |
| MX_5Y | C_{4v} | 2 |
| <i>trans</i> - MX_4Y_2 | D_{4h} | 4 |
| <i>cis</i> - MX_4Y_2 | C_{2v} | 2 |
| <i>mer</i> - MX_3Y_3 | C_{2v} | 3 |
| <i>fac</i> - MX_3Y_3 | C_{3v} | 0 |
| MX_6 | O_h | 0 |
| Eight Coordinate | | |
| MX_8 | O_h | 0 |
| MX_8 | D_{4d} | 0 |
| MX_8 | D_{2d} | $\neq 0$ |

antiprismatic (D_{4d}) symmetry have a zero EFG at M ; see Table 2.3.⁴⁴

Another way to interpret the zero EFG at M for the special case of square antiprismatic symmetry (D_{4d}) is to predict the values of the principal components of the EFG tensor using symmetry arguments. The D_{4d} MX_8 system contains an S_8 -axis in which M lies, along with two perpendicular mirror planes that intersect along the S_8 -axis. The largest component of the EFG tensor, V_{ZZ} , must lie along S_8 and must be zero since the angle between the S_8 -axis and the ligands is the magic angle; see Equation 2.27. The remaining components, V_{XX} and V_{YY} , are perpendicular to S_8 and each is perpendicular to one mirror plane; the presence of two perpendicular mirror planes requires that V_{XX} and V_{YY} are equal. Since V_{ZZ} is zero and the trace of the EFG tensor is necessarily zero, then both V_{XX} and V_{YY} must also be zero for an MX_8 system possessing ideal square antiprismatic symmetry.

Unexpectedly low EFGs can also occur for more complex charge arrangements. For example, a conical surface with apex at S_0 and cone angle equal to 109.47° (or $2 \times 54.74^\circ$) has a zero EFG at S_0 for any circular distribution of charge around the cone, equidistant from S_0 , as is the case for $MesMo(CO)_3$.⁴⁵ This results because the angle formed between the ligand tripod and the principal molecular axis is approximately equal to 54.74° , also known as the "magic angle" (*vide infra*); from Eq. (2.27) it is obvious that V_{ZZ} is zero for this particular case, since $\cos^2\theta \sim 1/3$, when $\theta = 54.74^\circ$. Other cases may be constructed whereby an infinite number of charges are distributed such that the EFG is zero at a given point, even for non-cubic systems, thereby allowing for highly irregular arrangements.⁴⁶ Some known examples of systems with small EFGs at the indicated metal center are: $Ru_3(CO)_{12}$,⁴⁷ $Mn_2(CO)_{10}$,^{48,49} $ReMn(CO)_{10}$,⁴⁹ and $CpV(CO)_4$.⁵⁰

Equation (2.27) emphasizes the profound effect that charges close to the nucleus have on the EFG, due to the r^{-3} dependence. This leads to the assumption that electrons which have a high probability of being near the nucleus of the atom play a major role in determining the EFG. For closed-shell atoms, the EFG is zero due to spherical symmetry; however, in a molecule, the surrounding charges create an electric field which perturbs the closed-shell electrons and distorts their spherical symmetry. The effective EFG is then given by: $V_{ZZ} = V_{ZZ}^0 [1 - \gamma(r)]$, where $\gamma(r)$ is the Sternheimer antishielding factor,⁵¹ which can be significant.

A more rigorous evaluation of the EFG involves partitioning the EFG into nuclear and electronic contributions;⁵² the latter term may be computed using quantum chemistry methods.

2.6. Nuclear Spin-Spin Coupling Interactions: Direct and Indirect

Nuclear spins, I_N and $I_{N'}$, may interact with one another via two fundamental mechanisms: the direct, **D**, and indirect, **J**, nuclear spin-spin coupling interactions. The former is a "through-space" interaction, analogous to the classical interaction between two bar magnets, and is generally referred to as the direct dipolar interaction. The direct dipolar Hamiltonian for a homonuclear spin-pair is given by:^{32,53}

$$\hat{\mathcal{H}}_D^{\text{homo}} = -\left(\frac{\mu_0}{4\pi}\right) \frac{\gamma_N \gamma_{N'} \hbar}{r_{NN'}^3} \left(3 \cos^2 \theta_D - 1\right) \left[\hat{I}_{Z,N} \hat{I}_{Z,N'} - \frac{1}{4} (\hat{I}_{+,N} \hat{I}_{-,N'} + \hat{I}_{-,N} \hat{I}_{+,N'}) \right], \quad (2.28)$$

where $\hat{I}_{Z,N}$ and $\hat{I}_{Z,N'}$ are the spin operators of the two coupled nuclei, I_N and $I_{N'}$, $r_{NN'}$ is the internuclear vector, \hat{I}_+ and \hat{I}_- are the raising and lowering operators with eigenvalues $[I(I+1) - (m+1)]^{1/2}$ and $[I(I+1) - m(m+1)]^{1/2}$, respectively, and θ_D is the angle between the dipolar vector, $r_{NN'}$ and B_0 , as indicated in Figure 2.12 (a). In a powdered sample, the internuclear dipolar vector samples all possible values of θ_D . For an isolated spin-pair, this orientation dependence is precisely mapped in a well-defined powder pattern, illustrated in Figure 2.12(b), known as the Pake doublet or Pake pattern, after its discoverer, G. E. Pake.¹⁰ The magnitude of **D** is measured in terms of the direct dipolar coupling constant, R_{DD} ,⁵³

$$R_{DD} = \frac{\mu_0}{4\pi} \frac{\hbar}{2\pi} \gamma_N \gamma_{N'} r_{NN'}^{-3}, \quad (2.29)$$

which may be determined directly from the separation between the "horns" ($\theta_D = 90^\circ$) or "shoulders" ($\theta_D = 0^\circ$) of the Pake doublet, as indicated in Figure 2.12(b). Typical R_{DD} values are on the order of 10^3 Hz. The same general theory applies for a heteronuclear spin-pair, however, Equation (2.28) is simplified considerably since the term involving the raising and lowering operators can be neglected.

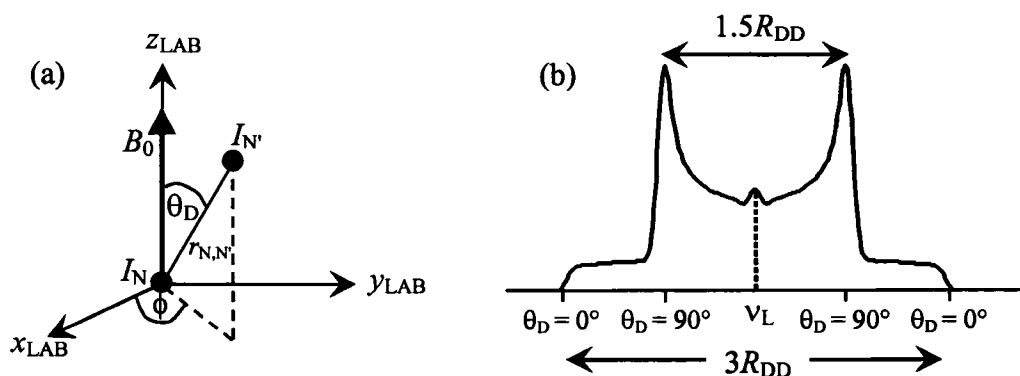


Figure 2.12: (a) The coordinate system for an isolated spin pair defining the orientation of $r_{NN'}$ with respect to B_0 . (b) Typical Pake doublet pattern for an isolated pair of *homonuclear* spin-1/2 nuclei. The angles $\theta_D = 0$ and 90° denote the orientation of $r_{NN'}$ with respect to B_0 ; the separation between "horns" or "shoulders" allows R_{DD} to be determined. Note, for a *heteronuclear* spin-pair, the separation between the horns and shoulders is R_{DD} and $2R_{DD}$, respectively.

The mechanism by which the *indirect* spin-spin coupling interaction, \mathbf{J} , operates is more complicated and has no direct dependence on $r_{NN'}^{-3}$; instead \mathbf{J} is controlled by the intervening electrons of N and N' and is described by a two-stage process, schematically depicted in Figure 2.13. First, nuclear spin, I_N , perturbs the electrons in its vicinity, $S_{Z,N}$, and this perturbation is carried via the electronic framework to a second nuclear spin, $I_{N'}$, where a small magnetic field is produced.

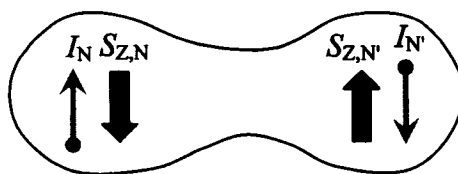


Figure 2.13: Schematic diagram of the indirect spin-spin coupling interaction, \mathbf{J} , showing an energetically-favourable configuration for nuclear spins, I_N and $I_{N'}$, and their respective electron spins, $S_{Z,N}$ and $S_{Z,N'}$, assuming $J(N,N')_{iso} > 0$.

The theory of \mathbf{J} was first described by Ramsey in 1953^{15f,g} in terms of three mechanisms: the Fermi contact (FC), spin-orbit (SO), and spin dipolar (SD) mechanisms. The FC mechanism accounts for the interaction between a nuclear spin and an electron spin which has a finite probability of being at the nucleus (*i.e.*, *s* electrons);

this term is purely isotropic and, hence, does not contribute to the anisotropy in \mathbf{J} . The SO mechanism describes the interaction between the nuclear magnetic moment and the orbital magnetic moment arising from the motion of the electrons and can be further divided into diamagnetic SO (DSO) and paramagnetic SO (PSO) contributions; the DSO mechanism depends on the ground electronic state and the PSO mechanism involves allowed excitations between the ground and singlet excited states. The third mechanism, SD, involves the interaction between the nuclear magnetic moment and the magnetic field arising from the spin of the electrons not located at the nucleus. For any given nuclear spin-spin coupling tensor, all three of these mechanisms may be important, and in general, none may *a priori* be considered negligible. In the early literature, it was common practice to assume the FC mechanism was the most important contributor to the isotropic part of \mathbf{J} , J_{iso} ; however, in a study of a comprehensive list of P,P-containing molecules using a DFT approach, we have shown that the PSO mechanism contributes significantly to \mathbf{J} in the presence of formal multiple P,P bonds. This research has been published as a full article in the *Journal of Physical Chemistry A*,⁵⁴ but the results will not be discussed here.

The \mathbf{J} -tensor is characterized by its isotropic and anisotropic values, and by its asymmetry parameter:^{32,53,55}

$$J_{\text{iso}} = (J_{11} + J_{22} + J_{33})/3, \quad (2.30)$$

$$\Delta J = J_{33} - \frac{J_{11} + J_{22}}{2}, \quad (2.31)$$

$$\eta_{\mathbf{J}} = \frac{J_{22} - J_{11}}{J_{33} - J_{\text{iso}}}, \quad (2.32)$$

respectively, where the principal components, J_{11} , J_{22} , and J_{33} , are ordered according to $|J_{33} - J_{\text{iso}}| \geq |J_{11} - J_{\text{iso}}| \geq |J_{22} - J_{\text{iso}}|$. Typical $^1J_{\text{iso}}$ values are on the order of 10^2 Hz; however, the largest reported value for $^1J_{\text{iso}}$ is +218 000 Hz for the $^{199}\text{Hg}, ^{199}\text{Hg}$ spin-pair in $\{[\text{Hg}_2(18\text{-crown-6})(15\text{-crown-5})(\text{H}_2\text{O})]^{2+}\}_2$.⁵⁶ A convenient form to express $\mathbf{J}(\text{N}, \text{N}')$ is in terms of a *reduced* coupling tensor, $\mathbf{K}(\text{N}, \text{N}')$, which is independent of the magnetogyric ratios, γ_{N} and $\gamma_{\text{N}'}$ of the two coupled nuclei, N and N':

$$\mathbf{K}(\mathbf{N}, \mathbf{N}') = \frac{4\pi^2 \cdot \mathbf{J}(\mathbf{N}, \mathbf{N}')}{h\gamma_N\gamma_{N'}}; \quad (2.33)$$

\mathbf{K} is expressed in SI units of $\text{kg m}^{-2} \text{s}^{-2} \text{A}^{-2}$ (equivalently, $\text{N A}^{-2} \text{m}^{-3}$ or $\text{T}^2 \text{J}^{-1}$).

Although the nature of the \mathbf{D} and \mathbf{J} interactions is fundamentally different, both are second-rank tensors of the same general form; hence, assuming like PASs, the total spin-spin coupling Hamiltonian may be written as follows:

$$\hat{\mathcal{H}}_{\mathbf{D}+\mathbf{J}} = h \mathbf{I}_N \cdot (\mathbf{D} + \mathbf{J}) \cdot \mathbf{I}_{N'}, \quad (2.34)$$

where \mathbf{D} is given by:

$$\mathbf{D} = R_{DD} \begin{bmatrix} 1 & 0 & 0 \\ 0 & 1 & 0 \\ 0 & 0 & -2 \end{bmatrix} \quad (2.35)$$

and is purely anisotropic; *i.e.*, the trace of \mathbf{D} is zero.

The total, $\mathbf{D}+\mathbf{J}$, spin-spin coupling Hamiltonian may be re-written as a sum of their isotropic and anisotropic components:

$$\hat{\mathcal{H}}_{\mathbf{D}+\mathbf{J}} = h J_{\text{iso}} \mathbf{I}_N \cdot \mathbf{I}_{N'} + h \mathbf{I}_N \cdot (\mathbf{D} + \mathbf{J}_T) \cdot \mathbf{I}_{N'}, \quad (2.36)$$

where \mathbf{J}_T is given by:

$$\mathbf{J}_T = -\frac{\Delta J}{3} \begin{bmatrix} 1 & 0 & 0 \\ 0 & 1 & 0 \\ 0 & 0 & -2 \end{bmatrix}. \quad (2.37)$$

Recognizing that \mathbf{D} (Eq. 2.35) and \mathbf{J}_T (Eq. 2.37) have similar forms, Equation 2.36 can be simplified to:

$$\hat{\mathcal{H}}_{\mathbf{D}+\mathbf{J}} = hJ_{\text{iso}} \mathbf{I}_N \cdot \mathbf{I}_{N'} + hR_{\text{eff}} \mathbf{I}_N \begin{bmatrix} 1 & 0 & 0 \\ 0 & 1 & 0 \\ 0 & 0 & -2 \end{bmatrix} \mathbf{I}_{N'}, \quad (2.38)$$

where R_{eff} is the *effective* dipolar coupling constant and has contributions from both R_{DD} and ΔJ :

$$R_{\text{eff}} = R_{DD} - \frac{\Delta J}{3}. \quad (2.39)$$

The dependence of R_{DD} on internuclear separation (Eq. 2.29) makes measurement of R_{eff} an attractive means of determining the bond length if the structure is unknown.^{55,57,59} However, the reliability of any NMR-based bond length determination depends critically on knowing the significance of the contribution of ΔJ to R_{eff} .

From the point of view of an experimentalist, the magnitude of J_{iso} is usually straightforward to determine; however, that for ΔJ is more difficult due to the interplay between ΔJ and R_{DD} . A number of experimental approaches for determining ΔJ are discussed in detail in the literature.^{58,59} Briefly, ΔJ may be measured via R_{eff} for solid samples^{24,27,60,61,62} or samples dissolved in liquid crystalline media using NMR spectroscopy.^{63,64,65,66,67} For small molecules, precise values of R_{eff} may be obtained from hyperfine coupling constants measured in molecular beam or high-resolution microwave spectroscopy experiments.^{68,69,70} The anisotropy of J is exceedingly difficult to quantify experimentally, due mainly to uncertainties in the motional averaging corrections for R_{DD} , especially if the difference between R_{eff} and R_{DD} is small (*i.e.*, $\leq 10\%$).

Chapter 3: Experimental Techniques, Data Processing and Theoretical Methods

3.1. Standard Techniques used in Solid-State NMR Spectroscopy

3.1.1. Magic-Angle Spinning

The most widely used technique in solid-state NMR is magic-angle spinning (MAS), which involves spinning a sample rapidly at an angle oriented at $\beta = \arccos(1/\sqrt{3}) \approx 54.7356^\circ$ with respect to the applied magnetic field. This angle is 'magical' in NMR spectroscopy because of the angular-dependent term, $(3\cos^2\beta - 1)$, which is contained in the theory of many NMR interactions; hence, by spinning samples at this precise angle, the angular-dependent term is effectively removed and the anisotropic NMR interactions are averaged to their isotropic values, provided the spinning rate is sufficiently fast with respect to a particular interaction. As an example, consider the magnetic shielding interaction for a spin-1/2 nucleus and assume axial symmetry, $\kappa = +1.00$. If the shielding anisotropy, Ω , is greater than the spinning speed, then rather than Ω being averaged to a single isotropic peak, a series of peaks called spinning sidebands, *ssb*, will result. The *ssbs* are separated at intervals equal to the spinning frequency and flank the isotropic peak. The isotropic peak is easily determined when more than one spinning speed is employed because the frequency corresponding to δ_{iso} is independent of spinning frequency.⁷¹

Shown in Figure 3.1 are ^{129}Xe NMR spectra of (a,b) MAS and (c) stationary samples of $\text{Na}_4\text{XeO}_6 \cdot 2\text{H}_2\text{O}$. When $\nu_{\text{rot}} < \nu_L \Omega$, the manifold of *ssbs* well-reproduces the overall shielding pattern and allows δ_{iso} , Ω , and κ to be determined; however, when $\nu_{\text{rot}} > \nu_L \Omega$, a more ambiguous pattern is obtained, from which only δ_{iso} can conclusively be determined.

Although information regarding the anisotropic shielding is often desirable, circumstances exist when such information is a hindrance. The ^{129}Xe NMR spectra in Figure 3.1 demonstrate that the anisotropic shielding interaction can be removed, provided the spinning rate is sufficiently fast. In many circumstances, however, maximum attainable spinning rates are simply too slow. The upper MAS limit is

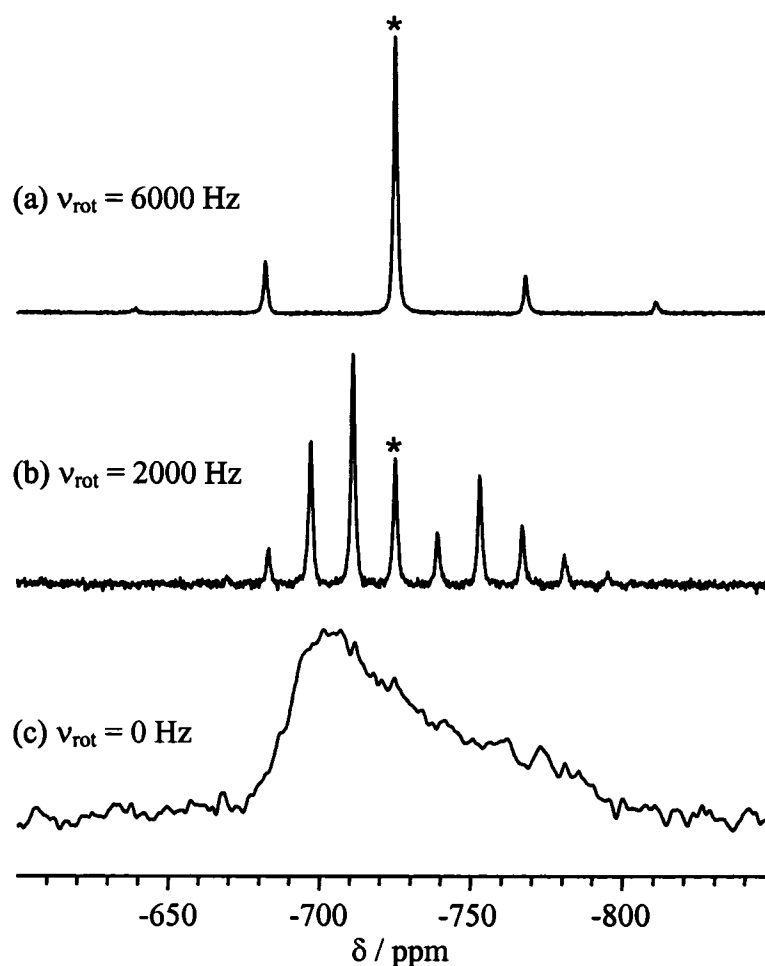


Figure 3.1: Solid-state $^{129}\text{Xe}\{^1\text{H}\}$ NMR spectra of MAS samples of $\text{Na}_4\text{XeO}_6 \cdot 2\text{H}_2\text{O}$ at variable spinning speeds. The isotropic chemical shift, $\delta_{\text{iso}} = -725.6$ ppm, is indicated in (a) and (b) with asterisks; $B_0 = 11.75$ T.

restricted by the rotor size; rotors with small outer diameters (o.d.) are able to spin much faster than those with large outer diameters. In our laboratory, the upper spinning speed limits are 7 kHz and 35 kHz for the largest (o.d. = 7.5 mm) and smallest (o.d. = 2.5 mm) rotors, respectively. This poses a problem, for example, in the study of quadrupolar nuclei with moderate to large quadrupole moments – the focus of this *Thesis*. In these cases, broad NMR lineshapes often result and the spinning speeds required to resolve the spinning sidebands from the second-order central transition lineshape are unachievable. To illustrate this, central transition ^{53}Cr NMR spectra are simulated at various spinning speeds for $\nu_L(^{53}\text{Cr}) = 28.179$ MHz, $C_Q(^{53}\text{Cr}) = 4.64$ MHz and $\eta_Q = 0.0$, and shown in Figure 3.2. The simulations indicate that spinning speeds of at least 25 kHz are required

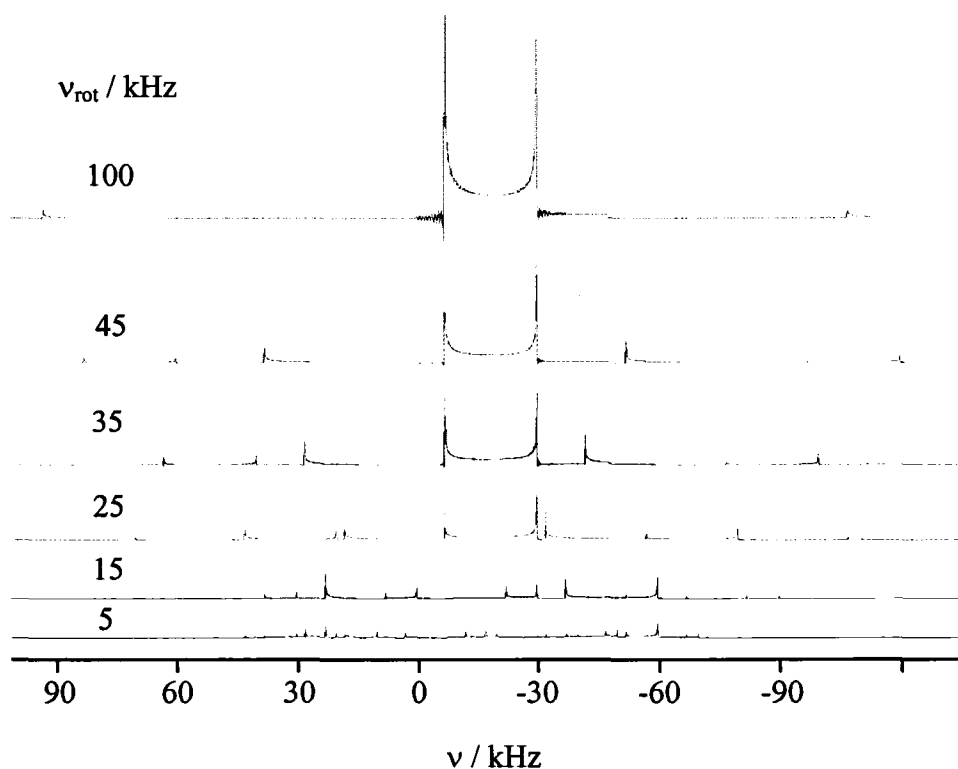


Figure 3.2: Simulations of central transition ^{53}Cr NMR spectra for $\nu_L(^{53}\text{Cr}) = 28.179$ MHz, $C_Q(^{53}\text{Cr}) = 4.64$ MHz and $\eta_Q = 0.0$, which corresponds to $\Delta \nu_{(+\frac{1}{2} \leftrightarrow -\frac{1}{2})}^{\text{Stationary}} \sim 100$ kHz. The spectra have been calculated using different spinning rates, ν_{rot} , to illustrate the dependence of the second-order quadrupolar lineshape on ν_{rot} .

to prevent overlap of the spinning sidebands with the centerband, a problem that is compounded by the fact that large rotors are required to facilitate ^{53}Cr NMR studies. In theory, it is possible to suppress spinning sidebands through the use of available pulse sequences such as TOSS⁷² (total suppression of spinning sidebands), PASS⁷³ (phase-altered spinning sidebands), Q-PASS,⁷⁴ and others;⁷⁵ however, these experiments are not practical for studying low-frequency quadrupolar nuclei due to the significant loss in signal intensity relative to the standard experiment.

3.1.2. Abundant Spins

The advantages and disadvantages of the presence of abundant spins, I , in a sample when conducting solid-state NMR experiments can be explained by the spin-spin

coupling interactions (**J** or **D**; *Section 2.6*). Although important structural information may be extracted from J_{iso} and R_{DD} (recall, from Eq. 2.29, the inverse relationship between R_{DD} and r_{IS}^3), strong I, S spin-spin couplings can also create overwhelming, broad signals, which obscure the NMR spectra for the observe nucleus, S . Hence, to successfully record " S " NMR spectra, while eliminating interfering I, S spin-spin interactions, high-power decoupling is applied to the abundant spin, I , thereby increasing the S/N, and allowing other relevant information for the S nucleus to be obtained. In addition, the magnetization can be transferred from I to S via the cross-polarization (CP) experiment, making the study of rare spins practical.

3.1.2.1. Decoupling

High-power decoupling of abundant spins is a routine double-resonance technique which can be applied to MAS or stationary samples, whereby the I channel is continuously irradiated during acquisition of the FID for the observe nucleus S ; this type of decoupling is referred to as continuous wave (CW) decoupling. The constant irradiation results in rapid interchanging of the I nuclear spin-state at a rate that is faster than the interaction (R_{DD} or **J**) to be removed. Since, in the solid state, $R_{\text{DD}}(I, S)$ values are generally sizable ($>10^3$ Hz), the power level of the I decoupling rf field, B_{1I} , is also on the order of 100 kHz; compared to typical solution NMR decoupling powers, solid-state methods require higher power. The experimentalist must therefore set with caution the duty cycle, which dictates the fraction of time that the rf power is on, to avoid damage to the probe. If the decoupler is left on too long, the rf coil heats up, causing sample heating (temperature gradients) and probe arcing, which, in turn, may cause serious damage to the probe, resulting in expensive repairs. When decoupling, acquisition times of 50 ms and duty cycles not exceeding 10 % are safe.

Of the many decoupling schemes, the simplest is CW decoupling, described above. A variation of CW decoupling, which generally provides better sensitivity and resolution, is two-pulse phase-modulated (TPPM)⁷⁶ decoupling. Rather than applying a constant pulse on the I channel during the acquisition time (AT), as in CW decoupling, TPPM decoupling applies a series of pulses of alternating phase. TPPM decoupling is easy to implement and provides results comparable or superior to those obtained with

CW decoupling. Other decoupling schemes are available: WHH-4,⁷⁷ MREV-8,⁷⁸ BR-24,⁷⁹ Lee-Goldburg,⁸⁰ FSLG-2⁸¹ and others.^{82,83,84}

3.1.2.2. Cross-Polarization

Another popular double-resonance NMR technique which capitalizes on the presence of abundant spins (usually ^1H) is cross-polarization.^{13d} CP is a solid-state NMR method that involves the transfer of magnetization from abundant spins, I , to rare spins, S , as a means of signal enhancement; the result is a theoretical enhancement on the order of γ_I/γ_S for S . A second advantage of the CP technique is that the pulse delay is chosen based on the spin-lattice relaxation time of the abundant spin, $T_1(I)$. Since $T_1(I)$ is typically much less than $T_1(S)$, a considerable savings in time is achieved when CP is employed. CP operates via the I, S dipolar interaction; hence, the main requirement is that I and S are in close proximity so that a strong dipolar interaction is established.

The simplest CP experiment is shown in Figure 3.3. The first step in the CP experiment is to apply a $(\pi/2)_x$ pulse on the I channel and to spin-lock the I magnetization in the y -direction. Next, the magnetization is transferred from I to S during the contact time (CT) or mixing time. The optimum transfer of $I \rightarrow S$ magnetization is obtained

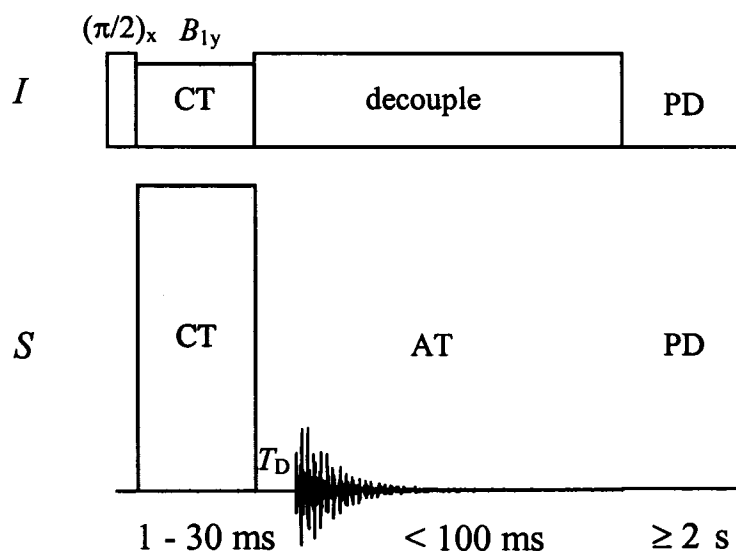


Figure 3.3: Pulse sequence for cross-polarization; CT is the contact time, T_D the dead time, AT the acquisition time, and PD the pulse delay.

when the so-called Hartmann-Hahn match^{13b} is achieved: $\alpha_I \gamma_I B_{1I} = \alpha_S \gamma_S B_{1S}$, where $\alpha_s = 1$ for $S = \frac{1}{2}$ nuclei and $\alpha_s = [S(S + 1) - m_S(m_S - 1)]^{1/2}$ for quadrupolar nuclei.²³ Note that this matching condition is periodically modulated by the time-dependent dipolar coupling under MAS conditions. A correct matching condition implies the I and S spins are precessing at the same effective frequency in their rotating frames of reference, hence, their energies are comparable, allowing for magnetization transfer. External factors that affect the Hartmann-Hahn match are the rotor spinning rate, magnetic field, and the choice of probe. Since CP relies on the dipolar interaction, the spinning rate must be chosen such that $R_{DD}(I, S)$ is not significantly reduced or removed.

Experimentally, the matching condition may be achieved by holding B_{1I} constant and varying B_{1S} , or *vice versa*, until a maximum intensity in the S NMR spectrum is obtained. The CT is on the order of milliseconds and depends on r_{IS} ; hence, CT must be optimized for each sample. After a short delay, called the dead time, T_D , the FID for the observe nucleus, S , is acquired during AT, while decoupling the I channel. Since the pulse delay is chosen based on $T_1(I)$, PD may be as short as 1 s.

Oftentimes a sample may contain several "like" rare spins in different chemical environments; *e.g.*, $-\text{CH}_3$, $-\text{CH}_2-$, $=\text{CH}-$, all of which benefit to different extents on a chosen Hartmann-Hahn match because of differences in their $R_{DD}(I,S)$ values. To obtain a matching condition which more evenly satisfies a range of environments, the *rf* amplitudes of the rare spins are varied in a step-wise fashion, as in variable amplitude CP (VACP),⁸⁵ or ramped in a continual fashion, as in RAMP CP.⁸⁶ Both VACP and RAMP CP generally provide superior overall enhancements than the single-contact CP experiment for samples which contain more than one rare-spin environment.

3.2. Experimental Strategy and Practical Considerations for Solid-State NMR Studies of Low-Frequency Quadrupolar Nuclei

3.2.1. High Applied Magnetic Field Strengths

Despite the inherent difficulties associated with solid-state NMR studies of low-frequency quadrupolar nuclei, such studies are becoming more common and feasible with the use of the highest possible magnetic field strengths, available sensitivity-enhancement techniques, and the appropriate choice of compounds. As

indicated in *Section 2.5*, the breadth of the central transition for a spin- $n/2$ nucleus is proportional to ν_Q^2/ν_L in Hz and ν_Q^2/ν_L^2 in ppm; hence, by employing high magnetic fields, the breadth of the central transition is significantly reduced due to the inverse relationship between $\hat{\mathcal{H}}_Q^{(2)}$ and B_0 . This is clearly illustrated in the ^{11}B NMR spectra of MAS samples of hexamethylborazine acquired at three applied magnetic field strengths, shown in Figure 3.4.⁸⁷ These spectra further demonstrate the dependence of the second-order quadrupolar shift on B_0 . Hypothetically, with the use of even higher B_0 s, the second-order quadrupolar lineshape of the central transition would eventually be reduced to an isotropic, featureless peak, from which the quadrupolar parameters could not be extracted.

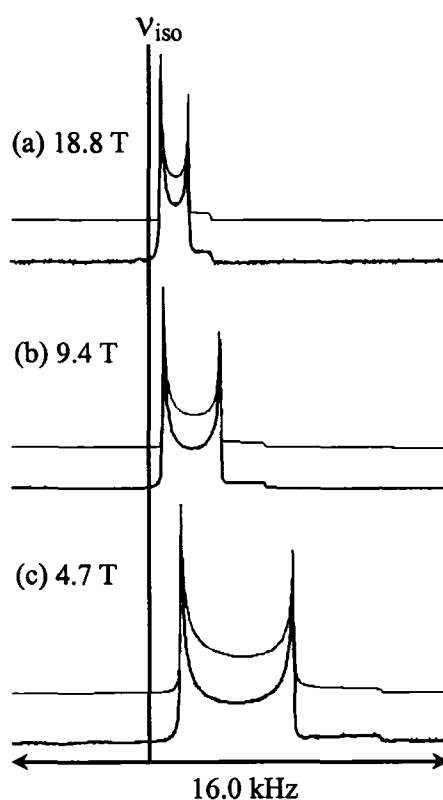


Figure 3.4: Simulated (top) and experimental (bottom) central transition ^{11}B NMR spectra of solid hexamethylborazine at three applied magnetic field strengths. The spectra shown in (a-c) were acquired using MAS rates of 8.1 kHz, 25.0 kHz, and 13.0 kHz, respectively. The vertical line indicates the isotropic frequency at each applied magnetic field. See Ref. 87.

Other benefits of employing high magnetic fields include an increase in sensitivity of the NMR experiment due to \hat{H}_z and more accurate determination of σ due to amplification of \hat{H}_s .⁸⁸ To further improve the quality of the NMR experiment, the use of enhancement techniques is encouraged.

3.2.2. Typical Pulse Sequences

Recently, the development of S/N and sensitivity-enhancement techniques has received considerable attention from the NMR community. Sensitivity-enhancement techniques may be divided into saturation or inversion experiments; the former method involves equalizing the populations of the satellite transitions to increase the population difference of the central transition, $\Delta p_{+1/2 \leftrightarrow -1/2}$, whereas the latter method involves modifying the satellite populations to increase $\Delta p_{+1/2 \leftrightarrow -1/2}$. The theoretical enhancement factors of $\Delta p_{+1/2 \leftrightarrow -1/2}$ for these techniques are $(I + 1/2)$ for saturation experiments and $(2I)$ for inversion experiments, where I is the observe nucleus. Alternatively, S/N-enhancement techniques may involve suppressing or attenuating various nuclear spin interactions present in the system. Several techniques have been previously discussed in *Section 3.1*: MAS, decoupling, and CP. MAS removes or averages anisotropic interactions and decoupling removes strong heteronuclear I, S dipolar interactions. An alternate S/N-enhancement technique used extensively in this *Thesis* is the quadrupolar Carr-Purcell Meiboom-Gill (QCPMG)⁸⁹ experiment. Before discussing the QCPMG experiment, its predecessor, the spin-echo experiment, will be presented.

3.2.2.1. Spin-Echo

The use of "echo" experiments in NMR was introduced in 1950 by Erwin Hahn¹⁴ as a method for measuring the spin-spin relaxation times, T_2 , in solution. The original spin-echo experiment involves application of two sequential $\pi/2$ pulses, followed by detection of the FID. In 1954, Hahn's original spin-echo experiment¹⁴ was modified slightly by Carr and Purcell⁹⁰ by replacing the second $\pi/2$ pulse with a π pulse. In this

Thesis, reference to the "spin-echo experiment" implies use of the revised echo experiment, which will now be discussed in detail.

A schematic diagram of the spin-echo pulse sequence⁹⁰ is shown in Figure 3.5 along with a depiction of the evolution of the spin dynamics at various stages during the pulse sequence. Application of the first $(\pi/2)_x$ pulse (i) forces the equilibrium magnetization aligned along the z -axis, M_0 , onto the y -axis, M_y . Due to the orientation dependence of the chemical shift interaction and inhomogeneities in B_0 , different crystallites in the sample experience slightly different chemical shifts and therefore precess at slightly different Larmor frequencies; hence, during time period τ , anisotropic dispersion of the spin-vectors in the xy -plane results (ii). Next, the $(\pi)_y$ pulse (iii) reverses the dephasing effect by refocusing the magnetization back along the y -axis after time τ , (iv). The free-induction decay is then detected (v) and, upon Fourier transformation, the NMR spectrum is obtained.

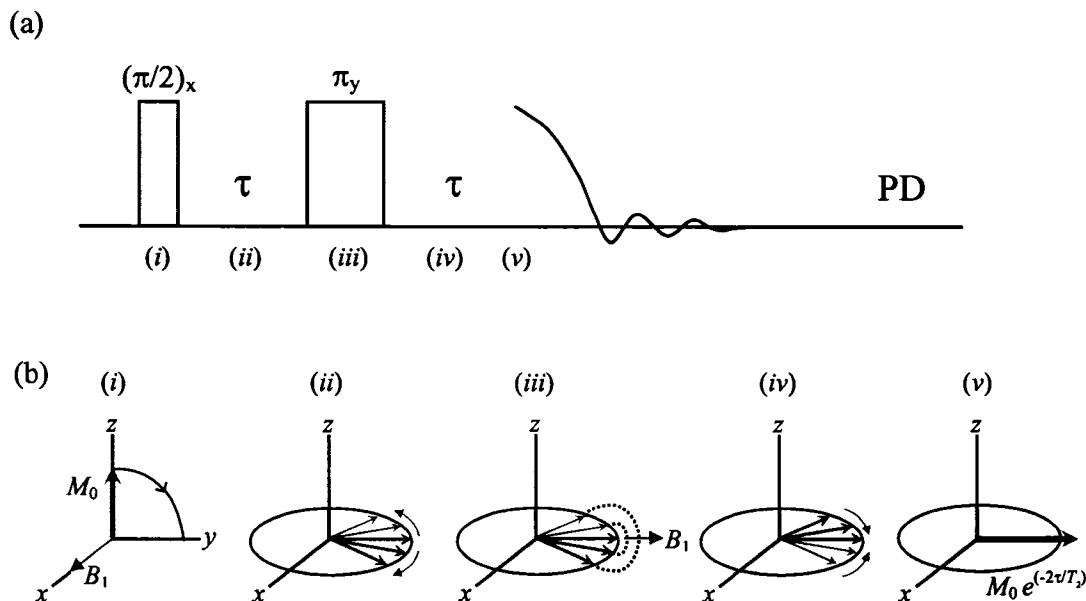


Figure 3.5: (a) Spin-echo experiment. (b) Depiction of spin dynamics in various stages of the spin-echo experiment: (i) application of the $(\pi/2)_x$ pulse forces magnetization along y -axis; (ii) during time period, τ , the individual spin vectors fan-out in xy -plane; (iii) application of π_y pulse effectively reflects the spin vectors in yz -plane; (iv) spin vectors refocus during the second τ period and at the end of τ , (v) magnetization is aligned along y -axis and described by: $M_0 \exp(-t/T_2)$.

The spin-echo experiment is often preferred over a standard one-pulse experiment when acquiring NMR spectra of stationary samples or systems that give rise to broad NMR spectra. Since broad NMR lineshapes necessarily have short FIDs, interference from instrument dead time and probe ringing (on the order of μs) at the beginning of the FID introduces artifacts, resulting in spectral distortions and a loss of pertinent information. Use of the "echo" effectively removes the probe ringing by refocusing the desired NMR signal at a later time. A proper setting of τ (on the order of μs) is crucial in obtaining accurate NMR lineshapes; if τ is too small, unnecessary data will be acquired and the point(s) prior to the "top of the echo" must be deleted; *i.e.*, the data must be left-shifted to give the proper NMR spectrum. On the other hand, if τ is too long, important NMR information is lost and an incorrect NMR lineshape is obtained. When employing MAS with the spin-echo experiment, rotor-synchronization must be used, which requires the condition, $\tau \propto n \nu_{\text{rot}}^{-1}$, to be satisfied.

In 1958, Meiboom and Gill⁹¹ extended Carr and Purcell's echo experiment by introducing a train of π -pulses following the echo pulse; this experiment was named after the authors who collectively discovered it: CPMG.⁹¹ The CPMG sequence allowed measurement of long T_2 values in solution without appreciable effects of translational diffusion. In 1989, Cheng and Ellis⁸⁹ were the first to apply the CPMG experiment to a half-integer spin quadrupolar nucleus, ^{87}Rb ($I = 3/2$), in their solid-state NMR study of Rb^+ adsorbed to α -alumina; the CPMG method allowed two Rb components to be identified based on differences in their T_2 values. Several years later, Larsen and co-workers⁹² discovered the CPMG experiment could be used as a means of signal enhancement for half-integer spin quadrupolar nuclei and termed the experiment "Q"CPMG, because of its application to quadrupolar nuclei.

3.2.2.2. *Quadrupolar Carr-Purcell Meiboom-Gill*

The QCPMG⁸⁹ pulse sequence, shown in Figure 3.6, involves the spin-echo experiment followed by a series of π -pulses and detection of the FID. The decay of the FID is primarily due to homogeneous interactions since the inhomogeneous interactions are refocused during the π -pulse train. A sample QCPMG FID is shown in Figure 3.7(a),

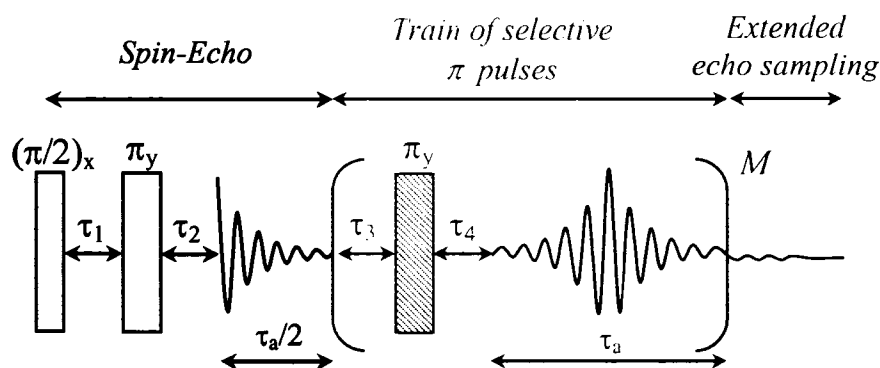


Figure 3.6: The quadrupolar Carr-Purcell Meiboom-Gill (QCPMG)⁸⁹ pulse sequence: the first segment is identical to the spin echo experiment, the second involves the train of refocusing π pulses, and the third shows the extended sampling period to ensure the FID is fully decayed. The spacing between spikelets, ν_{QCPMG} , is equal to τ_a^{-1} .

where the train of refocusing pulses is apparent from the characteristic comb-like appearance of M spin echos (SEs) at a specified separation. The QCPMG NMR spectrum, shown in Figure 5.7(b), also has a comb-like appearance and is divided into a manifold of evenly-spaced, relatively narrow SE sidebands or spikelets, centred at the transmitter or carrier frequency, ν_c . The QCPMG spikelet separation, ν_{QCPMG} , is equal to τ_a^{-1} . The overall spikelet manifold mimics that which would be obtained using the SE experiment, shown for comparison in Figure 3.7(c).

The benefits of employing the QCPMG experiment are numerous. The QCPMG technique offers the robustness and flexibility to study a range of systems of stationary and MAS samples, and provides NMR spectra that are of comparable or superior quality to those obtained using the conventional SE experiment; hence, the quadrupolar and anisotropic magnetic shielding interactions, as well as the relative orientation of their tensors, may be characterized in the usual way. Most important is that there is a substantial gain in signal-to-noise, $G_{\text{S/N}}$, allowing NMR spectra to be acquired in considerably less time; further, this provides an opportunity to study some traditionally challenging nuclei.

The QCPMG experiment concentrates the intensity from the broad SE powder pattern into the SE spikelets such that the total integrated intensity from the spikelets is comparable to that of the SE pattern. The signal gain for the QCPMG experiment, G , has been calculated by Amoureux and co-workers⁹³ and is given by: $G = 2T_2\nu_{\text{QCPMG}}$, where

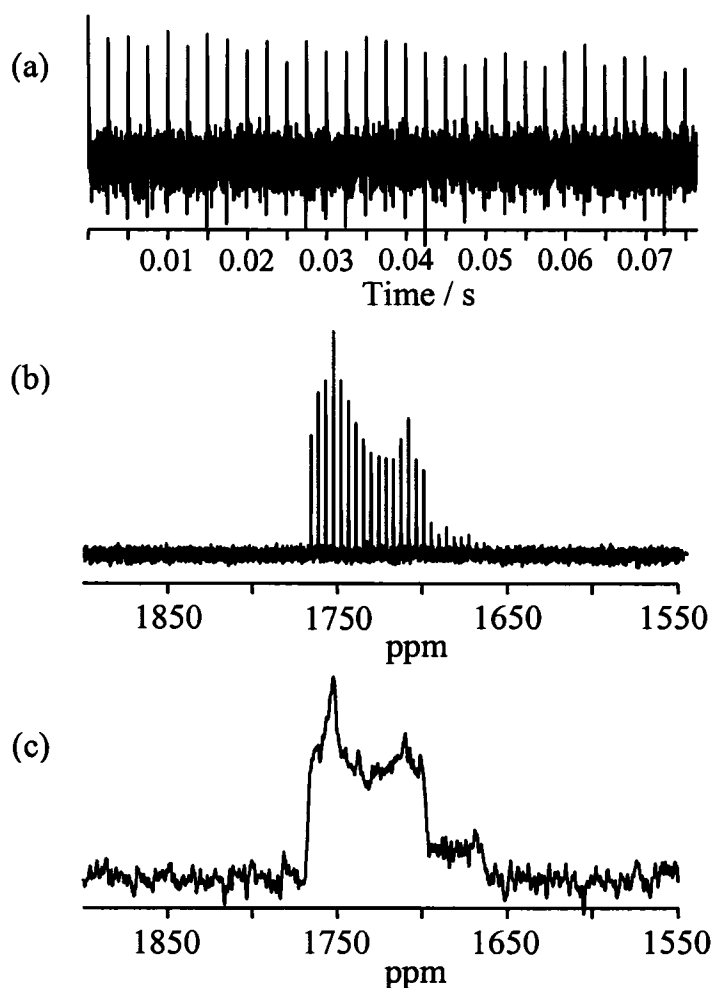


Figure 3.7: (a) ^{53}Cr QCPMG FID of a stationary sample of K_2CrO_4 acquired using $\tau_a = 2.0$ ms; (b) solid-state ^{53}Cr QCPMG NMR spectrum of an MAS sample of Cs_2CrO_4 with $\nu_{\text{QCPMG}} = 120$ Hz and $\nu_{\text{rot}} = 6000$ Hz; (c) conventional spin-echo ^{53}Cr NMR spectrum of an MAS sample of Cs_2CrO_4 with $\nu_{\text{rot}} = 6000$ Hz; (a-c) $B_0 = 11.75$ T.

T_2 is the time constant describing the overall decay of the spikelets in the FID of the QCPMG experiment (see Figure 3.7(a)); hence, a lower resolution (larger ν_{QCPMG}) results in a higher S/N. The key to a successful experiment is to choose a value for ν_{QCPMG} which makes a compromise between the gain in S/N and spectral resolution. The benefits of QCPMG are most pronounced in the study of systems with large magnetic shielding anisotropies and/or large second-order quadrupolar interactions.⁹⁴

Experimentally, the S/N enhancement for a QCPMG experiment depends on several variables, such as the number of echoes acquired, M , the acquisition time for *each* full echo (this dictates the spikelet spacing, ν_{QCPMG}), and the length of the FID. Another

factor to consider is the echo-train decay rate, $1/T_2$, which is governed by the sample of interest. If a sample has a short T_2 , utilizing the QCPMG experiment is not beneficial since the echo train would be reduced to a single echo, or very few echoes, yielding a spectrum similar to that obtained using a SE experiment.

Maximum enhancements for QCPMG spectra are achieved for systems with long T_2 values. While T_2 is a factor that must be considered when conducting an experiment, it is an intrinsic value and cannot be altered. For systems with long T_2 s, longer ATs, and thus higher M values, are possible. A second experimental factor that must be considered is the accuracy with which the $\pi/2$ and π *rf* pulses have been set. The slightest inaccuracies in the π pulse can cause a significant reduction in the gain in S/N, which will be amplified with higher M values due to the cumulative nature of this error. There is an interplay between AT, ν_{QCPMG} , and M . The separation between spikelets takes priority in this set of experimental factors; as a rule of thumb, approximately 25 to 30 spikelets are necessary to properly describe the QCPMG spectrum. The AT is generally limited by T_2 and is usually ≤ 100 ms, while typical M values range from 16 to 96.

3.2.3. Broad NMR Lineshapes

3.2.3.1. Radiofrequency Pulses and Excitation Profiles

Before discussing the method used to acquire broad NMR lineshapes, it is instructive to review *rf* pulses used in NMR. Illustrated in Figure 3.8 is a typical *rf* pulse used in an NMR experiment and its corresponding excitation profile in the frequency domain. The *rf* pulse is applied for duration T_p (on the order of 10 μs) at a specific location in the frequency domain, often referred to as the carrier frequency, ν_c ; during time, T_p , the oscillating magnetic field component of the *rf* pulse, B_1 , is turned on. The excitation profile in the frequency domain can be calculated from the FT of the pulse in the time domain, and is given by a $(\sin x)/x$ or $\text{sinc}x$ function of the form:

$$\frac{\sin[\pi(\nu - \nu_c)T_p]}{\pi(\nu - \nu_c)T_p} = \text{sinc}[\pi(\nu - \nu_c)T_p]. \quad (3.1)$$

Notice from Figure 3.8 that the B_1 amplitudes in the frequency domain are not uniform;

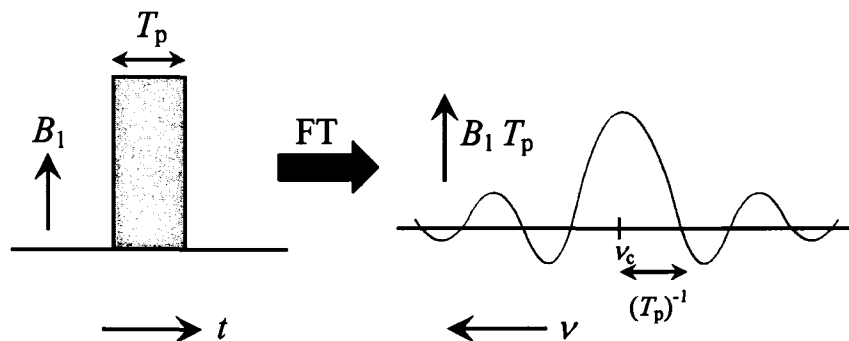


Figure 3.8: Relationship between the "square pulse" applied for duration T_p in the time domain and its frequency counterpart, the $\text{sinc}[\pi(\nu - \nu_c)T_p]$ function. The nutation behavior of the $\text{sinc}[\pi(\nu - \nu_c)T_p]$ function illustrates the non-uniform excitation profile of the square pulse.

in fact, only approximately 10 % of the region centred about ν_c is flat. Hence, to obtain uniform excitation, T_p^{-1} should be appreciably greater than the region to be excited.

The most commonly-used *rf* pulse in solid-state NMR experiments is a $\pi/2$ pulse. As outlined by Abragam,³⁶ either *selective* or *non-selective rf* pulses may be used when studying quadrupolar nuclei. Selective pulses excite the central transition, whereas non-selective pulses excite the central and satellite transitions. The non-selective $\pi/2$ pulse is optimized using a solution sample or a solid sample with cubic symmetry; the selective pulse is subsequently determined by dividing the non-selective $\pi/2$ pulse by $(I + 1/2)$.⁹⁵

The signal intensity of the central transition, $S(T_p)$, for a non-selective pulse displays oscillatory behavior described by:⁹⁶

$$S(T_p) = S_0 \sin \omega_1 T_p, \quad (3.2)$$

while $S(T_p)$ for a selective pulse is described by:⁹⁶

$$S(T_p) = \frac{S_0}{I + 1/2} \sin[(I + 1/2)\omega_1 T_p]. \quad (3.3)$$

The dependence of the signal intensity of the central NMR transition on nominal flip angle is illustrated in Figure 3.9 for $I = 3/2$ and $5/2$ nuclei according to Equations 3.2 and 3.3. From Figure 3.9, the optimum selective $\pi/2$ pulse is reduced by factor of 2 and 3 for $I = 3/2$ and $5/2$ nuclei, respectively, compared to the nominal *rf* pulse.

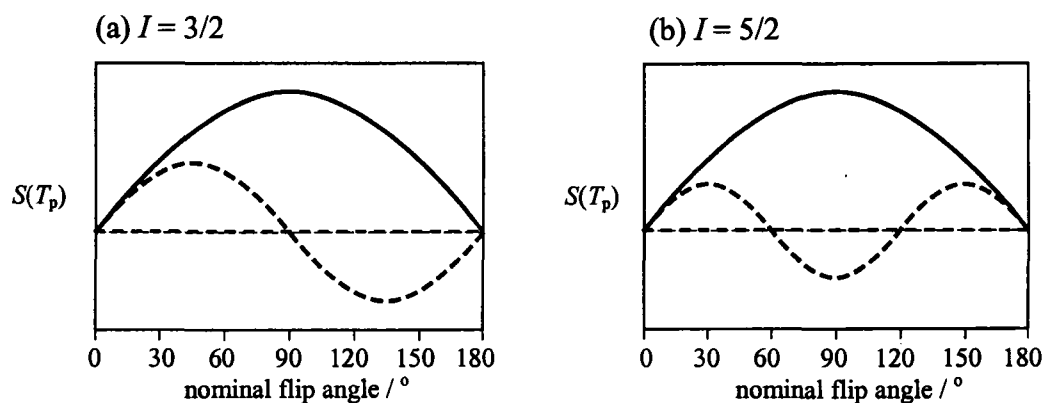


Figure 3.9: Dependence of the signal intensity of the central transition, $S(T_p)$, on the nominal pulse angle for a selective (---) and non-selective (—) pulse for (a) $I = 3/2$ and (b) $I = 5/2$; see Ref. 96.

Typical T_p values for selective $\pi/2$ *rf* pulses range from 5.0 to 2.0 μs , resulting in effective excitation ranges on the order of 40 to 100 kHz. For quadrupolar nuclei with sizable quadrupole moments, it is common for the second-order quadrupolar lineshape to significantly exceed the pulse excitation profile, making it impossible to uniformly excite the entire NMR spectrum in a single experiment; the result is acquisition of an incomplete spectrum or a distorted lineshape, which hampers extraction of any relevant NMR information. The problem of incomplete excitation is demonstrated in the ^{53}Cr QCPMG NMR spectrum of $\text{Cs}_2\text{Cr}_2\text{O}_7$, illustrated in Figure 3.10. To circumvent this problem, the spectrum must be acquired using the stepped-frequency technique.

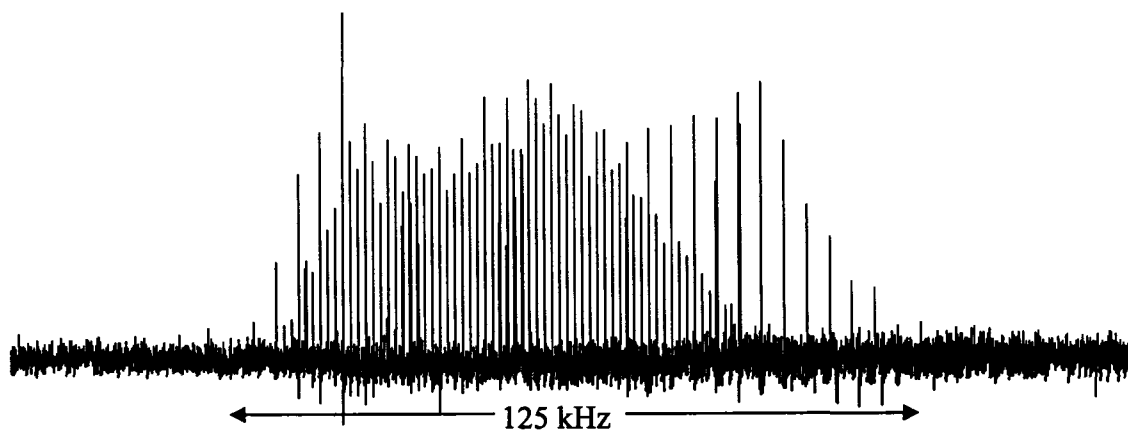


Figure 3.10: Solid-state ^{53}Cr QCPMG spectrum of $\text{Cs}_2\text{Cr}_2\text{O}_7$ demonstrating incomplete excitation; $B_0 = 18.8$ T, $\nu_{\text{QCPMG}} = 2$ kHz; total experiment time = 15.5 hr.

3.2.3.2. Stepped-Frequency Technique

The stepped-frequency technique⁹⁷ is employed to acquire broad NMR lineshapes and involves collecting a series of spectra with frequency-stepped offsets (*i.e.*, varied ν_c values) under identical experimental conditions. The step size for ν_c must be chosen such that it is less than the excitation profile of the pulse, T_p^{-1} , and the total number of sub-spectra required depends on the breadth of the full spectrum. For QCPMG experiments, it is critical that the position of ν_c is an integer multiple of the spikelet spacing, ν_{QCPMG} , otherwise, the final spectrum will have a non-uniform spikelet spacing throughout, as exemplified by the ^{53}Cr QCPMG NMR spectra for Ag_2CrO_4 , shown in Figure 3.11.

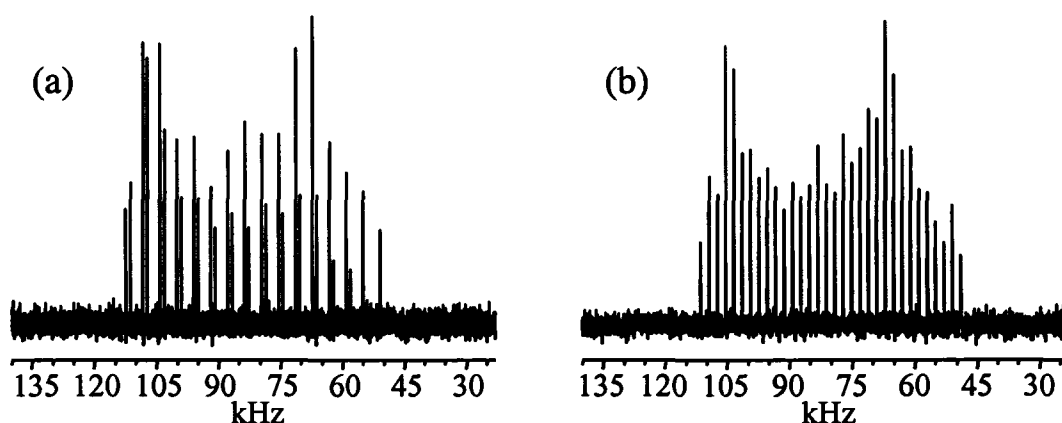


Figure 3.11: Solid-state ^{53}Cr QCPMG spectra of Ag_2CrO_4 acquired at 18.8 T using the stepped-frequency method and processed using the skyline projection technique. The spectrum shown in (a) is composed of three sub-spectra and demonstrates incorrect placement of ν_c , while the spectrum shown in (b) is composed of two sub-spectra and shows correct placement of ν_c .

3.3. Manipulation and Interpretation of Data

3.3.1. Skyline Projection Method

After collecting the necessary sub-spectra using the stepped-frequency technique, an assembling process is carried out which allows a single spectrum to be constructed from the series of sub-spectra in such a way that the resultant spectrum represents the true NMR lineshape. Two processing methods are demonstrated in Figure 3.12 for ^{53}Cr NMR spectra of $\text{Cs}_2\text{Cr}_2\text{O}_7$: variable offset cumulative spectra (VOCS)⁹⁸ and skyline projection.⁹⁹ VOCS simply involves adding the sub-spectra, whereas the skyline

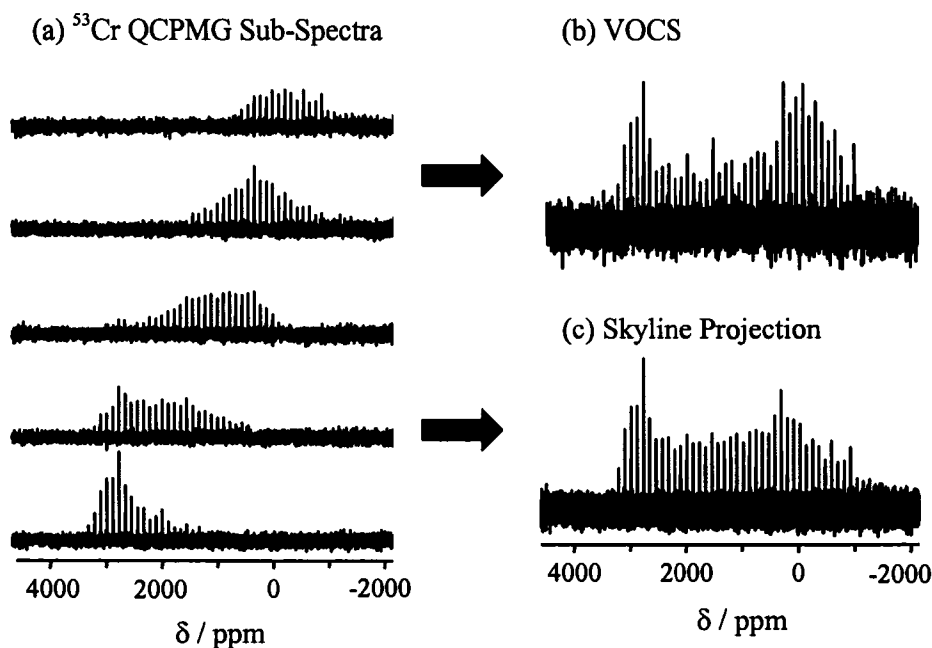


Figure 3.12: (a) The individual ^{53}Cr QCPMG sub-spectra of $\text{Cs}_2\text{Cr}_2\text{O}_7$ acquired using the stepped-frequency technique at 18.8 T. The total spectra shown in have been processed using (b) VOCS and the (c) skyline projection techniques, respectively.

projection method superimposes the sub-spectra to form, naturally, a "skyline projection". The VOCS method has been found to give misleading results due to overestimated intensities in regions where sub-spectra overlap (see Figure 3.12(b)); hence, the method of choice for the results presented herein is the skyline projection method. The skyline projection method provides a reasonably accurate representation of the true NMR lineshape and does not overestimate intensities in the overlapping spectral regions (Figure 3.12(c)); instead, the more intense of the two experiments is chosen, based on the assumption that the higher intensity spikelet corresponds to a region that was more properly excited.

A second example that demonstrates the utility of the stepped-frequency QCPMG technique and the skyline projection processing method is shown in Figure 3.13; the total ^{55}Mn NMR spectrum is comprised of fifteen sub-spectra with $\nu_{\text{QCPMG}} = 2$ kHz. Each sub-spectrum has very few spikelets and an ambiguous lineshape (see inset of Figure 3.13 for an exemplary sub-spectrum). When superimposed, however, the sub-spectra form a well-

defined, axially-symmetric quadrupolar lineshape, demonstrating the power of the stepped-frequency QCPMG experiment.

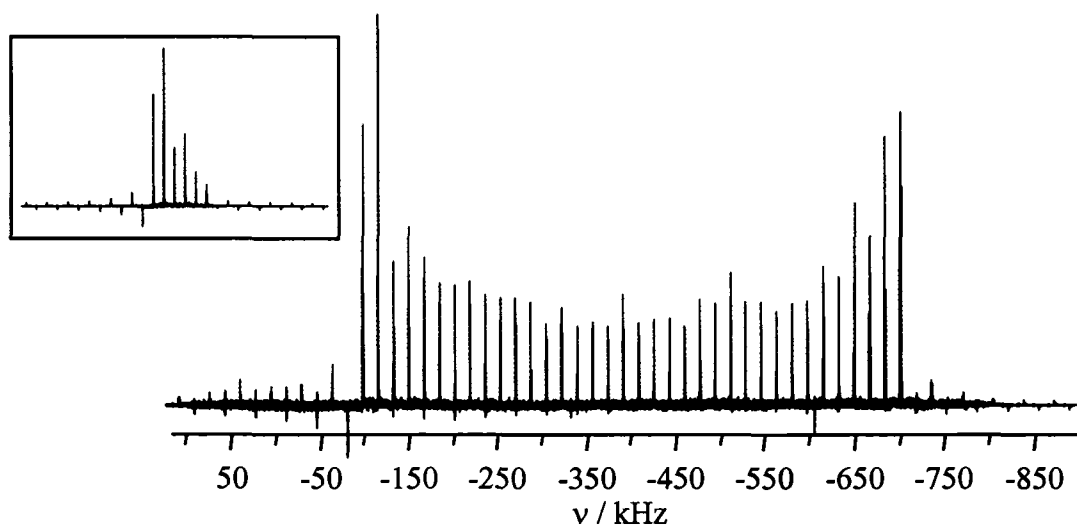


Figure 3.13: Stepped-frequency ^{55}Mn QCPMG spectrum of a stationary sample of an unidentified decomposition product of $\text{Mn}_2(\text{CO})_{10}$; $B_0 = 17.63$ T; $\nu(^{55}\text{Mn}) = 185.9$ MHz; the inset shows a single sub-spectrum. The total spectrum is the skyline projection of 16 sub-spectra with $\nu_{\text{QCPMG}} = 2.0$ kHz; each spectrum was acquired using a 1 s pulse delay and is the sum of 156. The entire spectrum is approximately 600 kHz broad and was obtained in 2 hours; $C_Q(^{55}\text{Mn}) = 60 \pm 1$ MHz and $\eta_Q = 0.0 \pm 0.02$.

3.3.2. Spectral Simulations

Once the NMR data have been acquired and processed, the next step is to interpret the results using available NMR simulation packages. In cases where several nuclear spin interactions contribute to the NMR spectrum, the observed lineshapes may be very complex, making it impossible to deduce the magnitude of the relevant parameters upon visual inspection or by rudimentary methods.^{38,100} By carrying out spectral simulations, the NMR lineshape may be separated into the various nuclear spin interactions that contribute to the overall spectrum. For example, a system which has significant contributions from the magnetic shielding and quadrupolar interactions requires the fitting of eight parameters: δ_{iso} , Ω , κ , C_Q , η_Q , α , β , γ . In this case, acquiring an NMR spectrum of an MAS sample would be beneficial, as it would, in favorable cases, average the magnetic shielding interaction, allowing δ_{iso} , C_Q and η_Q to be

determined. These three parameters would then be held constant when simulating an NMR spectrum of the stationary sample, aiding in the determination of the remaining five parameters.

Determination of a "best-fit" calculated spectrum is based on a systematic and manual iteration of the NMR interaction variables and a careful visual comparison with the experimental spectrum. To ensure that the "best-fit" is the unique solution, it is recommended that experiments be carried out at more than one B_0 , whenever possible, to rule out any ambiguities in the calculated spectrum.

Two simulation programs used routinely in our laboratory for the calculation of solid-state NMR spectra are WSOLIDS¹⁰¹ and SIMPSON.¹⁰² Spectra for a variety of solid-state NMR experiments may be calculated using either program; however, each has its advantages and limitations, as discussed below.

3.3.2.1. SIMPSON

SIMPSON (simulation of solid-state NMR spectra),¹⁰² although not entirely user-friendly, is more robust than WSOLIDS as it allows the user to explicitly specify the nuclear spin-system, internal Hamiltonian, and pulse sequence; in addition, experimental parameters (*rf* irradiation, time delays, transmitter offsets and phase cycling) and processing parameters (line broadening, phasing and zero-filling) may be specified, thus emulating an NMR spectrometer.

The simulation of an NMR experiment using SIMPSON involves the numerical evaluation of the Liouville-von Neumann time-dependent equation of motion, given by the commutator relation:¹⁰²

$$\frac{d}{dt}\rho(t) = -i[\hat{\mathcal{H}}(t), \rho(t)], \quad (3.4)$$

where $\rho(t)$ is the reduced density matrix describing the spin system and $\hat{\mathcal{H}}(t)$ is the time-dependent Hamiltonian describing the relevant nuclear spin interactions. A sample SIMPSON input file for the calculation of a QCPMG spectrum for a stationary sample is given in *Appendix 3.1*. Matrix manipulations describing the spin dynamics, which can be complex and time-intensive, are evaluated using state-of-the-art algorithms implemented in the C-language for efficiency. Once the calculation is complete, the results are

visualized and further processed using SIMPLOT, a program included in the SIMPSON package, or other external programs, such as Microsoft EXCEL, WINNMR, or WSOLIDS.¹⁰¹

The time required for a SIMPSON calculation depends on the complexity of the nuclear spin system, the magnitude of nuclear spin interactions and the type of experiment. Another factor affecting the length and quality of a SIMPSON simulation is the choice of *crystal file*. To replicate a powder sample, SIMPSON implements a powder averaging file, which specifies the number of crystallites distributed over a sphere. The time required for the calculation to complete is proportional to the number of orientations in the crystal file and the resolution of the calculated spectrum generally improves with larger crystal files. Some calculations require the largest available crystal files for reasonable results and may take many hours to complete a single iteration.

3.3.2.2. WSOLIDS

WSOLIDS¹⁰¹ is a user-friendly Windows-based program for the calculation of solid-state NMR spectra. Simulations using WSOLIDS are based on an analytical method which implements the efficient space-tiling algorithm of Aldermann and coworkers,¹⁰³ allowing calculations to be executed in a matter of seconds. When carrying out a simulation using WSOLIDS, the first step involves choosing an appropriate calculation model from a pre-composed list; this is the main drawback of WSOLIDS, since simulations involving multi-spin systems, multidimensional or advanced experiments (*e.g.*, QCPMG) are not possible. Several essential experimental parameters can be specified; namely, the spectral frequency, number of data points, and sweep width, while data processing features are limited to Gaussian- and Lorentzian-line broadening. A practical aspect of WSOLIDS is its ability to sequentially calculate spectra at more than one magnetic field. As well, there is a built-in tool for calculating the dipolar coupling constant, R_{DD} , (*Section 2.6*) for specified nuclei and a given internuclear bond length. Similar to SIMPSON, iterations of the calculated spectra are carried out manually; however, in WSOLIDS, the results are displayed instantaneously and do not have to be imported into a separate program for viewing.

An important difference between SIMPSON and WSOLIDS is their choice of convention for defining the chemical shift interaction and the Euler Angles. Care must be taken when converting from one convention to the other. The convention used in this *Thesis* has been discussed in *Section 2.4*.

3.4. Theoretical Approach: Computation of NMR Parameters

NMR spectroscopy is an essential analytical tool of the experimental chemist; however, computation of NMR parameters is a considerable challenge to the theoretician. Since NMR parameters depend on the electronic structure at or near the nucleus of interest, highly accurate descriptions of the nuclear core region are required to obtain reliable results; this may best be achieved with the use of large basis sets and high levels of theory, which drastically increase the computational time required. In recent years, the use of first-principles calculations to determine molecular or nuclear properties has become increasingly popular. This may be attributed to the significant advances that have been made in the development and improvement of accurate computational methods; namely, the *ab initio* approach and those based on density functional theory (DFT). In particular, DFT methods offer many benefits, such as their flexibility and reliability. DFT calculations may be carried out on large molecular systems containing heavy atoms, while producing accurate, reliable results at a low computational cost. Analogous calculations using, for example, restricted Hartree-Fock (RHF) methods, are generally not feasible and are limited to smaller molecules containing light atoms.

A significant component of this thesis is dedicated to the computation of NMR parameters *via* the zeroth-order regular approximation¹⁰⁴ DFT (ZORA DFT) method. The NMR module of the Amsterdam Density Functional (ADF) package^{105,106} is made up of three main components which allow the calculation of σ ,¹⁰⁷ \mathbf{J} ¹⁰⁸ and EFG¹⁰⁹ tensors. All calculations presented herein utilize the Vosko-Wilk-Nusair (VWN) local density approximation¹¹⁰ with the Becke¹¹¹-Perdew¹¹² generalized gradient approximation (GGA) for the exchange-correlation functional. ZORA-type basis sets, composed of Slater-type orbitals, have been primarily used in this work since they are known to describe the nucleus particularly well. When calculating NMR parameters, such as σ , \mathbf{J} , and EFG tensors, the largest possible basis sets are generally required to obtain accurate results;

hence, the double-zeta (DZ), triple-zeta doubly-polarized (TZ2P) or quadruple-zeta quadruply-polarized (QZ4P) basis sets have been employed herein. The ZORA formalism¹⁰⁴ allows inclusion of both scalar and spin-orbit relativistic effects: scalar relativistic theory involves contraction of *s*-orbitals, whereas spin-orbit relativistic theory introduces a coupling term between the spin and orbital angular momenta. Scalar relativistic effects are included in the spin-orbit relativistic theory. In general, computations presented herein have been carried out at both the non-relativistic and spin-orbit relativistic levels of theory. A detailed description underlying the ZORA DFT method and the NMR module is beyond the scope of this thesis and has been rigorously discussed elsewhere.^{107,108,109} A recent book which provides an excellent overview of quantum calculations of NMR parameters is recommended.⁵²

The theories of σ and \mathbf{J} were formalized by Ramsey^{158,33} in 1953 using second-order perturbation theory. Computational chemistry programs do not employ Ramsey's theory, but use an alternate approach by evaluating the second-derivative of the total energy with respect to μ_N and B_0 for σ , and with respect to μ_N and $\mu_{N'}$ for \mathbf{J} :

$$\sigma_{\alpha\beta} = \left(\frac{\partial^2 E}{\partial \mu_\alpha \partial B_\beta} \right)_{\mu, B=0} \quad \text{and} \quad \mathbf{J}(N, N')_{\alpha\beta} = \left(\frac{\partial^2 E}{\partial \mu_\alpha \partial \mu_\beta} \right)_{\mu_N, \mu_{N'}=0}, \quad \text{where } (\alpha, \beta = x, y, z). \quad (3.5)$$

Of the three NMR tensors that may be calculated using ZORA DFT, the EFG tensor may be considered the least computationally-demanding. The EFG tensor is a first-order property and depends only on the ground electronic state. Calculations of EFG tensors are generally carried out on a single molecule or ion, while extended charges are neglected because inclusion of higher-order coordination spheres is not practical. Nevertheless, since local charges have the most profound impact on the EFG (see Eq. 2.27), reasonable values may be computed; exceptions may apply to ionic or partially ionic systems for which the overall sum of long-range charges may be substantial.

When carrying out high-level calculations, the aim is to provide an accurate description of the system of interest. Calculated structures differ from the "true" structures in that they are rigid, isolated molecules or anions; therefore, lattice vibrations, intermolecular effects, solvent effects and hydrogen bonding are not accounted for in the calculations.¹¹³ For very large systems, truncation or modification of the actual structure may be necessary to reduce computational time; however, altering the immediate

environment about the region of interest should be avoided. Once the model system is selected, the appropriate basis sets and level of theory must be chosen. If heavy atoms are involved, then inclusion of relativistic effects may be necessary.

When the reliability of a method has been established, significant information can be gained from the computed results. For experimental NMR spectroscopists, the underlying goal is to understand the relationship between NMR observables and the molecular and electronic structure of a molecule. Computations can assist in attaining this goal in a number of ways. First, specific geometry modifications can be carried out in a systematic fashion, such as bond length or bond angle variation, to test the sensitivity of an NMR parameter to a geometrical variable. For example, molecular fragments can be isolated and the direct effect on the NMR parameters monitored. Second, information concerning the electronic structure in terms of the atomic orbitals that contribute to the molecular orbitals is explicitly provided; this can be useful in determining the origin of large magnetic shielding anisotropies. Third, experimental results can be rationalized and explained and the importance of relativistic effects investigated with the use of computations. In these cases, computations can help solve chemical problems or complement experimental data. Other benefits of employing first-principles calculations include the ability to determine the orientation of a given tensor in the molecular framework and to determine the sign of C_Q and J_{iso} , which may not be available from experiment. In summary, computational chemistry is a versatile and comprehensive tool that offers many benefits to the experimental chemist.

Chapter 4: Solid-State NMR Investigations of Exotic Nuclei

4.1. Prologue

Inspection of the NMR Periodic Table (Figure 2.6) reveals that most nuclei have at least one isotope that is magnetically-active and, further, 85 % of these nuclei are quadrupolar, *i.e.*, $I > 1/2$. Although, in theory, NMR studies are possible for any nucleus possessing a nuclear magnetic moment, such studies are not always practical. In solution, the receptivity, D , and linewidth factor, LF , of a particular nucleus are gauged by:³⁷

$$D = |\gamma_N|^3 I(I+1) \cdot \text{N.A.} \quad (4.1)$$

and

$$LF = \frac{(2I+3)Q^2}{I^2(2I-1)}, \quad (4.2)$$

respectively. These equations do not transfer exactly to NMR of quadrupolar nuclei in solids; nevertheless, they are useful in assessing the approximate sensitivity of a nucleus to NMR studies. Equation 4.1 demonstrates the importance of the magnetogyric ratio, γ , but does not consider the nuclear electric quadrupole moment. The linewidth factor takes into account Q , but as discussed in *Section 2.5*, the breadth of the NMR signal for a quadrupolar nucleus is more complicated in the solid state. To properly evaluate the potential study of a nucleus by NMR, the following parameters must be considered: γ , Q , I and natural abundance, N.A. The influence of these parameters on the NMR signal depends on the particular system of interest and external factors, such as B_0 . For quadrupolar nuclei, the magnitude of Q is often a factor which hampers NMR studies; for example, the nuclear quadrupole moment of ^{197}Au , $Q = 54.7 \text{ fm}^2$,³⁷ has severely hampered its study by NMR.¹¹⁴ Alternatively, for ^{103}Rh , despite the 100 % natural abundance of this spin-1/2 nucleus and the rich field of synthetic Rh chemistry, only a handful of ^{103}Rh NMR studies have been reported;^{115,116,117} the absence of NMR data for ^{103}Rh is attributed to the low γ , which is among the lowest values known, $\gamma(^{103}\text{Rh}) = -0.8468 \times 10^7 \text{ rad s}^{-1} \text{ T}^{-1}$.³⁷

Table 4.1 lists properties of selected nuclides that are less commonly studied by NMR, as well as the more familiar quadrupolar nucleus, ^{27}Al , and spin-1/2 nucleus, ^{13}C , for comparison. The nuclides examined in this *Thesis* include: ^{129}Xe , ^{131}Xe , ^{95}Mo and ^{53}Cr , and are highlighted in the Table. The spin-1/2 nucleus, ^{129}Xe , is an anomaly since, as mentioned in the *Introduction*, the NMR properties are rather favorable. The degree of difficulty for the remaining nuclei is based on the interplay of their nuclear properties. Both ^{131}Xe and ^{53}Cr have large Q s and low γ s; in addition, the N.A. for ^{53}Cr is appreciably low. For ^{95}Mo , a drawback is the small, rather than large, Q value (it is the fifth smallest known),³⁷ which often results in inefficient relaxation and long T_1 values; this, in combination with the low γ , renders ^{95}Mo NMR studies difficult. The final nuclear property that contributes to the ease with which a nuclide can be observed is the spin quantum number, I . Due to second-order quadrupolar broadening, the range of observable C_Q values is intimately related to I ; this relationship was previously described

Table 4.1: Relevant Nuclear Properties and Relative Receptivities for Selected Nuclei.³⁷

| <i>Nucleus</i> | I | N.A. / % | Q / fm^2 | $\gamma / 10^7 \text{ rad s}^{-1} \text{ T}^{-1}$ | Relative Receptivity |
|------------------|-----|----------|-------------------|---|------------------------------|
| $I > 1/2$ | | | | | $ D_N / D_{\text{Al-27}} $ |
| ^{99}Ru | 5/2 | 12.76 | +7.9 | -1.229 | 6.98×10^{-4} |
| ^{39}K | 3/2 | 93.2581 | +5.85 | 1.250 060 8 | 2.30×10^{-3} |
| ^{25}Mg | 5/2 | 10.0 | +19.94 | -1.638 87 | 1.30×10^{-3} |
| ^{37}Cl | 3/2 | 24.22 | -6.435 | 2.184 368 | 3.19×10^{-3} |
| ^{91}Zr | 5/2 | 11.22 | -17.6 | -2.497 43 | 5.15×10^{-3} |
| ^{27}Al | 5/2 | 100.0 | +14.66 | 6.976 271 5 | 1.00 |
| $I = 1/2$ | | | | | $ D_N/D_{\text{C-13}} $ |
| ^{13}C | 1/2 | 1.07 | 0.0 | 6.728 284 | 1.00 |

in *Section 2.5* and depicted in Figure 2.11. Lower spin numbers place higher restrictions on the C_Q values that can be measured; hence, in principle, measurable C_Q values are more restricted for ^{53}Cr and ^{131}Xe than for ^{95}Mo . In this *Chapter*, solid-state $^{129/131}\text{Xe}$ NMR studies on xenon difluoride and sodium perxenates will be presented. Subsequently, ^{95}Mo NMR studies of molybdate and octacyanomolybdate salts will be discussed in *Chapter 5* and, finally, ^{53}Cr NMR studies of chromate and dichromate salts will be presented in *Chapter 6*.

4.2. Prelude to Xenon NMR Spectroscopy

The ability of inert gases to form compounds was first realized in 1962 upon the formation of $\text{XeF}^+\text{PtF}_6^-$; since then, compounds involving krypton, xenon, radon, and most recently, argon have been reported.^{118,119,120,121,122,123,124} Of the noble gases, synthetic xenon chemistry is the most diverse and an extensive list of Xe(II), Xe(IV), Xe(VI) and Xe(VIII) compounds has been prepared.¹²⁵ One major limitation in xenon chemistry is that the formation of stable bonds with xenon is generally restricted to highly electronegative elements, such as fluorine and oxygen. Some well-known Xe compounds are XeF_2 , XeO_4 , and the perxenate anion, XeO_6^{4-} . Accounting for lone electron pairs and formal bonds, the expected molecular geometries of these compounds can be predicted.¹²⁶ Xenon difluoride has a trigonal bipyramidal arrangement of electron pairs, XeF_2E_3 , where E is a lone electron pair; this gives rise to a linear geometry with two axial fluorine ligands and three equatorial lone electron pairs. Xenon tetraoxide is tetrahedral with four formal double Xe,O bonds and no formal electron pairs on xenon. Lastly, the perxenate anion is octahedral; in this case, the two oxygen ligands in axial positions form double bonds with Xe, whereas the four oxygen ligands in equatorial positions form single bonds with Xe, thus satisfying octahedral geometry and an overall anionic charge of -4. Using similar arguments, what is the predicted geometry for XeF_6 ? Unlike the perxenate anion, XeF_6 has an extra lone electron pair; *i.e.*, XeF_6E . Despite this, recent theoretical studies¹²⁷ indicate that XeF_6 may adopt either an O_h or C_{3v} geometry; however, experimental studies suggest that XeF_6 does not adopt a discrete, octahedral unit, but forms an extended, polymeric structure.¹²⁸

Of the nine stable Xe isotopes, only two are NMR-active: ^{129}Xe and ^{131}Xe ; the preferred isotope for NMR studies is, undoubtedly, ^{129}Xe . The lack of interest expressed in ^{131}Xe NMR studies, regardless of the state of matter, is mainly due to the difficulties presented by its daunting nuclear properties; see Table 4.1. The primary chemical application for xenon is as a characterization tool for porous materials through the use of hyper-polarized xenon in ^{129}Xe NMR studies. The procedure involves flowing xenon gas through a solid material and obtaining information regarding pore size and shapes through the xenon magnetic shielding interaction. In this way, xenon acts as a mobile, chemical tag, allowing solid materials to be characterized in a non-invasive fashion. The

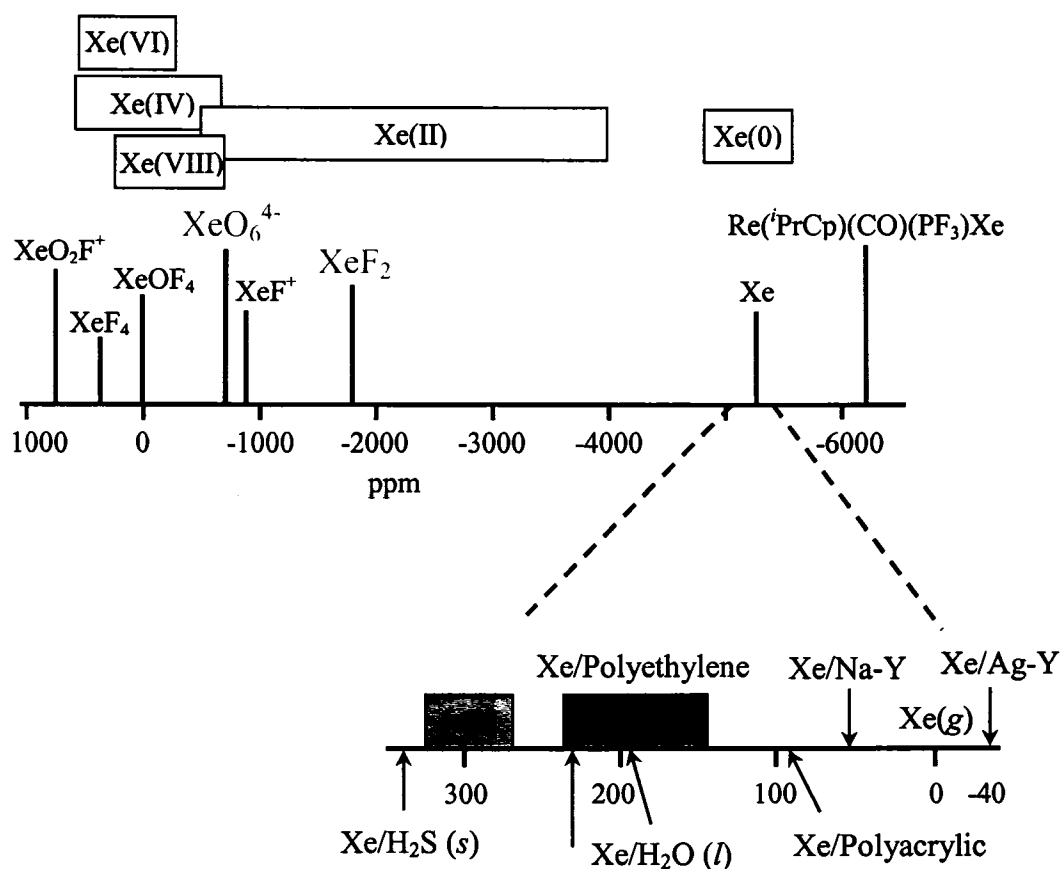


Figure 4.1: Xe chemical shift range, referenced with respect to the primary Xe chemical shift reference, XeOF₄ (neat liquid, 24 °C), indicating the most shielded, Re(ⁱPrCp)(CO)(PF₃)Xe, and least shielded, XeO₂F⁺, Xe compounds, along with other selected Xe systems; note, XeF₂ and XeO₆⁴⁻ are investigated in this *Thesis*. The Xe chemical shift range is often discussed in terms of the formal oxidation state of Xe, with Xe(0) being most shielded and Xe(VIII) being least shielded; however, from this Figure, the agreement is poor. Redrawn from Ref. 129.

success of this technique lies partially in the acute sensitivity of the Xe shielding interaction to subtle changes in the Xe environment, whether in a directly bonded compound, on the surface, in a pore, or flowing through a channel. Hyperpolarized xenon NMR spectroscopy is a thriving area of research that has been extensively reviewed.^{130,131,132,133,134,135} Although the direct observation of ^{129}Xe in chemically bound Xe species is rare,^{136,137} solution studies are abundant,¹²⁵ establishing a xenon chemical shift range of approximately 7000 ppm. The Xe chemical shift scale is shown in Figure 4.1. Qualitatively, the extent of shielding of the xenon nucleus appears to depend on the formal oxidation state of xenon and generally follows the trend: $\text{Xe}(0) > \text{Xe}(\text{II}) > \text{Xe}(\text{IV}) > \text{Xe}(\text{VI})$. $\text{Re}(\text{PrCp})(\text{CO})(\text{PF}_3)\text{Xe}$ is the most shielded, $\delta_{\text{iso}} \approx -6,179$ ppm,¹³⁸ and XeO_2F^+ is the least shielded xenon species, $\delta_{\text{iso}} \approx +704$ ppm, known to date.¹³⁹ Several reports in the literature state that the xenon of XeO_6^{4-} is the least shielded xenon; however, the previously reported chemical shift for XeO_6^{4-} , $+2077$ ppm,¹⁴⁰ is incorrect and the proper value is -748 ppm.¹²⁵

To date, the use of ^{131}Xe NMR to study compounds consists of a single solution-phase study;¹⁴¹ however, several investigations of atomic ^{131}Xe have been reported.^{142,143,144,145,146,147,148}

In this *Chapter*, three projects are presented. First, a solid-state NMR study of XeF_2 is reported, which represents the first direct examination of a solid Xe compound by ^{129}Xe NMR. Through a combined experimental solid-state ^{129}Xe NMR study, the xenon magnetic shielding tensor, σ , of XeF_2 has been characterized. The axially-symmetric xenon shielding tensor is highly anisotropic and demonstrates, for the first time, the importance of relativistic effects in determining Xe shielding tensors; these results are corroborated by ZORA DFT calculations for XeF_2 and other noble gas difluorides. The second study is an extension to the XeF_2 project and involves a computational investigation of the role of relativistic effects in determining shielding tensors for a series of linear molecules containing heavy atoms. By examining non-relativistic and spin-orbit relativistic ZORA DFT results for the shielding tensors, the onset of the importance of relativistic effects is probed and the validity of existing non-relativistic theories is questioned. Third, a $^{129/131}\text{Xe}$ NMR study of a solid Xe compound, sodium perxenate, is presented. Two forms of sodium perxenate, $\text{Na}_4\text{XeO}_6 \cdot x\text{H}_2\text{O}$ ($x = 0, 2$), are examined

using the two NMR-active Xe isotopes, ^{129}Xe and ^{131}Xe , to probe the local Xe environment. This study represents the first ^{131}Xe NMR study of a Xe compound in the solid state. Through measurement of the Xe EFG and shielding tensors for the perxenate anions, the sensitivity of the two interactions to local structural changes is compared and the feasibility of solid-state ^{131}Xe NMR studies is assessed.

4.3. Solid-State ^{129}Xe NMR Study of Xenon Difluoride, XeF_2

The research on XeF_2 has been published as a full article¹³⁶ in the *Journal of Physical Chemistry A* and is presented here in a slightly modified version. In the published version, the structure description indicates that XeF_2 crystallizes in space group $I4/m$, whereas the correct space group is $I4/mmm$. Also, there are a total of two XeF_2 molecules per unit cell and not nine, as quoted in the manuscript.¹³⁶

My role in this project is briefly outlined: to accommodate the air-sensitive XeF_2 , I designed a teflon sample insert for 4.0 and 5.0 mm ZrO_2 rotors, which served as a lid and prevented exposure to the air. I handled the sample in an inert atmosphere, where it was physically ground and packed into the rotor. I carried out all NMR experiments and computations, analyzed the results, and was principal author of the manuscript. Prof. Glenn Penner, co-author of the paper, carried out some preliminary work on XeF_2 and offered advice on the manuscript.

4.3.1. Introduction

One of the first xenon-containing molecules that has attracted interest from both an experimental and a theoretical point of view is xenon difluoride, XeF_2 - the simplest xenon-containing neutral molecule. Since the discovery of XeF_2 in 1962, the structure and bonding, as well as the thermodynamic and spectroscopic properties of this molecule have been the subject of theoretical^{127,149,150,151,152,153,154,155,156,157} and experimental scrutiny.^{158,159,160,161,162,163,164,165,166,167,168} The linear geometry of this centrosymmetric molecule was deduced from vibrational¹⁵⁸ spectra and confirmed by X-ray¹⁵⁹ and neutron diffraction¹⁶⁰ studies. More accurate bond lengths, determined from rotational Raman¹⁶¹ and high-resolution infrared¹⁶² spectra have subsequently been reported.

Numerous ^{129}Xe and ^{19}F NMR studies of XeF_2 have been undertaken in both solution and in the solid state. The earliest work, carried out by Hindermann and Falconer,¹⁶³ involved the use of solid-state ^{19}F NMR spectroscopy to measure the rigid-lattice second moment of XeF_2 at three applied magnetic field strengths, 0.7, 1.4, and 2.35 T, to determine the anisotropy of the ^{19}F magnetic shielding tensor, Ω . The value obtained, $|\Omega(\text{F})| = 105 \pm 10$ ppm, has been quoted numerous times in the literature and has been used to estimate $\Omega(\text{Xe})$ indirectly; however, given the minimal data and the relatively low applied magnetic fields available for ^{19}F NMR in 1969, the reported error in $\Omega(\text{F})$, ± 10 ppm, seems modest.

Jokisaari *et al.* investigated the secondary isotope effect of ^mXe on the ^{19}F magnetic shielding of XeF_2 in acetonitrile- d_3 .¹⁶⁴ Xenon difluoride is an excellent candidate for this type of study given that xenon has nine stable isotopes: ^{124}Xe (0.10%), ^{126}Xe (0.09%), ^{128}Xe (1.91%), ^{129}Xe (26.4%), ^{130}Xe (4.1%), ^{131}Xe (21.2%), ^{132}Xe (26.9%), ^{134}Xe (10.4%), and ^{136}Xe (8.9%).¹⁶⁹ A linear relationship was found between the one-bond secondary isotope effect on the ^{19}F magnetic shielding and the relative mass factor for the xenon isotopes.

The ^{129}Xe and ^{19}F spin-lattice relaxation times, T_1 , of XeF_2 in acetonitrile- d_3 have also been studied as a function of temperature and applied magnetic field strength.¹⁶⁵ These data indicate that for both ^{129}Xe and ^{19}F , the nuclear magnetic shielding anisotropy and spin-rotation mechanisms are the dominant T_1 mechanisms, while the dipole-dipole mechanism is estimated to be much less than 1%. The ^{129}Xe and ^{19}F T_1 data were further used to investigate the magnetic shielding anisotropy in XeF_2 , allowing for the first indirect measurement of $\Omega(\text{Xe})$. Two approaches were used, resulting in very different values for $\Omega(\text{Xe})$, 2416 ppm and 4722 ppm, and $\Omega(\text{F})$, 105 ppm¹⁶³ and 205 ppm; hence, the correct values of $\Omega(\text{Xe})$ and $\Omega(\text{F})$ remain an unsettled issue in the literature.

In the present study, solid-state ^{129}Xe and ^{19}F NMR spectroscopy, as well as non-relativistic and relativistic spin-orbit zeroth-order regular ZORA DFT calculations, are employed to directly determine the xenon and fluorine magnetic shielding tensors of XeF_2 . We report both the magnitude and sign of $^1J(^{129}\text{Xe}, ^{19}\text{F})_{\text{iso}}$ for solid XeF_2 and compare this with previous results determined from solution ^{129}Xe NMR studies of XeF_2 in various solvents,^{164,170} as well as with recent ZORA DFT calculations.^{127c,156,157}

Additional relativistic and non-relativistic shielding calculations on XeF₄ and KrF₂ are presented and compared with our results for XeF₂.

4.3.2. Nuclear Magnetic Shielding for Linear Molecules

The relevant definitions for nuclear magnetic shielding, σ , are given in *Section 2.4*. To recap, σ is necessarily axially-symmetric for linear molecules (see Table 2.2; $D_{\infty h}$); hence, only σ_{\parallel} and σ_{\perp} are required to characterize σ . Also, σ may be partitioned into diamagnetic, σ^{dia} , and paramagnetic, σ^{para} , components, which depend on the ground electronic state and excited electronic states, respectively, of the molecule. For a linear molecule, the paramagnetic shielding parallel to the bond axis, $\sigma_{\parallel}^{\text{para}}$, is exactly zero and $\sigma_{\parallel}^{\text{dia}} \approx \sigma(\text{free atom})$ ¹⁷¹. Several experimental NMR studies demonstrate that σ_{\parallel} is relatively invariant for linear compounds and is approximately equal to $\sigma(\text{free atom})$.^{172,173,174} The perpendicular component of the paramagnetic shielding, $\sigma_{\perp}^{\text{para}}$, is non-zero and difficult to determine accurately; however, Ramsey³³ and Flygare and Goodisman¹⁷¹ derived a convenient connection between the nuclear magnetic shielding constant and the nuclear spin-rotation constant, C_I , based on non-relativistic theory. For a linear molecule,

$$\sigma_{\perp} \approx -\left(\frac{m_p}{2m_e g_N}\right)\left(\frac{C_I}{B}\right) + \sigma^{\text{dia}}(\text{free atom}), \quad (4.3)$$

where m_p is the proton rest mass, m_e is the electron rest mass, g_N is the g -value of the nucleus of interest, and B is the rotational constant of the molecule. Hence, one can obtain accurate values of σ^{para} indirectly through measurement of C_I using molecular beam or high-resolution microwave experiments.^{35,174} A further important consequence of this relationship is that it allows *absolute* nuclear magnetic shielding scales to be established;^{31,33} however, the shielding scales thus obtained are strictly valid in the non-relativistic limit. The significance of relativistic effects in calculating nuclear magnetic shielding for heavy nuclei is an important issue which continues to attract a great deal of interest; here we give a few representative references.^{175,176,177,178,179,180,181,182,183,184} One result of relativistic effects on nuclear magnetic shielding is that $\sigma_{\parallel}^{\text{para}} \neq 0$ for linear molecules; this has been recently demonstrated in a series of non-relativistic and

relativistic calculations on the hydrogen halides, HX.^{177,185} While $\sigma_{\parallel}^{\text{para}}(\text{X}) = 0.0$ ppm for the non-relativistic calculations, analogous relativistic calculations yield non-zero values for $\sigma_{\parallel}^{\text{para}}(\text{X})$ and these values become increasingly significant for the heavier halides. For example, $\sigma_{\parallel}^{\text{para}}(\text{F}) = 3.2$ ppm for HF, while $\sigma_{\parallel}^{\text{para}}(\text{I}) = 840$ ppm for HI.¹⁸⁵ These are results from computational studies; however, no experimental studies of linear molecules have previously been reported where σ_{\parallel} deviates significantly from $\sigma(\text{free atom})$.

4.3.3. Experimental and Computational Details

4.3.3.1. Solid-State ^{129}Xe NMR Spectroscopy

A commercial sample of XeF_2 , purchased from Aldrich, was powdered and packed into a 4 mm outer diameter (o.d.) zirconia rotor in a nitrogen-filled glove box and sealed with an air-tight teflon end cap. All ^{129}Xe and ^{19}F NMR experiments were carried out at room temperature using a Chemagnetics CMX Infinity spectrometer ($B_0 = 4.7$ T), operating at spectrometer frequencies of 55.574 and 188.290 MHz for ^{129}Xe and ^{19}F , respectively. The magic-angle was set by maximizing the number of rotational echoes in the ^{79}Br NMR free-induction decay and spinning sidebands of the ^{79}Br NMR spectrum of KBr. One-pulse experiments were employed to acquire ^{129}Xe and ^{19}F NMR spectra. Decoupling parameters for $^{129}\text{Xe}\{^{19}\text{F}\}$ NMR spectra were optimized on a sample of teflon using cross-polarization (CP) ($^{19}\text{F} \rightarrow ^{13}\text{C}$) with high-power two-pulse phase modulated⁷⁶ (TPPM) ^{19}F decoupling. In the case of XeF_2 , because $T_1(^{19}\text{F})$ is very long (> 100 s) compared to $T_1(^{129}\text{Xe})$, the use of CP from $^{19}\text{F} \rightarrow ^{129}\text{Xe}$ is not beneficial. A one-pulse experiment with TPPM ^{19}F decoupling is more efficient and, hence, was used in the present study.

Acquisition of ^{129}Xe NMR spectra employed a spectral width of 800 kHz, $\pi/2$ pulse width of 2.0 μs , TPPM pulse width of 4.0 μs , acquisition time of 10.240 ms, and pulse delay of 60 s. All ^{19}F NMR spectra were acquired using a spectral width of 200 kHz, $\pi/2$ pulse width of 2.0 μs , acquisition time of 10.240 ms, and pulse delay of 1200 s. Simulations of ^{129}Xe and ^{19}F NMR spectra were carried out using WSOLIDS and/or SIMPSON. To account for ^{19}F - ^{19}F dipolar interactions, ^{19}F NMR spectra were also

analyzed using a memory function approach, as outlined by Hirschinger and co-workers.¹⁸⁶

The primary reference for ^{129}Xe NMR spectroscopy is OXeF_4 (neat liquid, 24°C), which is not readily available. A secondary reference often used is Xe(g) ; however, given that the chemical shift of xenon gas is sensitive to pressure and temperature changes, this is not an ideal reference sample. Our ^{129}Xe NMR spectra of XeF_2 are referenced with respect to external OXeF_4 (neat liquid, 24°C) at 0.0 ppm by determining the *absolute* ^{129}Xe frequency for XeF_2 . First, the absolute ^1H frequencies and chemical shifts of cyclohexane ($\nu(^1\text{H}) = 200.149112\text{ MHz}$, $\delta(^1\text{H})_{\text{iso}} = 1.430\text{ ppm}$) and tetramethylsilane ($\nu(^1\text{H}) = 200.148826\text{ MHz}$, $\delta(^1\text{H})_{\text{iso}} = 0.0\text{ ppm}$) were determined. Next, the absolute ^1H frequency of TMS and ^{129}Xe frequency of neat, liquid OXeF_4 at 24°C ($\Xi = 27.810186\text{ MHz}$)³⁷ were used to calculate the absolute ^{129}Xe frequency for OXeF_4 on our spectrometer ($\nu(^{129}\text{Xe}) = 55.661759\text{ MHz}$). This information, along with the absolute ^{129}Xe frequency of XeF_2 and Equation 2.10, was used to determine the chemical shift of solid XeF_2 . We have taken $\delta(\text{Xe}(\text{free atom})) = -5460\text{ ppm}$.¹³⁴ Our ^{19}F NMR spectra are referenced with respect to the primary ^{19}F NMR chemical shift reference, CCl_3F (neat liquid), $\Xi = 94.094011\text{ MHz}$.³⁷ The absolute ^{19}F frequency of CCl_3F (neat liquid) on our spectrometer was calculated, 188.328058 MHz , and used to determine the ^{19}F chemical shift of solid XeF_2 .

4.3.3.2. Quantum Chemical Calculations

DFT calculations of Xe, Kr and F magnetic shielding tensors were performed using the NMR module¹⁰⁷ of the ADF program.^{105,106} The TZ2P Slater-type ZORA basis sets, available with the ADF program, were employed for xenon, krypton, and fluorine. Our calculations were carried out using either an IBM RS/6000 workstation or a Linux-based cluster with dual AMD 1800+ Athlon processor nodes.

DFT calculations were performed on isolated XeF_2 , XeF_4 , and KrF_2 molecules at their equilibrium bond lengths, $r_e(\text{Xe,F}) = 1.9791\text{ \AA}$,¹⁶¹ $r_e(\text{Xe,F}) = 1.928970\text{ \AA}$,¹⁸⁷ and $r_e(\text{Kr,F}) = 1.87693\text{ \AA}$,¹⁶⁷ respectively, determined from Raman¹⁶¹ and high-resolution infrared^{167,187} spectroscopy. As well, the effect of bond length variation on the Xe, Kr,

and F magnetic shielding tensors of XeF₂ and KrF₂ was investigated by systematically varying $r_e(\text{Xe},\text{F})$ and $r_e(\text{Kr},\text{F})$ by ± 0.02 in 0.01 \AA increments. The shielding of the free atom values for Kr and Xe were also determined using both non-relativistic and spin-orbit relativistic ZORA DFT.

Noteworthy is that Vaara and Pyykkö¹⁸⁸ recently proposed an absolute shielding scale for xenon including relativistic effects and very large basis sets and found that $\sigma(\text{Xe}(\text{free atom})) = 6938 \pm 21 \text{ ppm}$. An absolute magnetic shielding scale has also been established for fluorine, where $\sigma(\text{CFCl}_3) = 189.9 \text{ ppm}$ at 303 K.¹⁸⁹

4.3.4. Results and Discussion

4.3.4.1. Solid-State ¹²⁹Xe NMR Spectroscopy

Shown in Figure 4.2 are experimental and calculated ¹²⁹Xe NMR spectra of an MAS sample of XeF₂ at two different spinning frequencies. The half-height linewidth,

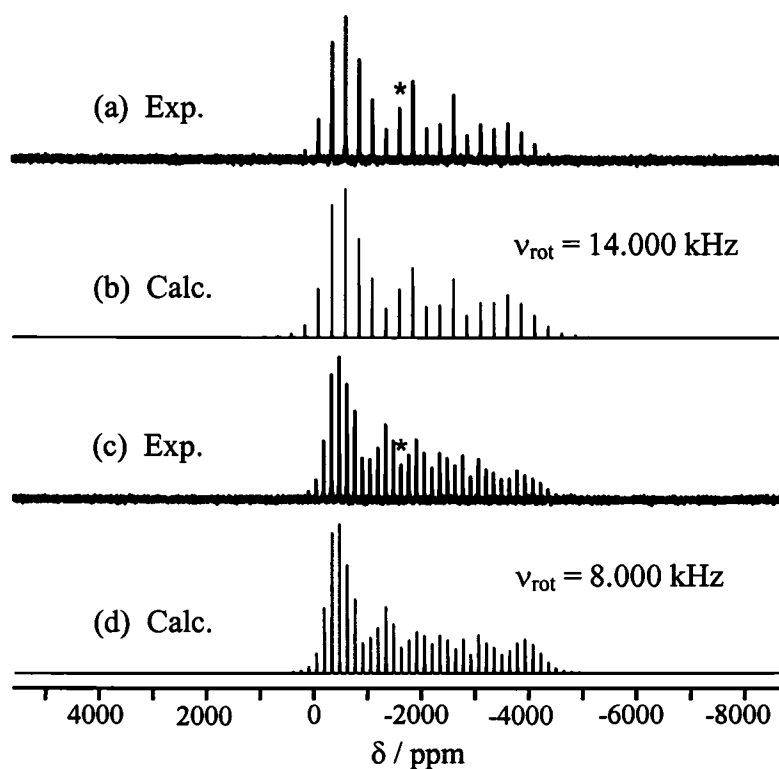


Figure 4.2: Experimental (a, c) and calculated (b, d) ¹²⁹Xe{¹⁹F} NMR spectra of an MAS sample of XeF₂ acquired with TPPM ¹⁹F decoupling. The half-height linewidth of the spinning sidebands, $\Delta\nu_{1/2}$, is $300 \pm 50 \text{ Hz}$. $\delta(^{129}\text{Xe})_{\text{iso}}$ is indicated by an asterisk in (a) and (c).

$\Delta\nu_{1/2}$, of the individual spinning sidebands is 300 ± 50 Hz. The isotropic ^{129}Xe chemical shift varied slightly with spinning frequency, which is expected given the sensitivity of ^{129}Xe chemical shifts to temperature.¹⁶⁴ The observed isotropic chemical shift of XeF_2 , $\delta_{\text{iso}} = -1603 \pm 5$ ppm, is characteristic of Xe(II) compounds.¹²⁵

The X-ray crystal structure of XeF_2 has been determined¹⁵⁹ and a model of the unit cell is shown in Figure 4.3. In crystalline XeF_2 , the molecules are aligned parallel in a body-centered array (space group $I4/mmm$) and the unit cell contains a total of two XeF_2 molecules. On the basis of symmetry arguments, the xenon and fluorine nuclear magnetic shielding tensors of solid XeF_2 must be axially symmetric, as evidenced by the lineshape of the ^{129}Xe NMR spectra (Figure 4.2). Of particular note is the enormous span, $\Omega = 4245 \pm 20$ ppm, which indicates that the chemical shift of a XeF_2 molecule oriented perpendicular to the applied magnetic field, B_0 , gives rise to an NMR signal which is 4245 ppm less shielded than that of a molecule oriented parallel to B_0 . The observed xenon shielding anisotropy for XeF_2 is the largest measured for xenon and represents the first direct measurement of $\Omega(\text{Xe})$ for a xenon compound.¹³⁶ The span of the shielding tensor for XeF_2 covers the entire known chemical shift range for Xe(II) compounds and approximately 62% of the total known xenon chemical shift range

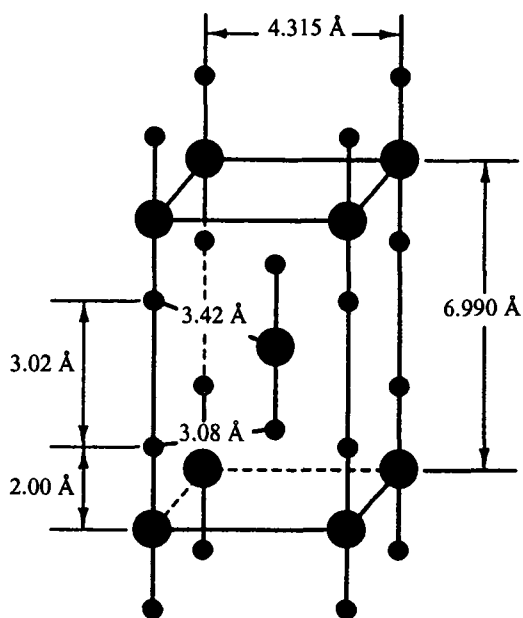


Figure 4.3: Unit cell of solid XeF_2 from Ref. 160; \bullet = xenon, \circ = fluorine.

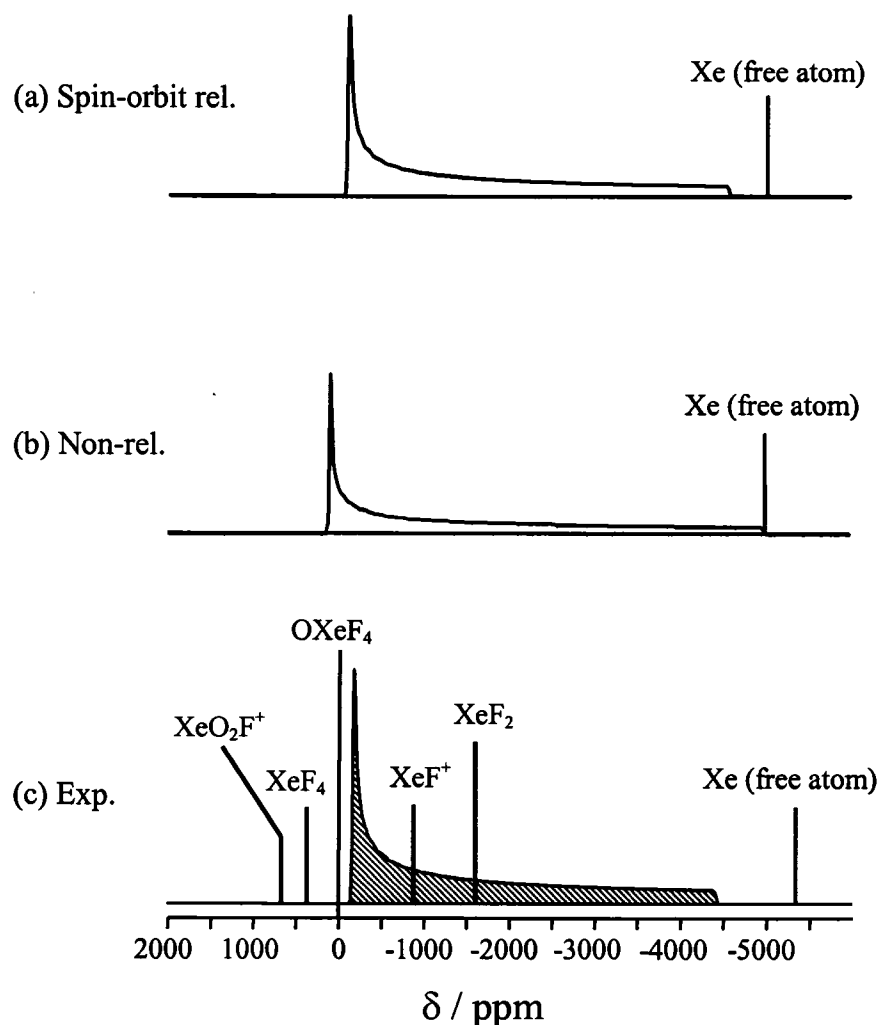


Figure 4.4: (a) Spin-orbit relativistic and (b) non-relativistic ZORA DFT calculations of $\Omega(\text{Xe})$ in XeF_2 , assuming $\delta(^{129}\text{Xe})_{\text{iso}} = -1603$ ppm. The isotropic ^{129}Xe chemical shift of the free Xe atom is shown with respect to $\delta(\text{XeF}_2)_{\parallel}$, calculated using $\sigma(\text{Xe (free atom)})_{\parallel} - \sigma(\text{XeF}_2)_{\parallel}$ from Table 4.2. (c) Experimentally-determined $\Omega(\text{Xe})$ in XeF_2 and isotropic chemical shifts of selected xenon compounds plotted on the known xenon chemical shift scale.¹⁴⁰

(~6880 ppm), as illustrated in Figure 4.4. The isotropic chemical shift range for Xe(II) compounds in various solvents is approximately 3400 ppm, ranging from -574 ppm for XeF^+ in SbF_5 at 25° C to -3967.5 ppm for $\text{C}_6\text{H}_5\text{Xe}^+$ in HF at -10° C.¹²⁵

A striking feature of the ^{129}Xe NMR spectrum (Figure 4.4(c)) is the position of the parallel component of the chemical shift tensor, $\delta_{\parallel} = -4433$ ppm, which differs from $\delta(\text{Xe}(\text{free atom}))$ by ~1000 ppm. This observation does not comply with non-relativistic theory,^{33,171} which predicts that $\sigma_{\parallel} = \sigma_{\parallel}^{\text{dia}} \approx \sigma(\text{free atom})$ for any linear molecule,

suggesting that relativistic effects play a significant role in determining nuclear magnetic shielding tensors for xenon.

Summarized in Table 4.2 are non-relativistic and spin-orbit relativistic ZORA DFT calculations of shielding tensors for Xe, XeF₂, KrF₂ and XeF₄. Our spin-orbit relativistic calculations for elemental Xe, $\sigma(\text{free atom}) = 6409$ ppm, are in good

Table 4.2: Calculated Magnetic Shielding Parameters for the Xenon Atom and Isolated XeF₂, XeF₄ and KrF₂ Molecules.*

| | | σ_{\parallel} / ppm | σ_{\perp} / ppm | σ_{iso} / ppm | Ω / ppm |
|------------------------------------|----------------|----------------------------|------------------------|-----------------------------|----------------|
| <i>Spin-orbit Relativistic DFT</i> | | | | | |
| Xe (free atom) | | | | 6409.4 | 0 |
| XeF ₂ | Xe | 5976.6 | 1521.8 | 3006.7 | 4454.8 |
| | F | 523.8 | 246.6 | 339.0 | 277.2 |
| XeF ₄ | Xe | 1534.6 | -159.7 | 405.0 | 1694.3 |
| | F [†] | 313.4 | -48.0 | 177.9 | 361.4 |
| KrF ₂ | Kr | 3303.7 | 1312.2 | 1976.0 | 1991.6 |
| | F | 510.7 | -161.2 | 62.8 | 671.9 |
| <i>Non-relativistic DFT</i> | | | | | |
| Xe (free atom) | | | | 5646.7 | 0 |
| XeF ₂ | Xe | 5653.2 | 586.5 | 2275.4 | 5066.7 |
| | F | 496.8 | 297.2 | 363.7 | 199.6 |
| XeF ₄ | Xe | -41.6 | 162.0 | 94.1 | -203.5 |
| | F [‡] | 271.3 | -22.8 | 172.0 | 294.1 |
| KrF ₂ | Kr | 3255.8 | 1040.3 | 1778.8 | 2215.5 |
| | F | 492.8 | -132.9 | 75.7 | 625.7 |

* Equilibrium geometries for XeF₂ from a Raman study and those for XeF₄ and KrF₂ from high-resolution infrared studies: $r_e(\text{Xe,F})$ in XeF₂ is 1.9791 Å, $r_e(\text{Xe,F})$ in XeF₄ is 1.928970 Å and $r_e(\text{Kr,F})$ in KrF₂ is 1.87693 Å; Refs. 161, 187, 167, respectively.

[†] For XeF₄, $\sigma(\text{F})$ is non-axially symmetric. The component along $r(\text{Xe,F})$ is $\sigma_{\parallel} = \sigma_{33}$ and that parallel to the molecular C_4 -symmetry axis is $\sigma_{\perp} = \sigma_{11}$; $\sigma_{11} = -48.0$ ppm, $\sigma_{22} = 268.3$ ppm, and $\sigma_{33} = 313.4$ ppm.

[‡] Assignment of σ_{\parallel} and σ_{\perp} as in (b); $\sigma_{11} = -22.8$ ppm, $\sigma_{22} = 267.4$ ppm, and $\sigma_{33} = 271.3$ ppm.

agreement with that determined by Vaara and Pyykkö,¹⁸⁸ $\sigma(\text{free atom}) = 6938 \pm 21$ ppm, while our non-relativistic result, 5647 ppm, differs by 1291 ppm. The spin-orbit relativistic results for XeF₂ indicate that $\Omega(\text{Xe}) = 4469$ ppm, which is in excellent agreement with our experimental value, 4245 ± 50 ppm, with a relative difference, $[\Omega(\text{Xe})_{\text{exp}} - \Omega(\text{Xe})_{\text{calc}}] / \Omega(\text{Xe})_{\text{exp}}$, of less than 10%, while the non-relativistic value, 5067 ppm, is ~800 ppm greater than the experimental value. Most important from Table 4.2 is the spin-orbit relativistic result for the parallel component of the Xe shielding tensor in XeF₂, which indicates that $\sigma(\text{free atom})$ is ~430 ppm more shielded than σ_{\parallel} for XeF₂ (Figure 4.4(a)), while results from non-relativistic calculations indicate that $\sigma_{\parallel} \approx \sigma(\text{free atom})$, as expected (Figure 4.4(b)). Hence, for relatively heavy nuclei such as xenon, it is clear that Ramsey's non-relativistic theory³³ is not strictly applicable.

To further investigate the importance of relativistic effects on the xenon magnetic shielding of XeF₂, the dependence of $\sigma_{\text{iso}}(\text{Xe})$ on $r(\text{Xe},\text{F})$ has been computed at bond lengths near r_e using ZORA DFT calculations. Upon varying $r(\text{Xe},\text{F})$, spin-orbit relativistic calculations indicate that $\partial\sigma(\text{Xe})_{\text{iso}}/\partial r \approx -403$ ppm Å⁻¹, while non-relativistic calculations yield, $\partial\sigma(\text{Xe})_{\text{iso}}/\partial r \approx -1016$ ppm Å⁻¹. The change in isotropic Xe shielding is less pronounced for the spin-orbit results because *both* the perpendicular and parallel shielding components become more deshielded upon increasing $r(\text{Xe},\text{F})$, leading to a reduced net effect in σ_{iso} ; in contrast, for non-relativistic calculations, σ_{\parallel} remains constant while the perpendicular component becomes more deshielded, resulting in a stronger dependence of σ_{iso} on $r(\text{Xe},\text{F})$.

Additional σ calculations carried out on KrF₂ and XeF₄ (Table 4.2) indicate that inclusion of relativistic effects is vital for XeF₄, but less important for KrF₂. For XeF₄, a dramatic increase in $\Omega(\text{Xe})$ from -204 to +1694 ppm is observed, while changes in $\Omega(\text{Kr})$ for KrF₂ are relatively minor. Overall comparison of results for $\sigma(\text{Xe})$ and $\sigma(\text{Kr})$ for XeF₂ and KrF₂ indicates that inclusion of relativistic effects is less important for KrF₂, which is expected given its lower atomic number.

It is now instructive to compare our $\Omega(\text{Xe})$ results for XeF₂ to those obtained in the literature, see Table 4.3. As previously mentioned, the work carried out by Jokisaari and co-workers¹⁶⁵ represents the first indirect measurement of $\Omega(\text{Xe})$ from ¹²⁹Xe and ¹⁹F

T_1 studies of XeF_2 dissolved in acetonitrile- d_3 . In favourable cases, interpretation of such data allows the determination of both $\Omega(\text{Xe})$ and $\Omega(\text{F})$ as well as the nuclear spin-rotation, SR, constants, $C_1(^{129}\text{Xe})$ and $C_1(^{19}\text{F})$. The analysis is complicated by the fact that one does not know the rotational correlation time, τ_2 , or the angular momentum correlation time, τ_j . In the case of XeF_2 dissolved in acetonitrile- d_3 , measurements of the spin-lattice relaxation rate, $R_1 = T_1^{-1}$, at variable temperatures and three different applied magnetic field strengths led to the conclusion that $\Omega(\text{Xe})/\Omega(\text{F}) = 21.6 \pm 0.7$. Using the value of $\Omega(\text{F})$, 105 ± 10 ppm, from early solid-state ^{19}F NMR measurements by Hindermann and Falconer,¹⁶³ and ratio of the xenon and fluorine shielding anisotropies, 21.6, yields $\Omega(\text{Xe}) \approx 2270$ ppm. In an alternative approach, the authors recognized that the square-root of the product of R_1^{CSA} and R_1^{SR} was independent of temperature and directly proportional to the applied magnetic field. In fact, one can show that:^{32,190}

$$(R_1^{\text{CSA}} R_1^{\text{SR}})^{1/2} = \left(\frac{4}{135}\right)^{1/2} \left(\frac{m_e}{m_p}\right) \left(\frac{\gamma_N \hbar}{\mu_N}\right) (\gamma B_0) \Omega^2, \quad (4.4)$$

Table 4.3: Xenon Magnetic Shielding and Indirect Nuclear ^{129}Xe , ^{19}F Spin-Spin Coupling Values for XeF_2 from this Study and the Literature.

| Method | $\Omega(\text{Xe})$ / ppm | $\Omega(\text{F})$ / ppm | $^1J(^{129}\text{Xe}, ^{19}\text{F})_{\text{iso}}$ / Hz |
|-----------------------------|----------------------------------|---------------------------------|---|
| Solid-State NMR | $4245 \pm 20^*$ | $150 \pm 20^*$ 105^\dagger | -5560^* |
| Solution NMR [‡] | 2416 or 4722^\S | 205^\S | $5550 \pm 20^{**}$ $5644.2 \pm 0.6^{\dagger\dagger}$ |
| Semi-empirical calculations | 5125 or $7185^{\ddagger\dagger}$ | ----- | ----- |
| ZORA DFT | 4469^* | 277^* | $-6038^{\S\S}$ -5958^{***} |

* This work.

† Ref. 163.

‡ XeF_2 dissolved in acetonitrile- d_3 .

§ Ref. 165.

** Ref. 170.

†† Ref. 164.

‡‡ Ref. 149.

§§ Ref.156.

*** Ref.157.

Substitution of $(R_1^{\text{CSA}} R_1^{\text{SR}})^{1/2}$, determined from experiment, and the known constants into Equation 4.4 led to $\Omega(\text{Xe}) = 4722$ ppm, which is in fair agreement with our solid-state NMR value, 4245 ppm. In obtaining the above expression it is assumed that the relationship between the nuclear spin-rotation tensor and magnetic shielding tensor is valid for xenon, a relatively heavy nucleus where relativistic effects are important.

Previous to the T_1 investigation of Jokisaari *et al.*,¹⁶⁵ the only data available for $\Omega(\text{Xe})$ were the very early LCAO-MO calculations of Jameson and Gutowsky,¹⁴⁹ who, employing two different models, predicted that $\Omega(\text{Xe}) = 5125$ or 7185 ppm. More recently, Jameson¹⁵⁰ made use of the approximation, $\Omega \approx -(3/2)[\sigma(\text{XeF}_2)_{\text{iso}} - \sigma(\text{free atom})]$, to estimate $\Omega(\text{Xe})$, 5895 ppm; however, as previously mentioned, this result is based on a non-relativistic model.

Table 4.4: Xenon Magnetic Shielding and Spin-Rotation Data for XeF_2 .

| | $\Omega(\text{Xe}) / \text{ppm}$ | $ C_{\perp}(^{129}\text{Xe}) / \text{kHz}$ | $ C_{\perp}(^{19}\text{F}) / \text{kHz}$ |
|---------------------------|----------------------------------|---|---|
| Jameson* | 5895 | 33.92 | 2.135 |
| Jokisaari <i>et al.</i> † | 2416 and 4722 | 54.1 and 27.7 | 6.13 and 3.14 |
| This work | 4245 | 24.4 | ---- |

Listed in Table 4.4 are results for $\Omega(\text{Xe})$, $C_{\perp}(^{129}\text{Xe})$ and $C_{\perp}(^{19}\text{F})$ in XeF_2 , from the literature and this work. Our result for $C_{\perp}(^{129}\text{Xe})$, 24.4 kHz, was calculated using our solid-state NMR value for $\Omega(\text{Xe})$ and the non-relativistic relationship between Ω and C_{\perp} .¹⁷¹ Although we have shown that relativistic effects are important for XeF_2 , this exercise is carried out for comparison with previous values. Jameson¹⁵⁰ followed the same approach, using $\Omega(\text{Xe}) = 5895$ ppm, to calculate $C_{\perp}(^{129}\text{Xe})$ and $C_{\perp}(^{19}\text{F})$, -33.92 kHz and -2.135 kHz, respectively; to a first approximation, the results are satisfactory. Jokisaari *et al.*¹⁶⁵ calculated the ^{129}Xe and ^{19}F spin-rotation constants according to the two aforementioned approaches. The first approach yielded values of 340 and 38.5 kHz for $C_{\perp}(^{129}\text{Xe})$ and $C_{\perp}(^{19}\text{F})$, respectively, while the second approach gave respective values of

* Ref. 150.

† Ref. 165; values of C_{\perp} given in ref. 165 have been divided by 2π .

174 and 19.7 kHz. We believe these values were mistakenly reported in kHz, but in fact are in rad s^{-1} . Dividing these values by 2π results in the values presented in Table 4.4. The value obtained for $C_{\perp}(^{129}\text{Xe})$ calculated using the second approach, 27.7 kHz, is in reasonable agreement with those obtained here and those reported by Jameson.¹⁵⁰

Expansions of a selected region of the ^{129}Xe NMR spectra of XeF_2 acquired *without* ^{19}F decoupling at two different spinning rates are shown in Figure 4.5. These spectra are characteristic of an AX_2 -spin system influenced by both the direct, $R_{\text{DD}}(^{129}\text{Xe}, ^{19}\text{F})$, and indirect, $^1J(^{129}\text{Xe}, ^{19}\text{F})$, nuclear spin-spin coupling interactions. The *indirect* spin-spin coupling splits each spinning sideband into a triplet, corresponding to the three possible combinations of ^{19}F nuclear spin states, $m(^{19}\text{F})$, of the two ^{19}F nuclei; *i.e.*, $\Sigma m(^{19}\text{F}) = -1, 0, +1$. The magnitude of $^1J(^{129}\text{Xe}, ^{19}\text{F})_{\text{iso}}$, 5566 ± 50 Hz, is easily

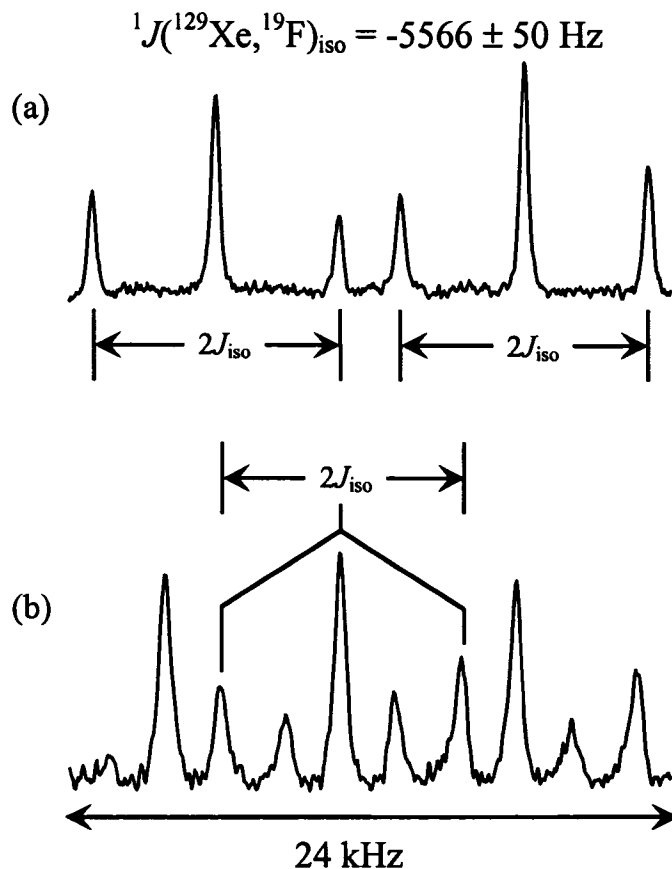


Figure 4.5: Expansions of ^{129}Xe NMR spectra of an MAS sample of XeF_2 acquired without ^{19}F decoupling at spinning frequencies of (a) 14.000 kHz and (b) 8.000 kHz.

determined by measuring the splitting between the centreband and either satellite peak, and confirmed by measuring this splitting at two different sample spinning rates. The $^{129}\text{Xe}, ^{19}\text{F}$ direct dipolar interactions (Equation 2.29) alter the relative intensities of the satellite peaks (Figure 4.5).⁵³ Experimentally, one measures the *effective* dipolar coupling, R_{eff} , which contains a contribution from the anisotropy of J_{iso} , ΔJ (see Equation 2.39).⁵³

For an AX_2 system, the relative signs of $^1J(^{129}\text{Xe}, ^{19}\text{F})_{\text{iso}}$ and R_{DD} may be determined, as outlined by Harris,¹⁹¹ by analyzing the spinning sideband manifolds of the centerband and each of the satellite subspectra. If R_{eff} makes a significant contribution to the stationary lineshapes, the effective spans of the satellite subspectra will differ: the subspectrum of one satellite will be stretched, while that of the other satellite will be squeezed with respect to the breadth of the central transition. In fact, one can show that the breadth of each subspectrum is given by:⁵³

$$\Delta\nu_{\pm m(^{19}\text{F})} = (\nu_{\parallel} - \nu_{\perp}) \pm 3\Sigma m(^{19}\text{F})R_{\text{eff}}, \quad (4.5)$$

where $\Sigma m(^{19}\text{F}) = -1, 0, +1$. In the case of XeF_2 , the centerband has a breadth of 235.9 kHz, the high frequency spinning sideband manifold is stretched (breadth ≈ 248.8 kHz) and the low frequency spinning sideband manifold is squeezed (breadth ≈ 219.7 kHz); making use of Equation 4.5 gives $R_{\text{eff}} \approx -4850 \pm 600$ Hz. Since only the relative signs of $^1J(^{129}\text{Xe}, ^{19}\text{F})_{\text{iso}}$ and $R_{\text{DD}}(^{129}\text{Xe}, ^{19}\text{F})$ can be determined, the absolute sign of either $^1J(^{129}\text{Xe}, ^{19}\text{F})_{\text{iso}}$ or $R_{\text{DD}}(^{129}\text{Xe}, ^{19}\text{F})$ must be known. For XeF_2 , R_{DD} is negative as a consequence of the negative value of $\gamma(^{129}\text{Xe})$. This result, along with the fact that $\sigma_{\parallel} > \sigma_{\perp}$, indicates that the relative signs of $^1J(^{129}\text{Xe}, ^{19}\text{F})_{\text{iso}}$ and $R_{\text{DD}}(^{129}\text{Xe}, ^{19}\text{F})$ are the same;¹⁹¹ therefore, $^1J(^{129}\text{Xe}, ^{19}\text{F})_{\text{iso}}$ must be negative, -5560 ± 50 Hz. Analogous qualitative analysis of the ^{19}F NMR spectra obtained with MAS supports this conclusion, as well as results from recent high-level calculations on XeF_2 .^{127c,156,157} The calculated values of $^1J(^{129}\text{Xe}, ^{19}\text{F})_{\text{iso}}$, -6030 Hz¹⁵⁶ and -5958 Hz,¹⁵⁷ are in very good agreement with our solid-state NMR value of $^1J(^{129}\text{Xe}, ^{19}\text{F})_{\text{iso}}$, -5560 ± 50 Hz, as well as the reported range of values from solution NMR in various solvents, ± 5579 to ± 5665 Hz.^{164,170}

In some cases, ΔJ can be obtained from NMR spectra of isolated spin-pairs.^{192,193} Using the above result for R_{eff} , and making use of the known value of $r(\text{Xe},\text{F})$ in XeF_2 to calculate R_{DD} (Equation 2.29), ΔJ can be determined. Substitution of $R_{\text{DD}}(^{129}\text{Xe}, ^{19}\text{F}) \approx -4060$ Hz, calculated using $r(\text{Xe},\text{F}) = 1.9791$ Å, and $R_{\text{eff}} \approx -4850$ Hz into Equation 2.39 gives $\Delta J = +2370$ Hz; the error in this value is estimated to be on the order of ± 1.8 kHz. Our experimental value for ΔJ , $+2380$ Hz, is of the same order of magnitude as that determined using ZORA DFT calculations, $\Delta J = 4048$ Hz.¹⁵⁶

The ^{129}Xe NMR spectra indicate that $^1J(^{129}\text{Xe}, ^{19}\text{F})_{\text{iso}}$ is insensitive to temperature changes brought upon by sample heating at the spinning speeds employed in this study. Previous ^{129}Xe and ^{19}F NMR studies of XeF_2 in acetonitrile- d_3 also found that $^1J(^{129}\text{Xe}, ^{19}\text{F})_{\text{iso}}$ is insensitive to temperature changes over the range 240 – 320 K.¹⁶⁴

4.3.4.2. ^{19}F NMR Spectroscopy

Shown in Figure 4.6 are experimental and calculated ^{19}F NMR spectra of XeF_2 acquired with MAS at two different spinning rates. Simulations of these spectra, using $^1J(^{129}\text{Xe}, ^{19}\text{F})_{\text{iso}} = -5560$ Hz, $R_{\text{DD}}(^{129}\text{Xe}, ^{19}\text{F}) = 4064$ Hz, and assuming that the Xe, F dipolar vector and σ_{\parallel} are coincident, provides $\delta(^{19}\text{F})_{\text{iso}} = -162 \pm 3$ ppm and $\Omega(\text{F}) = 160 \pm 20$ ppm. However, these simulations do not account for ^{19}F homonuclear dipolar coupling, which are known to contribute to the observed ^{19}F NMR lineshape ($M_2^{\text{homo}} = 2.65 \text{ G}^2$ or equivalently, $1.68 \times 10^9 \text{ rad}^2 \text{ s}^{-2}$)¹⁶³ due to the proximity of neighbouring fluorine atoms in the unit cell of XeF_2 (Figure 4.3). The significance of the ^{19}F - ^{19}F dipolar interaction was subsequently investigated using an analytical method based on stochastic theory involving the memory function, which describes the time-averaged fluctuations of the local dipolar field.¹⁸ The FID response function due to the dipolar interaction, obtained using the memory function approach, is given by:¹⁹⁴

$$G_D(t) = \exp\left\{M_2^{\text{homo}} \left[\frac{2}{3} f(\Gamma, \nu_{\text{rot}}, t) + \frac{1}{3} (\Gamma, 2\nu_{\text{rot}}, t) \right] \right\}, \quad (4.6)$$

$$\text{where } f(\Gamma, \nu_{\text{rot}}, t) = \frac{1}{\Gamma^2 + \nu_{\text{rot}}^2} \times \left\{ \frac{[(\Gamma^2 - \nu_{\text{rot}}^2)(1 - \cos \nu_{\text{rot}} t) + 2\Gamma \nu_{\text{rot}} \sin \nu_{\text{rot}} t] \exp(-\Gamma t)}{\Gamma^2 + \nu_{\text{rot}}^2} - \Gamma t \right\}$$

and $\Gamma = 1/\tau_c$. Here, τ_c is the correlation time describing the stochastic process of the

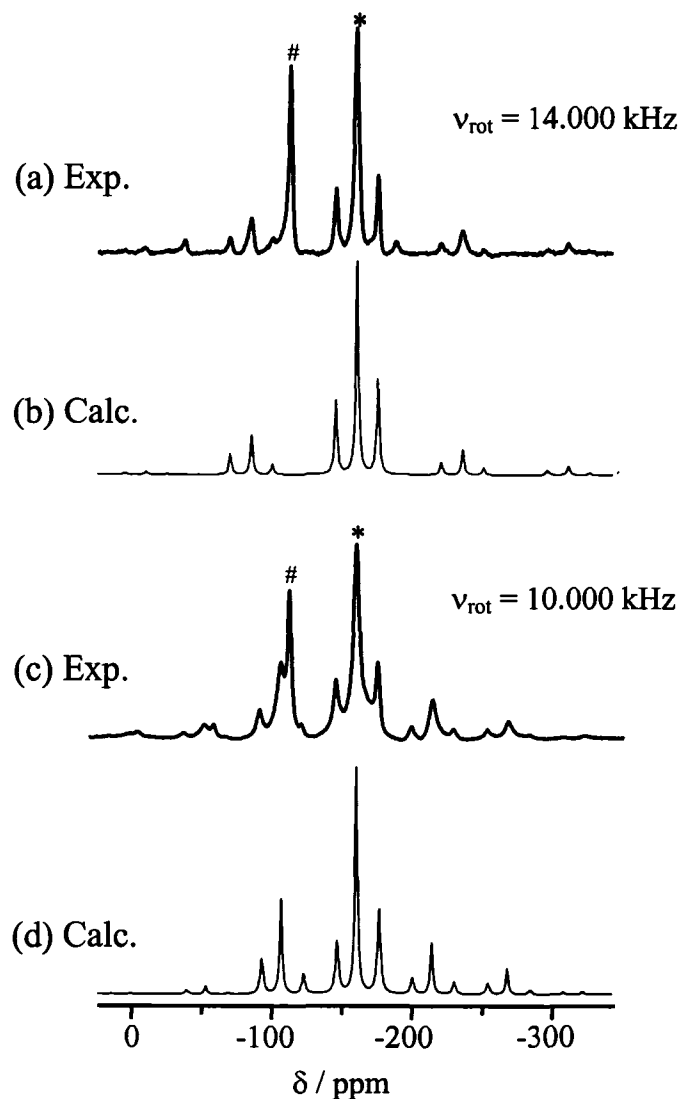


Figure 4.6: Experimental (a, c) and calculated (b, d) ^{19}F NMR spectra of an MAS sample of XeF_2 . The isotropic ^{19}F chemical shifts for XeF_2 and the teflon inserts of the rotor are indicated by * and #, respectively. The simulated ^{19}F NMR spectra do not include ^{19}F - ^{19}F dipolar coupling, which contribute $\sim 10\%$ to the relative intensities of the spinning sidebands in the observed ^{19}F NMR spectra (see text).

expectation values of the z-component of the spins due to the flip-flop operator and M_2 is the second moment. Simulations using $M_2^{\text{homo}} = 1.68 \times 10^9 \text{ rad}^2 \text{ s}^{-2}$ suggest that ^{19}F - ^{19}F dipolar coupling contributes $\sim 10\%$ to the lineshape of the ^{19}F NMR spectrum of XeF_2 and that $\Omega(^{19}\text{F}) = 150 \pm 20$ ppm; this value for $\Omega(^{19}\text{F})$ is within the error limits of that determined when ^{19}F - ^{19}F dipolar coupling was neglected. Using our best solid-state NMR values for $\Omega(\text{Xe})$, 4245 ppm, and $\Omega(\text{F})$, 150 ppm, gives a ratio, $\Omega(\text{Xe})/\Omega(\text{F})$, of

28.3, which is larger than that obtained by Jokisaari *et al.*, 21.6,¹⁶⁵ suggesting that the xenon and fluorine shielding anisotropies may be different in solution and the solid state. The early solid-state ¹⁹F NMR study by Hindermann and Falconer¹⁶³ determined $\Omega(\text{F})$ to be 105 ± 10 ppm (*vide supra*); however, we believe the reported error to be underestimated. Jokisaari *et al.*¹⁶⁵ used the method based on Equation 4.4 to determine $\Omega(\text{F})$, 205 ppm, for XeF₂ in acetonitrile. There have been experimental reports of $\Omega(\text{F})$ for XeF₄, ranging from 261 to 790 ppm,^{195,196} and other main-group fluorides; solid-state ¹⁹F NMR results indicate that for the series: SF₆, SeF₆, and TeF₆, $\Omega(\text{F})$ is 310 ppm, 370 ppm, and 215 ppm, respectively.¹⁹⁷

Experimental values of $\delta(^{19}\text{F})_{\text{iso}}$ have previously been determined for XeF₂, XeF₄, and the XeF₆-tetramer in solution: -199.6 ppm, -15.7 ppm, 118.3 ppm.¹²⁵ The difference between $\delta(^{19}\text{F})_{\text{iso}}$ for XeF₂ in solution and our solid-state NMR value, -162 ppm, is attributed to intermolecular effects, which are known to be predominantly deshielding.¹⁹⁸ Listed in Table 4.2 are ZORA DFT results for the shielding tensors in isolated XeF₂, XeF₄, and KrF₂ molecules. The *difference* in observed values of $\delta(\text{F})_{\text{iso}}$ between XeF₂ and XeF₄, ≈ 180 ppm, agrees well with our calculated value, $\sigma(\text{F})_{\text{iso}} \approx 161$ ppm. In addition, our calculated values of $\Omega(\text{F})$ for XeF₄ are within this range of observed values.^{195,196} Calculations were not carried out on XeF₆ because it exists as a tetramer in solution¹⁴⁰ and in the solid state, the structure is complicated by the presence of non-discrete polymeric units.^{199,200}

4.3.5. Conclusions

The xenon and fluorine magnetic shielding tensors in XeF₂ have been determined using solid-state ¹²⁹Xe and ¹⁹F NMR spectroscopy and ZORA DFT calculations. The first direct experimental measurement of $\sigma(\text{Xe})$ for XeF₂ in the solid state is reported and the lingering question of the magnitude of the ¹²⁹Xe magnetic shielding anisotropy in this compound has been resolved. The measured xenon anisotropy, $\Omega = 4245 \pm 20$ ppm, covers approximately 62% of the total known xenon chemical shift range. Analysis of ¹²⁹Xe NMR spectra allows determination of δ_{iso} , -1603 ± 3 ppm, and $^1J(^{129}\text{Xe}, ^{19}\text{F})_{\text{iso}}$, -5566 ± 50 Hz. Results from ¹⁹F NMR spectra indicate that $\Omega(\text{F})$, 150 ± 20 ppm and that

^{19}F - ^{19}F dipolar couplings contribute $\sim 10\%$ to the observed ^{19}F NMR lineshape.

Spin-orbit relativistic ZORA DFT calculations of $\sigma(\text{Xe})$ are in excellent agreement with our solid-state NMR results, with a relative error less than 10%. Most important is that this study provides the first direct evidence that consideration of relativistic effects is important in interpreting xenon magnetic shielding tensors both experimentally and theoretically; however, questions remain. How far down the Periodic Table can one go before Ramsey's non-relativistic theory breaks down? Our spin-orbit calculations show that relativistic effects play a minor role for Kr, but a significant role for Xe. Also, what influence do relativistic effects have on nuclear spin-rotation constants and their relationship with nuclear magnetic shielding constants? These questions are addressed in the following computational study.

4.4. Computational Investigation of Relativistic Effects on Magnetic Shielding Tensors for Linear Molecules

To further investigate the importance of relativistic effects on the magnetic shielding tensors of linear molecules, calculations have been performed on $ng\text{F}_2$ ($ng = \text{Kr}, \text{Xe}, \text{Rn}$), the 1:1 $\text{XeF}_2\text{-AsF}_5$ complex,²⁰¹ XeF^+ and a number of linear molecules containing heavy atoms, including the HX, TIX, Gr(XIII)F, and M(CO) series, where X = F, Cl, Br, I, Gr(XIII) = the group XIII elements: B, Al, Ga, In, Tl, and M = Pd, Pt. For the $ng\text{F}_2$ series, structures are known for KrF_2 and XeF_2 , as mentioned in the previous section; however, since the structure for RnF_2 is not known experimentally, a computationally-optimized structure has been employed.¹⁵¹ In the noble gas difluoride series, $r(ng, \text{F})$ increases from 1.8769 Å for $ng = \text{Kr}$, to 1.9791 Å for $ng = \text{Xe}$ and to 2.08 Å for $ng = \text{Rn}$. For $\text{XeF}_2\text{-AsF}_5$, the structure consists of $\text{XeF}^+\text{-AsF}_6^-$ ions connected by a bridging fluorine atom into FXeFAsF_5 units. The FXeF portion of the complex is near linear ($\angle \text{FXeF} = 178.9^\circ$) with terminal and bridging Xe,F bond lengths of 1.873 Å and 2.212 Å, respectively, and the FAsF_5 portion is roughly octahedral with an average terminal As,F bond length of 1.679 Å and a bridging As,F bond length of 1.813 Å, respectively. For the isolated XeF_2 molecule, $r(\text{Xe}, \text{F})$ is intermediate between the terminal and bridging Xe, F bond lengths in the 1:1 complex, $\text{XeF}^+\text{AsF}_6^-$. The calculated

Xe shielding tensors for XeF_2 , $\text{XeF}^+\text{AsF}_6^-$, and XeF^+ can be compared and the deviation of σ_{\parallel} (or pseudo σ_{\parallel} for $\text{XeF}_2\text{-AsF}_5$) from σ_{free} determined.

Results of non-relativistic and spin-orbit relativistic ZORA DFT calculations of shielding tensors for $ng\text{F}_2$, XeF^+ and $\text{XeF}^+\text{AsF}_6^-$ are summarized in Table 4.5. The difference in shielding values between σ_{free} and σ_{\parallel} has been computed to investigate the importance of relativistic effects in these systems. Our non-relativistic results indicate a negligible difference between σ_{free} and σ_{\parallel} for the compounds investigated, while the spin-orbit relativistic results indicate that $|\sigma_{\text{free}} - \sigma_{\parallel}|$ is non-negligible and increases significantly for KrF_2 , XeF_2 , $\text{XeF}^+\text{AsF}_6^-$, XeF^+ , and RnF_2 , respectively. The largest value is observed for RnF_2 , with $|\sigma_{\text{free}} - \sigma_{\parallel}| = 1868$ ppm, which is significant. In addition, the span of the shielding tensor increases within the $ng\text{F}_2$ series for both non-relativistic and spin-orbit calculations, as expected based on the increased Z ; the non-relativistic calculations yield larger values for the span, with the exception of RnF_2 , and generally more deshielded values for the principal components compared to the spin-orbit results. The span is smaller for the spin-orbit calculations as a consequence of a positive shielding contribution from the spin-orbit term to σ_{\perp} .

The computed Xe shielding results for "isolated" and "complexed" XeF_2 systems and experimentally-determined^{136,202} Xe chemical shift values are compared in Table 4.5. The experimental Xe chemical shift tensors for XeF_2 ¹³⁶ and $\text{XeF}_2\text{-AsF}_5$ ²⁰² are axially-symmetric with spans of 4245 and 5027 ppm, respectively. For both systems, the parallel component of the Xe chemical shift tensor is significantly deshielded relative to the free Xe atom, further indicating the importance of relativistic effects. The calculations, particularly the spin-orbit results, are successful in reproducing the large span and the significant difference between σ_{\parallel} and σ_{free} determined experimentally for both XeF_2 and $\text{XeF}^+\text{AsF}_6^-$. Further, the calculated values for $\text{XeF}^+\text{AsF}_6^-$ yield values for the span and $|\sigma_{\text{free}} - \sigma_{\parallel}|$ that are intermediate between those for XeF_2 and XeF^+ , which is intuitive, since the 1:1 Xe complex displays both XeF_2 and XeF^+ bonding characteristics.

Table 4.5: Calculated* ng Magnetic Shielding Tensors for ngF_2 , XeF^+ and XeF_2-AsF_5 and Experimentally-Determined Xe Chemical Shift Tensors for XeF_2 and XeF_2-AsF_5 .

| | Structural Reference | $r(ng,F) / \text{\AA}$ | $\sigma_{\perp} / \text{ppm}$ | $\sigma_{\parallel} / \text{ppm}$ | Ω / ppm | $ \sigma_{\text{free}} - \sigma_{\parallel} / \text{ppm}$ |
|--|----------------------|------------------------|-------------------------------|-----------------------------------|-----------------------|--|
| KrF₂ | | | | | | |
| nr | 167 | 1.87693 | 1040.3 | 3255.8 | 2215.5 | -7.8 |
| so | | | 1312.2 | 3303.7 | 1991.6 | 114.3 |
| XeF₂ | | | | | | |
| nr | 161 | 1.9791 | 586.5 | 5653.2 | 5066.7 | -6.5 |
| so | | | 1521.8 | 5976.6 | 4454.8 | 432.8 |
| exp [†] | 136 | | -188 | -4433 | 4245 | 1027 |
| RnF₂ | | | | | | |
| nr | 151 | 2.08 | 1144.5 | 10750.3 | 9605.8 | 5.3 |
| so | | | 6436.9 | 13576.1 | 7139.2 | 1867.9 |
| XeF⁺ | | | | | | |
| nr | 201 | 1.8730 | -4557.8 | 5647.4 | 10205.2 | -0.7 |
| so | | | -2533.2 | 5452.3 | 7985.5 | 957.1 |
| XeF⁺AsF₆^{-‡} | | | | | | |
| nr | 201 | (<i>t</i>) 1.8730 | -881.2 | 5631.8 | 6513.0 | 14.9 |
| so | | (<i>b</i>) 2.21181 | 185.1 | 5820.7 | 5635.6 | 588.7 |
| exp [†] | 202 | | 965 | -4062 | 5027 | 1398 |

Non-relativistic and spin-orbit relativistic ZORA DFT calculations on an extended series of linear molecules, HX, Gr(XIII)F, TIX and MCO, follow a similar trend, whereby $|\sigma_{\text{free}} - \sigma_{\parallel}|$ increases as Z increases for a particular series. To illustrate

*All non-relativistic (nr) and spin-orbit (so) relativistic calculations were carried out using the ZORA DFT method and TZ2P Slater-type basis sets.

[†] Note, these values correspond to the Xe *chemical shift* tensor, not the Xe magnetic shielding tensor; $\delta_{\text{free}} = -5460 \text{ ppm}^{134}$ was used to calculate $|\delta_{\text{free}} - \delta_{\parallel}|$.

[‡]The experimental geometry,²⁰¹ with $\langle FXeF \rangle = 178.9^\circ$, was employed in the calculations; hence, the calculated Xe shielding tensor for $XeF^+AsF_6^-$ deviates slightly from axial symmetry, $\kappa = +0.99$.

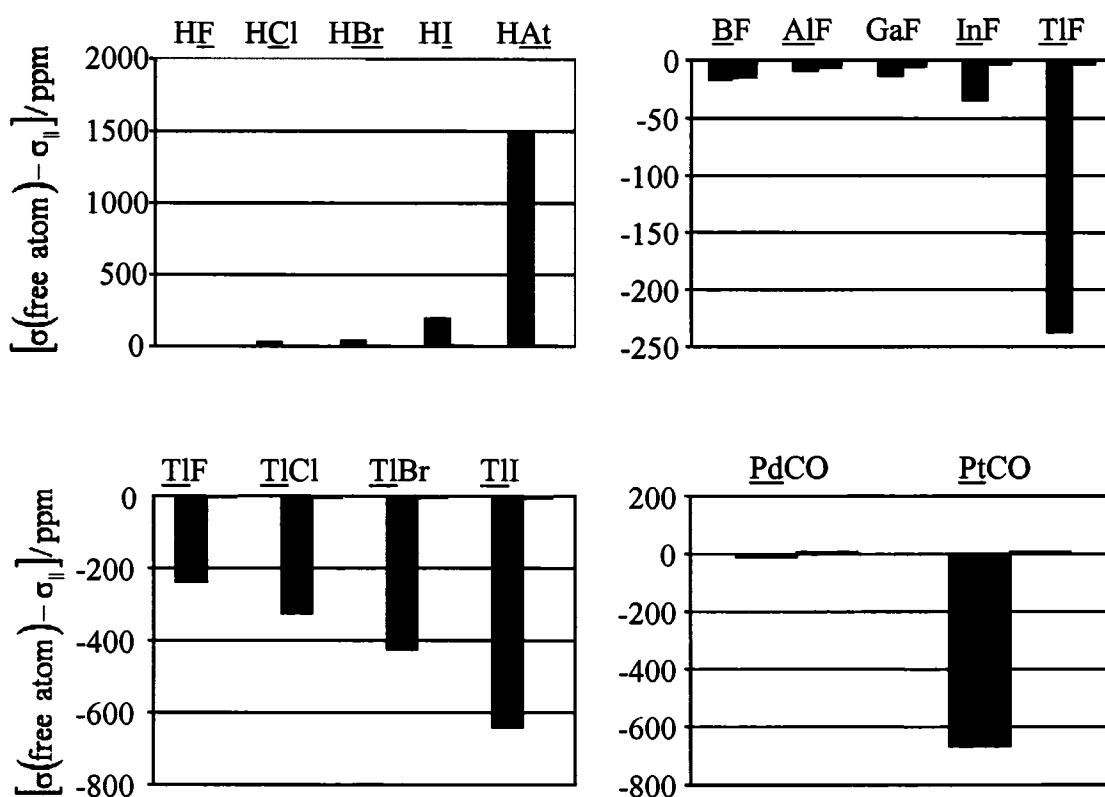


Figure 4.7: Selected plots of $[\sigma(\text{free atom}) - \sigma_{||}]$, calculated using non-relativistic (■) and spin-orbit relativistic (■) ZORA DFT calculations and TZ2P basis sets, for a series of linear molecules. The nucleus for which σ has been calculated is underlined.

this, $|\sigma_{\text{free}} - \sigma_{||}|$ values are plotted for the series and shown in Figure 4.7. The ZORA DFT formalism for calculating shielding tensors supports only closed-shell systems, hence, $\sigma(\text{free atom})$ for open-shell atoms could only be determined indirectly by interpolation; see *Appendix 4.1* for the corresponding shielding curve from which σ_{iso} for open-shell free atoms was extracted. For each HX, Gr(XIII)F, TlX and MCO series, $|\sigma_{\text{free}} - \sigma_{||}|$ increases dramatically with atomic number, conclusively demonstrating that inclusion of relativistic effects is important. For the HX series, the non-relativistic results for $|\sigma_{\text{free}} - \sigma_{||}|$ are near zero and indiscernible in the plots; however, the analogous spin-orbit results indicate a substantial increase from X = I to At. Similar results are observed for the spin-orbit $|\sigma_{\text{free}} - \sigma_{||}|$ results for MCO (M = Pd to Pt) and the Gr(XIII)F series (Gr(XIII) = B to Tl). For the TlX series, spin-orbit $|\sigma_{\text{free}} - \sigma_{||}|$ values increases uniformly from X = F to I. The comparatively large $|\sigma_{\text{free}} - \sigma_{||}|$ values for the TlX series results from dual relativistic

contributions from Tl ($Z = 81$) and the increasing Z in the X series. Together the results in Figure 4.7 illustrate the influence of relativity through the increased value of $|\sigma_{\text{free}} - \sigma_{\parallel}|$ for the variable nucleus as well as for the invariable nucleus in a particular series. Based on these results, inclusion of relativistic effects is important for fourth-row elements, $Z \geq 37$, and critical for fifth-row elements, $Z \geq 55$, in the Periodic Table.

Table 4.6: Experimentally-Deduced and Calculated Spans for Palladium and Platinum in the Linear Triatomic Molecules: PdCO and PtCO.

| | $\Omega(\text{"exp"}) / \text{ppm}$ | $\Omega(\text{calc,nr}) / \text{ppm}$ | $\Omega(\text{calc,so}) / \text{ppm}$ |
|--------------|-------------------------------------|---------------------------------------|---------------------------------------|
| <u>Pd</u> CO | 3017 ± 160 | 3381 | 3573 |
| <u>Pt</u> CO | 5485 ± 197 | 5220 | 5862 |

Recall from the previous section that nuclear magnetic shielding parameters can be determined experimentally from spin-rotation constants in rotational spectroscopy using the Flygare-Ramsey approach,^{33,171} however, this theory is based on a non-relativistic approach and therefore may not be suitable for molecules containing heavy atoms. What, then, are the consequences of employing a non-relativistic theory in cases for which relativity is known to affect magnetic shielding tensor? Are the experimental results valid? To examine this further, consider the metal carbonyls: PdCO and PtCO, which have been examined using microwave spectroscopy by Gerry and co-workers.^{203,204} The $C(^{105}\text{Pd})_I$ and $C(^{195}\text{Pt})_I$, spin-rotation constants were measured and the spans of the shielding tensors for PdCO and PtCO were deduced using Eq. 4.3 and assuming that $\sigma^{\text{dia}}(\text{free atom}) = \sigma_{\parallel}$; the spans were found to be 3017(160) and 5485(197) ppm, for PdCO and PtCO, respectively. These values can be compared to those computed using non-relativistic and spin-orbit relativistic ZORA DFT and are summarized in Table 4.6. The experimentally-deduced span for PtCO is intermediate between the non-relativistic and spin-orbit relativistic values, while that for PdCO is in closer agreement with the non-relativistic value. Calculations of shielding tensors for the metal carbonyls results in a larger calculated span when relativistic effects are included. The discrepancy between non-relativistic and relativistic calculated values of the span for PdCO and PtCO is only several hundred ppm, which is small given the large chemical

shift ranges for Pd and Pt, which are on the order of 10^3 ppm. Nevertheless, it should be stressed that the Ramsey-Flygare method only provides estimates of shielding parameters and should be used with caution when relativistic effects are expected to be important.

4.5. Solid-State $^{129/131}\text{Xe}$ NMR Studies of Sodium Perxenates

4.5.1. Introduction

The most stable xenon-containing compound is the perxenate anion, XeO_6^{4-} , which exists in numerous salts of varying levels of hydration, *e.g.*, Na_4XeO_6 ,²⁰⁵ $\text{Na}_4\text{XeO}_6 \cdot 2\text{H}_2\text{O}$,²⁰⁵ $\text{Na}_4\text{XeO}_6 \cdot 6\text{H}_2\text{O}$,²⁰⁶ and $\text{Na}_4\text{XeO}_6 \cdot 8\text{H}_2\text{O}$,²⁰⁷ $\text{K}_4\text{XeO}_6 \cdot 9\text{H}_2\text{O}$,²⁰⁸ as well as barium lanthanum,²⁰⁹ cesium,²¹⁰ calcium, strontium, and barium perxenates.²¹¹ The state of hydration of perxenates depends upon the method of preparation; for each synthetic route, several hydrates are produced. For example, following the synthesis of Malm *et al.*,²¹² an octahydrate²⁰⁷ and a pentahydrate,²¹³ among other unidentified phases, are formed,²⁰⁷ whereas, using the method of Corte,²¹⁴ three phases, the hexahydrate and two undetermined hydrates,²⁰⁶ are produced. For the dihydrate, three phases have been identified, but none fully characterized²⁰⁵ and, lastly, for the anhydrous perxenate, a single phase has been reported.²⁰⁵ The thermal stability of sodium perxenates has been investigated and the results indicate a loss of water at 200 °C and a loss of Xe at 375 °C.²¹⁵

In the literature, isotropic Xe chemical shifts are reported for XeO_6^{4-} in aqueous solution, -748 ppm, and for solid, anhydrous sodium perxenate, *ca.* -720 ppm;¹²⁵ however, no information on the anisotropic interactions has been reported.¹²⁵ The symmetry of the perxenate anion is described as approximately octahedral, which is an asset from an NMR point-of-view, since this leads to potentially small Xe anisotropic shielding and quadrupolar interactions, depending on the extent of distortion from O_h symmetry, as discussed in *Section 2.5.3*.

We have examined two forms of sodium perxenate(VIII), $\text{Na}_4\text{XeO}_6 \cdot x\text{H}_2\text{O}$ ($x = 0, 2$), using solid-state xenon NMR spectroscopy at a single, moderate applied magnetic field strength, $B_0 = 11.75$ T. The two NMR-active isotopes of xenon, ^{129}Xe ($I = 1/2$) and ^{131}Xe ($I = 3/2$), have been exploited to determine the Xe magnetic shielding and EFG

tensors, thus representing the first ^{131}Xe NMR study for a xenon-containing compound in the solid state. Through a series of $^{129/131}\text{Xe}$ NMR experiments on MAS or stationary samples of $\text{Na}_4\text{XeO}_6 \cdot x\text{H}_2\text{O}$ ($x = 0, 2$), the local Xe environment is examined.

4.5.2. Experimental Details

4.5.2.1. Synthesis and Structural Characterization of Sodium Perxenates

A form of sodium perxenate of unknown state of hydration, $\text{Na}_4\text{XeO}_6 \cdot x\text{H}_2\text{O}$, was prepared by Prof. Michael Gerken following a modified method of Huston and co-workers.²¹⁶ Powder X-ray diffraction (XRD) and thermal gravimetric analysis (TGA) were used to determine the level of hydration of the sample. Two TGA trials were performed over temperature ranges of 25 °C to 200 °C and 25 °C to 375 °C at a rate of 5 °C min^{-1} . In addition, the observed XRD pattern for $\text{Na}_4\text{XeO}_6 \cdot x\text{H}_2\text{O}$ was compared to calculated X-ray diffraction patterns of $\text{Na}_4\text{XeO}_6 \cdot 6\text{H}_2\text{O}$ and $\text{Na}_4\text{XeO}_6 \cdot 8\text{H}_2\text{O}$, whose structures are known.^{206,207} The experimental XRD pattern for powdered $\text{Na}_4\text{XeO}_6 \cdot x\text{H}_2\text{O}$ is given in *Appendix 4.2* along with the calculated XRD patterns for $\text{Na}_4\text{XeO}_6 \cdot 6\text{H}_2\text{O}$ and $\text{Na}_4\text{XeO}_6 \cdot 8\text{H}_2\text{O}$. The lack of agreement between either of the calculated XRD patterns and the experimentally-obtained XRD pattern suggested that the sample was either another hydrate or the anhydrous form. Subsequent ^1H NMR experiments confirmed the presence of H_2O , eliminating the anhydrous form as a possible candidate. TGA analysis indicates there are approximately two water molecules present, suggesting the sample is a dihydrate, $\text{Na}_4\text{XeO}_6 \cdot 2\text{H}_2\text{O}$.

To obtain the anhydrous salt, Na_4XeO_6 , the sample was heated under dynamic vacuum at 100 °C for 10 hours. The absence of water in the sample was confirmed by solid-state ^1H NMR spectroscopy. Raman spectroscopy was used to characterize both forms of sodium perxenate, $\text{Na}_4\text{XeO}_6 \cdot x\text{H}_2\text{O}$ ($x = 0, 2$), and their respective spectra are given in *Appendices 4.3 and 4.4 (vide infra)*.

4.5.2.2. Solid-State $^{129/131}\text{Xe}$ NMR Spectroscopy

Samples of $\text{Na}_4\text{XeO}_6 \cdot x\text{H}_2\text{O}$ ($x = 0, 2$) were powdered and packed into 4.0 mm or 7.0 mm o.d. zirconium rotors. All solid-state $^{129/131}\text{Xe}$ NMR spectra were acquired on an 11.75 T Bruker Avance NMR spectrometer operating at ^{129}Xe and ^{131}Xe frequencies of

139.132 MHz and 41.244 MHz. The suggested samples for referencing $^{129/131}\text{Xe}$ NMR spectra, given in Table 4.7, are not readily available; in fact, Freon-114 is no longer commercially available. Hence, the absolute frequency scale has been employed and is suggested for referencing $^{129/131}\text{Xe}$ NMR spectra. This method enables $^{129/131}\text{Xe}$ NMR spectra to be referenced with respect to the primary Xe NMR reference, XeOF_4 (neat liquid; 24 °C), at 0.00 ppm, without having access to the sample. A tutorial on calculating NMR chemical shifts using the absolute frequency method is outlined in *Appendix 4.5* using the ^{129}Xe chemical shift of $\text{Na}_4\text{XeO}_6 \cdot 2\text{H}_2\text{O}$ as an example.

Table 4.7: Useful Absolute Frequencies of Suggested Reference Samples for Xe NMR Studies.^{217,218}

| Sample | Isotope | $\bar{\nu}$ / Hz | δ_{iso} / ppm |
|--|-------------------|------------------|-----------------------------|
| XeOF_4 , neat liquid at 24 °C | ^{129}Xe | 27 810 184 | 0.0 |
| Na_4XeO_6 in H_2O at 30 °C | ^{129}Xe | 27 718 937 | -747.8 |
| Xe gas, zero pressure at 20 °C | ^{129}Xe | 27 660 478 | -5383 |
| Xe gas in Freon-114, <i>i.e.</i> , 1,2-dichlorotetrafluoroethane, at 30 °C | ^{129}Xe | 27 663 807 | -5263 |
| Xe gas in Freon-114 at 30 °C | ^{131}Xe | 8 200 531 | -5263 |
| XeO_4 in HF at -75 °C | ^{129}Xe | 27 807 764 | -85.8 |
| XeO_4 in HF at -75 °C | ^{131}Xe | 8 243 205 | -85.8 |

All $^{129/131}\text{Xe}$ NMR spectra were simulated using WSOLIDS and/or SIMPSON.

(i) $\text{Na}_4\text{XeO}_6 \cdot 2\text{H}_2\text{O}$

A 4.0 mm triple-resonance probe was used to acquire ^{129}Xe NMR spectra of stationary and magic-angle spinning (MAS) samples of $\text{Na}_4\text{XeO}_6 \cdot 2\text{H}_2\text{O}$ using either standard one-pulse or $I \rightarrow S$ cross-polarization (CP) methods, where I denotes ^1H and S denotes ^{129}Xe . High-power ^1H decoupling was used in all experiments. The magic angle was set by maximizing the number of rotational echoes in the ^{79}Br NMR free-induction decay of KBr. To calibrate the $\pi/2$ pulse for ^{129}Xe one-pulse experiments, the ^{13}C NMR resonance of adamantane was used; the respective ^{13}C and ^{129}Xe frequencies for

adamantane and sodium perxenate at 11.75 T are 125.800535 MHz and 139.138473 MHz, respectively. The anticipated long ^{129}Xe spin-lattice relaxation time, T_1 , for $\text{Na}_4\text{XeO}_6 \cdot 2\text{H}_2\text{O}$ impeded rapid acquisition for one-pulse ^{129}Xe experiments, hence, a smaller flip angle was used to decrease repetition times. Using a $\pi/4$ flip angle, pulse delays of 30 s to 600 s, sweep widths of 100 kHz and acquisition times of 10.2 ms were used to acquire ^{129}Xe NMR spectra of stationary and MAS samples of $\text{Na}_4\text{XeO}_6 \cdot 2\text{H}_2\text{O}$. For $^1\text{H} \rightarrow ^{129}\text{Xe}$ CP experiments, acquisition parameters were optimized on the $\text{Na}_4\text{XeO}_6 \cdot 2\text{H}_2\text{O}$ sample for spinning speeds ranging from 1342 to 6000 Hz. A ^1H $\pi/2$ pulse width of 4.25 μs , pulse delay of 2 s, and contact times of 7-9 ms were used for ^{129}Xe CP/MAS experiments. To determine the CP parameters, T_{IS} and $T_{1\rho}(^1\text{H})$, (see Section 3.1.2.2) for the dihydrate, a series of ^{129}Xe CPMAS experiments were performed whereby the ^{129}Xe NMR signal intensity was monitored as a function of contact time. The ^1H $T_{1\rho}$ and ^1H , ^{129}Xe cross-relaxation time, T_{IS} , were determined by performing a non-linear regression analysis²¹⁹ on the resulting plot (*vide infra*).

A 7.0 mm DR probe was used to acquire ^{131}Xe NMR spectra of a stationary sample of $\text{Na}_4\text{XeO}_6 \cdot 2\text{H}_2\text{O}$ using the QCPMG pulse sequence. The ^{37}Cl NMR resonance from a solid sample of KCl was used to calibrate the pulse width for ^{131}Xe NMR experiments. At 11.75 T, the respective frequencies of ^{37}Cl in KCl and ^{131}Xe in $\text{Na}_4\text{XeO}_6 \cdot 2\text{H}_2\text{O}$ are 40.802 MHz and 41.533 MHz. The non-selective solution $\pi/2$ pulse width was found to be 5.5 μs , yielding a solid, selective $\pi/2$ pulse of 2.75 μs and π pulse of 5.5 μs for $I = 3/2$. The QCPMG pulse sequence was used to acquire ^{131}Xe NMR spectra of $\text{Na}_4\text{XeO}_6 \cdot 2\text{H}_2\text{O}$. A sweep width of 100 kHz, acquisition time of 13.3 ms, and pulse delay of 1 s were used to acquire 142 848 scans. The π -pulse train was repeated 80 times using delays of 100 μs before and after each π pulse, and τ_a was set to 80 μs , which corresponds to a separation between spikes in the NMR spectrum, ν_{QCPMG} , of approximately 6.0 kHz. The frequency-stepped technique was employed and a total of fifteen ^{131}Xe NMR sub-spectra were required to collect the complete powder pattern. The transmitter or carrier frequency, ν_c , was adjusted in increments of 42 kHz, which is less than the pulse excitation profile, approximately 45 kHz. In addition, the tune and match of the ^1H and ^{131}Xe channels were carefully set prior to each experiment.

(ii) Na_4XeO_6

All $^{129/131}\text{Xe}$ NMR experiments were performed on stationary samples of Na_4XeO_6 using a 7.0mm ZrO_2 rotor that was 75 % full and a DR probe. To ensure the hygroscopic sample did not absorb H_2O , $\text{N}_2(\text{g})$ was continuously flowed over the anhydrous sample through the bearing-gas line to the probe. For ^{129}Xe NMR experiments, a simple one-pulse sequence was used with a sweep width of 100 kHz, acquisition time of 10.2 ms, $\pi/2$ pulse of 2.00 μs , and pulse delays varying from 2 s to 600 s. To estimate $T_1(^{129}\text{Xe})$ for Na_4XeO_6 , the progressive saturation technique²²⁰ was employed and four dummy pulses were applied before acquisition of 16 scans to ensure that a steady state was established. Solid-state ^{131}Xe NMR experiments were carried out using either a spin-echo or QCPMG⁸⁹ sequence. A selective $\pi/2$ pulse width of 2.00 μs , pulse delay of 1.0 s, acquisition times of 5.1 to 13.2 ms, and sweep widths of 20 kHz to 100 kHz, were used. For the ^{131}Xe QCPMG experiment, a sweep width of 50 kHz, spikelet spacing of 200 Hz, acquisition time of 8.6 ms, and 22 loops were used. The $T_1(^{131}\text{Xe})$ value was not accurately measured, but was believed to be short and a pulse delay of 1 s was found to suffice.

4.5.3. Results and Discussion

The two sodium perxenate samples, $\text{Na}_4\text{XeO}_6 \cdot x\text{H}_2\text{O}$ ($x = 0, 2$), were analyzed using Raman spectroscopy to probe the molecular symmetry of the two forms; the Raman spectra are given in *Appendices 4.3 and 4.4*. Raman and IR spectra can be used to infer the presence or absence of a center of inversion and, in favorable cases, to assign, or rule out, the point group of the molecule.²²¹ For molecules with an inversion center, the "mutual exclusion rule" applies, which states that, no normal mode may be both Raman and IR active – the two spectra are mutually exclusive; this arises since the dipole moment is antisymmetric to such an operation, whereas the polarizability is symmetric.²²² Hence, the Raman and IR spectra for molecules with O_h symmetry will be different from those for a molecule with, say, C_s symmetry. For O_h symmetry, three bands are Raman active, three are IR-active, and all are mutually exclusive; on the contrary, for C_s symmetry, all vibrational transitions are both Raman and IR active.

A previous infrared and Raman study of the perxenate(VIII) anion in aqueous solution made use of the mutual exclusion rule and identified five bands: three Raman bands and two IR bands, with no coincidences.²²³ A sixth vibrational band for solid perxenate was observed and attributed to a forbidden transition that became activated by lowered symmetry in the anion. A strong IR band at 685 cm⁻¹ was ascribed to the fundamental $\nu_3(T_{1u})$ band for the octahedral XeO₆ group, in agreement with a previous study.²²⁴

The Raman spectra obtained for the two sodium perxenates, Na₄XeO₆·2H₂O and Na₄XeO₆, examined herein (*Appendices 4.3 and 4.4*) indicate different environments. For Na₄XeO₆·2H₂O, six distinct bands were observed: 681.47, 651.29, 641.23, 602.35, 478.28, and 462.44 cm⁻¹. The presence of the band at 602 cm⁻¹ clearly indicates deviation from O_h symmetry since this band is not Raman-active for O_h symmetry. On the contrary, the Raman spectrum of the anhydrous sample contains three distinct bands and assigned according to the O_h point group as follows: $\nu_1(A_{1g}) = 684.04$ cm⁻¹, $\nu_2(E_g) = 654.12$ cm⁻¹, and $\nu_5(T_{2g}) = 468.91$ cm⁻¹. To further investigate the structures of Na₄XeO₆·2H₂O and Na₄XeO₆, ¹²⁹Xe and ¹³¹Xe NMR spectra were acquired. In the following sections, solid-state ^{129/131}Xe NMR results for Na₄XeO₆·2H₂O are presented, followed by those for anhydrous Na₄XeO₆.

4.5.3.1. Na₄XeO₆·2H₂O

(i) Solid-State ¹²⁹Xe NMR Results

Shown in Figure 4.8 are calculated and experimental solid-state ¹²⁹Xe{¹H} NMR spectra of Na₄XeO₆·2H₂O acquired using (a) a cross-polarization (CP) experiment with TPPM decoupling and (b, c) one-pulse ¹²⁹Xe NMR experiments; the best-fit simulated parameters, δ_{iso} , Ω , κ , are given in Table 4.8. A notable improvement in the resolution and S/N is apparent upon using the CP/TPPM experiment and MAS. The isotropic ¹²⁹Xe chemical shift is -725.6 ± 0.1 ppm with respect to the primary Xe chemical shift reference, XeOF₄ (neat liquid, 24 °C), and is close to literature values for aqueous and solid, anhydrous perxenate, -748 and *ca.* -720 ppm, respectively.¹²⁵ The anisotropic Xe shielding tensor, $\Omega = 95 \pm 5$ ppm, is indicative of deviations from octahedral symmetry,

in agreement with the observed Raman spectrum (*Appendix 4.3*). If XeO_6^{4-} were perfectly octahedral, an isotropic ^{129}Xe NMR signal would be observed; nonetheless, the observed Xe shielding anisotropy is small relative to the Xe chemical shift range, ~ 7000 ppm, indicating that structural deviations are slight. The Xe shielding tensor is, within error limits, axially-symmetric, $0.7 \leq \kappa \leq 1.0$; this suggests that although the XeO_6^{4-} anion is not octahedral, some symmetry elements may be present; since, for the Xe shielding tensor to be axially symmetric, there must be a C_n -axis ($n \geq 3$). Unfortunately,

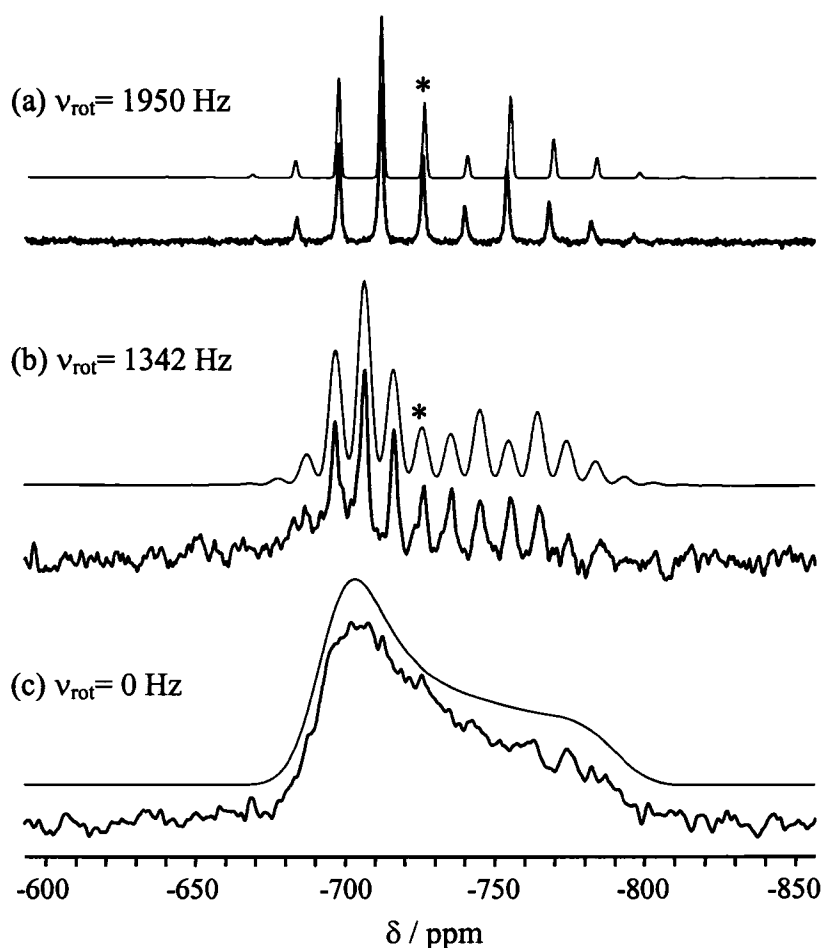


Figure 4.8: Simulated (top) and experimental (bottom) solid-state $^{129}\text{Xe}\{^1\text{H}\}$ NMR spectra of $\text{Na}_4\text{XeO}_6 \cdot 2\text{H}_2\text{O}$ acquired at 11.75 T using various spinning speeds; the spectrum shown in (a) was acquired using CP/TPPM with a pulse delay of 2 s and is the sum of 4096 scans; the spectra shown in (b, c) were acquired using a one-pulse experiment with a 30 s pulse delay and are the sum of 1916 and 6516 scans, respectively. Processing parameters for (a), (b) and (c) include linebroadening (15 Hz, 150 Hz, and 300 Hz, respectively) and zero-filling (16 384, 4096, and 8192, respectively). Best-fit simulated Xe shielding parameters are given in Table 4.8.

Table 4.8: Experimental Xe EFG and Shielding Parameters for $\text{Na}_4\text{XeO}_6 \cdot 2\text{H}_2\text{O}$ and Two Xe Polymorphs.*

| | $\delta_{\text{iso}} / \text{ppm}$ | C_Q / MHz | η_Q | Ω / ppm | κ |
|---|------------------------------------|--------------------|-----------------|-----------------------|-----------------------------|
| $\text{Na}_4\text{XeO}_6 \cdot 2\text{H}_2\text{O}$ | -725.6 ± 0.1 | 10.8 ± 0.5 | 0.48 ± 0.05 | 95 ± 5 | $0.7 \leq \kappa \leq +1.0$ |
| Polymorph 1 | -700 ± 0.5 | 3.5 ± 0.5 | 0.6 ± 0.1 | ----- [†] | ----- [†] |
| Polymorph 2 | -743 ± 0.5 | 3.5 ± 0.5 | 0.6 ± 0.1 | ----- [†] | ----- [†] |

determination of accurate σ values for axially-symmetric, or near axially-symmetric, σ tensors using the Herzfeld-Berger analysis for MAS samples is a well-known problem and precludes more accurate determination of κ .²²⁵

The $^{129}\text{Xe}\{^1\text{H}\}$ NMR spectra of both MAS samples and stationary samples of $\text{Na}_4\text{XeO}_6 \cdot 2\text{H}_2\text{O}$, shown in Figure 4.8, are noticeably broadened; the most plausible source of this broadening is ^{129}Xe , ^{23}Na dipolar coupling, $R_{\text{DD}}(^{129}\text{Xe}, ^{23}\text{Na})$. Since the structure of $\text{Na}_4\text{XeO}_6 \cdot 2\text{H}_2\text{O}$ has not been determined, an accurate value of $R_{\text{DD}}(^{129}\text{Xe}, ^{23}\text{Na})$ for $\text{Na}_4\text{XeO}_6 \cdot 2\text{H}_2\text{O}$ cannot be calculated; however, it may be estimated from the known structures of the hexa- and octahydrates of sodium perxenate, where the dipolar coupling involving the nearest Na neighbour yields, $R_{\text{DD}}(^{129}\text{Xe}, ^{23}\text{Na}) \sim 235 \text{ Hz}$. This value is comparable to the linebroadening that was applied to the simulated spectrum for the stationary sample, shown in Figure 4.8(c). In addition, the linewidth of the spinning sidebands, $\Delta\nu_{\text{ssb}}$, for the spectra of MAS samples, shown in Figures 4.8(b) and (a), is reduced from $400 \pm 15 \text{ Hz}$ to $200 \pm 10 \text{ Hz}$, respectively, suggesting that $R_{\text{DD}}(^{129}\text{Xe}, ^{23}\text{Na})$ is more effectively averaged by the higher MAS rate.

In the absence of detailed structural data, it is instructive to investigate the $I \rightarrow S$ (*i.e.*, $^1\text{H} \rightarrow ^{129}\text{Xe}$) CP dynamics to estimate the strength of the dipolar interaction and therefore the proximity of water molecules. In NMR, the theory of time-dependent processes, such as T_1 , T_2 , and $T_{1\rho}$, relaxation, is often described in terms of a time-dependent auto-correlation function, $C_x(\tau)$, and a frequency-dependent spectral density

* Since the Xe shielding interaction is negligible relative to the ^{131}Xe quadrupolar interaction, the anisotropic Xe shielding and Euler angles were not considered in the analysis of the ^{131}Xe NMR spectrum.

[†] The anisotropic Xe shielding parameters for the Xe polymorphs are undetermined, but are believed to be negligible.

function $J_x(\Delta\omega_{\text{eff}})$. The relationship between the cross-relaxation rate, T_{IS} , and dipolar interaction has long been established:^{36,226}

$$\frac{1}{T_{IS}} \approx (1/2)\sin^2\theta_1 \sin^2\theta_S M_{2,IS} J_x(\Delta\omega_{\text{eff}}) \propto r_{IS}^{-6}, \quad (4.7)$$

where the power density is given by:

$$J_x(\Delta\omega_{\text{eff}}) = \int_0^\infty d\tau \exp(i\Delta\omega_{\text{eff}}\tau) C_x(\tau) / \text{Tr} \left\{ \left(\sum_i b_{Si} I_{ix} \right)^2 \right\} \quad (4.8)$$

and the Van Vleck second moment, $M_{2,IS}$ is:

$$M_{2,IS} = \frac{4}{27} \gamma_I^2 \gamma_S^2 \hbar^2 I(I+1) \sum_i b_{Si}^2; \quad (4.9)$$

lastly, the auto-correlation function is

$$C_x(\tau) = \sum_i \left\{ b_{Si} I_{xi} \exp[-iP_2(\cos\theta_1)\overline{\mathcal{H}}\tau] b_{Si} I_{xi} \right\} + \sum_{k \neq i} \left\{ b_{Sk} I_{xk} \exp[-iP_2(\cos\theta_1)\overline{\mathcal{H}}\tau] b_{Si} I_{xi} \right\} \quad (4.10)$$

and

$$b_{Si} = -2P_2(\cos\theta_{Si}) / r_{Si}^3, \quad (4.11)$$

where the summation is over the i th set of I spins. Further details of Equations 4.7 – 4.11 will not be described herein, but can be found in references 36, 226, and 227. Of significance is the spatially-dependent $C_x(\tau)$ term and the dependence of T_{IS} on the effective sixth-order fall-off in the I, S distance; hence, there will be a significant contribution to T_{IS} for terms with small r_{IS} values and a minimal contribution to T_{IS} for large r_{IS} values; *e.g.*, non-protonated species. From Eq. 4.7 it is easy to understand that the ^1H , ^{129}Xe polarization build-up or cross-relaxation time, T_{IS} , is affected by molecular motion due to averaging of the I, S dipolar interaction.

The second CP parameter, the ^1H relaxation time in the rotating frame, $T_{1\rho}(^1\text{H})$, is also affected by motion and is specifically sensitive to motional rates on the order of $\omega_{1\text{H}} = \gamma_{1\text{H}} B_{1\text{H}}$; *i.e.*, $10^1 - 10^2$ kHz. When a motional process is occurring at a rate equal to $\omega_{1\text{H}}$, a minimum in $T_{1\rho}$ is reached ($\omega_{1\text{H}}\tau_c \sim 1$; τ_c is the correlation time of a given motion); however, motion that is occurring at a rate greater or less than $\omega_{1\text{H}}$, corresponds to a motional process in the fast or slow motional regime, respectively. In all cases, a series

of experiments, carried out as a function of temperature or ω_{1H} , are required to obtain information about the rate of motion.

Shown in Figure 4.9 is a plot of the normalized ^{129}Xe NMR signal intensity as a function of contact time for $\text{Na}_4\text{XeO}_6 \cdot 2\text{H}_2\text{O}$ to determine the CP parameters, T_{IS} and $T_{1\rho}(^1\text{H})$. Each point represents the normalized signal intensity from a $^{129}\text{Xe}\{^1\text{H}\}$ CP/TPPM experiment on an MAS sample at a rate of 6.000 kHz and is the sum of 128 scans. Non-linear regression analysis of the characteristic "rise-fall" curve, fit to the following equation:²²⁷

$$I = \frac{S_0 \{ \exp[-t_{CT} / T_{1\rho}(H)] - \exp[-t_{CT} / T_{IS}] \}}{[1 - T_{IS} / T_{1\rho}(H)]} \quad (4.12)$$

yields values for T_{IS} , $T_{1\rho}$, and the proportionality constant, S_0 , of 3.37 ms, 18.2 ms, and 1.45, respectively. For comparison, the T_{IS} values for the carbonyl, quaternary, and methyl carbons in di-*tert*-butyl oxalate are 2.94, 1.48, and 0.43 ms, respectively, and their

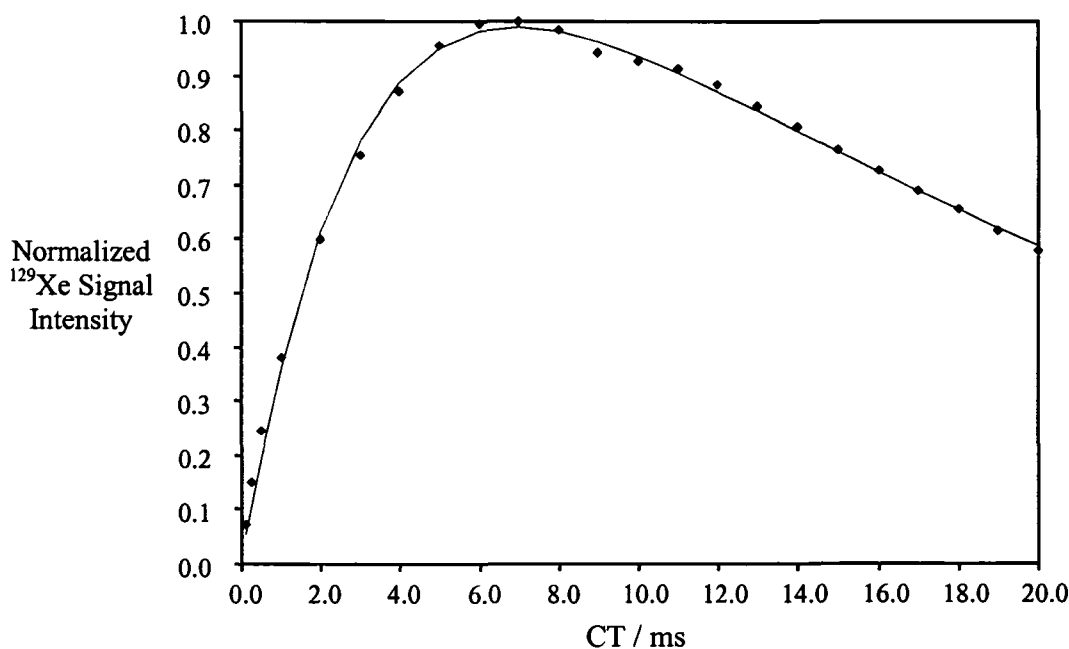


Figure 4.9: Summary of $^{129}\text{Xe}\{^1\text{H}\}$ CP/TPPM experiments for MAS samples of $\text{Na}_4\text{XeO}_6 \cdot 2\text{H}_2\text{O}$ ($B_0 = 11.75$ T, $\nu_{\text{rot}} = 6.000$ kHz). The plotted points represent the normalized ^{129}Xe NMR signal intensity as a function of ^{129}Xe , ^1H contact time and have been fitted to Equation 4.12 to determine the cross-polarization parameters, T_{IS} and $T_{1\rho}(^1\text{H})$.

respective $T_{1\rho}(\text{H})$ values are 2.9, 5.1, and 26.8 ms.²²⁸ The T_{IS} values for $\text{Na}_4\text{XeO}_6 \cdot 2\text{H}_2\text{O}$ and the carbonyl in di-*tert*-butyl oxalate are in close agreement; in these cases, the long T_{IS} values indicate weak heteronuclear dipolar interactions resulting from the remote protons and necessitating more time for the optimum transfer of magnetization.

Although measurement of T_{IS} provides valuable information about the general strength of the ^1H , ^{129}Xe dipolar interaction, the individual ^1H , ^{129}Xe distances cannot be determined. Nevertheless, the improved S/N obtained using the CP experiment relative to the one-pulse ^{129}Xe experiment demonstrates that the remote protons are sufficiently close to establish a sizable ^1H , ^{129}Xe dipolar interaction. The measured ^1H $T_{1\rho}$ value for $\text{Na}_4\text{XeO}_6 \cdot 2\text{H}_2\text{O}$, 18.2 ms, is closest to the methyl carbon $T_{1\rho}$ value, 26.8 ms, in di-*tert*-butyl oxalate. Long $T_{1\rho}(^1\text{H})$ values are beneficial as they allow the $^1\text{H} \rightarrow ^{129}\text{Xe}$ and $^1\text{H} \rightarrow ^{13}\text{C}$ magnetization to be successfully transferred before the protons relax in the rotating frame. When $T_{1\rho}(^1\text{H}) \leq T_{\text{IS}}$, CP becomes difficult, resulting in weak or negligible enhancements. In general, a single $T_{1\rho}(^1\text{H})$ value is usually obtained for all I -spins in a given sample due to spin diffusion, which arises because the protons are very tightly coupled and act as a single species. An exception is di-*tert*-butyl oxalate, where the protons of different functional groups have different $T_{1\rho}(^1\text{H})$ values, as indicated above.

Upon varying the contact time, the presence of two Xe signals, attributed to two polymorphs of $\text{Na}_4\text{XeO}_6 \cdot 2\text{H}_2\text{O}$, were realized in the ^{129}Xe NMR spectrum. One polymorph appeared at -743 ppm, to slightly low frequency of $\delta_{\text{iso}}(\text{Xe})$ for the dihydrate, and became apparent with the use of a long contact time (20 ms), while the second polymorph appeared at -700 ppm, to high frequency of $\delta_{\text{iso}}(\text{Xe})$, and was visible with the use of shorter contact times, ≤ 3 ms. From the contact times employed, it may be inferred that the ^1H s present in these polymorphs are farther from and closer to the Xe, respectively, than those in $\text{Na}_4\text{XeO}_6 \cdot 2\text{H}_2\text{O}$. The polymorphs became more pronounced using a one-pulse ^{129}Xe experiment with ^1H -decoupling; see Figure 4.10, suggesting that $T_{1\rho}(\text{H}) \sim T_{\text{IS}}$. Given the similar chemical shifts, it is reasonable to attribute these signals to polymorphic phases of the dihydrate or other states of hydration of sodium perxenate.

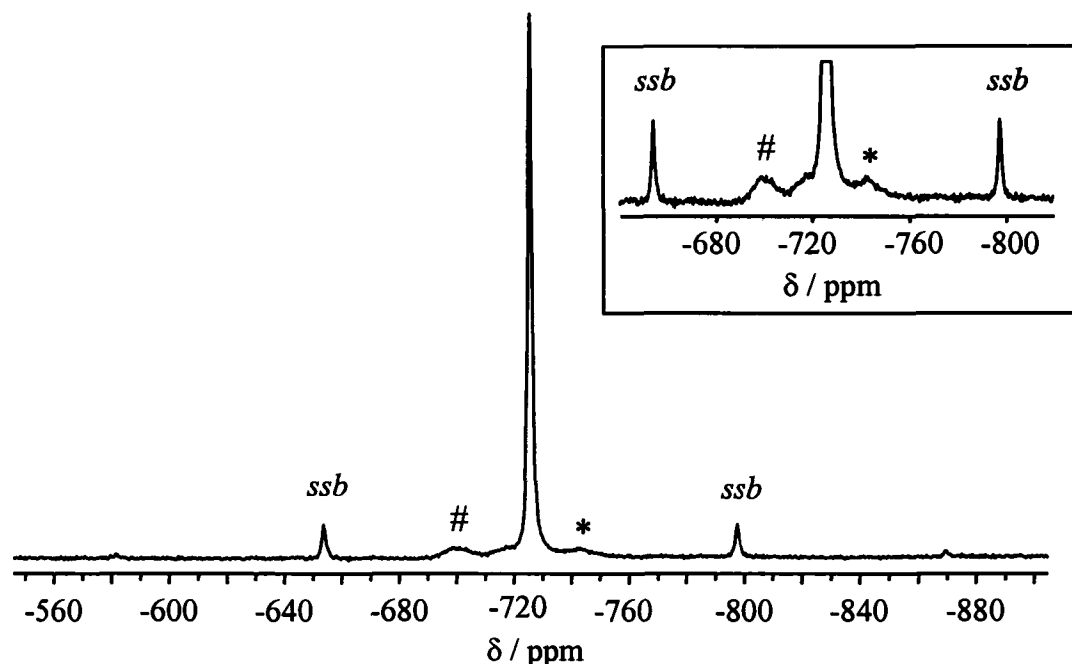


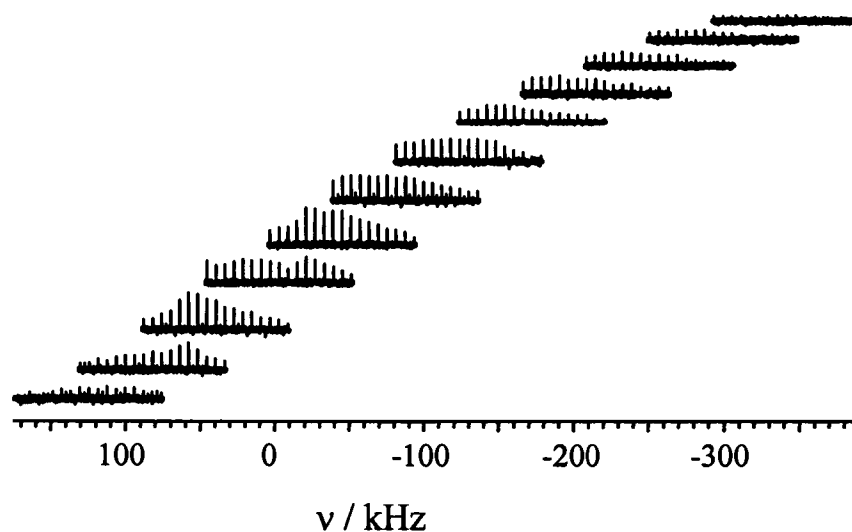
Figure 4.10: Solid-state $^{129}\text{Xe}\{^1\text{H}\}$ NMR spectrum of $\text{Na}_4\text{XeO}_6 \cdot 2\text{H}_2\text{O}$ acquired at 11.75 T ($\nu(^{129}\text{Xe}) = 139.132$ MHz) using a one-pulse experiment. Labeled in the spectrum are the spinning sidebands (*ssb*) from $\text{Na}_4\text{XeO}_6 \cdot 2\text{H}_2\text{O}$ and two polymorphs at -743 ppm (*) and -700 ppm (#). The inset is an expansion about the isotropic ^{129}Xe NMR signal for $\text{Na}_4\text{XeO}_6 \cdot 2\text{H}_2\text{O}$ showing more clearly the signals attributed to the two polymorphs (#, *). The spectrum was acquired using a pulse delay of 600 s, an MAS rate of 6.000 kHz, and is the sum of 300 scans.

(ii) Solid-State ^{131}Xe NMR Results

Shown in Figure 4.11 are ^{131}Xe QCPMG spectra of $\text{Na}_4\text{XeO}_6 \cdot 2\text{H}_2\text{O}$ acquired using the stepped-frequency technique at 11.75 T. Selected sub-spectra are shown in Figure 4.11(a) and the full ^{131}Xe NMR spectrum, processed using the skyline projection method, is shown in Figure 4.11(b). The resulting ^{131}Xe NMR spectral breadth is approximately 500 kHz and corresponds to a $C_Q(^{131}\text{Xe})$ value on the order of 10 MHz; this immediately indicates deviation of the XeO_6^{4-} anion from O_h symmetry, in agreement with ^{129}Xe NMR and Raman data. In addition, the acute sensitivity of the Xe EFG tensor to small changes in the local Xe environment relative to the Xe shielding tensor is realized. While the anisotropic Xe shielding tensor is only 95 ppm, the Xe quadrupolar interaction is much larger – a consequence of the large nuclear ^{131}Xe quadrupole moment which amplifies structural distortions. The large breadth of the ^{131}Xe NMR pattern

required fifteen ^{131}Xe NMR spectra and three weeks of experiment time to obtain the full spectrum! The ^{131}Xe NMR lineshape is unusual and does not represent a characteristic quadrupolar pattern. The shielding anisotropy, determined from the ^{129}Xe NMR results,

(a) Stepped-frequency ^{131}Xe NMR Spectra



(b) Skyline-Projection ^{131}Xe NMR Spectrum

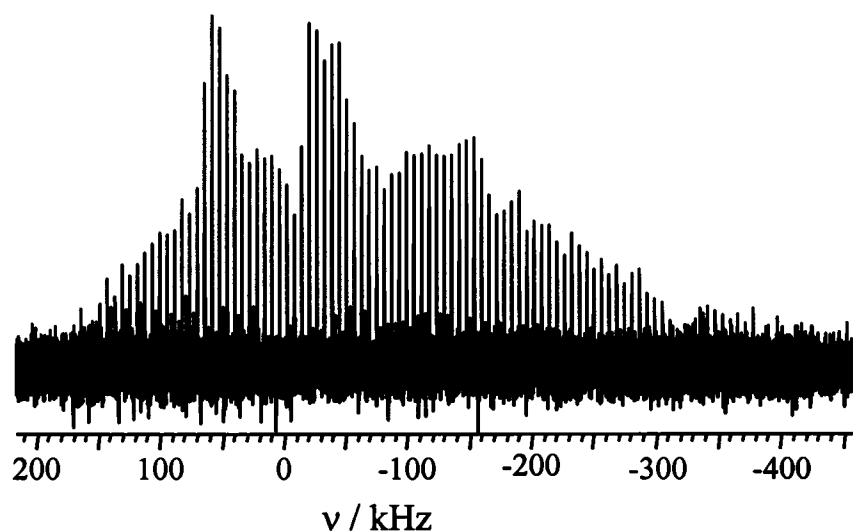


Figure 4.11: (a) Selected stepped-frequency ^{131}Xe NMR spectra of a stationary sample of $\text{Na}_4\text{XeO}_6 \cdot 2\text{H}_2\text{O}$ acquired using the stepped-frequency technique at 11.75 T ($\nu(^{131}\text{Xe}) = 41.244$ MHz); a total of fifteen sub-spectra comprise the (b) skyline projection ^{131}Xe NMR spectrum. Each spectrum is the sum of 142,848 scans and was acquired using a 1 s pulse delay and $\nu_{\text{QCPMG}} = 6055$ Hz.

is negligible, $\Omega = 95 \text{ ppm} = 3.9 \text{ kHz}$, relative to the second-order quadrupolar interaction, 500 kHz, and therefore does not explain the observed lineshape. Hence, it is reasonable to assume that the Xe polymorphs previously observed in the ^{129}Xe NMR spectrum at $\delta_{\text{iso}} = -700 \text{ ppm}$ and -743 ppm must make significant contributions to the ^{131}Xe NMR spectrum. The narrow component, observed near the center of the ^{131}Xe pattern, is attributed to the two polymorphs and the broad signal to the main component, $\text{Na}_4\text{XeO}_6 \cdot 2\text{H}_2\text{O}$. The simulated spectrum, along with the experimental spectrum, is shown in Figure 4.12 and the best-fit parameters are given in Table 4.8. The simulation contains three sites with percent contributions of 92:4:4, for $\text{Na}_4\text{XeO}_6 \cdot 2\text{H}_2\text{O}$ and the two polymorphs, respectively. Although it appears that the two minor polymorphs are present in small quantities, their contribution to the ^{131}Xe spectrum is significant due to their much smaller C_Q values relative to $\text{Na}_4\text{XeO}_6 \cdot 2\text{H}_2\text{O}$. Having acquired the ^{131}Xe NMR

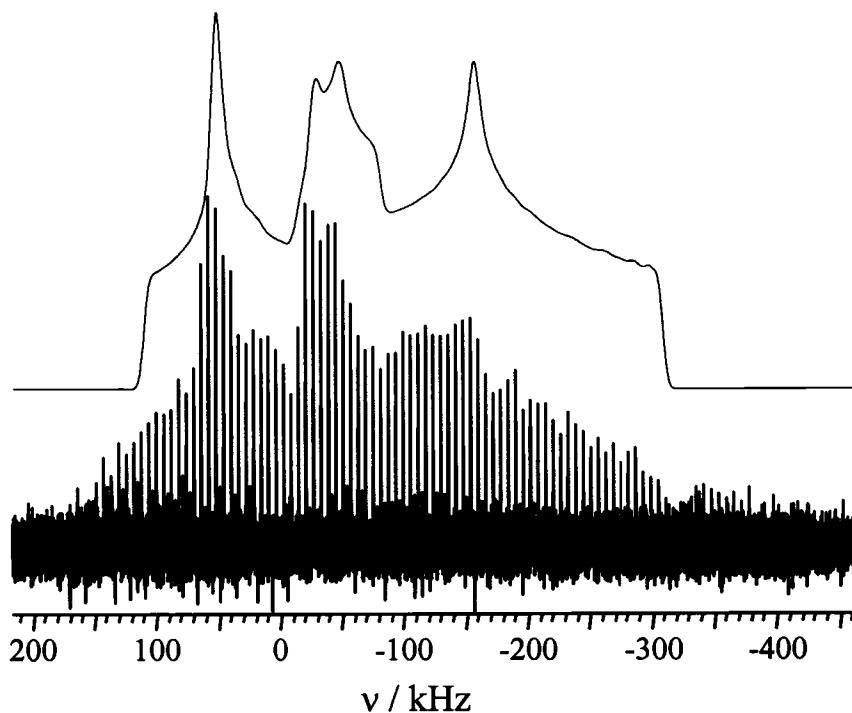


Figure 4.12: Simulated (top) and experimental (bottom) ^{131}Xe NMR spectra of $\text{Na}_4\text{XeO}_6 \cdot 2\text{H}_2\text{O}$ at 11.75 T ($\nu(^{131}\text{Xe}) = 41.244 \text{ MHz}$). The broad ^{131}Xe NMR signal is attributed to $\text{Na}_4\text{XeO}_6 \cdot 2\text{H}_2\text{O}$ and the narrow, central component is the sum of two sites attributed to two Xe polymorphs of the main sample, $\text{Na}_4\text{XeO}_6 \cdot 2\text{H}_2\text{O}$. The best-fit shielding and quadrupolar parameters for $\text{Na}_4\text{XeO}_6 \cdot 2\text{H}_2\text{O}$ and the two polymorphs are listed in Table 4.8.

spectrum at a single applied magnetic field prevents more definitive interpretation of the results for $\text{Na}_4\text{XeO}_6 \cdot 2\text{H}_2\text{O}$ and the polymorphic phases; nevertheless, these preliminary results clearly demonstrate that the main Xe species has a large C_Q value of approximately 10 MHz.

4.5.3.2. Na_4XeO_6

(i) Solid-State ^{129}Xe NMR Results

Shown in Figure 4.13 is a ^{129}Xe NMR spectrum of a stationary Na_4XeO_6 sample. The shape of the ^{129}Xe NMR signal is isotropic, indicating that Xe must reside in a site of octahedral symmetry, as suggested by the Raman spectrum (*Appendix 4.4*). The isotropic chemical shift of the anhydrous sample, $\delta_{\text{iso}} = -721 \pm 1$ ppm, is slightly deshielded with respect to the dihydrate, $\delta_{\text{iso}} = -725.6 \pm 0.1$ ppm, and the width-at-half-height, $\Delta\nu_{1/2}$, of the ^{129}Xe NMR signal, 3700 ± 100 Hz, is substantial. Since the anisotropic Xe shielding interaction is zero for a site of octahedral symmetry, and the indirect spin-spin, spin-rotation, paramagnetic and quadrupolar interactions are irrelevant relaxation mechanisms for ^{129}Xe in Na_4XeO_6 , the breadth of the ^{129}Xe NMR signal must arise from the ^{129}Xe ,

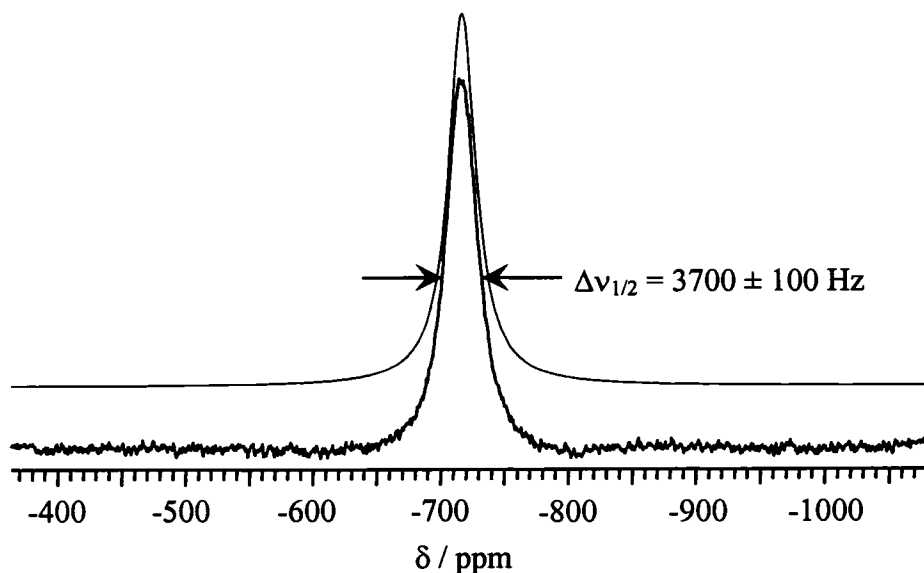


Figure 4.13: Simulated (top) and experimental (bottom) solid-state ^{129}Xe NMR spectra of a stationary sample of Na_4XeO_6 acquired at 139.132 MHz using a spin-echo sequence, a pulse delay of 2 s and 1600 scans. A Lorentzian linebroadening function of 3700 Hz was applied to the simulated spectrum.

^{23}Na dipolar interaction. This conclusion is supported by the rapid decay of the ^{129}Xe FID, < 0.3 ms; however, the apparent Lorentzian ^{129}Xe NMR lineshape is perplexing and no explanation can be given at this time.

To determine the spin-lattice relaxation time, $T_1(^{129}\text{Xe})$, for Na_4XeO_6 , the progressive saturation technique was employed; this entails systematically varying the pulse delay and monitoring the ^{129}Xe NMR signal intensity for a series of experiments. A total of 4 dummy scans were applied prior to acquisition of 8 scans to ensure a steady state was established for each experiment. A summary of these experiments is plotted in Figure 4.14 for pulse delays ranging from 2 s to 800 s. The data were fit to the following equation,²²⁹

$$S_\tau = S_\infty [1 - \exp(-\tau/T_1)], \quad (4.13)$$

where S_τ and S_∞ are the signal intensities at time τ and the time required for the sample to be fully relaxed, respectively, and τ is the time between pulses. The $T_1(^{129}\text{Xe})$ value was determined to be 89 ± 5 s, demonstrating that T_1 relaxation is inefficient for Na_4XeO_6 – a typical occurrence for compounds of high symmetry. In contrast, $T_2(^{129}\text{Xe})$ is very short, *i.e.*, $T_2 \ll T_1$, which is not surprising in NMR studies of solid compounds. Further

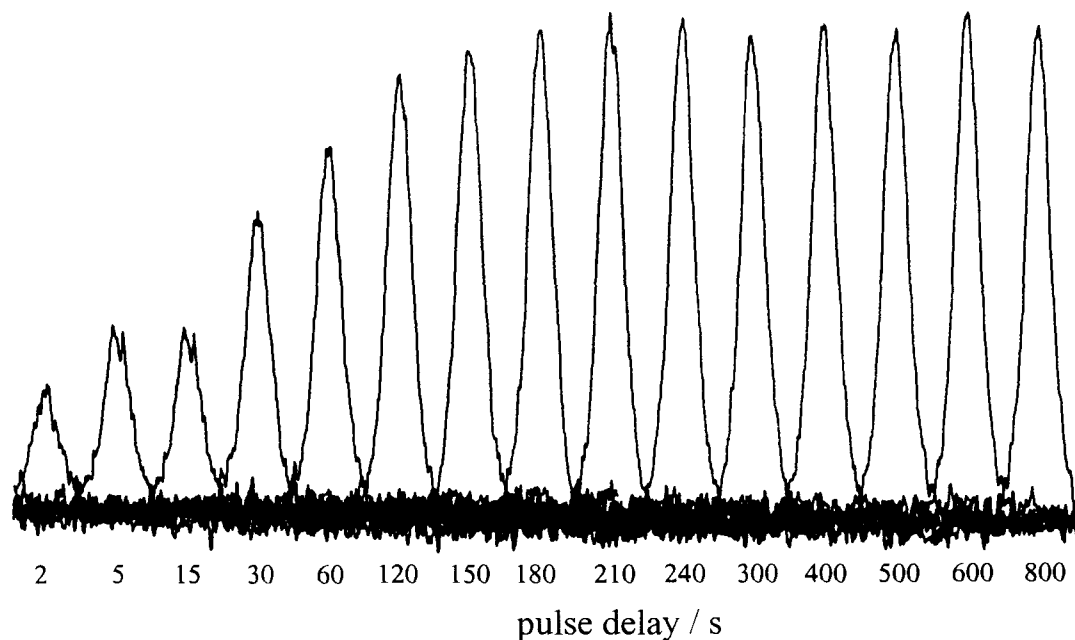


Figure 4.14: ^{129}Xe NMR spectra of anhydrous Na_4XeO_6 acquired using the progressive saturation method²²⁰ for the determination of $T_1(^{129}\text{Xe})$.

details concerning the nature of the T_1 and T_2 relaxation mechanisms require additional experiments, for example, as a function of temperature or magnetic field.

(ii) Solid-State ^{131}Xe NMR Results

Solid-State ^{131}Xe NMR spectra of Na_4XeO_6 are shown in Figure 4.15 and are remarkably different from that of the dihydrate (Figure 4.11). The isotropic ^{131}Xe NMR lineshape clearly indicates an octahedral environment for XeO_6^{4-} , in agreement with Raman and ^{129}Xe NMR spectra. Interestingly, the linewidth of the ^{131}Xe NMR signal, $\Delta\nu_{1/2} = 1200$ Hz, is significantly less than that of the ^{129}Xe NMR signal, $\Delta\nu_{1/2} = 3700$ Hz; in fact, the ratio of the linewidths, $\Delta\nu_{1/2}(^{129}\text{Xe}) / \Delta\nu_{1/2}(^{131}\text{Xe}) = 3.1$, is roughly equal to the ratio of their respective resonance frequencies, $\Xi(^{129}\text{Xe})/\Xi(^{131}\text{Xe}) = 3.4$. This strongly suggests that broadening of the ^{129}Xe and ^{131}Xe NMR signals arises from the dipolar interaction, which is directly related to the product of the magnetogyric ratios of the coupled nuclei; *i.e.*, $^{129/131}\text{Xe}$ and ^{23}Na , and, thus, explains the greater breadth of the ^{129}Xe NMR signal relative to its quadrupolar counterpart, ^{131}Xe .

The $T_1(^{131}\text{Xe})$ value for Na_4XeO_6 was not accurately determined, but was found to be short; *i.e.*, < 1 s, by monitoring the ^{131}Xe NMR signal intensity as a function of pulse delay. The $T_2(^{131}\text{Xe})$ was similarly short, < 5 ms, but sufficiently long to carry out a QCPMG experiment. The QCPMG experiment holds information about both homogeneous and inhomogeneous interactions present in the sample. While homogeneous interactions contribute to the linewidth of the individual spikelets, inhomogeneous interactions contribute to the whole NMR lineshape. For anhydrous Na_4XeO_6 , the homogeneous interactions appear to be negligible, as evidenced by the narrow spikelets, with linewidths of 30 ± 5 Hz. As mentioned above, the ^{131}Xe , ^{23}Na dipolar interaction is the suggested inhomogeneous interaction that contributes to the breadths of the ^{129}Xe and ^{131}Xe NMR signals.

The ^{131}Xe NMR results for the dihydrate and anhydrous sodium perxenate demonstrate the acute sensitivity of the Xe EFG tensor to small changes in the local environment. Upon dehydration of $\text{Na}_4\text{XeO}_6 \cdot 2\text{H}_2\text{O}$, the XeO_6^{4-} anion assumes octahedral symmetry, and the quadrupolar coupling constant reduces drastically from ten to zero MHz, corresponding to observed ^{131}Xe linewidths of 500 kHz and 1200 Hz, respectively.

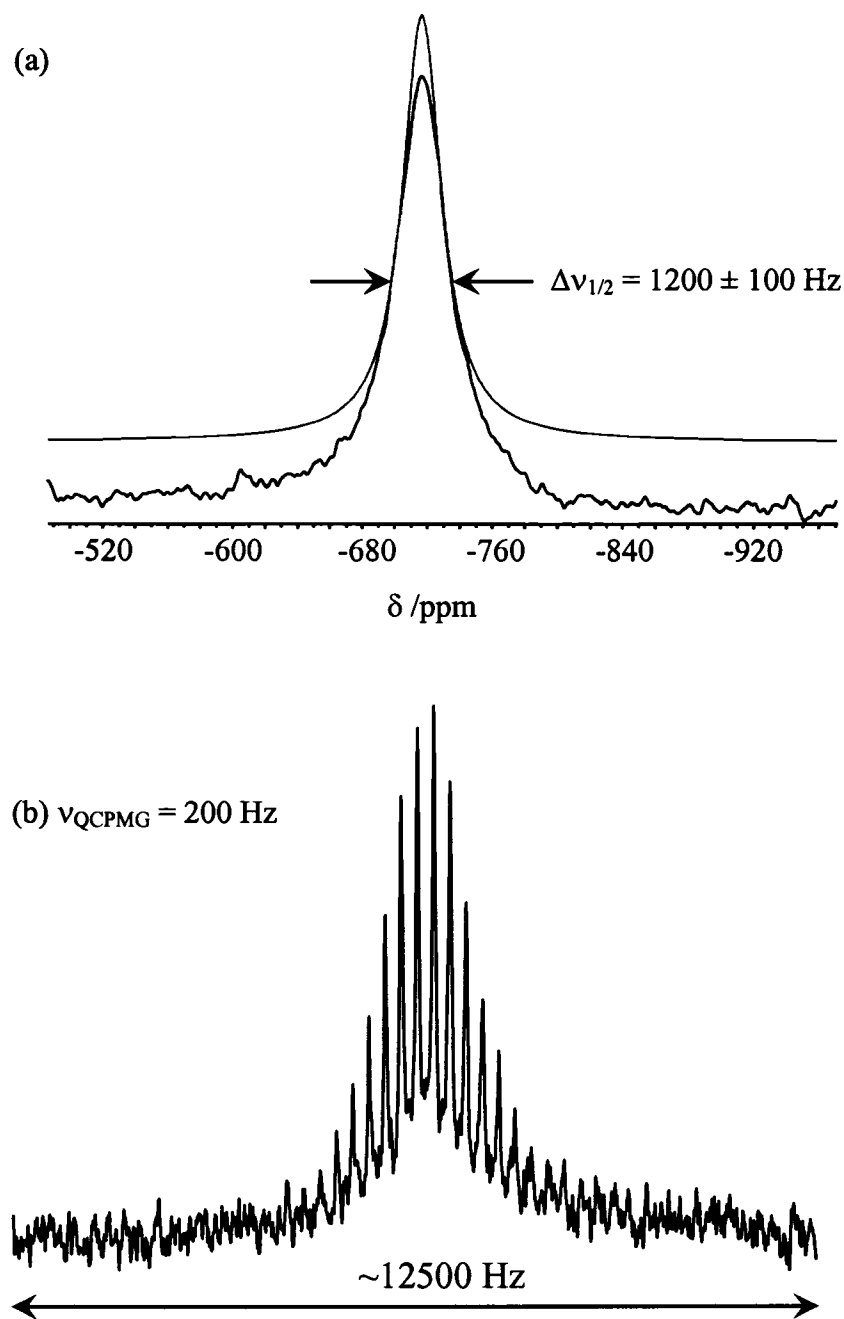


Figure 4.15: Solid-state ^{131}Xe NMR spectra of stationary samples of anhydrous sodium perxenate acquired at 41.244 MHz using (a) spin-echo (52,432 scans) and (b) QCPMG (53,024 scans, $\nu_{\text{QCPMG}} = 200$ Hz) experiments. Also shown in (a) is a simulated spectrum (top) to which a Lorentzian linebroadening function of 1200 Hz has been applied. The slight discrepancy in the linewidths between the experimental and simulated spectra shown in (a) results because a Lorentzian/Gaussian apodization function of 100 Hz was applied to the experimental spectrum upon Fourier transform.

The extremely broad ^{131}Xe NMR signal for the dihydrate arises from the large ^{131}Xe quadrupole moment, which amplifies small changes in the local structure; this, in combination with the low magnetogyric ratio of ^{131}Xe , leads to the conclusion that, although solid-state ^{131}Xe NMR studies are possible, in most cases they are impractical –

Table 4.9: Calculated* and Experimental ^{131}Xe Nuclear Quadrupolar Coupling Constants.

| | Method | Calc. $C_Q(^{131}\text{Xe})$ / MHz | Isotopomer | Exp. $C_Q(^{131}\text{Xe})$ / MHz | Ref. |
|------------------|--------|---------------------------------------|--|--------------------------------------|------|
| XeAgF | nr | -90.28 | $^{131}\text{Xe}^{107}\text{Ag}^{19}\text{F}$ | -82.77 | 230 |
| | so | -104.28 | $^{131}\text{Xe}^{109}\text{Ag}^{19}\text{F}$ | -82.93 | |
| XeAgCl | nr | -86.60 | $^{131}\text{Xe}^{107}\text{Ag}^{35}\text{Cl}$ | -78.05 | 230 |
| | so | -97.31 | $^{131}\text{Xe}^{109}\text{Ag}^{35}\text{Cl}$ | -78.29 | |
| XeNe | nr | -0.76 | $^{131}\text{Xe}^{20}\text{Ne}$ | 0.3878 | 231 |
| | so | 0.87 | $^{131}\text{Xe}^{22}\text{Ne}$ | 0.3875 | |
| XeKr | nr | -2.83 | ----- | ----- | 231 |
| | so | 0.65 | $^{131}\text{Xe}^{84}\text{Kr}$ | 0.7079 | |
| XeAr | nr | -1.57 | ----- | ----- | 231 |
| | so | 1.13 | $^{131}\text{Xe}^{39}\text{Ar}$ | 0.7228 | |
| XeHCl | nr | -11.43 | ----- | ----- | 232 |
| | so | -8.05 | $^{131}\text{Xe}^1\text{H}^{35}\text{Cl}$ | -4.9 | |
| XeHF | nr | -17.86 | ----- | ----- | 233 |
| | so | -14.03 | $^{131}\text{Xe}^1\text{H}^{19}\text{F}$ | -8.589 | |
| XeAuF | nr | -91.88 | ----- | ----- | 234 |
| | so | -156.04 | $^{131}\text{Xe}^{197}\text{Au}^{19}\text{F}$ | -134.5 | |
| XeH ⁺ | nr | -342.07 | $^{131}\text{Xe}^1\text{H}^+$ | -369.50 | 235 |
| | so | -399.31 | $^{131}\text{Xe}^2\text{H}^+$ | -369.33 | |
| XeF ₂ | nr | -559.63 | ----- | ----- | |
| | so | -628.23 | | | |

* All calculations were carried out using the ZORA DFT method and TZ2P basis sets.

such studies are simply too time-demanding. To demonstrate this further, known $C_Q(^{131}\text{Xe})$ values, determined from microwave spectroscopy and calculated using high-level ZORA DFT for a series of linear molecules, including XeF_2 , are given in Table 4.9; note that no attempt was made to include vibrational averaging in these calculations, which would be particularly important for *ng-ng* type systems.

From Table 4.9, the ZORA DFT calculations qualitatively reproduce the trend of experimentally determined $C_Q(^{131}\text{Xe})$ values, but slightly overestimate their magnitudes. In general, the $C_Q(^{131}\text{Xe})$ values are much too large to attempt ^{131}Xe NMR studies. Of the listed molecules, the only candidates that could be plausibly studied by solid-state ^{131}Xe NMR are *ng-ng* and Xe-HX ($X = \text{Cl}, \text{Br}$) prototypes; however, these are examples of compounds that are loosely bound by Van der Waals forces in the gas phase and dissociate in the solid state.

In *Section 4.3*, a solid-state ^{129}Xe NMR study of XeF_2 was presented. As a point of interest, how broad would the ^{131}Xe NMR spectrum for XeF_2 be, if acquired on an 11.75 T NMR system? Taking into account the apparent overestimation of the calculations, a $C_Q(^{131}\text{Xe})$ value of 400 MHz is assumed, as well as an axially-symmetric EFG tensor, as dictated by the $D_{\infty h}$ point group symmetry. Neglecting all other NMR interactions, the ^{131}Xe NMR signal would span nearly 550 MHz. To acquire such a spectrum would, quite literally, take a lifetime to complete! With current pulse sequences and magnetic field strengths, the study of XeF_2 and similar compounds by solid-state ^{131}Xe NMR spectroscopy is out of the question.

4.5.4. Conclusions

The solid-state $^{129/131}\text{Xe}$ NMR study of $\text{Na}_4\text{XeO}_6 \cdot 2\text{H}_2\text{O}$ and Na_4XeO_6 represents an interesting case where structural information may be obtained in the absence of crystal structure data through the measurement of the Xe shielding and quadrupolar interactions for the two magnetically-active Xe isotopes, ^{129}Xe and ^{131}Xe . For $\text{Na}_4\text{XeO}_6 \cdot 2\text{H}_2\text{O}$, distortions in the local Xe environment from O_h symmetry have been detected through measurement of the Xe magnetic shielding tensor, which is axially-symmetric and spans 95 ppm, and the EFG tensor, which has a large quadrupolar coupling constant of approximately 10.3 MHz. In contrast, the resultant isotropic ^{129}Xe and ^{131}Xe NMR peaks

for anhydrous Na_4XeO_6 indicate true O_h symmetry. The Xe quadrupolar interaction is highly sensitive to small structural changes, resulting from the large ^{131}Xe quadrupole moment; unfortunately, this is a serious drawback in the study of molecular Xe systems in the solid state, since acquisition of ^{131}Xe NMR spectra for more complex systems is clearly impractical at this time. On the contrary, the ^{129}Xe NMR results are promising in that both MAS and stationary samples can be studied with relative ease and in reasonable experiment times; furthermore, the moderate value of $\gamma(^{129}\text{Xe})$ is advantageous and does not impose impractical restrictions on the magnetic field that may be used.

Some questions concerning the ^{129}Xe and ^{131}Xe NMR lineshapes for Na_4XeO_6 remain unanswered. Why are the $^{129/131}\text{Xe}$ NMR lineshapes for anhydrous Na_4XeO_6 Lorentzian? Is the XeO_6^{4-} anion undergoing rapid motion? Further NMR investigations which probe the ^{23}Na nucleus may provide insight into this curious observation.

Chapter 5: Solid-State ^{95}Mo NMR Studies

5.1 Overview of ^{95}Mo NMR Studies

Molybdenum is an important transition metal that has useful applications in nitrogen-fixating enzymes,^{236,237} molecular electronic devices,²³⁸ and catalyses.²³⁹ Despite its prevalence in modern chemistry, molybdenum has received little attention from the solid-state NMR community, primarily because the two NMR-active isotopes of molybdenum, ^{95}Mo and ^{97}Mo , fall into the category of "low-gamma" quadrupolar nuclei. Both ^{95}Mo and ^{97}Mo are spin-5/2 nuclei with low NMR receptivities and moderate natural abundances (^{95}Mo : $\Xi = 6.547$ MHz, N.A. = 15.92 %; ^{97}Mo : $\Xi = 6.685$ MHz, N.A. = 9.46 %).³⁷ The preferred isotope for NMR studies is ^{95}Mo , since its nuclear quadrupole moment, $|Q|$, is an order of magnitude less than that for ^{97}Mo (^{95}Mo : $Q = -0.022 \times 10^{-28} \text{ m}^2$; ^{97}Mo : $Q = 0.17 \times 10^{-28} \text{ m}^2$).³⁷ Unfortunately, the small $Q(^{95}\text{Mo})$ creates an additional impediment for ^{95}Mo NMR studies in the solid state – long spin-lattice relaxation times,²⁴⁰ which further increase the time required to obtain an adequate ^{95}Mo NMR signal.

In spite of the low-receptivity of ^{95}Mo , hundreds of ^{95}Mo NMR studies have been carried out in solution on a variety of diamagnetic Mo(0), Mo(II), Mo(IV), and Mo(VI) compounds, establishing a Mo chemical shift range of approximately 8000 ppm.²⁴¹ The difficulties associated with solid-state ^{95}Mo NMR studies are not as problematic for solution studies; for example, ^{95}Mo spin-lattice relaxation times are very short in solution due to the efficient nature of the T_1 quadrupolar mechanism and the linewidths of ^{95}Mo NMR signals in solution are orders of magnitude less than those in the solid state.

Solid-state ^{95}Mo NMR studies are, inevitably, less extensive and have focused on selected diamagnetic compounds whose nuclear site symmetries fulfill the requirements of small EFGs at Mo. Initial solid-state ^{95}Mo NMR studies were carried out at applied magnetic fields as low as 2.11 T, forcibly limiting the quality of the work due to the marginally-adequate signal-to-noise. Conducting solid-state ^{95}Mo NMR studies at magnetic fields equal to or less than 9.4 T presents an incredible challenge since the Zeeman interaction is proportional to B_0 , which reduces the sensitivity of the NMR experiment and the ability to characterize the full shielding tensor; in addition, second-

order quadrupolar broadening (in ppm) is inversely proportional to B_0^2 and is consequently enhanced at lower magnetic fields. Early research therefore neglected the anisotropic Mo shielding interaction and focused on determining the Mo quadrupolar parameters.^{240,242,243,244,245} For example, the first solid-state ^{95}Mo NMR study of $\text{Mo}(\text{CO})_6$ was carried out in 1977 by Nolle²⁴² who analyzed the central NMR transition at 2.11 and 2.14 T; only the ^{95}Mo quadrupolar interaction was considered and a ^{95}Mo nuclear quadrupolar coupling constant of 1.41 kHz was obtained. Mastikhin *et al.*²⁴⁵ later observed the central transition of $\text{Mo}(\text{CO})_6$ at 7.05 T, but concluded that the EFG at Mo was zero based on a relatively narrow NMR signal. Subsequently, Ellis and co-workers²⁴⁶ observed both the central and satellite NMR transitions of $\text{Mo}(\text{CO})_6$ at 9.4 T, but they did not analyze their results. Approximately two decades after the initial ^{95}Mo NMR study on $\text{Mo}(\text{CO})_6$,²⁴² Eichele *et al.*²⁴⁷ reinvestigated the ^{95}Mo NMR spectrum of $\text{Mo}(\text{CO})_6$ at 9.4 T and observed both the central and satellite transitions; in their analysis, both the Mo EFG and anisotropic shielding interactions were found to be non-negligible: $C_Q(^{95}\text{Mo}) = 91$ kHz and $\Omega = 22$ ppm. In the earlier study carried out by Nolle,²⁴² the contribution to the ^{95}Mo NMR lineshape from anisotropic Mo shielding was neglected, resulting in an overestimation of $C_Q(^{95}\text{Mo})$; nevertheless, disregarding contributions from the anisotropic Mo shielding interaction at 2.11 and 2.14 T was a logical assumption as the effects would be subtle at such low magnetic fields.

The importance of the anisotropic Mo shielding interaction and the relative orientation of Mo shielding and EFG tensors in analyzing solid-state ^{95}Mo NMR spectra of Mo compounds was first demonstrated in 1990 by Ellis and co-workers in their ^{95}Mo NMR study of molybdates, polymolybdates, and molybdenum-alumina based catalysts at 9.4 T.^{246,248,249} Similarly, Bastow²⁴⁰ realized that the central transition ^{95}Mo NMR lineshapes of a series of binary Mo compounds were largely controlled by anisotropic Mo shielding, but no effort was made to analyze the data.

More recent reports capitalize on the availability of high-field magnets to examine molybdenum(0) mesitylene tricarbonyl,⁴⁵ molybdenum(IV)octacyanide²⁵⁰ and re-examine a series of monomolybdate and polymolybdate salts,²⁵¹ thus demonstrating the feasibility of high-field solid-state ^{95}Mo NMR studies. The study of $\text{MesMo}(\text{CO})_3$ was carried out at 17.63 T and represents the first report of a highly anisotropic Mo shielding

tensor. In fact, the ^{95}Mo NMR lineshape of the central transition was found to be overwhelmed by the anisotropic Mo shielding interaction, $\Omega = 775$ ppm, whereas the Mo quadrupolar interaction was found to be comparatively small, with $C_Q(^{95}\text{Mo}) = -0.96$ MHz. More recently, significant contributions from both the anisotropic Mo shielding and quadrupolar interactions for two symmetry forms of the octacyanomolybdate(IV) anion have been reported;²⁵⁰ this study represents the largest Mo shielding anisotropies observed to date and will be the subject of discussion in *Section 5.3*. Of the few solid-state ^{95}Mo NMR studies, accurate information on the anisotropic Mo shielding interaction is lacking; however, the above-mentioned studies on $\text{MesMo}(\text{CO})_3$, $\text{Mo}(\text{CN})_8^{4-}$, and $\text{Mo}(\text{CO})_6$ demonstrate that the anisotropic Mo shielding interaction can be significant.

For the specific case of molybdate salts, there is a major void in the solid-state ^{95}Mo NMR literature on anisotropic Mo shielding parameters and the relative orientation of the Mo shielding and EFG tensors. To date, only the isotropic Mo chemical shifts and quadrupolar parameters have been reported for a series of molybdate salts,^{243,245,246,247,251} with the exception of sodium molybdate dihydrate, for which the span of the shielding tensor was roughly estimated to be 200 ppm.²⁴⁷ Since most NMR studies on molybdates have been carried out either at low magnetic fields or with the use of MAS, measurement of shielding anisotropy and the Euler angles has not been possible. The recent ^{95}Mo NMR study carried out at 19.6 T would have been a prime opportunity to characterize the anisotropic Mo shielding interaction for the molybdate and polymolybdate salts studied; however, only MAS samples were investigated and, hence, only the quadrupolar parameters and isotropic chemical shifts were reported.²⁵¹

5.2. Solid-State ^{95}Mo NMR Studies of A(I) and A(II) Molybdenum Oxide Salts

Here, solid-state ^{95}Mo NMR results for several molybdate salts, $\text{A}(n)\text{MoO}_4$ ($n = \text{I, II}$) and Bi_2MoO_6 , are presented. The molybdate family, MoO_4^{2-} , is a popular choice for preliminary ^{95}Mo NMR studies for two complementary reasons: the Mo EFG and anisotropic Mo shielding interactions are sufficiently small to enable facile detection, yet adequately sensitive to allow subtle changes in MoO_4^{2-} from T_d symmetry to be detected through characterization of the Mo EFG and shielding tensors, as well as their relative orientations. According to the point-charge approximation (*Section 2.5.3.*), the EFG at

Mo should be zero for an ideal tetrahedral MoO_4^{2-} anion; however, structural distortions in the local MoO_4^{2-} environment and contributions from the extended crystal lattice induce a non-zero EFG at Mo.

The primary goal of this research is to characterize the anisotropic Mo shielding interaction for the A(I) and A(II) molybdate salts and to assess the relative importance of the Mo shielding and quadrupolar interactions. To determine the Mo shielding and quadrupolar interactions, as well as the relative orientation of their tensors, ^{95}Mo NMR experiments have been carried out on MAS and/or stationary A(I) MoO_4 and A(II) MoO_4 samples at moderate, 11.75 T, and/or high, 17.63 T, applied magnetic fields. Second, the assumed relationship between the extent of distortion of the MoO_4^{2-} anions and the observed ^{95}Mo quadrupolar coupling constants is investigated and the validity of the PCA in predicting EFGs is addressed.

5.2.1. Experimental Details

All molybdate salts ($\text{A}(n)\text{MoO}_4$ ($n = \text{I, II}$) $\text{A} = \text{Li, K, Rb, Cs, Ca, Sr, Cd, Ba, Pb}$) and Bi_2MoO_6 were commercially available and used without further purification. Since molybdate salts are known to form polymorphs, the samples were analyzed using powder X-ray diffraction, XRD. The structures of all A(I) and A(II) molybdate salts were confirmed by powder XRD, except Bi_2MoO_6 , for which the structure was not determined.

(i) Solid-State ^{95}Mo NMR Experiments at 11.75 T

Solid-state ^{95}Mo NMR spectra were acquired on a Bruker Avance NMR spectrometer operating at 32.603 MHz. Samples were powdered and packed into 7.0 mm (o.d.) ZrO_2 rotors and a 7.0 mm DR probe was used for experiments on both MAS and stationary samples. Either a one-pulse or a spin-echo sequence was employed. The primary NMR reference for ^{95}Mo NMR studies, a 2.0 M solution of Na_2MoO_4 with $\delta_{\text{iso}} = 0.00$ ppm, was used for referencing and pulse width calibration. Solution $\pi/2$ pulses of 6.00 or 6.85 μs were found, corresponding to a solid, selective $\pi/2$ pulse of 2.00 and 2.33 μs , respectively. Sweep widths of 50 or 100 kHz, acquisition times of 10 – 50 ms and pulse delays ranging from 2 – 20 s were used. Spinning rates were set to 6000 Hz, except Cs_2MoO_4 , for which the spinning rate was set to 3000 Hz.

(ii) Solid-State ⁹⁵Mo NMR Experiments at 17.63 T

All experiments were performed on stationary molybdate samples using a Varian Inova NMR spectrometer operating at a frequency of 48.843 MHz for ⁹⁵Mo. Samples were powdered and packed into 5.0 mm glass NMR tubes and a 5.0 mm single-channel probe was used. The primary Mo NMR reference, a 2.0 M solution of Na₂MoO₄, was used for referencing, $\delta_{\text{iso}} = 0.00$ ppm, and pulse width calibration. Solution $\pi/2$ pulses of 9.3 or 10.2 μs were found, corresponding to solid, selective $\pi/2$ pulses of 3.1 and 3.4 μs , respectively. Either a QCPMG or spin-echo sequence was employed. Acquisition times of 0.130 – 0.358 s, sweep widths of 15 – 50 kHz, τ values of 80 μs and 102 μs or 80 μs and 112 μs , pulse delays of 10 – 20 s, and a total of 8 – 1024 scans were summed before Fourier transformation. QCPMG π pulse trains were repeated 32 – 72 times and the separation between spikelets in the QCPMG experiments, ν_{QCPMG} , was set to either 200 or 250 Hz.

Simulations of ⁹⁵Mo NMR spectra of MAS and stationary samples acquired at 11.75 T were carried out using WSOLIDS,¹⁰¹ while those acquired at 17.63 T were carried out using SIMPSON¹⁰² and WSOLIDS. SIMPSON simulations employed either the *zcw986*, *zcw4180* or *zcw10945* crystal files,¹⁰² available in the SIMPSON package.

5.2.2. Results and Discussion

5.2.2.1. Structure of A(I) and A(II) Molybdate Salts

Structural data for the A(I) = Li, K, Rb, Cs and A(II) = Ca, Sr, Ba, Pb, Cd, Bi molybdate salts investigated herein are summarized in Table 5.1 and their crystal lattices are depicted in *Appendix 5.1*. The general structure of molybdates is comprised of discrete MoO₄²⁻ tetrahedra which are linked to cation-polyhedra by shared vertices.¹⁹⁹ The coordination of the cation polyhedra is partially determined by the size of the cation. In general, larger cations form higher-coordination polyhedra, resulting in more notable distortions in the molybdate anion from T_d symmetry. The extent of distortion may be gauged by the bond angle variance, σ^2 , defined in Table 5.1; however, the accuracy of σ^2 depends on the accuracy of the method used to determine the structure.

The A(II) monomolybdates, where A(II) = Ca, Sr, Ba, Cd, Pb, are isostructural and crystallize in the tetrahedral $I4_1/a$ space group (Table 5.1); this structure is preferentially adopted for ABO_4 -type compounds with large A(II) cations.²⁵² The alkali metal molybdates, $A(I)_2MoO_4$, crystallize in the rhombohedral $R-3$, monoclinic $C2/m$, or orthorhombic $Pnma$ space groups for A(I) = Li, K, and Rb, and Cs, respectively. The majority of the cations, K, Rb, Sr, Ba, Cd, Ca, Pb, form polyhedra with oxygen with a coordination number of eight, whereas the smaller Li cations form tetrahedra and the Cs cations form polyhedra with coordination numbers 9 and 11.

Table 5.1: Summary of Structural Data for Molybdate Salts.

| Molybdate | Space Group | Crystal Symmetry | Point Symmetry at Mo | Bond Angle Variance, σ^{2*} |
|-------------|---------------|-------------------------------|----------------------|------------------------------------|
| Li_2MoO_4 | $R-3$ (148) | Rhombohedral ²⁵³ | I | 2.28 |
| K_2MoO_4 | $C2/m$ (12) | Monoclinic ²⁵⁴ | m | 3.30 |
| Rb_2MoO_4 | $C2/m$ (12) | Monoclinic ²⁵⁵ | m | 14.58 |
| Cs_2MoO_4 | $Pnma$ (62) | Orthorhombic ²⁵⁵ | m | 0.63 |
| $CaMoO_4$ | $I4_1/a$ (88) | Tetragonal ²⁵⁶ | $\bar{4}, m$ | 18.02 |
| $SrMoO_4$ | $I4_1/a$ (88) | Tetragonal ^{256,257} | $\bar{4}, m$ | 8.30 |
| $CdMoO_4$ | $I4_1/a$ (88) | Tetragonal ²⁵⁸ | $\bar{4}, m$ | 527.75 |
| $BaMoO_4$ | $I4_1/a$ (88) | Tetragonal ²⁵⁹ | $\bar{4}, m$ | 3.27 |
| $PbMoO_4$ | $I4_1/a$ (88) | Tetragonal ²⁶⁰ | $\bar{4}, m$ | 6.94 |
| Bi_2MoO_6 | N.D. | N.D. | N.D. | N.D. |

5.2.2.2. Solid-State ^{95}Mo NMR Studies of Molybdate Salts

Presented in Figure 5.1 are experimental and calculated solid-state ^{95}Mo NMR spectra of MAS samples of $A(I)_2MoO_4$; the best-fit calculated parameters are given in Table 5.2 along with those previously-determined, when available. Second-order quadrupolar lineshapes are observed for the central NMR transition of all molybdate

* The standard variance of the (O, Mo, O) bond angle is defined as:

$$\sigma^2 = \frac{1}{5} \sum_{i=1}^6 (\theta_i - 109.47^\circ)^2, \text{ where } \theta_i \text{ is the } i^{\text{th}} \text{ O, Mo, O bond angle.}$$

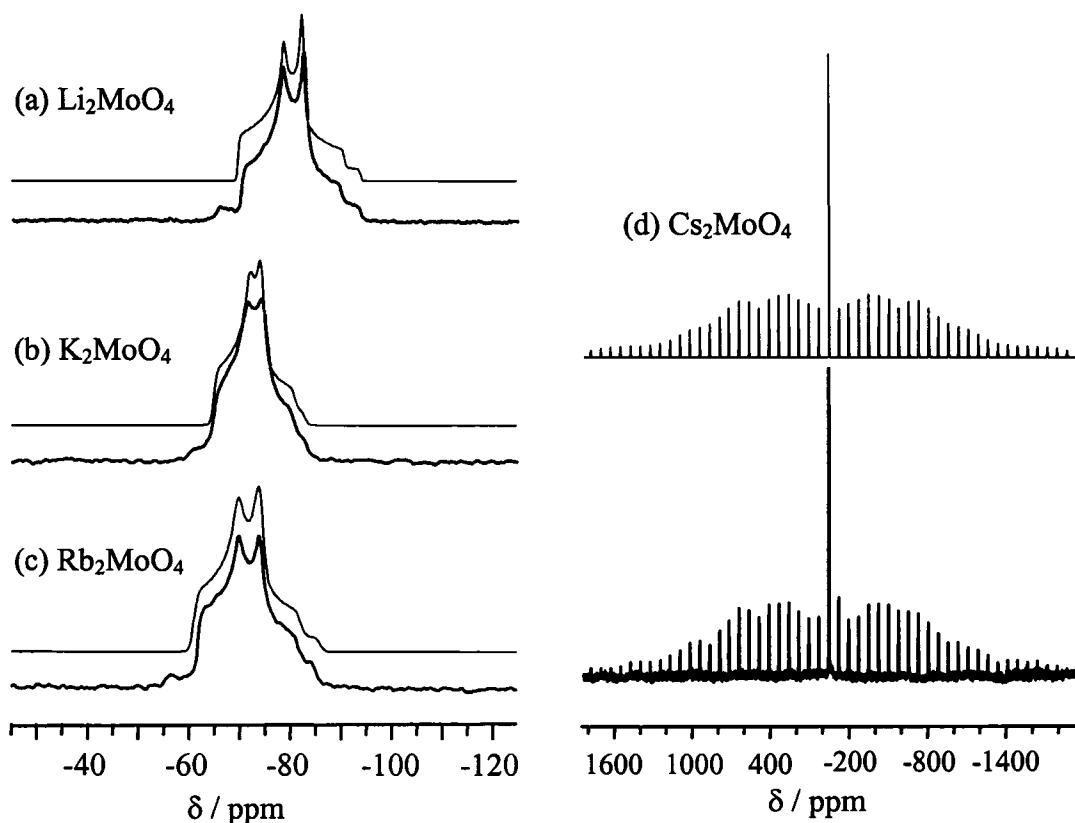


Figure 5.1: Simulated (top) and experimental (bottom) ^{95}Mo NMR spectra of MAS samples of alkali molybdate salts acquired using a one-pulse experiment at 11.75 T. The spectra are the sum of 6471, 2665, 2051, 4930 scans, respectively, and were acquired at spinning rates of (a-c) $\nu_{\text{rot}} = 6$ kHz and (d) $\nu_{\text{rot}} = 3$ kHz using pulse delays of 10 s. Gaussian linebroadening functions of (a-d) 50 Hz, 25 Hz, 20 Hz, and 20 Hz; respectively, were applied to the FIDs prior to Fourier transformation.

salts, except for Cs_2MoO_4 . Of the alkali metal molybdates, the Mo coordination is most regular for Cs_2MoO_4 and forms a near ideal tetrahedron with minor O, Mo, O angular deviations ($\sigma^2 = 0.63$; Table 5.1) and bond length differences of 0.01 Å. The small structural distortions are evident in the central transition ^{95}Mo NMR signal (intense, central peak) for Cs_2MoO_4 , which is isotropic and shows no apparent broadening from the second-order quadrupolar interaction. To determine the EFG parameters for Cs_2MoO_4 , the satellite transitions were observed at a slow MAS rate, $\nu_{\text{rot}} = 3000$ Hz; spectral analyses gives resultant δ_{iso} , C_Q , and η_Q values of -22 ppm, 340 kHz and 0.45, respectively. The apparent C_Q value of zero measured by d'Espinoise de Lacaillerie and co-workers²⁵¹ in their ^{95}Mo MAS NMR study of Cs_2MoO_4 at 19.6 T is a consequence of

Table 5.2: Isotropic Chemical Shifts and Mo Quadrupolar Parameters for A(I)MoO₄, A(II)MoO₄ and Bi₂MoO₆.

| A(I) | δ_{iso} / ppm | C_Q / MHz | η_Q | B_0 / T | Reference |
|----------------------------------|-----------------------------|--------------------|-----------------|-----------|-----------|
| Li | -26.0 ± 0.5 | 1.27 ± 0.03 | 0.70 ± 0.05 | 11.75 | this work |
| | -26 | 1.26 | 0.6 | 19.6 | 251 |
| | -72 | ~ 0 | ND | 7.05 | 245 |
| K | -17.2 ± 0.5 | 1.27 ± 0.03 | 0.60 ± 0.05 | 11.75 | this work |
| | -17 | 1.27 | 0.6 | 19.6 | 251 |
| | -24, 12, 2 | 1.5, 1.3, ~ 0 | ND, ND, 0 | 7.05 | 245 |
| Rb | -21.5 ± 0.5 | 1.09 ± 0.02 | 0.75 ± 0.06 | 11.75 | this work |
| Cs | -22.0 ± 0.4 | 0.34 ± 0.02 | 0.45 ± 0.05 | 11.75 | this work |
| | -21 | 0 | ND | 19.6 | 251 |
| | -25 | 0 | ND | 7.05 | 245 |
| A(II) | | | | | |
| Ca | 46 ± 2 | 2.895 ± 0.05 | 0.0 | 11.75 | this work |
| | 46 | 2.94 | 0.1 | 19.6 | 251 |
| | 35 | 2.7 | 0 | 7.05 | 245 |
| Sr | -1.0 ± 0.5 | 2.26 ± 0.02 | 0.0 | 11.75 | this work |
| Cd | 131.3 ± 0.6 | 3.05 ± 0.03 | 0.0 | 11.75 | this work |
| Ba | -35.4 ± 0.6 | 1.68 ± 0.05 | 0.08 ± 0.08 | 11.75 | this work |
| | -35 | 1.68 | 0.1 | 19.6 | 251 |
| | -45 | 1.6 | ND | 7.05 | 245 |
| Pb | 118 ± 2 | 2.03 ± 0.03 | 0.0 | 11.75 | this work |
| | 118 | 2.03 | 0.1 | 19.6 | 251 |
| | 108 | 1.9 | 0 | 7.05 | 245 |
| Bi ₂ MoO ₆ | -72.7 ± 1.0 | 2.85 ± 0.05 | 0.31 ± 0.06 | 11.75 | this work |

observing only the central NMR transition and that the second-order quadrupolar interaction would be substantially reduced at such a high magnetic field; however, the reported isotropic chemical shift is in agreement with that measured herein.

For Li, K, and Rb molybdate, the δ_{iso} , C_Q and η_Q values were determined by analyzing the second-order quadrupolar lineshape of the central transition ^{95}Mo NMR spectra; their Mo EFG tensors deviate considerably from axial symmetry, in agreement with their crystal symmetry and absence of a principal C_3 -axis. The isotropic chemical shifts and quadrupolar parameters are similar for Li, K, and Rb molybdate and are within the experimental error limits of previous studies (Table 5.2). Since K_2MoO_4 and Rb_2MoO_4 are isostructural, the similarity in their observed parameters is not surprising (Table 5.1; *Appendix 5.1*).

In an attempt to relate the observed $C_Q(^{95}\text{Mo})$ values to the molybdate structures, the bond angle variance, σ^2 , has been calculated; see Table 5.1. For Li_2MoO_4 , the small cationic radius ($r_{\text{cat}} = 0.73 \text{ \AA}$)²³⁷ induces small deviations from T_d symmetry, whereas, the larger cationic radius of Rb, $r_{\text{cat}} = 1.75 \text{ \AA}$,²³⁷ is reflected in its calculated σ^2 value. On the basis of the PCA, the measured $C_Q(^{95}\text{Mo})$ values are expected to increase as follows: $\text{Rb}_2\text{MoO}_4 > \text{K}_2\text{MoO}_4 > \text{Li}_2\text{MoO}_4$; however, this trend is not observed. In fact, of the three A(I) molybdates, Rb_2MoO_4 has the largest cation and the largest bond angle variance (Table 5.1), yet it has the smallest $C_Q(^{95}\text{Mo})$ value (Table 5.2). This result suggests that either the structural data used to calculate σ^2 is inaccurate or the observed $C_Q(^{95}\text{Mo})$ values for Li, K, and Rb do not depend exclusively on the local distortions of the MoO_4^{2-} anion from T_d symmetry, but that long-range effects may play a significant role in determining the EFG at Mo. An alternate explanation is that the MoO_4^{2-} anion is undergoing rotational motion which averages the ^{95}Mo quadrupolar interaction and affects the shape and breadth of the observed ^{95}Mo NMR spectra. The presence of motion could result in either a narrowing or broadening of the ^{95}Mo NMR lineshape. This phenomenon was observed by Schurko and co-workers²⁶¹ in an investigation of polymetallates; however, variable-temperature NMR studies are required to determine the presence of motion, which is not practical for solid-state ^{95}Mo NMR studies.

Shown in Figure 5.2 are experimental and calculated solid-state ^{95}Mo NMR spectra of MAS samples of A(II)MoO_4 , $\text{A(II)} = \text{Cd, Sr, Ba}$ and Bi_2MoO_6 ; their isotropic ^{95}Mo chemical shifts (Table 5.2) cover a range of approximately 200 ppm, demonstrating the sensitivity of the Mo shielding interaction. A previous ^{95}Mo NMR investigation²⁴⁵ claimed a correlation between internuclear Mo, O distance and ^{95}Mo NMR chemical

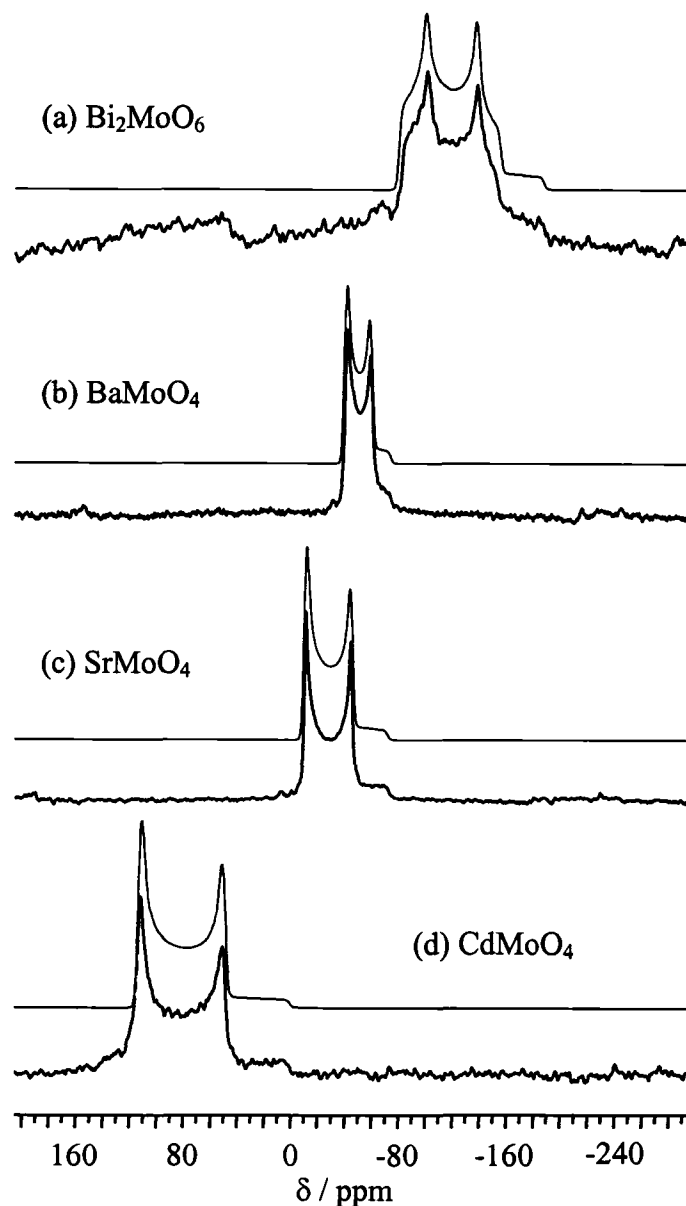


Figure 5.2: Simulated (top) and experimental (bottom) ^{95}Mo NMR spectra of MAS samples of (a-d) Bi_2MoO_6 , SrMoO_4 , BaMoO_4 , and CdMoO_4 . The spectra were acquired using a one-pulse experiment at $B_0 = 11.75$ T and $\nu_{\text{rot}} = 6$ kHz and are the sum of (a-d) 64014, 7724, 2319, and 2067 scans, respectively. Pulse delays of (a-d) 20 s, 20 s, 10 s, and 30s, respectively, were used and Gaussian functions of (a-d) 60 Hz, 50 Hz, 20 Hz, and 50 Hz; respectively, were applied to the FIDs prior to Fourier transformation.

shifts exists; however, based on our data, as well as theirs, there is no correlation. The Mo EFG tensors for the isostructural Sr, Ba, and Cd molybdate salts are axially-symmetric, as required by the S_4 point symmetry of Mo in the tetrahedral $I4_1/a$ space

group, whereas that for Bi_2MoO_6 deviates noticeably from axial symmetry, indicating significant distortions in the molybdate unit and the absence of a C_n -axis ($n \geq 3$). The observed $C_Q(^{95}\text{Mo})$ values for the A(II) molybdates are larger than those obtained for the A(I) molybdates (Table 5.2), due to the presence of larger cations which induce greater distortions from T_d symmetry.

Solid-state ^{95}Mo NMR results presented herein for A(I) and A(II) molybdates may be compared to those previously reported for Li_2MoO_4 , K_2MoO_4 , Cs_2MoO_4 and BaMoO_4 , whose δ_{iso} , C_Q , η_Q values are also given in Table 5.2. The isotropic ^{95}Mo chemical shifts and quadrupolar parameters are in agreement, within the reported experimental errors, with those recently reported²⁵¹ in the high-field ^{95}Mo NMR MAS study of monomolybdates. From Table 5.2, it is clear that carrying out experiments at low magnetic fields, 7.05 T, often prevents accurate determination of quadrupolar parameters and that high magnetic fields (11.75 T, 19.6 T) drastically improve the accuracy of the results.

5.2.2.3. Investigation of Anisotropic Mo Shielding in Molybdate Salts

We have demonstrated that the Mo EFG tensors of A(I) and A(II) molybdate salts may be characterized by acquiring ^{95}Mo NMR spectra of MAS samples; moreover, our results are superior or comparable to those previously reported in the literature. The anisotropic Mo shielding interaction, however, remains uncharacterized for the molybdate salts. To investigate this, as well as the relative orientation of Mo EFG and shielding tensors, we have acquired solid-state ^{95}Mo NMR spectra of stationary A(I) and A(II) molybdate samples. To properly analyze these spectra, the following eight parameters must be determined: δ_{iso} , C_Q , η_Q , Ω , κ , α , β , γ . Three of these parameters, δ_{iso} , C_Q , η_Q , are accurately known for the majority of the samples, with the exception of CaMoO_4 and PbMoO_4 , from MAS experiments (Table 5.2; Figures 5.1 and 5.2); thus, only the anisotropic Mo shielding parameters and Euler angles remain to be determined. When possible, spectra have been obtained at two magnetic fields, 11.75 and 17.63 T, to aid in the analyses and to ensure more accurate results; furthermore, X-ray data is used to help assign the Euler angles (*vide infra*). Results for the A(I) = Li, Cs, K, Rb molybdates are presented first, followed by those for the A(II) = Ca, Sr, Cd, Ba, Pb molybdate series.

Before ^{95}Mo NMR results for the A(I) molybdates are presented, it is instructive to review the symmetry elements present in their structures (Table 5.1). First, the crystal structures of the A(I) = Li, K, Rb, and Cs molybdates indicate the absence of a principal C_n -axis ($n \geq 3$), which permits deviation of the Mo shielding and EFG tensors from axial symmetry; this was previously observed upon analyses of the ^{95}Mo NMR spectra of MAS samples of the A(I) molybdates and characterization of their Mo EFG tensors (Table 5.2). Second, the structures for K, Rb, and Cs molybdate (Table 5.1) indicate the presence of a crystallographic mirror plane in which Mo and two oxygen atoms lie; the mirror plane controls the relative orientation of the Mo shielding and EFG tensors by forcing one principal component from each of the Mo shielding and EFG tensor to be perpendicular to the plane while the remaining two components to lie in the plane. The exact relative orientation of the two tensors is determined by visual inspection of the simulated spectra compared to experiment. The final A(I) molybdate, Li_2MoO_4 , crystallizes in the rhombohedral $R\bar{3}$ space group and the lone symmetry element for Mo is the identity operator, I ; hence, no special restrictions are placed on either the symmetry of the Mo shielding tensor or the Euler angles.

Shown in Figure 5.3 are ^{95}Mo NMR spectra of stationary samples of K_2MoO_4 (top) and Rb_2MoO_4 (bottom) acquired at two magnetic fields, 11.75 T and 17.63 T. The ^{95}Mo NMR spectra acquired at 17.63 T, shown on the right in Figure 5.3, have been obtained using the QCPMG experiment, which divides the overall ^{95}Mo NMR lineshape into a manifold of spikelets. The QCPMG technique provides a significant savings-in-time and gain in signal-to-noise over conventional echo experiments, while allowing the relevant Mo EFG and shielding parameters to be extracted upon standard spectral analysis. The best-fit parameters for K_2MoO_4 and Rb_2MoO_4 are given in Tables 5.2 and 5.3.

Similarities in the crystal structures of K_2MoO_4 and Rb_2MoO_4 (Table 5.1; *Appendix 5.1*) are reflected in the ^{95}Mo NMR lineshapes. The magnitude of the anisotropic Mo shielding tensors is significant for K_2MoO_4 and Rb_2MoO_4 ; as highlighted by the simulated spectra calculated with and without Ω (Figure 5.3 (b) and (c)). From the simulated spectra, the importance of the Mo shielding interaction is comparable to the

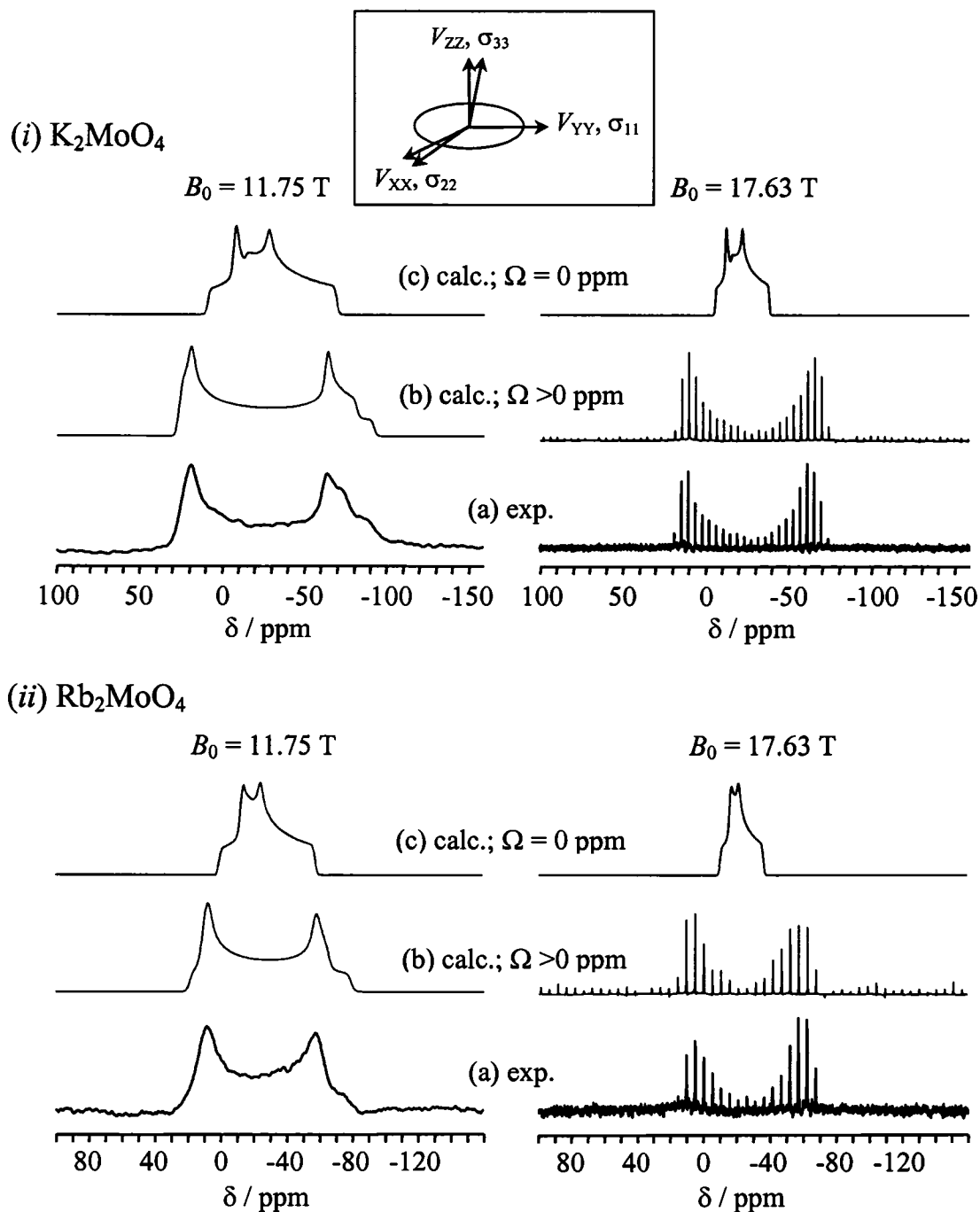


Figure 5.3: Experimental (a) and simulated (b, c) solid-state ^{95}Mo NMR spectra of stationary samples of (i) K_2MoO_4 and (ii) Rb_2MoO_4 acquired at 11.75 T (left) and 17.63 T (right). The spectra shown (b) represent the best-fit simulated spectra and the corresponding parameters are given in Tables 5.2 and 5.3; the spectra in (c) neglect contributions from the anisotropic Mo shielding interaction. The inset (top, center) shows the relative orientation of the principal components of the Mo shielding and EFG tensors for both K_2MoO_4 and Rb_2MoO_4 . Acquisition parameters for the experimental spectra are given in *Appendix 5.2*.

Table 5.3: Anisotropic Mo Shielding Parameters and Euler Angles for A(I) and A(II) Molybdate Salts.

| A(I) or A(II) | Ω / ppm | κ | $\alpha, \beta, \gamma / ^\circ$ |
|---------------|----------------|------------------|----------------------------------|
| Li | 125 ± 10 | $+0.30 \pm 0.1$ | $8 \pm 3, 30 \pm 5, 43 \pm 5$ |
| K | 82 ± 5 | $+0.66 \pm 0.05$ | $90, 5 \pm 2, 0$ |
| Rb | 72 ± 10 | $+0.50 \pm 0.05$ | $90, 7 \pm 2, 0$ |
| Cs | 30 ± 3 | -0.50 ± 0.1 | $0, 90, 0$ |
| Ca | 88 ± 5 | -1.00 | $0, 90, 0$ |
| Sr | 63 ± 10 | -1.0 ± 0.1 | $0, 90, 0$ |
| Cd | 95 ± 10 | -1.0 ± 0.1 | $0, 90, 0$ |
| Ba | 55 ± 10 | -1.0 ± 0.25 | $0, 90, 9 \pm 2$ |
| Pb | 58 ± 5 | -1.00 | $0, 90, 0$ |

quadrupolar interaction. This is not surprising, given the small ^{95}Mo quadrupole moment, which effectively reduces the importance of the Mo quadrupolar interaction while strengthening the Mo shielding interaction.

The Mo shielding tensors of the K and Rb molybdate salts deviate significantly from axial symmetry for the two salts, as previously observed for their respective EFG tensors and consistent with X-ray data. In addition, the magnitude and orientation of the Mo shielding tensor ($\kappa > 0$) are similar for the two salts. Also significant is the relative orientation of the Mo EFG and shielding tensors, shown in the inset of Figure 5.3, which indicates that V_{YY} and σ_{11} are collinear and perpendicular to the mirror plane, while V_{XX} and σ_{22} and V_{ZZ} and σ_{33} lie in the mirror plane, but each pair deviates slightly (less than 10°) from coincidence. These orientations were obtained using a trial-and-error approach of manually iterating the Euler angles in the simulations, while satisfying the restrictions imposed by the crystal symmetry; *i.e.*, the crystal symmetry requirements are fulfilled since $\alpha = 90^\circ$, whereas β and γ were determined by visual inspection of the simulated spectra. That our ^{95}Mo NMR spectra have been acquired at magnetic fields of moderate, 11.75 T, and high, 17.63 T, strength and for both MAS and stationary samples lends

confidence to the accuracy of the results for K_2MoO_4 and Rb_2MoO_4 . At the fields employed here, inclusion of the anisotropic Mo shielding interaction is essential.

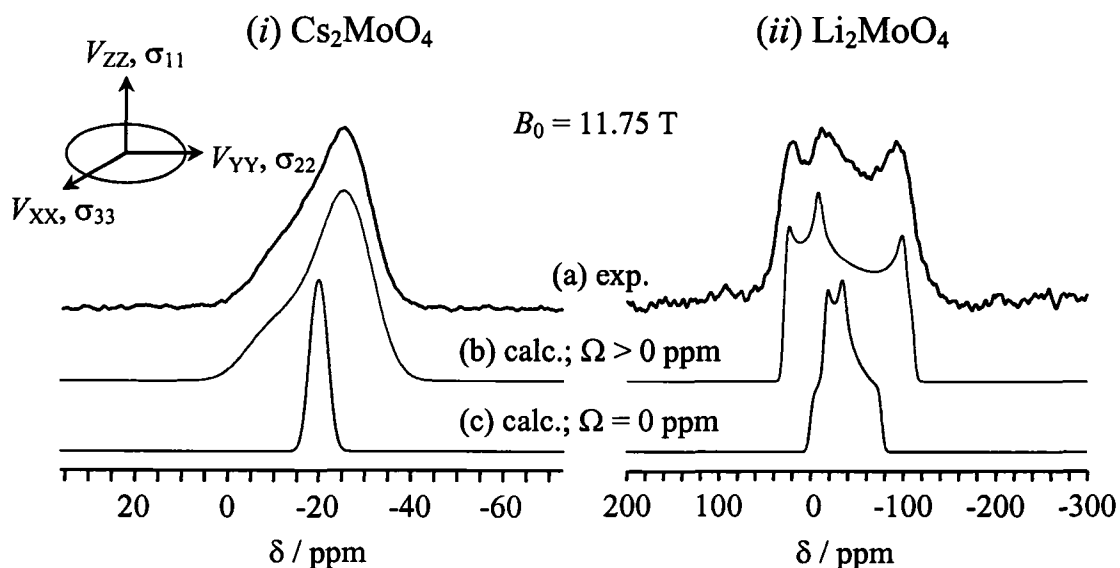


Figure 5.4: Experimental (a) and simulated (b, c) ^{95}Mo NMR spectra of stationary samples of (i) Cs_2MoO_4 (left) and (ii) Li_2MoO_4 (right) acquired using a one-pulse experiment at 11.75 T. The inset shows the relative orientation of the principal components of the Mo shielding and EFG tensors for Cs_2MoO_4 , corresponding to $\alpha, \beta, \gamma = 0, 90, 0^\circ$. The parameters for the best-fit calculated spectra for Cs_2MoO_4 and Li_2MoO_4 , shown in (b), are given in Tables 5.2 and 5.3; the simulated spectra shown in (c) neglect anisotropic Mo shielding. Acquisition parameters are given in *Appendix 5.2*.

Shown in Figure 5.4 are solid-state ^{95}Mo NMR spectra of Cs_2MoO_4 (left) and Li_2MoO_4 (right) acquired at a single magnetic field, 11.75 T; the best-fit calculated parameters are given in Tables 5.2 and 5.3. The ^{95}Mo EFG and shielding interactions for Cs_2MoO_4 are small compared to those found for K_2MoO_4 and Rb_2MoO_4 , due to the near ideal tetrahedral symmetry of the MoO_4^{2-} anion in the Cs salt;²⁵⁵ nevertheless, the Mo shielding anisotropy, $\Omega = 30 \pm 3$ ppm, makes a substantial contribution to the observed ^{95}Mo NMR lineshape (Figure 5.4 (b) and (c)), resulting in a broad, asymmetric peak. Both the Mo shielding and EFG tensors deviate considerably from axial symmetry, owing to the absence of a principal C_3 -axis in the MoO_4^{2-} anion.

Despite the shared feature of a mirror plane for the three alkali metal molybdates, $\text{A(I)} = \text{K, Rb, Cs}$, the overall orientation of the Mo shielding tensors and the Euler angles

for Cs_2MoO_4 are different from those for K_2MoO_4 and Rb_2MoO_4 . The best-fit simulated spectrum for Cs_2MoO_4 indicates that $\kappa < 0$, whereas $\kappa > 0$ for K_2MoO_4 and Rb_2MoO_4 ; in addition, the Euler angles for Cs_2MoO_4 , $\alpha, \beta, \gamma = 0, 90, 0^\circ$, indicate that V_{YY} and σ_{22} are co-linear and perpendicular to the mirror plane, while the remaining pairs, V_{XX} and σ_{33} and V_{ZZ} and σ_{11} , are collinear and lie in the plane of the mirror (see inset of Figure 5.4); this orientation differs from that previously obtained for K and Rb molybdate (see inset of Figure 5.3).

The ^{95}Mo NMR spectrum of Li_2MoO_4 , shown on the right in Figure 5.4, has an unusual and distinct lineshape that arises from the reduced point symmetry at Mo. In the rhombohedral $R\bar{3}$ space group, there are no symmetry elements for Mo, besides the identity operator (Table 5.1); hence, no restrictions are placed on the relative orientations of the Mo EFG and shielding tensors. Using the δ_{iso} , C_Q , and η_Q values previously determined from MAS data (Figure 5.1, Table 5.2) has enabled the remaining parameters to be determined upon manual iteration and visual comparison of the experimental and simulated spectra. The best-fit parameters, given in Table 5.3, indicate non-coincident Mo shielding and EFG tensors. In addition, the measured Mo shielding tensor deviates from axial symmetry and has a considerable anisotropy, 125 ppm, compared to those previously observed for the A(I) and A(II) molybdate salts. Together the anisotropic Mo shielding tensor and Euler angles have a strong influence on the observed ^{95}Mo NMR lineshape, as evidenced by inspection of the simulated spectra calculated with and without contributions from Ω , shown in Figure 5.4 (b) and (c), respectively. The accuracy of the results obtained from analyses of MAS and stationary samples of Li_2MoO_4 at 11.75 T would greatly improve by conducting similar experiments at a second, preferably higher, magnetic field.

Experimental and best-fit calculated ^{95}Mo NMR spectra of stationary samples of the isostructural A(II) = Ca, Sr, Cd, Ba, Pb molybdates are presented in Figure 5.5; ^{95}Mo NMR spectra for BaMoO_4 and SrMoO_4 have been acquired at two magnetic fields, 11.75 T and 17.63 T, while those for CaMoO_4 , PbMoO_4 , and CdMoO_4 have been acquired at a single magnetic field, 11.75 T. The point symmetry of Mo in the $I4_1/a$ space group is a four-fold inversion axis, S_4 , which necessitates axially-symmetric Mo EFG ($\eta_Q = 0$) and shielding ($\kappa = \pm 1.0$) tensors. The isotropic Mo chemical shifts and quadrupolar

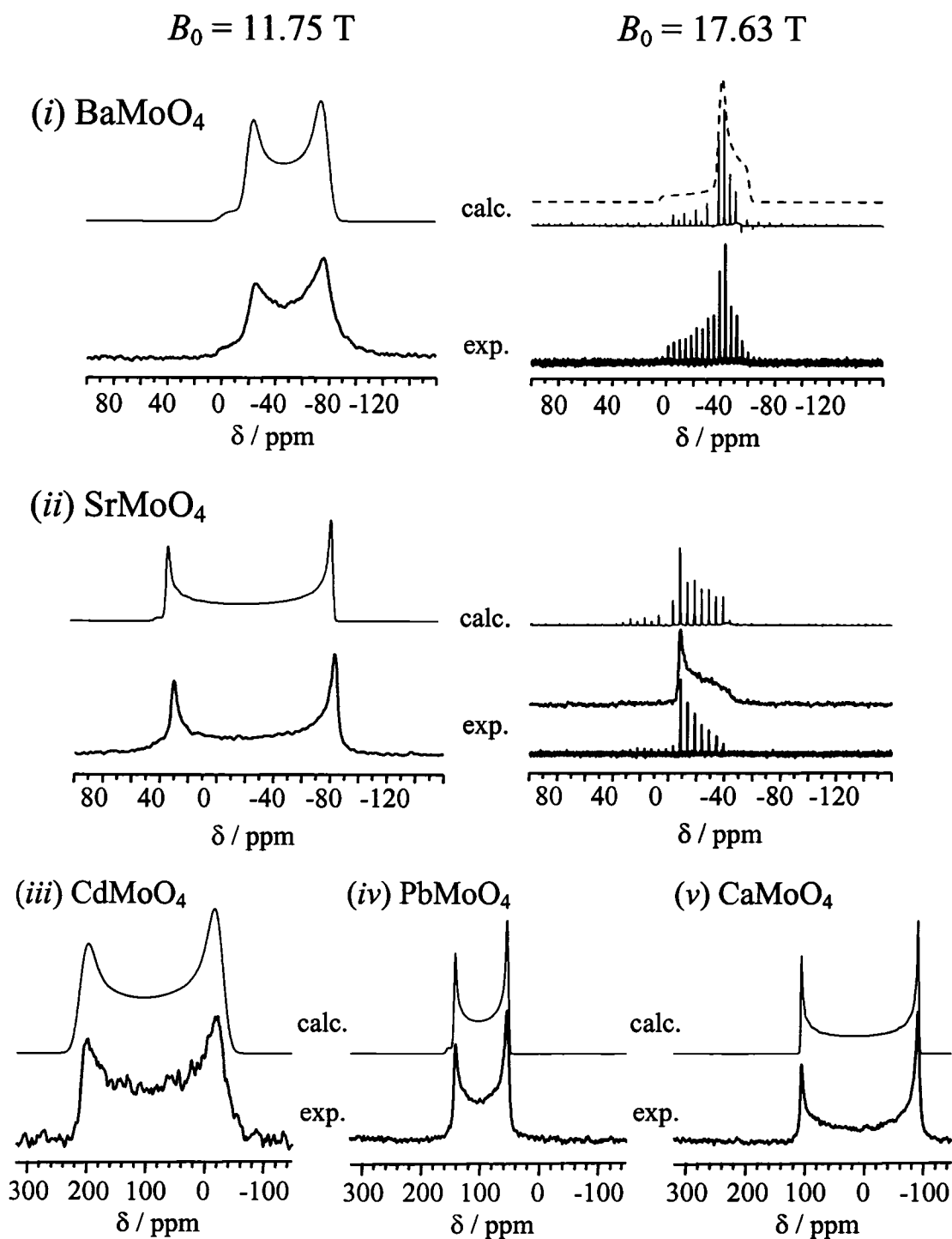


Figure 5.5: Simulated (top) and experimental (bottom) solid-state ^{95}Mo NMR spectra of stationary samples of (i) BaMoO_4 and (ii) SrMoO_4 , acquired at 11.75 T (left) and 17.63 T (right), and (iii) CdMoO_4 , (iv) PbMoO_4 , and (v) CaMoO_4 , acquired at 11.75 T. The parameters used to calculate the best-fit simulated spectra (top) are given in Tables 5.2 and 5.3. Acquisition parameters for the experimental spectra are given in *Appendix 5.2*.

parameters were previously determined herein for Ba, Sr, and Cd molybdate (Table 5.2; Figure 5.2); however, those for Ca and Pb molybdate were not obtained since ^{95}Mo NMR spectra of MAS samples were not acquired. Nevertheless, δ_{iso} , C_Q and η_Q values have been determined for Ca and Pb molybdate by d'Espinose de Lacaillerie *et al.*²⁵¹ at 19.6 T; these values served as the starting parameters in our analyses. Unfortunately, the authors did not consider the crystal symmetry of Ca and Pb molybdate and concluded that the Mo EFG tensors were non-axially symmetric, with $\eta_Q = 0.1$, which is not permitted for the $I4_1/a$ space group. Our Mo quadrupolar parameters for Ca and Pb molybdate obey the crystal symmetry ($\eta_Q = 0.0$) and are in close agreement with those previously determined (Table 5.2).

To highlight the characteristic ^{95}Mo NMR lineshapes of the isostructural A(II) molybdates as well as differences in their breadths, their experimental ^{95}Mo NMR spectra are plotted in Figure 5.6. The sense of the Mo shielding tensor is identical for the A(II) molybdates with σ_{11} being the unique component and $\sigma_{22} = \sigma_{33}$, *i.e.*, $\kappa = -1.0$. Variations in the breadths of the ^{95}Mo NMR lineshapes arise from the different magnitudes of the Mo EFG and anisotropic Mo shielding interaction. For BaMoO_4 , PbMoO_4 , SrMoO_4 , CaMoO_4 , and CdMoO_4 , the magnitude of the observed $C_Q(^{95}\text{Mo})$ values (Table 5.2) increases steadily, and a similar trend is observed for their respective shielding anisotropies. Inspection of Tables 5.1 and 5.2 suggests that the increase in $C_Q(^{95}\text{Mo})$ is a direct consequence of the increasing distortion of the molybdate anion from T_d symmetry; *i.e.*, σ^2 . As σ^2 increases, $C_Q(^{95}\text{Mo})$ consistently increases for the A(II) molybdates; in fact, for Ca, Sr, Ba, and Pb molybdate, this relationship is nearly linear with $R^2 = 0.98$. That the calculated σ^2 value for CdMoO_4 well-exceeds any other A(II) molybdate may be attributed to poor structural data obtained from an X-ray powder diffraction study; the structures of the remaining molybdates, A(II) = Ca, Sr, Ba, and Pb, are believed to be more accurate.

The results for the A(II) molybdates further stress the significance of the anisotropic Mo shielding interaction on the ^{95}Mo NMR spectra of the A(II) molybdates; in fact, inclusion of anisotropic Mo shielding in the calculated spectra actually reduces the breadth of the observed ^{95}Mo NMR lineshapes relative to those calculated with the quadrupolar interaction alone, as illustrated in Figure 5.7. This narrowing is a

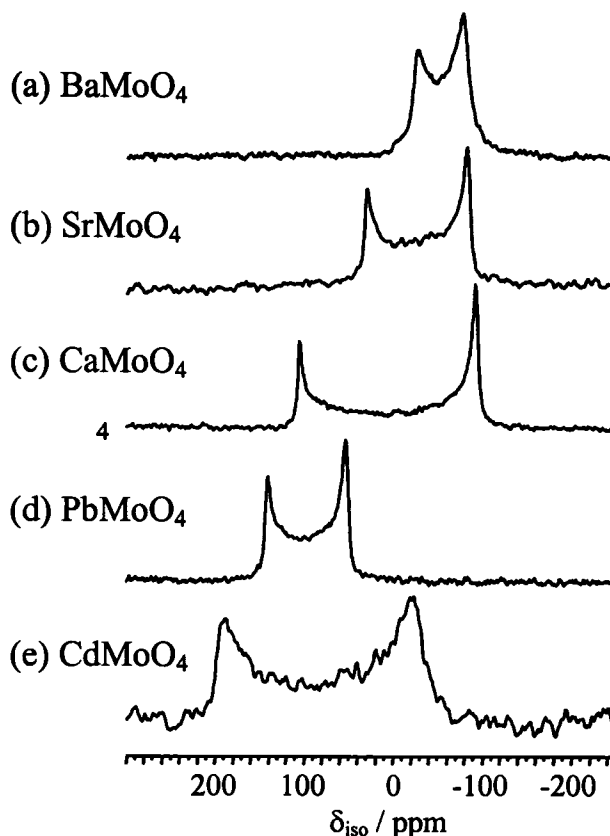


Figure 5.6: Experimental ^{95}Mo NMR spectra of isomorphous (a-e) Ba, Sr, Ca, Pb, and Cd molybdate acquired using a one-pulse experiment at 11.75 T. See Figure 5.5 for simulated spectra and Tables 5.2 and 5.3 for best-fit parameters.

consequence of the orientation of the Mo shielding tensor ($\kappa = -1.0$), as well as its orientation relative to the Mo EFG tensor. For the A(II) molybdates, the presence of an S_4 -axis and mirror plane restricts the orientation of the Mo EFG and shielding tensors: one principal component of each of the Mo EFG and shielding tensors must be parallel to S_4 and the presence of a crystallographic mirror plane requires one pair of components to be perpendicular to the mirror plane. From our simulations, the relative orientation of the Mo EFG and shielding tensors, shown in Figure 5.7, is identical for Ca, Sr, Cd, and Pb molybdate, with $\alpha, \beta, \gamma = 0, 90, 0^\circ$; hence, the unique component of the EFG, V_{ZZ} , and shielding tensor, σ_{11} , are parallel to S_4 , while V_{YY} and σ_{22} and V_{XX} and σ_{33} are perpendicular to S_4 . A slightly different orientation is found for BaMoO_4 , with $\alpha, \beta, \gamma = 0, 90, 9 \pm 2^\circ$; resulting in a minor deviation of V_{YY} and σ_{22} and V_{XX} and σ_{33} from coincidence.

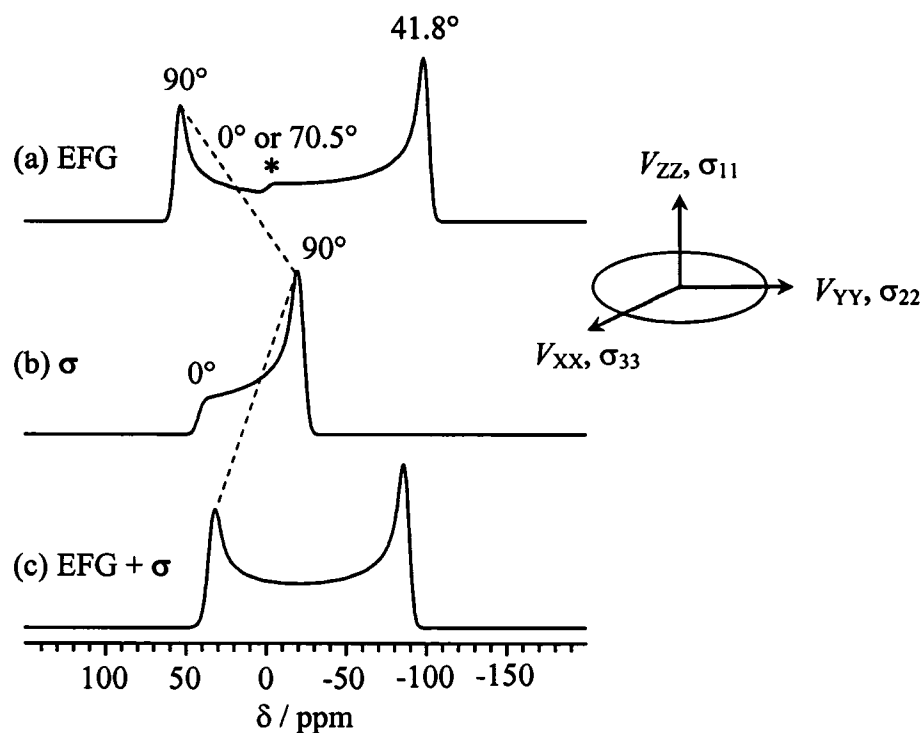


Figure 5.7: Simulated ^{95}Mo NMR spectra of SrMoO_4 showing the individual (a) EFG and (b) shielding interactions and (c) the sum of their contributions at $B_0 = 11.75$ T. The relative orientation of the principal components of the Mo EFG and shielding tensors is shown on the right for $\alpha, \beta, \gamma = 0, 90, 0^\circ$.

5.2.2.4. Assessing the Feasibility of Solid-State ^{95}Mo NMR Studies

The results presented herein on A(I) and A(II) molybdates demonstrate the feasibility and practicality of solid-state ^{95}Mo NMR studies. High-quality ^{95}Mo NMR spectra have been obtained in reasonable times for a variety of molybdate samples. Experiments on MAS samples required times ranging from 6 hours to 43 hours, while experiments on stationary samples ranged from 3 minutes, using the QCPMG experiment, to 22 hours using a spin-echo experiment; the QCPMG experiment drastically reduced experiment times, while allowing the Mo shielding and EFG tensors to be fully characterized. One drawback to solid-state ^{95}Mo NMR studies is the long $T_1(^{95}\text{Mo})$ values, which are believed to be on the order of minutes for some molybdates; this hampered our ^{95}Mo NMR study of stationary samples of Bi_2MoO_6 and resulted in very little signal after many hours.

5.2.3. Conclusions

Solid-state ^{95}Mo NMR results for a series of A(I) and A(II) molybdate salts have enabled full characterization of the Mo EFG and shielding interactions. For all samples studied here, the Mo EFG tensor is sufficiently small to resolve the central transition ^{95}Mo NMR signal with the use of MAS at spinning rates of 3.0 or 6.0 kHz; this is largely due to the small ^{95}Mo quadrupole moment which results in relatively narrow ^{95}Mo NMR quadrupolar lineshapes for MAS samples. When possible, we have compared our ^{95}Mo quadrupolar parameters with those available in the literature and have found that our results are superior or comparable to existing data. Most importantly, while previous studies do not consider the effects from the anisotropic Mo shielding interaction, we have characterized the anisotropic Mo shielding tensors as well as the relative orientation of the Mo EFG and shielding tensors. Through the use of experimental data on both MAS and stationary samples of selected A(I) and A(II) molybdate salts, we have found that the anisotropic Mo shielding interaction makes a comparable contribution to the observed ^{95}Mo NMR lineshape as the Mo quadrupolar interaction at the fields employed here, resulting in an interesting array of ^{95}Mo NMR lineshapes. The importance of the anisotropic Mo shielding interaction is effectively increased due to the small ^{95}Mo quadrupole moment.

The A(II) cations appear to induce greater structural distortions in the MoO_4^{2-} anion (Table 5.1), which are reflected in the Mo EFG and shielding tensors. The measured $C_Q(^{95}\text{Mo})$ and anisotropic Mo shielding values for the A(II) molybdates are notably larger than the analogous A(I) molybdates. In fact, the extent of distortion from T_d symmetry was generally found to be reflected in the observed $C_Q(^{95}\text{Mo})$ values; anomalous cases may be attributed to inaccurate structural data and, therefore, inaccurate σ^2 values.

The success of our ^{95}Mo NMR study on the A(I) and A(II) molybdate salts encouraged the study of an interesting eight-coordinate Mo(IV) anion, $\text{Mo}(\text{CN})_8^{4-}$, by solid-state ^{95}Mo NMR and computational chemistry. In this study, approximate dodecahedral, D_{2d} , and approximate square antiprismatic, D_{4d} , forms of $\text{Mo}(\text{CN})_8^{4-}$ have been examined and the Mo shielding and quadrupolar interactions, as well as their relative orientations, have been characterized. In theory, these two forms should be

readily distinguishable using solid-state ^{95}Mo NMR since, based on the simple point-charge approximation (*Section 2.5.3.*), the former is predicted to have a non-zero EFG at Mo, while the EFG for the latter is predicted to be zero. Through a dual experimental and computational investigation, this study demonstrates the breakdown of the PCA for the specific case of ideal square antiprismatic symmetry. These results have been published²⁵⁰ as a full article entitled, "*A Solid-State ^{95}Mo NMR and Computational Investigation of Dodecahedral and Square Antiprismatic Octacyanomolybdate(IV) Anions: Is the Point-Charge Approximation an Accurate Probe of Local Symmetry?*" by Michelle A. M. Forgeron and Roderick E. Wasylishen in the *Journal of the American Chemical Society* and will be presented here in a slightly modified version.

5.3. Solid-State ^{95}Mo NMR Study of Octacyanomolybdate(IV) Anions

5.3.1. Introduction

Interest in transition metal cyanides dates back to the early 1700s with the discovery of Prussian Blue.²⁶² In recent years, interest in cyanometalates has been revived, in part, due to the utility of these anions as the building blocks of magnetic clusters and networks.^{263,264,265,266,267} The classic textbook²³⁷ examples of eight-coordination transition metal cyanides are the molybdenum and tungsten octacyanide anions,^{199,268} which have been known for nearly 100 years.²⁶⁹ These anions exist in both diamagnetic and paramagnetic forms, where the metal is in a formal oxidation state of +4 or +5, respectively.^{237,262,270} Of particular interest is the ability of the (Mo,W) octacyanide anions to adopt different molecular arrangements which may be approximately²⁷¹ described by the polyhedra illustrated in Figure 5.8. In the solid state, the diamagnetic Mo(IV) analogue, $[\text{Kr}]4d^2$, exhibits structures with approximate dodecahedral, D_{2d} , symmetry, as in $\text{K}_4\text{Mo}(\text{CN})_8 \cdot 2\text{H}_2\text{O}$,^{272,273,274} and square antiprismatic, D_{4d} , symmetry, as in $\text{Tl}_4\text{Mo}(\text{CN})_8$.²⁷⁵ Recent *ab initio* CASPT2 calculations indicate that the ground-state energies of these isolated polytopes differ by approximately 4 kcal mol⁻¹,²⁷⁶ with the D_{4d} form being the more stable of the two, and both being considerably lower than the cubic form.²⁷⁷ In solution, the preferred stereochemical arrangement of cyanide ligands is an issue of debate. To this end, uv-vis²⁷⁸ Raman,^{279,280,281,282} infrared,^{280,281,282,283} and NMR^{284,285,286,287} spectroscopic, as well as a variety of

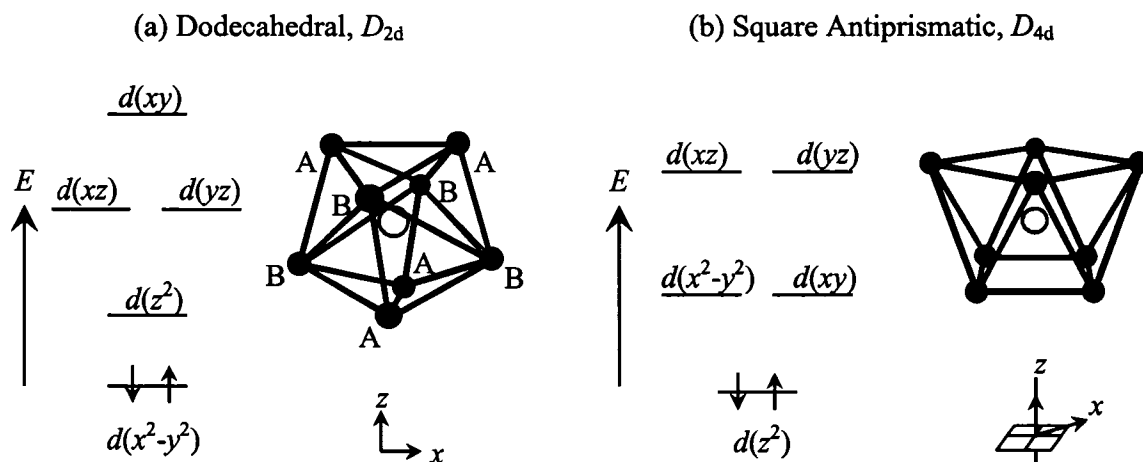


Figure 5.8: Idealized structural forms of the dodecahedral (a) and square antiprismatic (b) diamagnetic $\text{Mo}(\text{CN})_8^{4-}$ anions.²⁸⁸ For dodecahedral symmetry, the two types of cyanide ligands are labeled A and B, and for square antiprismatic symmetry, all cyanide ligands are equivalent due to the molecular symmetry. Partial electronic energy level diagrams for the $\text{Mo}(\text{CN})_8^{4-}$ anions possessing ideal D_{2d} and D_{4d} symmetry are also shown. The ordering of molecular orbitals (MOs) corresponds to the orientation of the $\text{Mo}(\text{CN})_8^{4-}$ anions in the indicated coordinate system and the MO labels specify the dominant atomic orbital contributions localized on Mo.

theoretical,^{276,289,290} studies have been carried out to investigate the structure of $\text{Mo}(\text{CN})_8^{4-}$ in solution. In addition, studies involving the electronic structure,^{276,291,292} electron-transfer reactions,²⁹³ electrochemistry,²⁹⁴ and photomagnetic^{295,296,297} properties of octacyanomolybdate, as well as applications towards molecular magnets,^{263,298} continue to appear in the current literature.

Previous solution NMR studies consist of an early ^{13}C NMR study²⁸⁴ of ^{13}C -enriched $\text{K}_4\text{Mo}(\text{CN})_8 \cdot 2\text{H}_2\text{O}$ in aqueous solution and a variable-temperature ^{13}C NMR study²⁸⁵ of $[\text{N}(n\text{-C}_3\text{H}_7)_4]_4\text{Mo}(\text{CN})_8$ in a 90:10 $\text{CHClF}_2\text{-CH}_2\text{Cl}_2$ mixture. In the former study, a single carbon resonance was observed and the authors addressed three possible explanations with the only realistic one being either the D_{4d} structure or D_{2d} with rapid intramolecular exchange of cyanide ligands.²⁸⁴ The latter study²⁸⁵ suggests a D_{2d} structure with rapid internal rearrangement of the two types of CN^- ligands via the concerted Hoard-Silverton pathway, facilitated by a low energy barrier. Subsequent ^{95}Mo NMR studies^{286,287} of $\text{K}_4\text{Mo}(\text{CN})_8 \cdot 2\text{H}_2\text{O}$ in aqueous solutions concluded that the anion must possess D_{2d} symmetry since, based on the point-charge approximation, the observed ^{95}Mo linewidths of approximately 75 Hz are too large for compounds of cubic

or square antiprismatic symmetry, where the EFG was expected to be zero. Similar conclusions were derived from ^{14}N and ^{95}Mo spin-lattice relaxation data, which indicated an effective ^{95}Mo quadrupolar coupling constant, C_Q , of approximately 3.6 MHz in aqueous solution.²⁸⁷ A recent theoretical investigation seems to have ended the dispute on the symmetry of the anion in solution by concluding that a dynamic equilibrium between the D_{2d} and D_{4d} configurations must occur to account for all experimental bands in the electronic spectrum,²⁷⁶ the interconversion between the two forms is facilitated by the small relative displacement of cyanide ligands ($\sim 15^\circ$).²⁹⁹

The most thoroughly studied octacyanomolybdate is the K salt, $\text{K}_4\text{Mo}(\text{CN})_8 \cdot 2\text{H}_2\text{O}$. Investigations of this compound in the solid state consist of ^{14}N NQR^{300,301} and several single-crystal X-ray diffraction studies,^{272,273,274} these studies indicate that there are six distinct cyanide ligands. No solid-state NMR studies of $\text{K}_4\text{Mo}(\text{CN})_8 \cdot 2\text{H}_2\text{O}$ or any other octacyanomolybdate salt have been reported; however, the benefits of employing solid-state NMR are numerous. First, based on X-ray diffraction results,^{272,273,274,275} the problems of molecular dynamics or interconversion between more than one symmetry form is not an issue in the solid state since the molecular structure is rigid, apart from molecular librations.^{272,273,274} Second, solid-state NMR spectroscopy is ideally suited, in particular, of the Mo nucleus, because of the acute sensitivity of the Mo σ and EFG tensors, to subtle changes in the local environment about Mo. Hence, undertaking separate studies of the approximate D_{2d} and D_{4d} symmetry forms of the $\text{Mo}(\text{CN})_8^{4-}$ anion will allow proper characterization and a thorough understanding of their NMR parameters in the solid state, which may ultimately provide insight into results obtained in solution.

In the present study, diamagnetic octacyanomolybdate(IV) salts with approximate D_{2d} symmetry, $\text{K}_4\text{Mo}(\text{CN})_8 \cdot 2\text{H}_2\text{O}$, and approximate D_{4d} symmetry, $\text{Ti}_4\text{Mo}(\text{CN})_8$, have been examined using solid-state ^{95}Mo NMR spectroscopy at moderate (11.75 T) and high (17.63, 21.1 T) applied magnetic field strengths using the double-frequency sweep (DFS)³⁰² in combination with the quadrupolar Carr-Purcell Meiboom-Gill (QCPMG)⁸⁹ experiment or simply the QCPMG experiment, and by computational means, employing ZORA DFT and RHF methods.

The NMR interactions of importance for ^{95}Mo in the octacyanomolybdate(IV) anions, under conditions where $\hat{H}_z \gg \hat{H}_Q$, are the quadrupolar, \hat{H}_Q , and magnetic shielding (chemical shift), \hat{H}_s , interactions, which are described in detail in *Sections 2.4* and *2.5*. Recall from *Section 2.5.3* that the PCA can be used to estimate the EFG at a nucleus and that molecules possessing tetrahedral, cubic, or square antiprismatic symmetry have a zero EFG at their centre. It is important to stress that the square antiprism is a special case of D_{4d} symmetry; any deviation of θ_i (Equation 2.27) from the magic angle will result in a structure which, although it may retain D_{4d} symmetry, no longer sustains the essential square antiprismatic symmetry that results in a zero EFG at Mo, according to the PCA. Experimentally, however, structural deviations from ideal symmetry, whether square antiprismatic, tetrahedral, or octahedral, are inevitable, resulting in small, measurable EFGs, *i.e.*, C_Q s. This has been demonstrated in the previous *Section* for a series of molybdate salts whose observed $C_Q(^{95}\text{Mo})$ values vary from 0.34 MHz to 3.08 MHz, depending on the extent of distortion from T_d symmetry.^{247,251} Nonetheless, based on the PCA, the $\text{Mo}(\text{CN})_8^{4-}$ anions possessing approximate dodecahedral and square antiprismatic symmetry should result in ^{95}Mo NMR spectra that are significantly different, allowing the two structures to be easily distinguished.

5.3.2. Experimental and Computational Details

5.3.2.1. Solid-State ^{95}Mo NMR Spectroscopy

Samples of $\text{K}_4\text{Mo}(\text{CN})_8 \cdot 2\text{H}_2\text{O}$ were either purchased from Aldrich and used without further purification or synthesized³⁰³ according to literature procedures; $\text{Ti}_4\text{Mo}(\text{CN})_8$ was synthesized according to a literature procedure.²⁷⁵ The samples were powdered and packed into 5.0 mm glass NMR tubes or 7.0 mm o.d. ZrO_2 rotors. Solid-state ^{95}Mo NMR experiments were performed on Bruker Avance (11.75 T) and Varian Inova (17.63 and 21.1 T) spectrometers, operating at spectral frequencies of 32.55, 48.68, and 58.57 MHz, respectively, and using double-resonance MAS probes. The accepted Mo chemical shift reference,³⁷ a 2.0 M aqueous solution of $\text{Na}_2\text{MoO}_4 \cdot 2\text{H}_2\text{O}$ ($\delta_{\text{iso}} = 0$ ppm), was used for referencing and pulse width calibration. Employing a

standard one-pulse experiment, typical solution $\pi/2$ pulse widths of 6.0 – 10.3 μs were obtained. The QCPMG pulse sequence, $(\pi/2)_x-\tau_1-\pi_y-\tau_2-(\tau_a/2)-[\tau_3-\pi_y-\tau_4-\tau_a]_M-\tau_d$, was used to acquire ^{95}Mo NMR spectra of $\text{K}_4\text{Mo}(\text{CN})_8 \cdot 2\text{H}_2\text{O}$ at 11.75 and 17.63 T and $\text{Tl}_4\text{Mo}(\text{CN})_8$ at 11.75 T, while the combined DFS/QCPMG experiment was used to collect ^{95}Mo NMR spectra of $\text{Tl}_4\text{Mo}(\text{CN})_8$ at 21.1 T. Spectral sweep widths of 100 kHz were employed at 11.75 T, 500 kHz at 17.63 T, and 1.0 MHz at 21.1 T. Acquisition times of 25 – 65 ms, solid selective $\pi/2$ pulse widths, $[(\text{solution } \pi/2)/(I + 1/2)]$, of 2.0 – 3.4 μs , pulse delays of 8 – 10 s and pulse train repetitions, M , of 32 – 48 were used. High-power ^1H decoupling was used for $\text{K}_4\text{Mo}(\text{CN})_8 \cdot 2\text{H}_2\text{O}$ at 11.75 T. The spin-echo delays, τ_1 , τ_2 , τ_3 , and τ_4 , varied between 80 μs and 110 μs and are used to minimize effects from probe ringing. The spikelet spacing, ν_{QCPMG} , equal to τ_a^{-1} , where τ_a is the acquisition time for a complete echo, was 500 Hz for the K salt at 17.63 T, 500 Hz for the Tl salt at 21.1 T, and 1940 Hz for the K and Tl salts at 11.75 T. For ^{95}Mo NMR spectra of $\text{Tl}_4\text{Mo}(\text{CN})_8$ acquired at 21.1 T using the DFS/QCPMG pulse sequence, the DFS pulse was 1.0 ms with low and high offsets of 1.0 MHz and 100 kHz, respectively.

Attempts at acquiring ^{95}Mo QCPMG NMR spectra of magic-angle spinning (MAS) samples of $\text{K}_4\text{Mo}(\text{CN})_8 \cdot 2\text{H}_2\text{O}$ and $\text{Tl}_4\text{Mo}(\text{CN})_8$ at 11.75 T were unsuccessful due to insufficient rotor spinning speeds for 7.0 mm rotors.

Solid-state ^{13}C NMR spectra of $\text{K}_4\text{Mo}(\text{CN})_8 \cdot 2\text{H}_2\text{O}$ and $\text{Tl}_4\text{Mo}(\text{CN})_8$ were collected on a Bruker Avance 500 ($B_0 = 11.75$ T; $\nu_L(^{13}\text{C}) = 125.8$ MHz) spectrometer; high-power ^1H decoupling was used for the K salt. Samples of solid $\text{K}_4\text{Mo}(\text{CN})_8 \cdot 2\text{H}_2\text{O}$ and $\text{Tl}_4\text{Mo}(\text{CN})_8$ were powdered and packed into 7.5 mm and 4.0 mm o.d. ZrO_2 rotors, respectively. Due to the anticipated long ^{13}C spin-lattice relaxation times for solid $\text{K}_4\text{Mo}(\text{CN})_8 \cdot 2\text{H}_2\text{O}$ and $\text{Tl}_4\text{Mo}(\text{CN})_8$, 45° flip angles corresponding to pulse widths of 2.75 and 3.00 μs , respectively, and unoptimized pulse delays of 600 s were used to avoid saturation of the magnetization. Sweep widths of 100 kHz and spinning frequencies of 6.8 kHz and 12.0 kHz were used for the K and Tl salts, respectively.

Simulations of ^{95}Mo and ^{13}C NMR spectra of $\text{K}_4\text{Mo}(\text{CN})_8 \cdot 2\text{H}_2\text{O}$ and $\text{Tl}_4\text{Mo}(\text{CN})_8$ were carried out using SIMPSON¹⁰² or WSOLIDS.¹⁰¹

5.3.2.2 Quantum Chemical Calculations

Non-relativistic and spin-orbit relativistic ZORA DFT¹⁰⁴ calculations of molybdenum and carbon magnetic shielding and molybdenum EFG tensors for isolated octacyanomolybdate(IV) anions possessing D_{2d} and D_{4d} symmetry were performed using the NMR module¹⁰⁷ of the ADF program.^{105,106} The QZ4P or DZ Slater-type ZORA basis sets, available with the ADF program, were employed for Mo, C, and N.

ZORA DFT calculations of EFG¹⁰⁹ and magnetic shielding tensors were performed on the isolated $\text{Mo}(\text{CN})_8^{4-}$ anion using experimental structures determined from single-crystal X-ray diffraction studies^{272,273,274,275} (C_s symmetry for the K salt and C_1 symmetry for the Tl salt); as well, analogous calculations on idealized structures of $\text{Mo}(\text{CN})_8^{4-}$ possessing D_{2d} and square antiprismatic symmetry were carried out. The molecular coordinates used for the idealized $\text{Mo}(\text{CN})_8^{4-}$ anions are included in *Appendix 5.3*. In addition, a calculation carried out at the non-relativistic level employing ZORA DZ basis sets, was performed on $\text{Tl}_4\text{Mo}(\text{CN})_8$ by including the first coordination sphere of four Tl cations, *i.e.*, within a distance of 4.85 Å from Mo, to test the effects of inclusion of the Tl cations on the Mo EFG and magnetic shielding tensors. Further Mo EFG and magnetic shielding tensor calculations were carried out on isolated molybdenum-containing anions and compounds possessing T_d or O_h symmetry: MoO_4^{2-} ,³⁰⁴ MoS_4^{2-} ,³⁰⁵ MoSe_4^{2-} ,³⁰⁶ and $\text{Mo}(\text{CO})_6$,³⁰⁷ to establish the accuracy of the calculated molybdenum magnetic shielding (chemical shift) scale and to compare EFGs calculated using quantum chemistry computations with those determined using the PCA. Lastly, non-relativistic ZORA DFT calculations of the Mo EFG tensors were carried out on a series of isolated, idealized anions possessing D_{4d} symmetry, as well as various rotamers of $\text{Mo}(\text{CN})_8^{4-}$, including O_h symmetry. The hypothetical $\text{Mo}(\text{CN})_8^{4-}$ anion possessing O_h symmetry, *i.e.*, a cube, was generated from that possessing D_{4d} symmetry by rotating the upper portion of the square antiprism with respect to the bottom portion by 45 degrees. A total of nine rotamers were subsequently generated by rotating the upper portion of the O_h structure in increments of 5° until the square antiprismatic structure was restored (D_{4d} symmetry retained). The ZORA DZ basis sets were used for all atoms, except the calculation on the O_h rotamer, for which ZORA QZ4P basis sets were used due to convergence problems when using ZORA DZ basis sets.

Idealized structures were generated using the average bond lengths and bond angles from the crystal structures, while ensuring that the symmetry operations of the appropriate point groups (T_d , O_h , D_{2d} and D_{4d}) were obeyed. For D_{2d} symmetry, two types of CN⁻ ligands (A and B) were generated (Figure 5.8). For all calculations, the molecules were oriented with Mo at the origin and the principal molecular axes along the z-axis.

Calculated isotropic Mo magnetic shielding values were converted to calculated isotropic chemical shift values by first setting the calculated chemical shift value of Mo(CO)₆ to its accepted experimental value, $\delta(\text{ref})_{\text{iso,calc}} = -1860$ ppm, and subsequently converting the calculated $\sigma_{\text{iso,calc}}$ values for the remaining Mo compounds to $\delta_{\text{iso,calc}}$ using: $\delta(\text{sample})_{\text{iso,calc}} = \sigma(\text{ref})_{\text{iso,calc}} - \sigma(\text{sample})_{\text{iso,calc}} - 1860$ ppm.

To determine contributions from the paramagnetic shielding, σ^{para} , to the principal components of the Mo magnetic shielding tensor, non-relativistic ZORA DFT calculations were carried out using the EPR module³⁰⁸ of the ADF program. Calculations were performed on isolated, idealized, closed-shell D_{2d} and D_{4d} Mo(CN)₈⁴⁻ anions using DZ basis sets for all atoms.

Calculations of the Mo EFG tensor were repeated at the RHF level of theory using Parallel Quantum Solutions³⁰⁹ and MOLPRO³¹⁰. RHF calculations were carried out on the isolated D_{4d} Mo(CN)₈⁴⁻ anion as well as the aforementioned rotamers (O_h symmetry through to square antiprismatic D_{4d} symmetry in 5° increments). In all RHF calculations, the minimal 3-21G basis set was employed for Mo due to a limited basis set selection. Nuclear quadrupolar coupling constants were subsequently calculated (in frequency units) using $C_Q = eQV_{ZZ}/h$. Conversion of V_{ZZ} from atomic units to V m⁻² was carried out using the factor, 9.71736×10^{21} V m⁻² per atomic unit.¹⁶⁹

Point-charge calculations of V_{ZZ} were carried out on models possessing T_d , O_h , and D_{4d} symmetry using Equation 2.27. The atomic charges for Mo, C, N, and O were taken from spin-orbit relativistic ZORA DFT calculations using QZ4P basis sets.

5.3.3. Results and Discussion

5.3.3.1 $K_4Mo(CN)_8 \cdot 2H_2O$: Approximate Dodecahedral Symmetry

Shown in Figure 5.9 are solid-state ^{95}Mo QCPMG NMR spectra of stationary, powdered samples of $K_4Mo(CN)_8 \cdot 2H_2O$ acquired at 11.75 and 17.63 T, along with their best-fit simulated spectra; the best-fit parameters are listed in Table 5.4. The separation between spikelets, ν_{QCPMG} , 1940 Hz and 500 Hz at 11.75 and 17.63 T, respectively, provides a well-defined ^{95}Mo NMR lineshape and adequate S/N. In addition, the relative breadths of the ^{95}Mo NMR spectra illustrate the benefits of employing higher magnetic fields due to the inverse scaling of the second-order quadrupolar interaction with B_0 . Assuming the quadrupolar interaction is the only important internal interaction, the breadth of the NMR lineshape for a quadrupolar nucleus acquired at 17.63 T is roughly

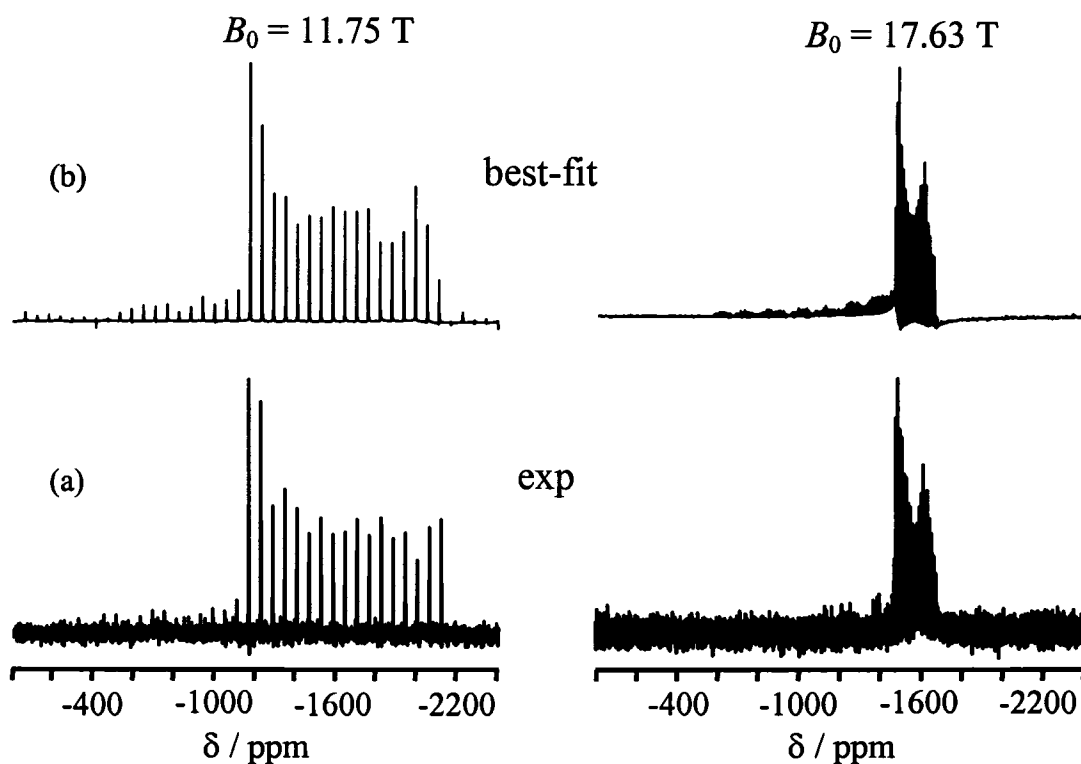


Figure 5.9: Experimental (a) and best-fit simulated (b) QCPMG ^{95}Mo central transition NMR spectra of a solid stationary sample of $K_4Mo(CN)_8 \cdot 2H_2O$ acquired at 11.75 T (left) and 17.63 T (right). The parameters used to calculate the simulated spectra are given in Table 5.4. A total of 24 682 and 4 480 transients were summed for spectra acquired at 11.75 T at 17.63 T, respectively.

1.5 times narrower in frequency units than that at 11.75 T. However, upon inspection of Figure 5.9, the observed breadth of the ^{95}Mo NMR spectrum of $\text{K}_4\text{Mo}(\text{CN})_8 \cdot 2\text{H}_2\text{O}$ acquired at 17.63 T (10.5 kHz) appears to be approximately one-fourth the breadth (one-third in Hz) of that at 11.75 T (32.5 kHz). The difference in the ratio must arise from the magnitude of the Mo magnetic shielding tensor and the relative orientation of the EFG and magnetic shielding tensors (*vide infra*).

To aid in interpreting the ^{95}Mo NMR spectra, it is useful to refer to X-ray diffraction data. $\text{K}_4\text{Mo}(\text{CN})_8 \cdot 2\text{H}_2\text{O}$ crystallizes in space group $Pnma$ and the anion is approximately described by D_{2d} symmetry. For ideal D_{2d} symmetry, there are two perpendicular mirror planes, resulting in two crystallographically distinct cyanide

Table 5.4: Experimental and Calculated Mo σ and EFG Parameters for $\text{K}_4\text{Mo}(\text{CN})_8 \cdot 2\text{H}_2\text{O}$.

| $\delta_{\text{iso}} / \text{ppm}^*$ | Ω / ppm | κ | C_Q / MHz | η_Q | $\alpha, \beta, \gamma / ^\circ$ |
|--|-----------------------|--------------------|--------------------|-------------------|----------------------------------|
| <i>Experimental: Solid-State ^{95}Mo NMR</i> | | | | | |
| -1322 ± 5 | 1160 ± 30 | -0.987 ± 0.013 | (-7.08 ± 0.05) | 0.065 ± 0.030 | $0 \pm 30, 90, 0$ |
| <i>Calculated:[†] Scalar + Spin-Orbit Relativistic</i> | | | | | |
| -1223^\ddagger | 971 | -0.996 | -7.08 | 0.027 | 88, 90, 0 |
| <i>Calculated:^{§§§§§§§§} Non-relativistic</i> | | | | | |
| -1186^\S | 1016 | -0.928 | -7.32 | 0.026 | 122, 90, 177 |
| <i>Calculated: Non-relativistic (Ideal D_{2d} $\text{Mo}(\text{CN})_8^{4-}$ anion)</i> | | | | | |
| -1212 | 993 | -1.00 | -7.47 | 0.00 | NA, ^{**} 90, 0 |

* Calculated isotropic chemical shifts were determined using $\delta(\text{ref})_{\text{iso,calc}} = -1860.0$ ppm for $\text{Mo}(\text{CO})_6$ and $\delta(\text{sample})_{\text{iso,calc}} - \delta(\text{ref})_{\text{iso,calc}} = \sigma(\text{ref})_{\text{iso,calc}} - \sigma(\text{sample})_{\text{iso,calc}}$.

[†] ZORA DFT calculations using QZ4P basis sets were performed on the isolated $\text{Mo}(\text{CN})_8^{4-}$ anion using coordinates as determined from single-crystal X-ray structure data.

[‡] Spin-orbit: for $\text{Mo}(\text{CO})_6$, $\sigma(\text{ref})_{\text{iso,calc}} = 1572.3$ ppm and $\delta(\text{ref})_{\text{iso,calc}} = -1860$ ppm.

[§] Non-relativistic: for $\text{Mo}(\text{CO})_6$, $\sigma(\text{ref})_{\text{iso,calc}} = 1229.4$ ppm and $\delta(\text{ref})_{\text{iso,calc}} = -1860$ ppm.

^{**} Due to the axial symmetry of the CS and EFG tensors, the calculated lineshape for the ^{95}Mo NMR spectrum is invariant to angle, α .

ligands, labeled A and B in Figure 5.8. In contrast, the experimental structure possesses a single mirror plane, in which Mo and four carbon atoms (two C_A and two C_B) lie, resulting in six crystallographically unique carbon atoms; hence, the actual point group symmetry of the experimental anion is C_s .²⁷³ Our ^{13}C NMR spectrum of an MAS sample of $\text{K}_4\text{Mo}(\text{CN})_8 \cdot 2\text{H}_2\text{O}$ (not shown) reveals six resolved ^{13}C signals, in agreement with both X-ray^{272,273,274} and ^{14}N NQR^{300,301} data. The small deviation from D_{2d} symmetry is apparent from the near axially-symmetric Mo EFG and magnetic shielding tensors (Table 5.4) and carbon magnetic shielding tensors.

Shown in Figure 5.10 are the individual contributions from the Mo magnetic shielding and EFG tensors to the ^{95}Mo NMR spectra of $\text{K}_4\text{Mo}(\text{CN})_8 \cdot 2\text{H}_2\text{O}$ determined from the best-fit experimental parameters in Table 5.4. At the fields employed here, the anisotropic Mo magnetic shielding makes approximately equal contributions to the ^{95}Mo central transition NMR spectra as the quadrupolar interaction — a common occurrence for heavy nuclei with large chemical shift ranges, such as Mo. The experimental quadrupolar coupling constant, $C_Q = (-)7.08$ MHz, is approximately twice that deduced from solution ^{14}N and ^{95}Mo T_1 measurements, $C_Q = 3.61$ MHz.²⁸⁷ Since the sign of $C_Q(^{95}\text{Mo})$ for $\text{K}_4\text{Mo}(\text{CN})_8 \cdot 2\text{H}_2\text{O}$ cannot be determined from ^{95}Mo NMR experiments, it is inferred from our DFT calculations and assumed to be correct, given the accuracy of the magnitude of the calculated C_Q values. The anisotropic Mo magnetic shielding tensor spans 1160 ppm and is among the largest reported⁴⁵ for a Mo compound. The isotropic Mo chemical shift, $\delta_{\text{iso}} = -1322 \pm 5$ ppm, for solid $\text{K}_4\text{Mo}(\text{CN})_8 \cdot 2\text{H}_2\text{O}$ indicates that the Mo is shielded by 14 ppm compared to that for an aqueous solution of $\text{K}_4\text{Mo}(\text{CN})_8 \cdot 2\text{H}_2\text{O}$, -1308 ppm.³¹¹ The observed lineshape and breadth of the ^{95}Mo NMR spectrum is highly sensitive to the orientation of the principal components of the Mo EFG tensor and the Mo magnetic shielding tensor, as well as their relative orientation. The crystallographic mirror plane in $\text{K}_4\text{Mo}(\text{CN})_8 \cdot 2\text{H}_2\text{O}$ restricts the relative orientation of the Mo σ and EFG tensors: one component of each of the tensors must lie perpendicular to this plane and the remaining two components must lie in the plane. Recognizing that the only possible orientation for the largest, and unique, component of the EFG tensor, V_{ZZ} , is perpendicular to the mirror plane leaves the orientation of the magnetic shielding tensor to be determined. Given that σ has near axial symmetry, $\kappa = -0.987$, either σ_{11} or σ_{33}

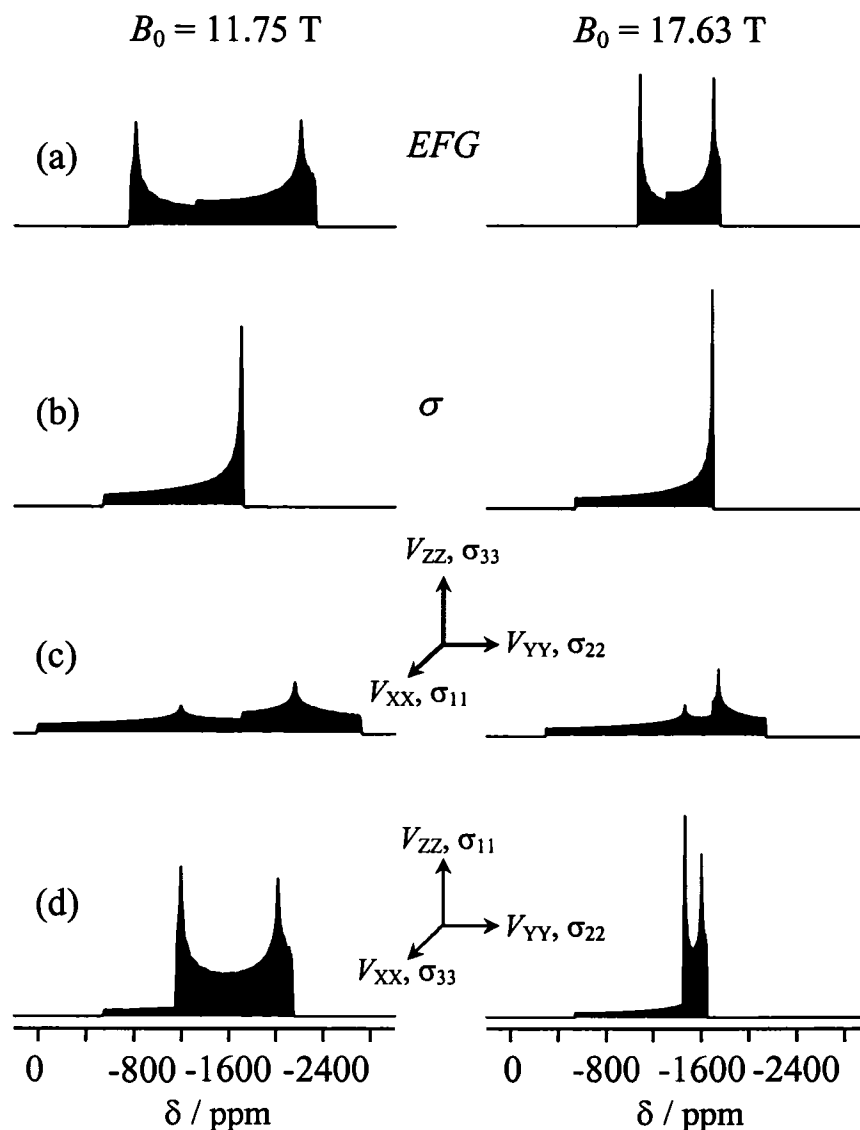


Figure 5.10: Simulations of central transition ^{95}Mo NMR spectra of solid, stationary $\text{K}_4\text{Mo}(\text{CN})_8 \cdot 2\text{H}_2\text{O}$ to show the individual contributions from the EFG (a) and σ (b) interactions. The sum of these interactions is shown in (c, d) using two possible relative orientations of the EFG and σ tensors. Simulations which best match the experimental spectra are shown in (a) and the corresponding best-fit simulation parameters are given in Table 5.4.

must be co-linear with V_{ZZ} . Shown in Figures 10(c) and (d) are two possible relative orientations of the EFG and σ tensors. From these simulations, the only orientation consistent with experiment is that where V_{ZZ} and σ_{11} are co-linear and perpendicular to the mirror plane; hence, $\beta = 90^\circ$ and $\gamma = 0^\circ$ (Figure 10(d)). This orientation, in

combination with the magnitudes of the Mo σ and EFG tensors, explains the apparent squeezing of the spectrum at 17.63 T and the origin of the low-intensity spikelets on the high frequency side of the powder pattern, which are barely discernable from the noise. Although these peaks are weak, they are present in all experiments and occur at the expected spacing, ν_{QCPMG} . The remaining Euler angle, α , is not restricted by the crystal symmetry and was determined by systematically varying the angle and visually comparing the resultant simulated spectrum with experiment; values of $\alpha = 0 \pm 30^\circ$ were found to provide a good fit with the experimental spectra.

To help rationalize the significant EFG and large observed Mo magnetic shielding anisotropy for $\text{K}_4\text{Mo}(\text{CN})_8 \cdot 2\text{H}_2\text{O}$, relativistic and non-relativistic ZORA DFT computations of the Mo magnetic shielding and EFG tensors were carried out on the isolated $\text{Mo}(\text{CN})_8^{4-}$ anion³¹² using the experimental X-ray structure. The calculated results are given in Table 5.4 and, despite our calculations being carried out on the isolated anion, $\text{Mo}(\text{CN})_8^{4-}$, the results are in good agreement with experiment. Although results for the isotropic magnetic shielding values using spin-orbit relativistic and non-relativistic calculations differ by several hundred ppm, their respective *chemical shift* values are in good agreement with experiment. In addition, values for Ω , κ , C_Q and η_Q are similar for the spin-orbit relativistic and non-relativistic values.

For comparison, calculations of the Mo magnetic shielding and EFG tensors were also carried out on the $\text{Mo}(\text{CN})_8^{4-}$ anion with imposed D_{2d} symmetry and results obtained from non-relativistic DFT calculations are summarized in Table 5.4. As expected, the Mo magnetic shielding and EFG tensors for ideal D_{2d} symmetry are axially symmetric and differences in the magnitudes of these tensors between the idealized D_{2d} model and the experimental structure are minor. Still, the calculated results for ideal D_{2d} $\text{Mo}(\text{CN})_8^{4-}$ are useful in providing insight into the origin of the large observed and calculated Mo magnetic shielding anisotropy. The magnetic shielding is governed by the paramagnetic shielding term,^{33c,35} which operates via mixing of occupied and virtual molecular orbitals (MOs) of appropriate symmetry that are centered on the nucleus of interest. Hence, inspection of the energy level diagram (Figure 5.8(a)) and the contribution of atomic orbitals to the MOs is required to understand the magnetic shielding for D_{2d} $\text{Mo}(\text{CN})_8^{4-}$. Examination of our ZORA DFT calculations for ideal D_{2d} $\text{Mo}(\text{CN})_8^{4-}$ indicates that the

HOMO, as well as many low-lying virtual orbitals, are dominated by Mo *d*-orbitals. The ordering of selected energy levels for D_{2d} $\text{Mo}(\text{CN})_8^{4-}$ (Figure 5.8(a)) is in agreement with that determined by others.^{276,313,314,315} In addition to the MOs, the magnitude and orientation of the Mo magnetic shielding tensor in the molecular frame must be considered. For D_{2d} symmetry there are two unique magnetic shielding tensor components, σ_{11} and $\sigma_{22} = \sigma_{33}$, referring to the magnetic shielding components oriented perpendicular and parallel to the molecular *z*-axis, respectively. Since the unique

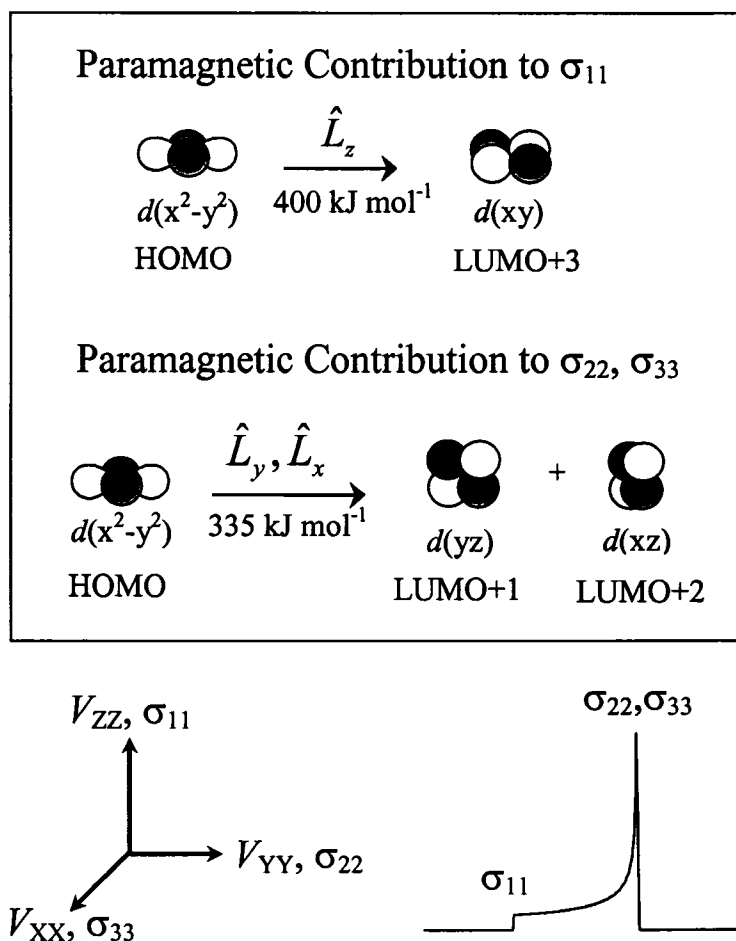


Figure 5.11: Origin of the paramagnetic shielding contribution to the principal components of the Mo magnetic shielding tensor, $\sigma_{ii}^{\text{para}}$, for D_{2d} $\text{Mo}(\text{CN})_8^{4-}$, as determined by our DFT calculations. Symmetry-allowed mixing between occupied and virtual Mo *d*-dominated molecular orbitals via the orbital angular momentum operators, \hat{L}_x , \hat{L}_y , and \hat{L}_z give rise to $\sigma_{ii}^{\text{para}}$. The relative orientation of the Mo σ and EFG tensors in the molecular frame (*i.e.*, V_{XX} , V_{YY} and V_{ZZ} are coincident with the *x*, *y*, *z*-axes), along with the Mo σ powder pattern, is shown to help visualize and rationalize the mixing of orbitals.

component of the Mo magnetic shielding tensor for $D_{2d} \text{Mo}(\text{CN})_8^{4-}$, σ_{11} , is oriented along the molecular z -axis, orbitals contributing to σ_{11} must lie in the xy -plane and the symmetry-allowed mixing of these orbitals occurs via rotation about the z -axis. According to our calculations on ideal $D_{2d} \text{Mo}(\text{CN})_8^{4-}$, the most plausible source of the large paramagnetic contribution to σ_{11} is mixing of occupied $d(x^2-y^2)$ and unoccupied $d(xy)$ orbitals via the z -component of the orbital angular momentum operator, \hat{L}_z , as mixing of these orbitals is both symmetry-allowed³¹⁶ and their energy difference is small (Figure 5.11). Mixing of $d(x^2-y^2)$ and $d(xy)$ occurs between several MOs and each makes a substantial contribution to $\sigma_{11}^{\text{para}}$; the most substantial contribution involves mixing of the HOMO with the LUMO+12, LUMO+3, and LUMO+13. In this case, the largest contribution of the paramagnetic term is governed by the most favorable overlap, rather than the smallest energy gap. Mixing of the orbitals in the xy -plane via \hat{L}_z only influences the shielding component along the z -axis; furthermore, rotations which affect σ_{11} do not affect $\sigma_{22} = \sigma_{33}$ and vice versa. Since the $d(xz)$ and $d(yz)$ orbitals are degenerate, rotations involving $d(x^2-y^2)$ via \hat{L}_y or \hat{L}_x result in contributions to the paramagnetic shielding of σ_{22} and σ_{33} (Figure 5.11). This mixing involves the HOMO, $d(x^2-y^2)$, with each of the following degenerate pairs of $d(xz)$ or $d(yz)$ dominated virtual orbitals: LUMO+1, +2, LUMO+5, +6, and LUMO+9, +10. For comparison, the difference in the total paramagnetic shielding between σ_{11} and $\sigma_{22} = \sigma_{33}$ is 933 ppm, whereas, the difference in the total diamagnetic shielding between σ_{11} and $\sigma_{22} = \sigma_{33}$, 12 ppm, is negligible. Together, the total diamagnetic and paramagnetic contributions result in a large deshielding of the principal components for ideal $D_{2d} \text{Mo}(\text{CN})_8^{4-}$, $\sigma_{\text{iso}} = 936$ ppm (spin-orbit relativistic; Table 5.4), with respect to the bare nucleus, $\sigma_{\text{iso}} \approx 4317.7$ ppm.³¹⁷

5.3.3.2. $\text{Ti}_4\text{Mo}(\text{CN})_8$: Approximate Square Antiprismatic Symmetry

Shown in Figure 5.12 are experimental and best-fit simulated solid-state ^{95}Mo QCPMG (11.75 T) and DFS/QCPMG (21.1 T) NMR spectra of a stationary sample of $\text{Ti}_4\text{Mo}(\text{CN})_8$, possessing approximate D_{4d} symmetry. The parameters used to calculate

the best-fit ^{95}Mo NMR spectra (Figure 5.12(b)) are listed in Table 5.5. The separation between spikelets is approximately 1940 Hz at 11.75 T and 500 Hz at 21.1 T. These spectra immediately suggest that structural deviations in the $\text{Mo}(\text{CN})_8^{4-}$ anion from square antiprismatic symmetry must be significant since, according to the PCA, a null EFG at Mo is predicted for an ideal square antiprism; instead, the ^{95}Mo NMR spectrum for $\text{Tl}_4\text{Mo}(\text{CN})_8$ is more than twice the breadth of that for $\text{K}_4\text{Mo}(\text{CN})_8 \cdot 2\text{H}_2\text{O}$.

According to the crystal structure for $\text{Tl}_4\text{Mo}(\text{CN})_8$,²⁷⁵ structural deviations present in the anion are significant, reducing the point group symmetry from D_{4d} to C_1 . The average parameters determined from the X-ray diffraction study²⁷⁵ are: $r(\text{Mo,C})_{\text{avg}} = 2.150 \pm 0.019 \text{ \AA}$, $r(\text{C,N})_{\text{avg}} = 1.163 \pm 0.013 \text{ \AA}$, and $\langle \text{Mo,C,N} \rangle_{\text{avg}} = 175.8 \pm 1.8^\circ$. The parameter which deviates most from ideal symmetry is the Mo-C-N bond angle, which must be 180° for a square antiprismatic structure. Deviations from square antiprismatic symmetry are evident in the ^{13}C (not shown; MAS sample) NMR spectra of $\text{Tl}_4\text{Mo}(\text{CN})_8$;

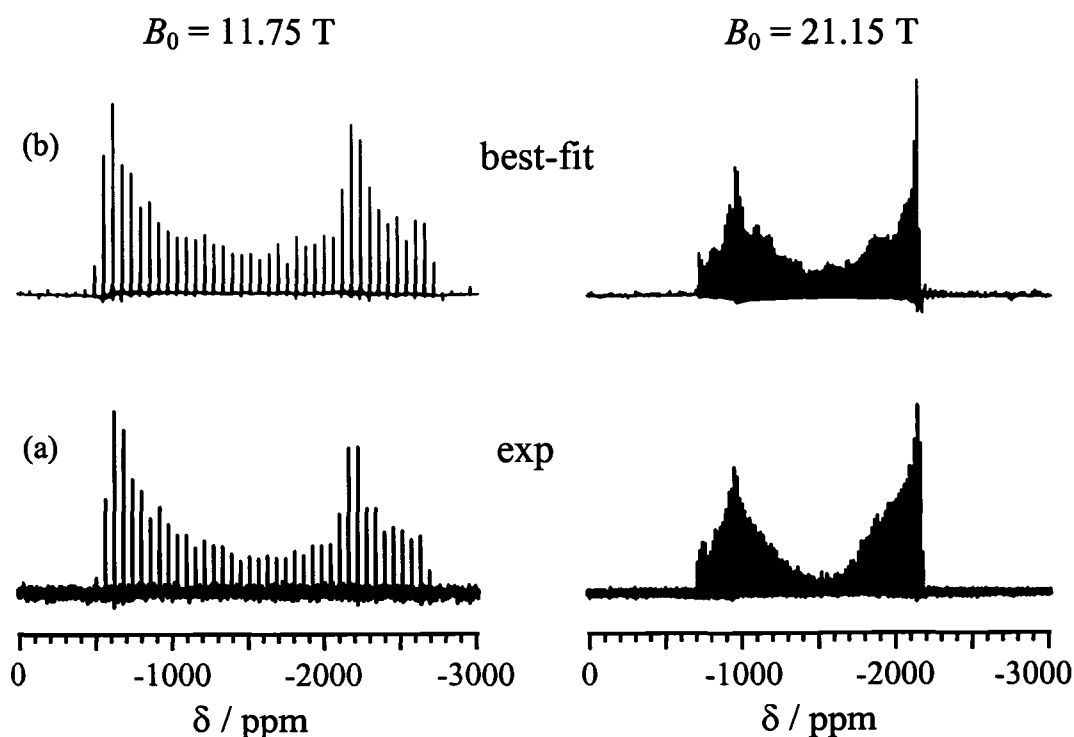


Figure 5.12: Experimental (a) and best-fit simulated (b) ^{95}Mo central transition NMR spectra of a solid stationary sample of $\text{Tl}_4\text{Mo}(\text{CN})_8$ acquired using the QCPMG pulse sequence at 11.75 T (left) and the DFS/QCPMG pulse sequence at 21.15 T (right). The parameters used to calculate the simulated spectra are given in Table 5.5. A total of 31 760 transients were summed for $\text{Tl}_4\text{Mo}(\text{CN})_8$ at 11.75 T and 8 192 at 21.15 T.

at 11.75 T the eight carbon atoms are not fully resolved, resulting in overlapping ^{13}C NMR signals with chemical shifts varying over approximately 15 ppm between 147 ppm and 162 ppm; however, if the structure were truly a square antiprism, a single carbon peak would appear in the ^{13}C NMR spectrum. These structural deviations were, therefore, initially thought to explain the large, observed EFG at Mo for $\text{Ti}_4\text{Mo}(\text{CN})_8$.

Similar to the K salt, non-relativistic and spin-orbit relativistic ZORA DFT calculations were carried out on the isolated $\text{Mo}(\text{CN})_8^{4-}$ anion using the structure determined from a single-crystal X-ray diffraction study;²⁷⁵ *i.e.*, approximate D_{4d} symmetry, and are summarized in Table 5.5. The calculated results are in good agreement with experiment and also predict a significant EFG at Mo and a large Mo shielding anisotropy. The main discrepancy between the best-fit and calculated parameters are the values for η_Q ; nevertheless, the calculations are correct in predicting a

Table 5.5: Experimental and Calculated Mo σ and EFG Parameters for $\text{Ti}_4\text{Mo}(\text{CN})_8$.

| $\delta_{\text{iso}} / \text{ppm}^*$ | Ω / ppm | κ | C_Q / MHz | η_Q | $\alpha, \beta, \gamma / ^\circ$ |
|--|-----------------------|------------------|--------------------|-----------------|----------------------------------|
| <i>Experimental: Solid-State ^{95}Mo NMR</i> | | | | | |
| -1350 ± 10 | 1350 ± 30 | $+0.50 \pm 0.05$ | $+6.35 \pm 0.15$ | 0.50 ± 0.08 | $90 \pm 5, 0, 0$ |
| <i>Calculated:[†] Scalar + Spin-Orbit Relativistic</i> | | | | | |
| -1308^\ddagger | 989 | +0.50 | +6.34 | 0.86 | 92, 171, 9 |
| <i>Calculated:^{*****} Non-relativistic $\text{Mo}(\text{CN})_8^{4-}$</i> | | | | | |
| -1273^\S | 980 | +0.50 | +6.60 | 0.82 | 95, 168, 8 |
| <i>Calculated: Non-relativistic (Ideal D_{4d} $\text{Mo}(\text{CN})_8^{4-}$ anion)</i> | | | | | |
| -1263 | 722 | +1.00 | +6.92 | 0.00 | 90, 0, NA ^{**} |

* Calculated isotropic chemical shifts were determined using $\delta(\text{ref})_{\text{iso,calc}} = -1860.0$ ppm for $\text{Mo}(\text{CO})_6$ and $\delta(\text{sample})_{\text{iso,calc}} = \sigma(\text{ref})_{\text{iso,calc}} - \sigma(\text{sample})_{\text{iso,calc}} - 1860.0$ ppm

[†] ZORA DFT calculations using QZ4P basis sets were performed on the isolated $\text{Mo}(\text{CN})_8^{4-}$ anion using coordinates as determined from X-ray crystallography.

[‡] Spin-orbit: for $\text{Mo}(\text{CO})_6$, $\sigma(\text{ref})_{\text{iso,calc}} = 1572.3$ ppm and $\delta(\text{ref})_{\text{iso,calc}} = -1860$ ppm.

[§] Non-relativistic: for $\text{Mo}(\text{CO})_6$, $\sigma(\text{ref})_{\text{iso,calc}} = 1229.4$ ppm and $\delta(\text{ref})_{\text{iso,calc}} = -1860$ ppm.

^{**} Due to the axial symmetry of the CS and EFG tensors, the calculated lineshape for the ^{95}Mo NMR spectrum is invariant to angle, γ .

large deviation from axial symmetry. Inclusion of the first coordination sphere of four Tl cations (within a distance of 4.85 Å from Mo) in the non-relativistic ZORA DFT calculation does not significantly alter the EFG and σ parameters: $C_Q = 6.21$ MHz, $\eta_Q = 0.70$, $\sigma_{\text{iso}} = 801.4$ ppm, $\Omega = 741$ ppm and $\kappa = +0.65$.

While deviations from square antiprismatic symmetry for $\text{Tl}_4\text{Mo}(\text{CN})_8$ are significant, the magnitude of the Mo EFG is larger than anticipated. The individual contributions from the Mo magnetic shielding and quadrupolar interactions to the ^{95}Mo NMR spectra, obtained from the best-fit experimental parameters in Table 5.5, are illustrated in Figure 5.13. The observed EFG at Mo for $\text{Tl}_4\text{Mo}(\text{CN})_8$ is $C_Q = (+)6.35$ MHz; again, the sign of $C_Q(^{95}\text{Mo})$ was inferred from the DFT calculations. The span of the Mo shielding tensor for the Tl salt, 1350 ppm, represents the largest reported value for Mo. For $\text{Tl}_4\text{Mo}(\text{CN})_8$, the crystal symmetry does not dictate the relative orientations of the σ and EFG tensors; hence, the Euler angles were obtained by manual iteration and visual comparison with the experimental ^{95}Mo NMR spectra obtained at 11.75 and 21.15 T. Two arbitrary orientations are shown in Figure 5.13(c) and (d) to illustrate the sensitivity of the lineshape on the Euler angles. The simulation which best fits the experimental spectra corresponds to the relative orientation of EFG and σ tensors where: $V_{XX} \parallel \sigma_{22}$, $V_{YY} \parallel \sigma_{11}$, and $V_{ZZ} \parallel \sigma_{33}$, shown in Figure 5.13(d). That the principal components of the EFG and σ tensors are, within experimental error, coincident is fortuitous since the crystal symmetry does not dictate such an orientation for $\text{Tl}_4\text{Mo}(\text{CN})_8$; however, the excellent fits obtained at 11.75 and 21.15 T support this solution. According to the ZORA DFT calculations for the anion in $\text{Tl}_4\text{Mo}(\text{CN})_8$ (Table 5.5), the σ and EFG tensors have the same general orientation as that determined by experiment, with slight deviations from coincidence ($< 10^\circ$) between principal components of the σ and EFG tensors.

The values obtained for the Mo EFG and the span of the Mo shielding tensor for $\text{Tl}_4\text{Mo}(\text{CN})_8$ are surprisingly comparable to those observed for $\text{K}_4\text{Mo}(\text{CN})_8 \cdot 2\text{H}_2\text{O}$. In previous ^{95}Mo NMR studies of $\text{K}_4\text{Mo}(\text{CN})_8 \cdot 2\text{H}_2\text{O}$ dissolved in isotropic liquids, results were interpreted on the strict basis that the D_{4d} structure has a zero EFG; however, our solid-state ^{95}Mo NMR results indicate that when structural deviations are considered, not

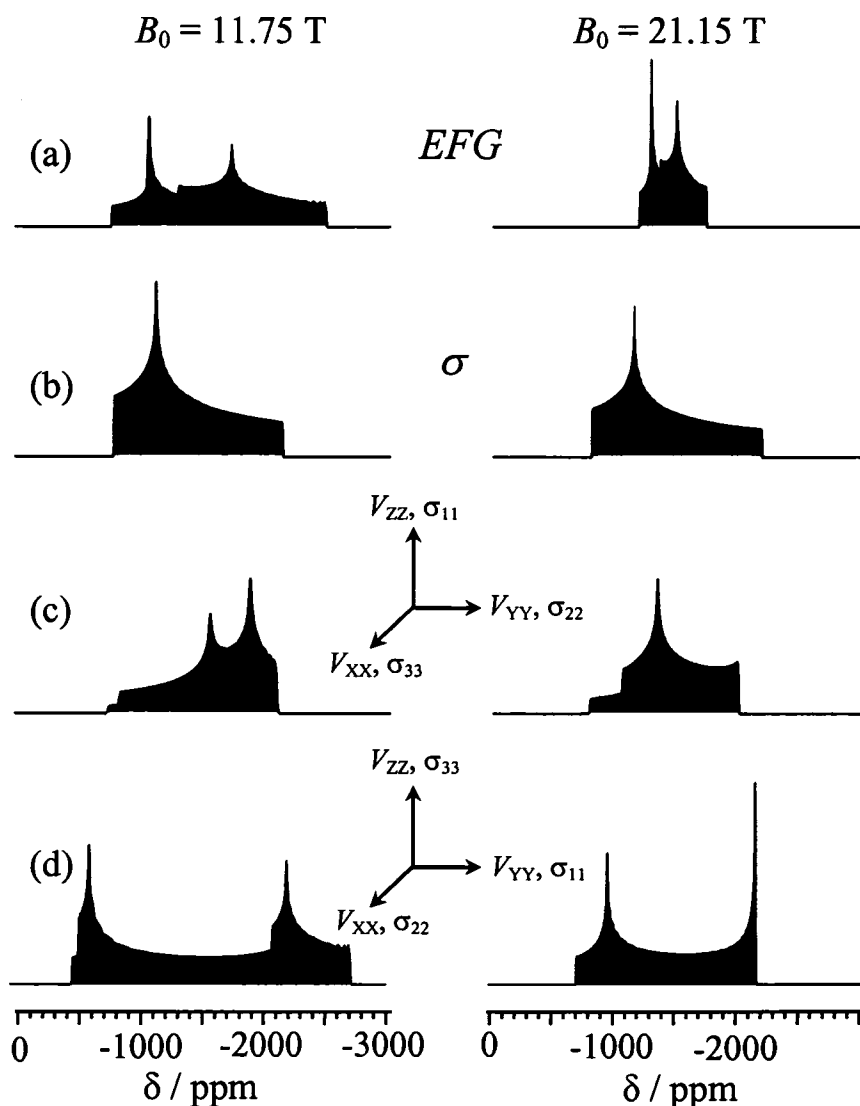


Figure 5.13: Simulations of central transition ^{95}Mo NMR spectra of solid, stationary $\text{Tl}_4\text{Mo}(\text{CN})_8$ to show the contributions from the EFG (a) and σ (b) interactions. The sum of these interactions is shown (c, d) using two possible relative orientations of the EFG and σ tensors. The simulations which best match the experimental spectra are shown in (d) and the simulation parameters are given in Table 5.5.

only is the EFG at Mo non-zero, it is significant and comparable in magnitude to that observed for the D_{2d} structure.

Although the magnitudes of the σ and EFG parameters are similar for $\text{K}_4\text{Mo}(\text{CN})_8 \cdot 2\text{H}_2\text{O}$ and $\text{Tl}_4\text{Mo}(\text{CN})_8$ (Tables 5.4 and 5.5), the symmetry, sign and relative orientation of these tensors differ considerably. The sign of C_Q is negative for D_{2d} $\text{K}_4\text{Mo}(\text{CN})_8 \cdot 2\text{H}_2\text{O}$, but positive for D_{4d} $\text{Tl}_4\text{Mo}(\text{CN})_8$, and the skew of the magnetic

shielding tensor is also different. The σ tensor for $\text{K}_4\text{Mo}(\text{CN})_8 \cdot 2\text{H}_2\text{O}$ is near axial symmetry, with σ_{11} being the unique component ($\kappa = -0.987$), while the skew is reversed for $\text{Tl}_4\text{Mo}(\text{CN})_8$. For the Tl salt, the σ tensor deviates considerably from axial symmetry, with a positive skew, $\kappa = +0.5$, and principal components, $\delta_{11} = -788$ ppm, $\delta_{22} = -1125$ ppm, and $\delta_{33} = -2138$ ppm. The relative orientation of the Mo σ and EFG tensors for the two salts is also different. In each case, the principal components of the σ and EFG tensors are coincident and V_{ZZ} must be parallel to the highest molecular symmetry axis; however, the exact orientation of the tensors is different for the two salts (see Figures 5.10(d) and 5.13(d)).

It is interesting to compare the Mo shielding tensors for the D_{2d} and D_{4d} $\text{Mo}(\text{CN})_8^{4-}$ to the g -tensors for the analogous paramagnetic Mo(V) systems. While NMR spectroscopy has been used to investigate the structure of diamagnetic $\text{Mo}(\text{CN})_8^{4-}$ anions, ESR has similarly been used to study the structure of $\text{Mo}(\text{CN})_8^{3-}$ anions.^{273,314,318,319} In one ESR investigation,³¹⁴ the authors calculated the ordering of d -orbitals for ideal D_{2d} and D_{4d} symmetry to determine the sense of the g -tensors in order to rationalize the structure of $\text{Mo}(\text{CN})_8^{3-}$. They concluded that $d(x^2-y^2)$ is the ground-state orbital for D_{2d} symmetry, while $d(z^2)$ is the ground-state orbital for D_{4d} symmetry, in agreement with our ZORA DFT calculations for the ideal D_{2d} and D_{4d} $\text{Mo}(\text{CN})_8^{4-}$ anions (Figure 5.8). They further determined that the anisotropic g -tensors are axially-symmetric with $g_{\perp} > g_{\parallel}$ for D_{2d} symmetry and $g_{\parallel} > g_{\perp}$ for D_{4d} symmetry. Hence, just as the sense of the σ tensor changes for the diamagnetic D_{2d} and D_{4d} $\text{Mo}(\text{CN})_8^{4-}$ anions, the sense of the g -tensors changes for the analogous paramagnetic systems.

Initially, the lowered symmetry in $\text{Tl}_4\text{Mo}(\text{CN})_8$ was presumed to explain the non-zero EFG at Mo for ($C_Q = +6.35$ MHz) and the disagreement with the PCA. To investigate this further, EFG and σ tensor calculations were carried out on idealized models of $\text{Mo}(\text{CN})_8^{4-}$ with D_{4d} symmetry (Table 5.5). Surprisingly, the calculated results for square antiprismatic $\text{Mo}(\text{CN})_8^{4-}$ indicate that the large EFG at Mo remains, but the Mo EFG tensor is now axially symmetric, as expected. Before discussing the non-zero EFG further, the calculated magnetic shielding anisotropy for the $\text{Mo}(\text{CN})_8^{4-}$ anion possessing square antiprismatic symmetry will be discussed.

Similar to the strategy used for the K salt, the large anisotropy in the Mo shielding tensor for $\text{Ti}_4\text{Mo}(\text{CN})_8$ is rationalized in terms of the paramagnetic shielding contributions to the principal components of the magnetic shielding tensor; the following results pertain to the ideal square antiprismatic $\text{Mo}(\text{CN})_8^{4-}$ anion. The reader is referred to selected energy levels for square antiprismatic $\text{Mo}(\text{CN})_8^{4-}$, shown in Figure 5.8(b). Recalling that the Mo shielding tensor for $\text{Ti}_4\text{Mo}(\text{CN})_8^{4-}$ is oriented such that σ_{33} is along

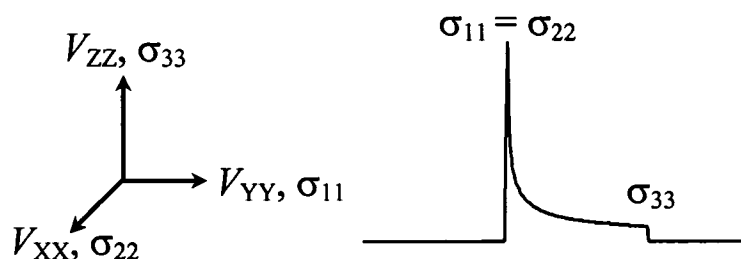
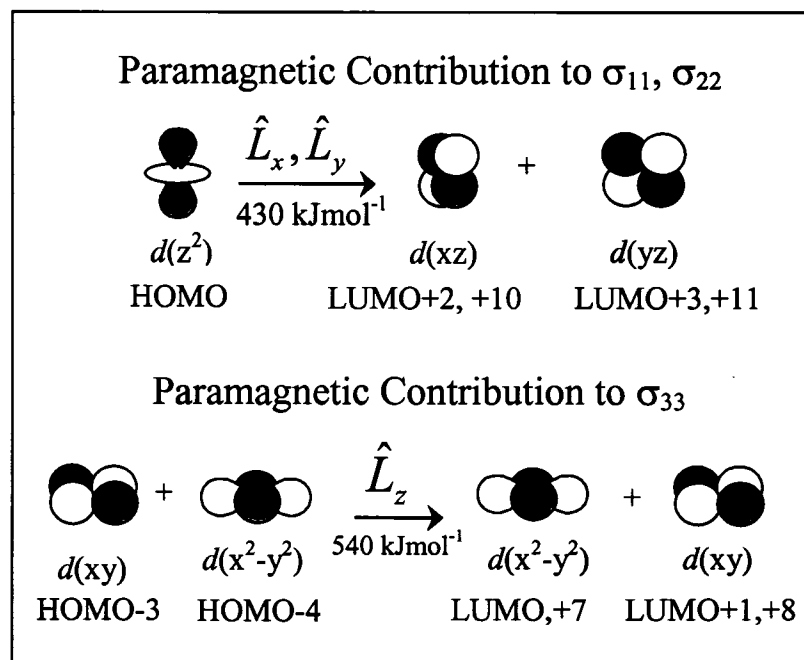


Figure 5.14: Origin of the paramagnetic shielding contribution to the principal components of the Mo magnetic shielding tensor, $\sigma_{ii}^{\text{para}}$, for D_{4d} $\text{Mo}(\text{CN})_8^{4-}$. Symmetry-allowed mixing between occupied and virtual Mo d -dominated molecular orbitals via the angular momentum operators, \hat{L}_x , \hat{L}_y , and \hat{L}_z give rise to $\sigma_{ii}^{\text{para}}$. The relative orientation of the Mo σ and EFG tensors in the molecular frame (*i.e.*, V_{xx} , V_{yy} and V_{zz} are coincident with the x , y , z -axes), along with the Mo σ powder pattern, are shown to help visualize and rationalize the mixing of d -orbitals.

the z -axis and σ_{22} , σ_{11} are along the x,y -axes, respectively, indicates that contributions to σ_{22} , σ_{11} involve rotations about the x,y -axes, thereby mixing $d(z^2)$ with $d(xz)$ and $d(yz)$ (Figure 5.14). This mixing involves the two lowest energy gaps, is both allowed³¹⁶ and favorable, and is responsible for the deshielding of σ_{11} and σ_{22} . Contributions to σ_{33} involve mixing of the $d(xy)$ and $d(x^2-y^2)$ orbitals via \hat{L}_z . The smaller paramagnetic contribution to σ_{33} results from the larger energy gaps between occupied(HOMO-3,-4) and virtual (LUMO,+1,+7,+8) orbitals of Mo $d(xy)$ and $d(x^2-y^2)$ character. Contributions from the total diamagnetic and paramagnetic terms result in an overall deshielding for square antiprismatic $\text{Mo}(\text{CN})_8^{4-}$, $\sigma_{\text{iso}} = 1020$ ppm (spin-orbit relativistic; Table 5.5), with respect to the bare Mo nucleus, $\sigma_{\text{iso}} \approx 4317.7$ ppm.

5.3.3.3 Quantum Chemical Investigation of the PCA for D_{4d} Symmetry

To test the reliability of the DFT calculations of the Mo EFG and σ tensors for $\text{Mo}(\text{CN})_8^{4-}$, which indicate a significant EFG at Mo for both approximate and ideal square antiprismatic symmetry and are in disagreement with the PCA, calculations of Mo EFG and σ tensors were performed on representative Mo compounds of ideal symmetry; namely, the tetrahedral molybdate anion in Na_2MoO_4 ,³⁰⁴ the tetrathiomolybdate anion in $[(\text{C}_2\text{H}_5)_4\text{N}][\text{MoS}_4]$,³⁰⁵ the tetraselenomolybdate anion in $[(\text{C}_6\text{H}_5)_4\text{P}]_2[\text{MoSe}_4]$,³⁰⁶ and the octahedral molecule, $\text{Mo}(\text{CO})_6$.³⁰⁷ The experimental Mo chemical shift values of these compounds cover approximately 60 % of the chemical shift range for molybdenum. Our calculations were performed on isolated, idealized structures of these Mo compounds, as well as $\text{Mo}(\text{CN})_8^{4-}$ anions possessing D_{2d} , D_{4d} , and O_h symmetry; the results are summarized in Table 5.6. Considering that the calculations are performed on isolated molecules or anions with ideal symmetry and do not account for solvent effects, our calculated δ_{iso} values are in good agreement with experimental values.^{247,320} Furthermore, results for the calculated Mo EFG tensor for compounds of T_d and O_h symmetry are in accord with the PCA in that a zero EFG is predicted; however, a significant EFG is calculated for the isolated $\text{Mo}(\text{CN})_8^{4-}$ anion possessing square antiprismatic (D_{4d}) symmetry, contrary to the PCA which indicates the EFG at Mo is necessarily zero.

Initially, the origin of the non-zero EFG at Mo for the isolated square antiprismatic $\text{Mo}(\text{CN})_8^{4-}$ anion was thought to arise from the two d -electrons localized in Mo $d(z^2)$ atomic orbitals. To investigate this further, calculations were performed on isolated $\text{Mo}(\text{CN})_8^{2-}$, where the formal charge on Mo is +6 and there are no valence d -electrons; however, non-relativistic calculations indicate that the large EFG in the Mo(VI) system remains and is slightly larger ($C_Q = -8.4$ MHz) than that for the Mo(IV) anion. In the hypothetical Mo(VI) system, the highest occupied MOs have zero contribution from Mo $4d$ -orbitals, whereas the lowest unoccupied MOs are largely dominated by Mo d -orbitals. Hence, it appears that the valence d -electrons are not the source of the EFG for either the Mo(IV) or the Mo(VI) system. Similar results were found when calculations were performed on $\text{Zr}(\text{CN})_8^{4-}$, a hypothetical anion where Zr is ideally d^0 . In this case, both the standard ZORA DZ basis set for Zr and a modified Zr

Table 5.6: Calculated NMR Parameters for Isolated, Idealized Model Compounds of High Symmetry and Experimental Mo Chemical Shift Values.

| Symmetry | Molecule | $\delta_{\text{iso, exp}} / \text{ppm}$ | $\delta_{\text{iso, calc}} / \text{ppm}^{*,\dagger}$ | $\sigma_{\text{iso}} / \text{ppm}$ | C_Q / MHz | η_Q |
|----------|-------------------------------|---|--|------------------------------------|--------------------|----------|
| T_d | MoO_4^{2-} | 0 | 347 | -636 | 0.00 | ---- |
| T_d | MoS_4^{2-} | 2259 ³²⁰ | 2282 | -2571 | 0.00 | ---- |
| T_d | MoSe_4^{2-} | 3145 ³²⁰ | 2970 | -3259 | 0.00 | ---- |
| O_h | $\text{Mo}(\text{CO})_6$ | -1860 | -1860 | 1571 | 0.00 | ---- |
| O_h | $\text{Mo}(\text{CN})_8^{4-}$ | ----- | -1287 [‡] | 656 | 0.00 | ---- |
| D_{4d} | $\text{Mo}(\text{CN})_8^{4-}$ | -1375 | -1263 | 974 | +6.92 | 0.00 |
| D_{2d} | $\text{Mo}(\text{CN})_8^{4-}$ | -1350 | -1212 | 923 | -7.47 | 0.00 |

* ZORA DFT spin-orbit calculations using QZ4P basis sets.

† Calculated isotropic chemical shifts were determined using $\delta(\text{ref})_{\text{iso, calc}} = -1860.0$ ppm for $\text{Mo}(\text{CO})_6$ and $\delta(\text{sample})_{\text{iso, calc}} = \sigma(\text{ref})_{\text{iso, calc}} - \sigma(\text{sample})_{\text{iso, calc}} - 1860.0$ ppm.

‡ The spin-orbit relativistic calculation for O_h $\text{Mo}(\text{CN})_8^{4-}$ did not converge; hence, non-relativistic ZORA DFT was employed using QZ4P basis sets. An analogous calculation was carried out on the secondary reference, $\text{Mo}(\text{CO})_6$: $\sigma_{\text{iso}} = 1229.4$ ppm, $\delta_{\text{iso}} = -1860$ ppm, to determine the calculated chemical shift for O_h $\text{Mo}(\text{CN})_8^{4-}$. QZ4P basis sets were used.

basis set, in which all 4*d*-orbitals were removed, were employed. In both cases, the calculations yield an EFG at Zr that is large, but is several times smaller than the analogous Mo calculation using standard ZORA DZ basis sets: $eq_{zz}({}^{91}\text{Zr})_{\text{DZ}} = 0.37 \times 10^{21} \text{ V m}^{-2}$, $eq_{zz}({}^{91}\text{Zr})_{\text{modified DZ}} = 0.15 \times 10^{21} \text{ V m}^{-2}$, and $eq_{zz}({}^{95}\text{Mo})_{\text{DZ}} = 0.79 \times 10^{21} \text{ V m}^{-2}$. These results indicate that the large EFG is not solely linked to the *d*-electrons. Lastly, a ZORA DFT EFG calculation was carried out on MoF_8^{4-} and, again, a large EFG was computed, indicating that the extended CN⁻ ligand is not the source of the EFG at Mo.

Failure of the PCA for the above cases motivated us to carry out a calculation using actual point charges, q_i , in lieu of the CN⁻ ligands. This involved replacing each carbon and nitrogen atom with a point charge, equivalent to the charge predicted by RHF calculations, such that the overall molecular charge for the "anion", $\text{Mo}(q_{\text{C}}q_{\text{N}})_8^{4-}$ is -4. The calculated result is in accord with the PCA with a zero EFG for D_{4d} symmetry. This implies that the asymmetry in the distribution of the ligand charge gives rise to the non-zero EFG at Mo and Zr.

Since the PCA holds for cubic $\text{Mo}(\text{CN})_8^{4-}$, but fails for the square antiprismatic analogue, we carried out calculations of the Mo EFG tensor during the transition from O_h to D_{4d} symmetry in an attempt to understand the EFG at Mo for D_{4d} $\text{Mo}(\text{CN})_8^{4-}$. Both non-relativistic ZORA DFT and RHF calculations of the Mo EFG tensor for various rotamers of $\text{Mo}(\text{CN})_8^{4-}$ were carried out. The $\text{Mo}(\text{CN})_8^{4-}$ anion possessing cubic symmetry served as our starting structure and subsequent rotamers were generated by rotating the top portion of the cube in steps of 5° about the principal, z-axis, while holding the bottom fragment of the cube fixed. A total of 10 rotamers were generated from O_h $\text{Mo}(\text{CN})_8^{4-}$, each possessing D_{4d} symmetry, with the square antiprism (Figure 5.8(b)) representing our final structure. Shown in Figure 5.15(a) is a plot of the calculated $C_Q({}^{95}\text{Mo})$ values as a function of deviation from cubic symmetry. According to the PCA, the EFG at Mo is zero for *all* rotamers, including the square antiprism; however, the DFT and RHF calculations indicate that once the cubic symmetry of $\text{Mo}(\text{CN})_8^{4-}$ is broken, a dramatic increase in the EFG is observed. The EFG at Mo remains high, but slowly decreases and reaches a local minimum at 45°; *i.e.*, the square antiprism. The general agreement in the trends for the calculated EFGs at Mo obtained

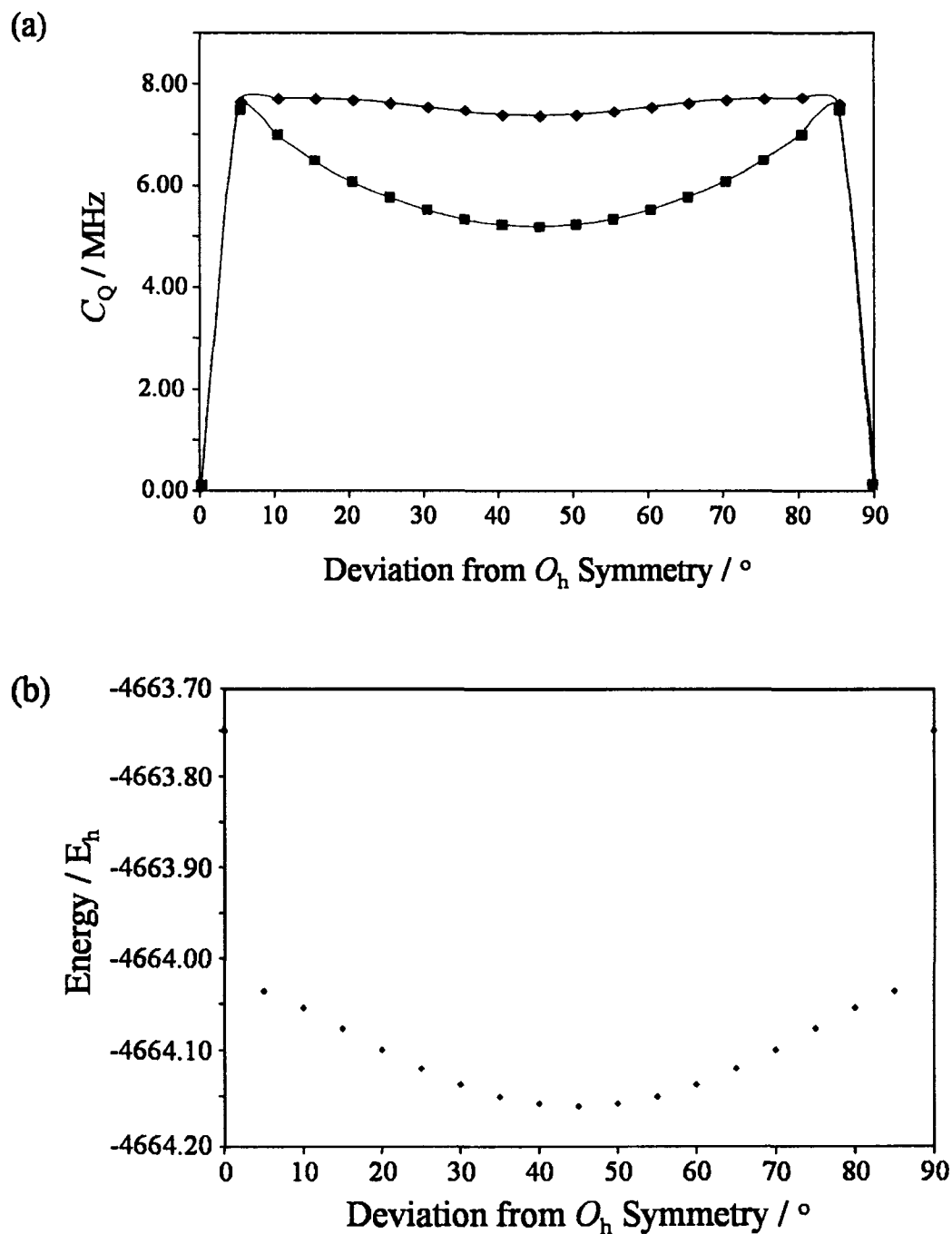


Figure 5.15: (a) Non-relativistic $C_Q(^{95}\text{Mo})$ values for $\text{Mo}(\text{CN})_8^{4-}$ rotamers as a function of deviation from cubic symmetry. Using the PCA, a zero EFG at Mo results for all rotamers. ZORA DFT calculations, \blacklozenge , and RHF, \blacksquare , calculations. (b) Total energy, calculated at the RHF level, for $\text{Mo}(\text{CN})_8^{4-}$ rotamers as a function of deviation from cubic symmetry. For conversion purposes, $1E_h = 4.359\,748\,2(26) \times 10^{-18} \text{ J}$.

using two methods is reassuring. In particular, both methods calculate axially-symmetric Mo EFG tensors for all rotamers and a zero EFG at Mo for O_h symmetry, but a non-zero and substantial EFG at Mo for square antiprismatic symmetry, lending confidence to our calculated and experimental results. Nevertheless, according to the PCA, *both* O_h and square antiprismatic symmetries should result in a zero EFG.⁴⁶

The total energy, calculated at the RHF level, is also plotted for the various rotamers as a function of deviation from O_h symmetry and shown in Figure 5.15(b). The energy curve is smooth for all rotamers except for that possessing O_h symmetry, where an abnormally-large increase in energy is observed. Although the calculation did converge for the square prismatic rotamer, the sudden discontinuity in the energy curve is problematic. The lowest calculated energy is found for the ideal square antiprism, indicating that this configuration is the most stable for the $\text{Mo}(\text{CN})_8^{4-}$ anion.

Magnetic shielding calculations were also carried out on the above D_{4d} $\text{Mo}(\text{CN})_8^{4-}$ rotamers (Figure 5.16). Results for O_h $\text{Mo}(\text{CN})_8^{4-}$ are not shown in Figure 5.16 since this calculation required use of a higher basis set for convergence. The principal components

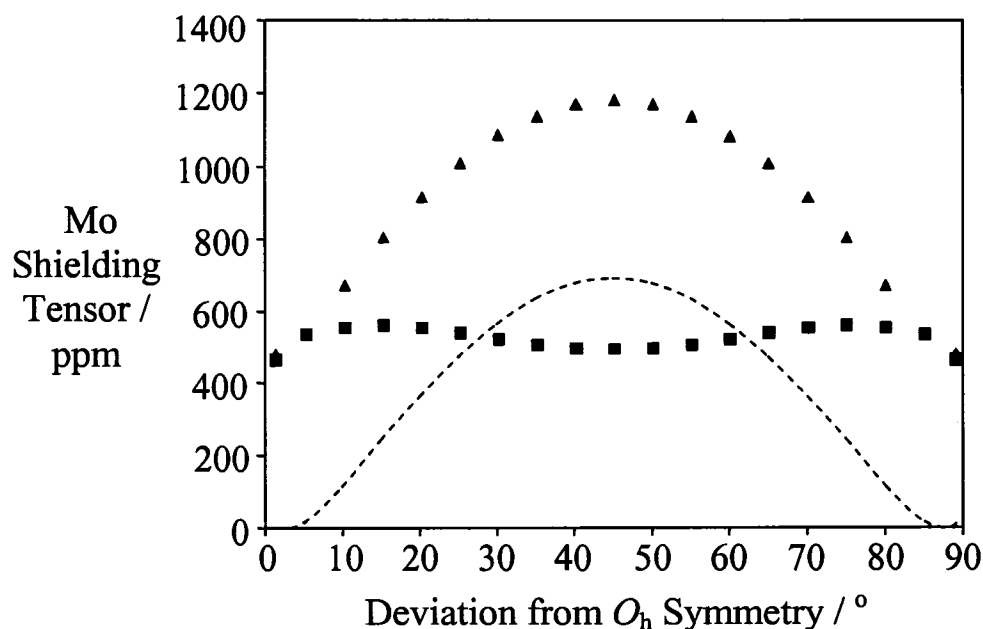


Figure 5.16: Components of the axially-symmetric Mo shielding tensor, $\sigma_{11} = \sigma_{22}$ ■, σ_{33} ▲, and span = ----, for $\text{Mo}(\text{CN})_8^{4-}$ rotamers as a function of deviation from ideal cubic symmetry, calculated using non-relativistic ZORA DFT.

of the Mo σ tensor are shown in Figure 5.16, where it is clear that σ_{33} largely governs both the isotropic and anisotropic magnetic shielding. The profiles of σ_{iso} and Ω for the rotamers show a steady increase upon rotation from O_h symmetry, with maxima at square antiprismatic symmetry. The increase in the anisotropic shielding can be understood by considering the orientation of the shielding tensors and inspecting the contribution from the paramagnetic shielding, σ^{para} , to the principal components for each rotamer. In each case, σ_{33} is co-linear with the z-axis; hence, contributions from σ^{para} to σ_{33} involve mixing of $d(xy)$ and $d(x^2-y^2)$ orbitals via \hat{L}_z , whereas mixing of $d(z^2)$ and $d(xz)$, $d(yz)$ via \hat{L}_x and \hat{L}_y contribute to σ_{11} , σ_{22} . The increase in σ_{33} upon increased deviation from O_h symmetry is due to an increase in the energy gap involving $d(xy)$ and $d(x^2-y^2)$ orbitals, as well as a gradual decrease in the percent contribution of these atomic orbitals to the molecular orbitals; the end result is a decrease in the contribution of σ^{para} to σ_{33} , and, thus, an increase in σ_{33} . The paramagnetic contribution to σ_{11} and σ_{22} remains relatively constant upon rotation as the molecular orbitals involving Mo $d(z^2)$, $d(xz)$, and $d(yz)$ atomic orbitals do not change significantly during the transition from O_h to square antiprismatic symmetry for the $\text{Mo}(\text{CN})_8^{4-}$ rotamers.

5.3.4. Conclusions

Solid-state ^{95}Mo NMR spectroscopy is an ideal method for examining the two forms of $\text{Mo}(\text{CN})_8^{4-}$ anions possessing approximate dodecahedral and square antiprismatic symmetry. The magnitudes of the Mo EFG and magnetic shielding anisotropy are significant for both $\text{K}_4\text{Mo}(\text{CN})_8 \cdot 2\text{H}_2\text{O}$ and $\text{Ti}_4\text{Mo}(\text{CN})_8$; however, the sign and relative orientations of the EFG and magnetic shielding tensors result in ^{95}Mo NMR spectra which are strikingly different for the two forms. Our calculations on $\text{Mo}(\text{CN})_8^{4-}$ anions possessing ideal dodecahedral and square antiprismatic symmetry indicate a substantial EFG at Mo for *both* structures; this result is in contrast to the PCA, which predicts a zero EFG for D_{4d} $\text{Mo}(\text{CN})_8^{4-}$ and a non-zero EFG for D_{2d} $\text{Mo}(\text{CN})_8^{4-}$. Although the origin of the non-zero EFG for square antiprismatic $\text{Mo}(\text{CN})_8^{4-}$ is not clear, our calculations indicate it does not exclusively arise from the Mo d -electrons or the

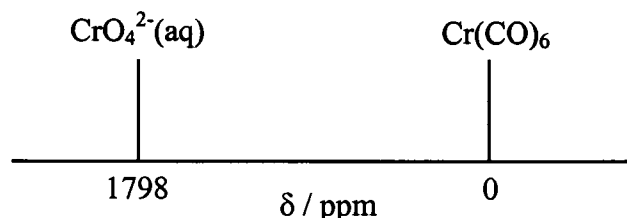
diatomic nature of the cyanide ligand. High-level quantum chemical calculations have provided insight into the origin of the large EFG and Mo magnetic shielding anisotropies in $\text{K}_4\text{Mo}(\text{CN})_8 \cdot 2\text{H}_2\text{O}$ and $\text{Tl}_4\text{Mo}(\text{CN})_8$ and allowed the Mo magnetic shielding and EFG tensors, as well as their relative orientations, to be characterized.

Chapter 6: Solid-State ^{53}Cr NMR Studies of CrO_4^{2-} and $\text{Cr}_2\text{O}_7^{2-}$ Salts

6.1 Introduction

Chromium is an early transition metal element that has found important applications in chemistry and physics, including synthesis,³²¹ asymmetric catalyses,³²² and superconductivity.³²³ The Gr(VI) elements, chromium ($Z = 24$) and molybdenum ($Z = 42$), share many parallels in both synthetic inorganic and organometallic chemistry and in NMR spectroscopy. They form an interesting array of d^0 to d^6 complexes, such as the classic Gr(VI) ternary oxides and hexacarbonyls; in fact, these compounds serve as reference compounds for ^{53}Cr and $^{95/97}\text{Mo}$ NMR studies; see Figure 6.1. The unfavorable nuclear properties of ^{53}Cr and ^{95}Mo , given in Figure 6.1, place them in the category of challenging nuclei to study by NMR – both are half-integer spin quadrupolar nuclei with small magnetic moments and relatively low natural abundances. Although both isotopes

$$^{53}\text{Cr}: \text{NA} = 9.501 \%, I = 3/2, Q = -15.0 \text{ fm}^2, \gamma = -1.5152 \times 10^7 \text{ rad T}^{-1} \text{ s}^{-2}$$



$$^{95}\text{Mo}: \text{NA} = 15.92 \%, I = 5/2, Q = -2.2 \text{ fm}^2, \gamma = -1.751 \times 10^7 \text{ rad T}^{-1} \text{ s}^{-2}$$

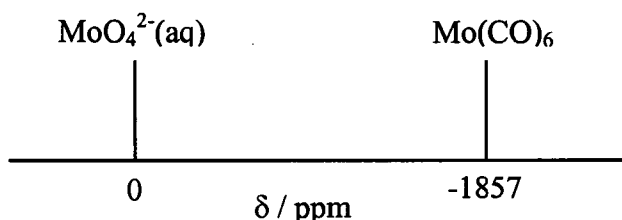


Figure 6.1: Selected view of the Cr and Mo NMR chemical shift scales, showing typical NMR reference compounds, along with relevant ^{53}Cr and ^{95}Mo nuclear properties.³⁷ The primary reference for $^{95/97}\text{Mo}$ NMR studies is a 2.0 M aqueous solution of Na_2MoO_4 , while that for chromium is $\text{Cr}(\text{CO})_6$ dissolved in chloroform; however, a preferred, secondary reference for ^{53}Cr NMR studies is a saturated aqueous solution of Cs_2CrO_4 with $\delta_{\text{iso}} = 1798.0 \text{ ppm}$; Ref. 37.

present challenges to the NMR spectroscopist, the degree of difficulty for ^{53}Cr NMR studies exceeds that for ^{95}Mo . The lower natural abundance and sensitivity of ^{53}Cr relative to ^{95}Mo make it more difficult and time-consuming to obtain a ^{53}Cr NMR signal; in addition, the large quadrupole moment causes rapid relaxation in solution and broader signals in the solid state. These unfavorable properties have largely dissuaded ^{53}Cr NMR studies; as a result, isotropic ^{53}Cr chemical shifts and line widths are known for less than 100 compounds in solution,³²⁴ including an array of Cr(0) and Cr(VI) compounds, including pentacarbonylchromium-carbenes ($\text{Cr}(\text{CO})_5\text{XY}$), chromyl halides (CrO_2X_2), halochromates (CrO_3X^-), chromates (CrO_4^{2-}), dichromates ($\text{Cr}_2\text{O}_7^{2-}$), polychromates ($\text{Cr}_3\text{O}_{10}^{2-}$), and prototypal $\text{Cr}(\text{CO})_x(\text{PF}_3)_{6-x}$ compounds. Solution ^{53}Cr NMR results for these compounds have established a general trend that hexacoordinate Cr(0) compounds are 1700 to 1900 ppm more shielded than tetracoordinate Cr(VI) compounds, as exemplified by $\text{Cr}(\text{CO})_6$ and CrO_4^{2-} in Figure 6.1. A similar result is found for the analogous Mo compounds; in fact, the chemical shift differences between the Gr(VI) ternary oxides and the Gr(VI) hexacarbonyls are nearly equal for Gr(VI) = Cr and Mo, as depicted in Figure 6.1.

A promising result from many of the solution ^{53}Cr NMR studies is the observation of narrow linewidths, which indicate small EFGs at the Cr nucleus for these molecules and, consequently, presents an opportunity for conducting solid-state ^{53}Cr NMR studies. To date, very few solid-state ^{53}Cr NMR studies have been carried out and, furthermore, most are restricted to paramagnetic, ferromagnetic, and antiferromagnetic compounds, including CdCr_2Se_4 , CuCr_2S_4 , GdCrO_3 , ErCrO_3 , and $\text{CrH}_{0.93}$.^{325,326} Several years ago, the first solid-state ^{53}Cr NMR study of diamagnetic octahedral d^6 and tetrahedral d^0 Cr compounds was reported by our laboratory;³²⁷ however, the use of low applied magnetic field strengths ($B_0 = 7.05$ T and 9.4 T) and conventional one-pulse or spin-echo techniques limited the narrow selection of compounds examined to $\text{Cr}(\text{CO})_6$ and several $\text{A}(\text{I})_2\text{CrO}_4$ salts – all of which have small quadrupolar coupling constants, *i.e.*, $C_Q(^{53}\text{Cr}) \leq 1.75$ MHz; nevertheless, this study demonstrates that solid-state ^{53}Cr NMR studies are possible, even at low B_0 s. The current study is an extension to this work³²⁷ and involves an expanded list of A(I) and A(II) chromate salts, A(I) = Li, K, Rb, Cs, Ag and A(II) = Mg, Ca, Sr, Ba, Pb, and A(I) dichromate salts, A(I) = K and Cs.

To overcome the difficulties associated with solid-state ^{53}Cr NMR studies, high-field magnets and sensitivity-enhancement techniques have been utilized. Specifically, magnetic field strengths of 11.75 T and 18.8 T and the QCPMG experiment have been employed in this study to decrease experiment times while obtaining high-quality ^{53}Cr NMR spectra. The use of high magnetic fields is advantageous in effectively narrowing the central NMR transition due to the inverse relationship between the second-order quadrupolar broadening and B_0 (Sections 2.5 and 3.2.1), while the QCPMG experiment (Section 3.2.2.2.) offers a significant gain in signal-to-noise over traditional techniques. Our solid-state ^{131}Xe (Chapter 4) and ^{95}Mo (Chapter 5) NMR results, as well as several literature reports,^{47,89,92,250,328} have demonstrated the utility of the QCPMG technique, especially when studying challenging nuclei. Without the QCPMG experiment, the success of the current ^{53}Cr NMR study would have been severely hampered, if not impossible.

Similar to the molybdate salts, the chromate and dichromate salts are excellent test cases for assessing the expediency of solid-state ^{53}Cr NMR studies. The goal of this research is to characterize the Cr EFG and magnetic shielding tensors and, when possible, compare the Cr(VI) quadrupolar and shielding parameters for the A(I) and A(II) chromate salts presented here with the corresponding series of A(I) and A(II) molybdate salts presented in Chapter 5. We have previously demonstrated in the investigation of A(I) and A(II) molybdate salts that the anisotropic shielding interaction is crucial in analyzing solid-state ^{95}Mo NMR spectra. Will the role of the shielding anisotropy for Cr, a first-row transition metal element, be as significant as that for a second-row element? How do the magnitudes of the ^{53}Cr C_Q values compare with those for Mo? Lastly, what are the effects of distortion from ideal symmetry on the Cr EFG tensors for the chromate and dichromate salts? To address these questions, solid-state ^{53}Cr NMR experiments on a series of chromate and dichromate anions and ZORA DFT calculations of the Cr EFG and shielding tensors for isolated CrO_4^{2-} and $\text{Cr}_2\text{O}_7^{2-}$ anions have been performed.

6.2. Experimental Details

All samples of chromate and dichromate salts are commercially available and were used without further purification. The A(I) and A(II) chromate and A(I) dichromate

salts were analyzed using powder X-ray diffraction, XRD, to identify their structures due to their known tendency to form polymorphic phases.

6.2.1. Solid-State ^{53}Cr NMR Spectroscopy

Samples were powdered and packed into 5.0 mm or 7.5 mm (ZrO_2) o.d. rotors. Solid-state ^{53}Cr NMR experiments were performed on Bruker Avance (11.75 T) and Varian Inova (18.8 T) spectrometers, operating at respective spectral frequencies of 28.23 MHz and 45.14 MHz. A saturated, aqueous solution of Cs_2CrO_4 was used for referencing, with $\delta_{\text{iso}} = 1798.0$ ppm, and pulse width calibration. Employing a standard one-pulse experiment, typical solution $\pi/2$ pulse widths of 7.0 – 7.6 μs were obtained, which correspond to solid, selective $\pi/2$ pulse widths of 3.5 – 3.8 μs and $\gamma B_1/2\pi$ values of 83.3 kHz and 65.8 kHz, respectively. The QCPMG⁸⁹ pulse sequence was used to collect all ^{53}Cr NMR spectra of CrO_4^{2-} and $\text{Cr}_2\text{O}_7^{2-}$ salts at 11.75 T and 18.8 T; the frequency-stepped technique⁹⁷ was employed when the breadths of the ^{53}Cr NMR spectra exceeded the pulse width excitation profile; see *Section 3.2.3.2*. Summarized in *Appendix 6.1* are the number of steps required at 11.75 T and 18.8 T, along with the QCPMG spikelet spacing and the time required to collect the entire ^{53}Cr NMR spectrum at 18.8 T, for each compound investigated. Sweep widths of 100 kHz were employed at 11.75 T and varied between 200 and 500 kHz at 18.8 T; acquisition times of 16 – 122 ms, τ values of 80 – 100 μs , pulse delays of 1 – 10 s and pulse train repetitions, M , of 30 – 96 were used. The spikelet spacing, ν_{QCPMG} , varied from 200 Hz to 5000 Hz, and was chosen based on the breadth of the powder pattern. For samples containing protons, ^1H decoupling was applied and an optimized $\pi/2$ pulse of 10.0 μs was used. For Pb chromate as well as K and Cs dichromate, ^{53}Cr NMR spectra were acquired at a single magnetic field of 18.8 T.

Solid-state ^{53}Cr NMR spectra of magic-angle spinning (MAS) samples were obtained at 11.75 T for Cs_2CrO_4 and at 18.8 T for Rb_2CrO_4 using spinning rates of 6000 Hz and 6250 Hz, respectively.

Simulations of ^{53}Cr NMR spectra of the chromate and dichromate salts were carried out using SIMPSON¹⁰² and WSOLIDS.¹⁰¹ Large crystal files were generally necessary to calculate adequate-quality ^{53}Cr NMR spectra when using SIMPSON,

particularly when trying to emulate broad ^{53}Cr NMR lineshapes. The class of *zcw* crystal files, ranging in size from 4180 to 28656, was employed. Lastly, problems of insufficient excitation were experienced when experimental pulse widths were used in the simulations; to avoid use of the stepped-frequency technique in these circumstances, much shorter pulses were used in lieu of the experimental pulses to properly excite the required spectral breadth.

6.2.2. Quantum Chemical Calculations

Non-relativistic and spin-orbit relativistic ZORA DFT¹⁰⁴ calculations of chromium magnetic shielding and EFG tensors were performed using the NMR module¹⁰⁷ of the ADF program.^{105,106} The TZ2P Slater-type ZORA basis sets, available with the ADF program, were employed for Cr and O. Calculations were performed on the isolated CrO_4^{2-} or $\text{Cr}_2\text{O}_7^{2-}$ anions. Idealized structures, which fulfilled the point group requirements of T_d and C_{2v} symmetry for CrO_4^{2-} or $\text{Cr}_2\text{O}_7^{2-}$ anions, respectively, served as the reference structures for the calculations. The idealized structures were generated using $r(\text{Cr}, \text{O}) = 1.6542 \text{ \AA}$ and $\angle(\text{O}, \text{Cr}, \text{O}) = 109.47^\circ$, for CrO_4^{2-} , and $r(\text{Cr}, \text{O}_{\text{terminal}}) = 1.63 \text{ \AA}$, $r(\text{Cr}, \text{O}_{\text{bridge}}) = 1.79 \text{ \AA}$, $\angle(\text{O}_{\text{terminal}}, \text{Cr}, \text{O}_{\text{terminal}}) = 109.47^\circ$, and $\angle(\text{Cr}, \text{O}_{\text{bridge}}, \text{Cr}) = 126^\circ$, for $\text{Cr}_2\text{O}_7^{2-}$. Structural modifications were then made to these idealized structures; specifically, $r(\text{Cr}, \text{O})$ and $\angle(\text{O}, \text{Cr}, \text{O})$ were varied for CrO_4^{2-} , and $\angle(\text{Cr}, \text{O}_{\text{bridge}}, \text{Cr})$ was varied for $\text{Cr}_2\text{O}_7^{2-}$, and the effects on the Cr EFG and shielding tensors were monitored.

6.3. Results and Discussion

6.3.1. Structure of A(I) and A(II) Chromate Salts

Before the ^{53}Cr NMR results are presented, a summary of relevant crystallographic information for the A(I) and A(II) chromate and A(I) dichromate salts investigated herein is given in Table 6.1. The crystal symmetry often provides useful information when analyzing NMR results; for example, the point symmetry of Cr in CaCrO_4 requires that the Cr EFG and shielding tensors be axially symmetric due to the presence of a four-fold inversion rotation axis, S_4 ; however, for the remaining chromate and dichromate salts, axially-symmetric Cr EFG and shielding tensors are not required by

the point group symmetry. The structures of the tetragonal and orthorhombic A(I) and A(II) chromate salts (Table 6.1) possess a crystallographic mirror plane in which the Cr atoms and two oxygen ligands lie; this imposes restrictions on the orientation of the Cr EFG and shielding tensors, as was previously demonstrated in *Chapter 5* in the analyses of the ^{95}Mo NMR spectra for the A(I) and A(II) molybdate and D_{2d} octacyanomolybdate(IV) salts.

Table 6.1: Summary of Structural Data for Chromate Salts

| Chromate | Space Group | Crystal Symmetry | Symmetry at Cr |
|---|-------------------|-----------------------------|----------------|
| $\text{Li}_2\text{CrO}_4 \cdot 2\text{H}_2\text{O}$ | $P2_12_12_1$ (19) | Orthorhombic ³²⁹ | 1 |
| K_2CrO_4 | $Pnam$ (62) | Orthorhombic ³³⁰ | m |
| Rb_2CrO_4 | $Pnam$ (62) | Orthorhombic ³³¹ | m |
| Ag_2CrO_4 | $Pmnb$ (62) | Orthorhombic ³³² | m |
| Cs_2CrO_4 | $Pnam$ (62) | Orthorhombic ³³³ | m |
| $\text{MgCrO}_4 \cdot 2\text{H}_2\text{O}$ | $Cmcm$ (63) | Orthorhombic ³³⁴ | mm |
| BaCrO_4 | $Pnma$ (62) | Orthorhombic ³³⁵ | m |
| CaCrO_4 | $I4_1/amd$ (141) | Tetragonal ³³⁶ | $\bar{4}2m$ |
| SrCrO_4 | $P2_1/n$ (14) | Monoclinic ³³⁷ | 1 |
| PbCrO_4 | $P2_1/n$ (14) | Monoclinic ³³⁷ | 1 |
| $\alpha\text{-K}_2\text{Cr}_2\text{O}_7$ | $P\bar{1}$ (2) | Triclinic ³³⁸ | 1 |
| $\text{Cs}_2\text{Cr}_2\text{O}_7$ | $P\bar{1}$ (2) | Triclinic ³³⁹ | 1 |

6.3.2. Solid-State ^{53}Cr NMR Studies of Chromate Salts

In the current study, all solid-state ^{53}Cr NMR spectra have been acquired using the QCPMG experiment, which has proven to be invaluable. Illustrated in Figure 6.2 are representative ^{53}Cr NMR spectra of MAS samples of Cs_2CrO_4 acquired using rotor synchronization; *i.e.*, $\tau \propto (n\nu_{\text{rot}})^{-1}$. From Figure 6.2, it is apparent that the S/N is greatly enhanced using the QCPMG experiment and, by choosing a sufficiently small ν_{QCPMG} value, 120 Hz, the overall envelope of the ^{53}Cr QCPMG lineshape (Figure 6.2(b)) is well-resolved, mimicking that obtained using the spin-echo experiment (Figure 6.2(a)). Significantly longer experiment times would clearly be required for the spectrum

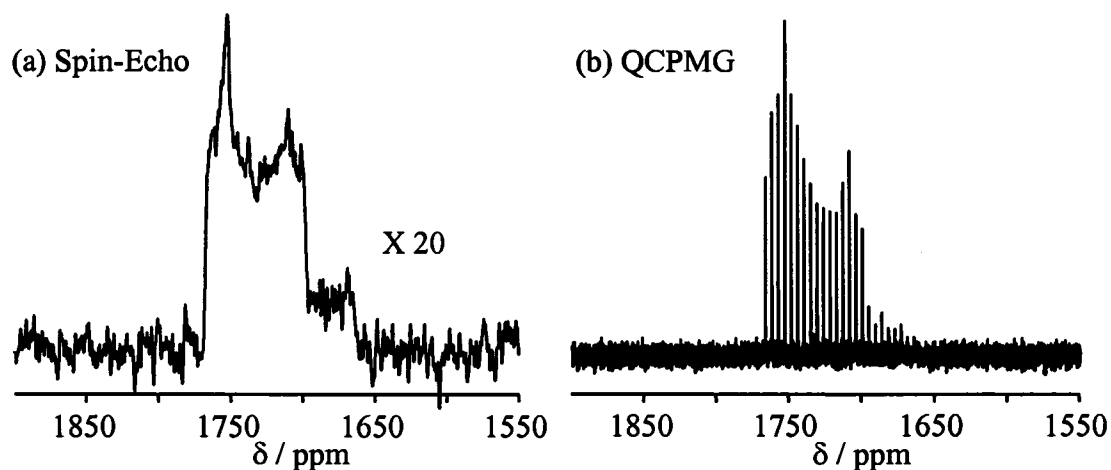


Figure 6.2: Solid-state ^{53}Cr NMR spectra of MAS samples of Cs_2CrO_4 acquired under identical experimental conditions at 11.75 T using a spinning rate of 6.000 kHz with a rotor-synchronized (a) spin-echo and (b) QCPMG pulse sequence, respectively. The vertical scale of the spectrum shown in (a) has been scaled by a factor of 20 to match that shown in (b).

acquired using the spin-echo experiment to be of comparable quality as that acquired using the QCPMG experiment.

In the following Section, solid-state ^{53}Cr NMR results will be presented, in sequence, for the A(I) chromates, the chromate hydrates and the A(II) chromates. Following the experimental NMR results, structural distortions of the chromates from T_d symmetry will be evaluated in an attempt to establish a trend with the observed $C_Q(^{53}\text{Cr})$ values. Before concluding with a comparison of experimental results for the chromate and molybdate salts, ZORA DFT calculations of Cr EFG and shielding tensors will be discussed.

Presented in Figure 6.3 are experimental and simulated ^{53}Cr QCPMG NMR spectra of stationary samples of the isomorphous orthorhombic A(I) = Cs, Rb, K, and Ag chromate salts acquired at 11.75 T and 18.8 T; the corresponding best-fit calculated parameters are given in Table 6.2. The well-defined ^{53}Cr NMR lineshapes are characteristic of those dominated by the second-order quadrupolar interaction; consequently, the ^{53}Cr NMR lineshapes are significantly reduced at 18.8 T, due to the inverse scaling of the second-order quadrupolar broadening with B_0^2 (in ppm). The Cr quadrupolar coupling constants, $C_Q(^{53}\text{Cr})$, for Cs, K, and Rb chromate are relatively small, *i.e.*, < 2 MHz, and their lineshapes are sufficiently narrow to be acquired in a

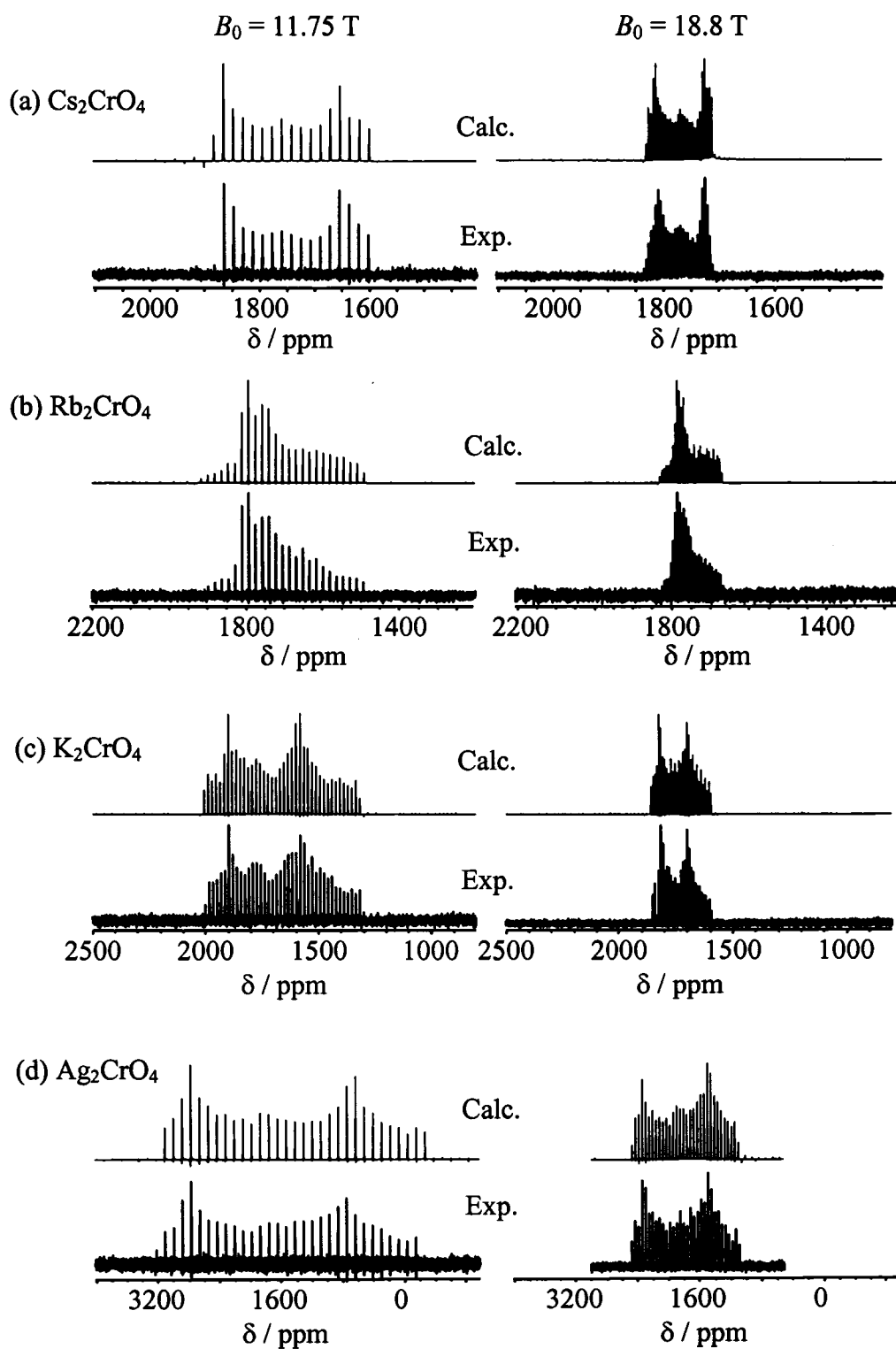


Figure 6.3: Simulated (top) and experimental (bottom) QCPMG ^{53}Cr NMR spectra of stationary samples of (a) Cs_2CrO_4 , (b) Rb_2CrO_4 , (c) K_2CrO_4 , and (d) Ag_2CrO_4 acquired at 11.75 T (left) and 18.8 T (right); the best-fit parameters are given in Table 6.2.

Table 6.2: Experimentally-Determined Cr Quadrupolar and Shielding Parameters for A(I) and A(II) Chromate and A(I) Dichromate Salts.

| | $\delta_{\text{iso}} / \text{ppm}$ | C_Q / MHz | η_Q | Ω / ppm | κ | $\alpha, \beta, \gamma / ^\circ$ |
|--|------------------------------------|--------------------|-------------|-----------------------|--------------|----------------------------------|
| A(I)₂CrO₄ | | | | | | |
| Li (1) | 1735 ± 15 | 4.00 ± 0.06 | 0.30 ± 0.05 | ----- | ----- | ----- |
| Li (2) | 1780 ± 15 | 1.80 ± 0.10 | 0.15 ± 0.10 | ----- | ----- | ----- |
| K | 1762 ± 4 | 1.76 ± 0.30 | 0.43 ± 0.05 | 20 ± 10 | 0.15 ± 0.10 | 10 ± 10, 90, 0 |
| Rb | 1773 ± 2 | 1.28 ± 0.02 | 0.80 ± 0.03 | 30 ± 5 | -0.7 ± 0.2 | 0 ± 20, 90, 0 |
| Cs | 1778 ± 4 | 1.23 ± 0.02 | 0.23 ± 0.02 | 28 ± 5 | -0.95 ± 0.05 | 90, 8 ± 3, 0 |
| Ag | 1985 ± 5 | 4.10 ± 0.05 | 0.28 ± 0.03 | 100 ± 30 | 0.0 ± 0.3 | 0, 0, 0 |
| A(II)CrO₄ | | | | | | |
| Mg | 1730 ± 10 | 2.62 ± 0.05 | 0.38 ± 0.03 | ----- | ----- | ----- |
| Ca | 1680 ± 10 | 4.55 ± 0.05 | 0.00 | ----- | ----- | ----- |
| Sr | 1770 ± 20 | 5.0 ± 0.1 | 0.68 ± 0.05 | ----- | ----- | ----- |
| Ba | 1750 ± 20 | 5.00 ± 0.05 | 0.14 ± 0.03 | ----- | ----- | ----- |
| Pb | 1865 ± 20 | 4.4 ± 0.1 | 0.85 ± 0.05 | ----- | ----- | ----- |
| A(I)₂Cr₂O₇ | | | | | | |
| Cs | 1780 ± 30 | 7.25 ± 0.10 | 0.30 ± 0.05 | ----- | ----- | ----- |
| K (1) | 1775 ± 50 | 7.48 ± 0.10 | 0.30 ± 0.05 | ----- | ----- | ----- |
| K (2) | 1730 ± 50 | 8.28 ± 0.10 | 0.21 ± 0.05 | ----- | ----- | ----- |

single experiment at both 11.75 T and 18.8 T (see *Appendix 6.1*). In contrast, $C_Q(^{53}\text{Cr})$ for Ag_2CrO_4 is significantly larger, corresponding to a breadth of ~64 kHz at 18.8 T, thus, necessitating use of the stepped frequency technique at both magnetic fields.

Deviation of the Cr EFG tensors from axial symmetry is apparent for the isomorphous A(I) = Cs, Rb, K, Ag chromates, consistent with their crystal symmetry, which indicates the absence of a C_n ($n \geq 3$) axis. The highest asymmetry parameter, found for Rb_2CrO_4 , is reflected in its ^{53}Cr NMR lineshapes, which are significantly different from those for Cs, K, and Ag chromate.

The measured anisotropy of the Cr shielding tensor is generally small for the A(I) chromates, with the largest value being 100 ± 30 ppm for Ag_2CrO_4 ; see Table 6.2. The small shielding anisotropies are not surprising given that the CrO_4^{2-} anions are d^0 -systems. The absence of Cr d -electrons indicates there are no low-lying d -dominated molecular orbitals, which are often the origin of large shielding anisotropies. Despite the minor contribution from Ω , agreement between the simulated and experimental spectra for the A(I) chromates has been found to improve significantly when Ω is included, particularly for Cs_2CrO_4 . That spectra have been acquired at two magnetic fields of considerable strength has allowed the Cr EFG and shielding parameters, as well as the relative orientation of their tensors, to be determined with reasonable accuracy. For K and Rb chromate, the relative orientation of the Cr EFG and shielding tensors is the same, within experimental error, with the following pairs of principal components being coincident: V_{ZZ} and σ_{11} , V_{YY} and σ_{22} , and V_{XX} and σ_{33} . For Ag_2CrO_4 , the Cr EFG and shielding tensors share the same PAS, while, for Cs chromate: V_{YY} and σ_{11} are coincident and V_{ZZ} and σ_{33} and V_{XX} and σ_{22} are roughly coincident. These orientations were determined by visual inspection of the experimental and simulated ^{53}Cr NMR spectra at 11.75 and 18.8 T.

QCPMG ^{53}Cr NMR spectra for the chromate hydrates, $\text{Li}_2\text{CrO}_4 \cdot 2\text{H}_2\text{O}$ and $\text{MgCrO}_4 \cdot 2\text{H}_2\text{O}$, are presented in Figure 6.4 and the calculated parameters are given in Table 6.2. Of the compounds investigated, the hydrated chromates were most problematic, from an experimental point-of-view, because of their naturally short T_2 values. This reduced the robustness of the QCPMG experiment by limiting the number of π -pulses that could gainfully be applied in a single scan. Degradation of the ^{53}Cr FID was amplified at the higher magnetic field, thus counteracting the gain in signal-to-noise that would normally be achieved; this is particularly visible in the ^{53}Cr NMR spectrum of $\text{MgCrO}_4 \cdot 2\text{H}_2\text{O}$, where $T_{2,\text{eff}} \sim 15$ ms at 11.75 T and $T_{2,\text{eff}} < 5$ ms at 18.8 T. Regardless of the T_2 degradation, the quality of the spectra at the two magnetic fields sufficed to analyze the results. Only contributions from the Cr quadrupolar interaction were considered and resultant $C_Q(^{53}\text{Cr})$ values of 3.96 MHz and 2.62 MHz for $\text{Li}_2\text{CrO}_4 \cdot 2\text{H}_2\text{O}$ and $\text{MgCrO}_4 \cdot 2\text{H}_2\text{O}$, respectively, were found. The small $C_Q(^{53}\text{Cr})$ for $\text{MgCrO}_4 \cdot 2\text{H}_2\text{O}$ allowed the ^{53}Cr NMR spectra to be acquired in a single experiment, whereas several

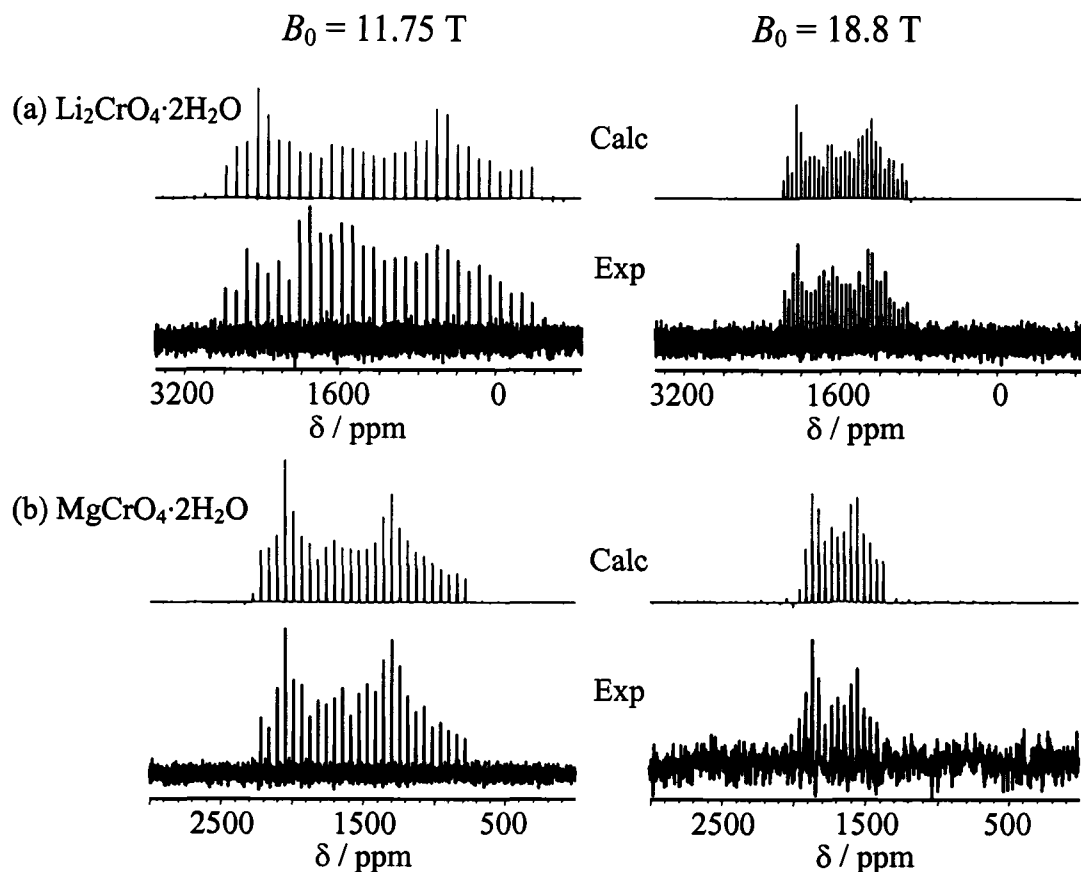


Figure 6.4: Simulated (top) and experimental (bottom) QCPMG ^{53}Cr NMR spectra of stationary samples of (a) $\text{Li}_2\text{CrO}_4 \cdot 2\text{H}_2\text{O}$ and (b) $\text{MgCrO}_4 \cdot 2\text{H}_2\text{O}$ acquired at 11.75 T (left) and 18.8 T (right); the best-fit parameters are given in Table 6.2.

steps were required for $\text{Li}_2\text{CrO}_4 \cdot 2\text{H}_2\text{O}$ at both fields (see *Appendix 6.1*). The ^{53}Cr NMR spectra of $\text{Li}_2\text{CrO}_4 \cdot 2\text{H}_2\text{O}$ show evidence of a second Cr species, with a significantly smaller $C_Q(^{53}\text{Cr})$ value, near the central portion of the powder pattern. Since the crystal structure for $\text{Li}_2\text{CrO}_4 \cdot 2\text{H}_2\text{O}$ indicates a single Cr site, the central site is attributed to a known form of anhydrous Li_2CrO_4 (hexagonal, $R\text{-}3$ space group), labelled as Li(2) in Table 6.2.³⁴⁰ The simulated spectra shown in Figure 6.4 do not take into account this second site; however, the quadrupolar parameters have been estimated and are given in Table 6.2.

The final class of chromate salts that is investigated herein are the A(II) = Ca, Sr, Ba, Pb, chromates; the experimental and simulated ^{53}Cr QCPMG NMR spectra of the A(II) chromates are shown in Figure 6.5 and the corresponding best-fit parameters are given in Table 6.2. In general, the ^{53}Cr NMR lineshapes exceeded the pulse excitation

profile, thus requiring the spectra to be acquired using the stepped-frequency technique, as summarized in *Appendix 6.1*. The measured $C_Q(^{53}\text{Cr})$ values for the A(II) chromates are notably larger than those for the A(I) chromates due to greater distortions in the CrO_4^{2-} anion from tetrahedral symmetry. For CaCrO_4 , the Cr EFG tensor is necessarily axially symmetric, as dictated by the crystal symmetry, whereas those for SrCrO_4 , BaCrO_4 , and PbCrO_4 deviate from axial symmetry to different extents, as reflected in their respective ^{53}Cr NMR lineshapes. The ^{53}Cr NMR spectra of the A(II) chromates could be adequately simulated at the magnetic fields employed here with contributions from the Cr quadrupolar interaction alone. Given the magnitude of the observed $C_Q(^{53}\text{Cr})$ values, effects from the anisotropic Cr shielding interaction are negligible. Inclusion of Cr shielding anisotropies comparable to those found for the A(I) chromates, *i.e.*, $\Omega \leq 100$ ppm, had no apparent effect on the observed ^{53}Cr NMR lineshapes.

When discussing the ^{53}Cr NMR spectra of the chromate salts, it is important to recognize the possibility of motion of the CrO_4^{2-} anions, which may influence the lineshapes and breadths of the observed ^{53}Cr NMR spectra. This phenomenon was previously observed for several quadrupolar nuclei, $^{185/187}\text{Re}$, ^{55}Mn , ^{75}As , in prototypal XO_4 -compounds in a solid-state NMR and computational study by Schurko and co-workers.²⁶¹ In this study, a variety of lineshapes were found to arise due to rotational and chemical exchange processes. By carrying out variable-temperature studies, insight into motional processes was provided through predictable changes in the observed lineshapes and breadth as a function of temperature. Effects on the NMR spectra, and the measured quadrupolar coupling constants, were not consistent for all systems examined; in fact, both an increase and a decrease in the effective C_Q values were found for different systems when the temperature was decreased. In the present ^{53}Cr NMR study of chromate salts, investigating the presence of motion of the CrO_4^{2-} anions is not practical, given the existing difficulties associated with ^{53}Cr NMR studies at a single temperature.

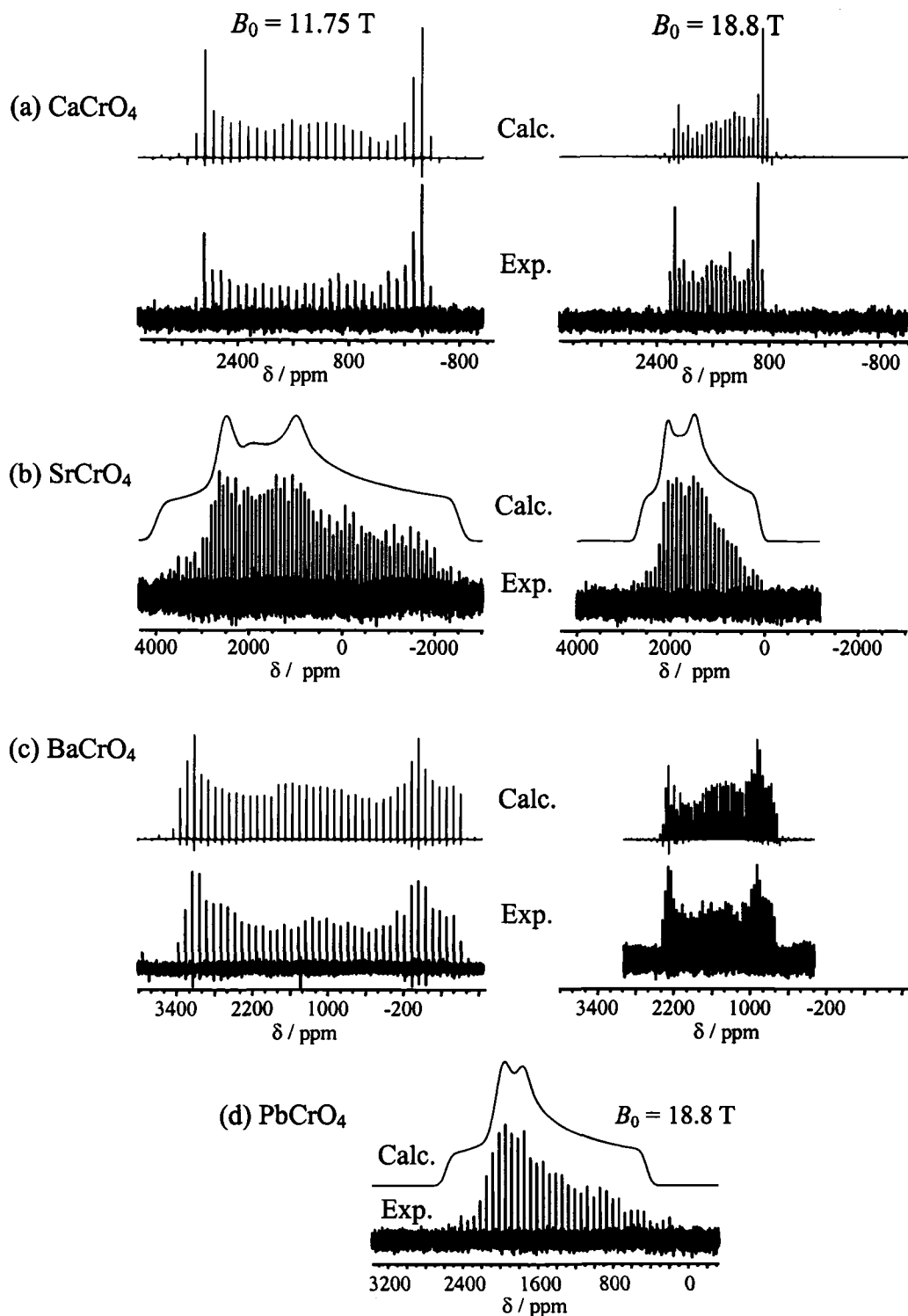


Figure 6.5: Simulated (top) and experimental (bottom) QCPMG ^{53}Cr NMR spectra of stationary samples of (a) CaCrO_4 , (b) SrCrO_4 , (c) BaCrO_4 , and (d) PbCrO_4 acquired at 11.75 T (left) and 18.8 T (right); the best-fit parameters are given in Table 6.2.

6.3.3. Relating Cr NMR Parameters to Structure

Considerable efforts have been made to correlate structural features, such as bond length and bond angle, with NMR parameters, such as δ_{iso} , ${}^1J(N, N')_{\text{iso}}$, and C_Q . These relationships are generally empirically-based and are supported by, often hand-waving arguments, such as electronegativity, electron density, and *s*-hybridization of orbitals; nevertheless, empirical relationships can provide useful structural information when the arguments are sound and strong correlations are found. Experimentally-determined correlations are often valid for specific compound-types; for example, a linear relationship has been found between $\delta({}^{29}\text{Si})_{\text{iso}}$ and $r(\text{Si}, \text{O})$, as well as $\delta({}^{29}\text{Si})_{\text{iso}}$ and $\langle \text{O}, \text{Si}, \text{O} \rangle$ for a group of 20 silicates.³⁴¹ A second example, determined by Bryce and Wasylishen in their preliminary ${}^{53}\text{Cr}$ NMR study,³²⁷ is an apparent trend between the largest deviation of $\langle \text{O}, \text{Cr}, \text{O} \rangle$ from 109.47° and the measured $C_Q({}^{53}\text{Cr})$ values for three chromate salts: Cs_2CrO_4 , K_2CrO_4 , and $(\text{NH}_4)_2\text{CrO}_4$; however, a more accurate approach would consider the average of the six possible $\langle \text{O}, \text{Cr}, \text{O} \rangle$ values rather than the single, largest deviation of $\langle \text{O}, \text{Cr}, \text{O} \rangle$ from 109.47° .

The argument that a direct correlation between $C_Q({}^{53}\text{Cr})$ and local structural distortions of the CrO_4^{2-} anion from T_d symmetry should exist is intuitive, based on the Point-Charge Approximation (Section 2.5.3.). To assess the validity of such an argument for the A(I) and A(II) chromates studied herein, the following structure parameters were calculated using available crystal data: the bond length distortion, Δr ,

$$\Delta r = \frac{1}{4} \sum_{i=1}^4 \left[\frac{r_i - r_{\text{avg}}}{r_{\text{avg}}} \right]^2 \quad (6.1)$$

and bond angle variance, σ^2 ,

$$\sigma^2 = \frac{1}{5} \sum_{i=1}^6 \left(\theta_i - 109.47^\circ \right)^2, \quad (6.2)$$

where, r_i and r_{avg} are the individual and average Cr, O internuclear bond lengths, respectively, θ_i is the i^{th} $\langle \text{O}, \text{Cr}, \text{O} \rangle$ and 109.47° is the angle for an ideal tetrahedron; these values, along with δ_{iso} , C_Q and η_Q , are summarized in Appendix 6.2 for the A(I) and A(II) chromates and plots of δ_{iso} versus Δr and $C_Q({}^{53}\text{Cr})$ versus σ^2 are shown in Figure 6.6(a) and (b), respectively.

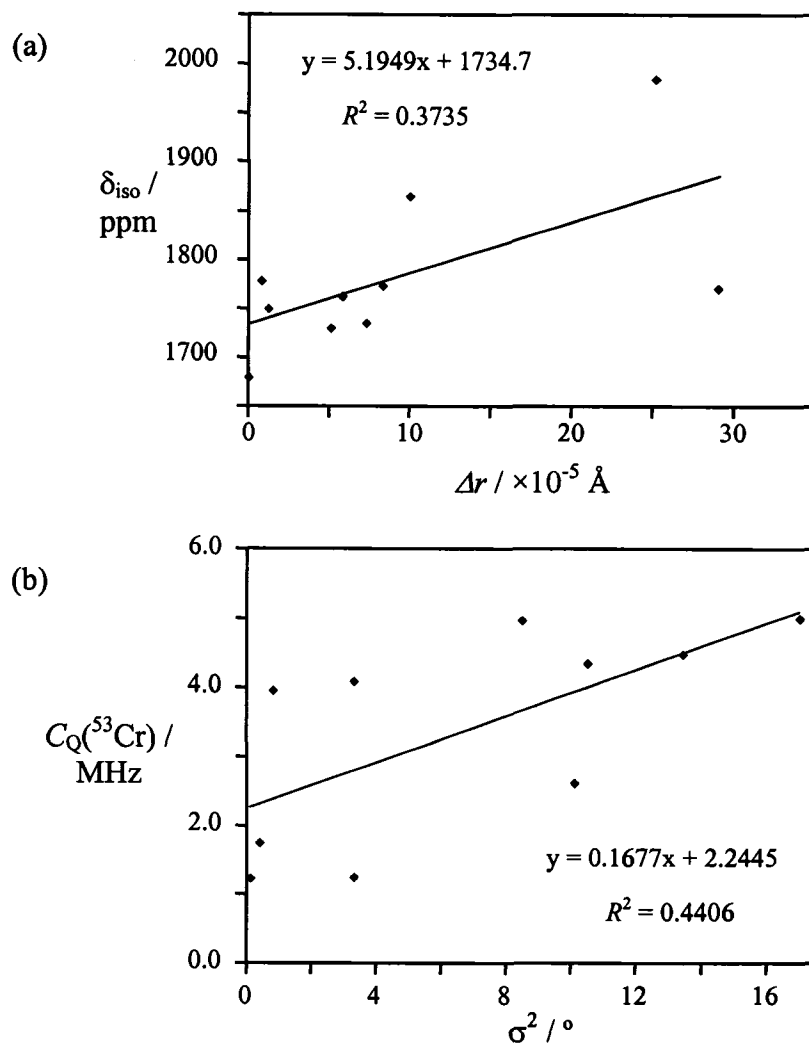


Figure 6.6: Dependence of experimentally-determined δ_{iso} and $C_Q(^{53}\text{Cr})$ values on structural parameters, Δr and σ^2 , respectively, for the A(I) and A(II) chromates. Structural parameters, Δr and σ^2 , were calculated using Equations 6.1 and 6.2, respectively, and available crystal data; these values are tabulated in *Appendix 6.2*.

To conclude that a direct relationship between the structural parameters and NMR parameters holds for the A(I) and A(II) chromates would be an overstatement. From Figure 6.6, it is clear that the correlation between δ_{iso} and Δr and between $C_Q(^{53}\text{Cr})$ and σ^2 is extremely poor, as evidenced by the R^2 values. The lack of agreement is not surprising since all structural distortions collectively contribute to the resultant δ_{iso} and $C_Q(^{53}\text{Cr})$ values. This suggests that, in addition to contributions from the local

environment, the extended lattice must make significant contributions to the EFG; to investigate this further, the DFT-based program, WIEN2k,³⁴² could be employed.

To further investigate the effects of local structural imperfections on the magnitude of the Cr EFG and anisotropic Cr shielding values for the A(I) and A(II) chromates, ZORA DFT calculations were employed. The reference structure for the chromate anion was constructed such that the requirements of T_d symmetry; *i.e.*, $\angle(\text{O}, \text{Cr}, \text{O}) = 109.47^\circ$, were fulfilled and $r(\text{Cr}, \text{O}) = 1.6542 \text{ \AA}$. Induced structural manipulations of the chromate anion included modifying a *single* Cr, O bond length about its reference value by $\pm 10\%$ and varying a single $\angle(\text{O}, \text{Cr}, \text{O})$ value from T_d symmetry by $\pm 10^\circ$. The effects of these forced distortions on $C_Q(^{53}\text{Cr})$ and the anisotropy, or span, of the Cr shielding tensor, Ω , were monitored and selected results are plotted in Figure 6.7.

Upper and lower experimental limits for the Cr, O bond lengths and (O, Cr, O) bond angles for the A(I) and A(II) chromates can be established from available crystal structure data. Since in the calculations, a single Cr, O bond length and a single (O, Cr, O) bond angle were independently modified, the upper and lower experimental limits for $r(\text{Cr}, \text{O})$ and $\angle(\text{O}, \text{Cr}, \text{O})$ involve the shortest and longest individual Cr, O bond lengths and the smallest and largest (O, Cr, O) angles; boundaries can be established for each of the A(I) and A(II) chromates. Taking into account the bond length criteria from crystal structure data and referring to Figure 6.7 indicates that $-2.2 \text{ MHz} \leq C_Q(^{53}\text{Cr}) \leq +4.5 \text{ MHz}$ are predicted for A(I) chromates and $-8.6 \text{ MHz} \leq C_Q(^{53}\text{Cr}) \leq +8.6 \text{ MHz}$ for the A(II) chromates. Similarly, based on bond angle criteria, ZORA DFT results predict: $-5 \text{ MHz} \leq C_Q(^{53}\text{Cr}) \leq +10 \text{ MHz}$ for the A(I) chromates and $-10 \text{ MHz} \leq C_Q(^{53}\text{Cr}) \leq +10 \text{ MHz}$ for the A(II) chromates. Lastly, ZORA DFT calculations predict $\Omega < 80 \text{ ppm}$ for both the A(I) and A(II) chromates. The ZORA DFT calculated results for the Cr EFG and shielding tensors correctly indicate that larger $C_Q(^{53}\text{Cr})$ values are found for the A(II) than the A(I) chromates and small Cr shielding anisotropies are predicted. Based on the calculated results, the (O, Cr, O) bond angle has a more profound effect on $C_Q(^{53}\text{Cr})$ than the internuclear Cr, O distance. Secondly, ZORA DFT calculations correctly predict that the Cr EFG tensor is extremely sensitive to local structural changes in the CrO_4^{2-} anion

and that contributions from the anisotropic Cr shielding are generally small; *i.e.*, $\Omega < 100$ ppm. Although the ZORA DFT calculations serve as a useful guide for assessing the

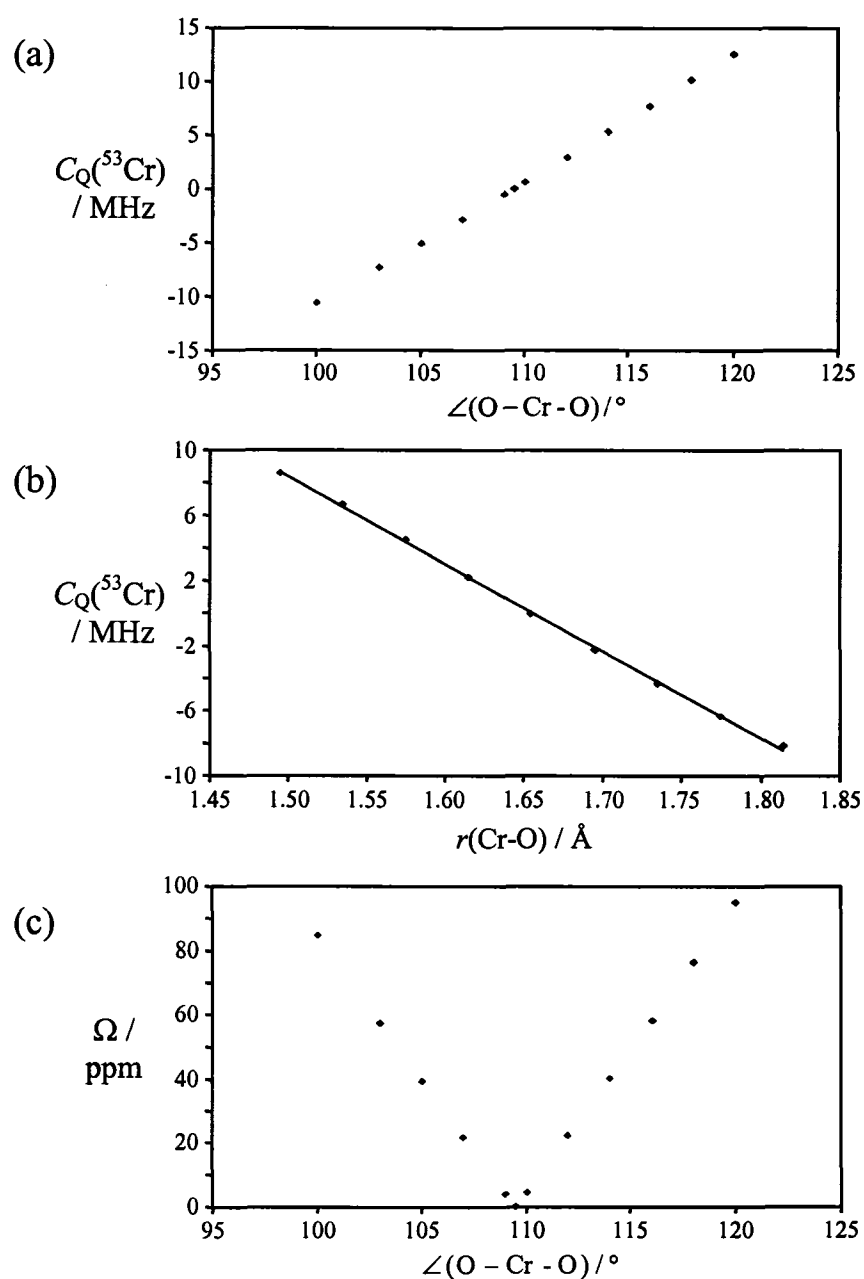


Figure 6.7: ZORA DFT results of the effects of (a) $\angle(\text{O}, \text{Cr}, \text{O})$ and (b) $r(\text{Cr}, \text{O})$ on $C_Q(^{53}\text{Cr})$ and (c) $\angle(\text{O}, \text{Cr}, \text{O})$ on the Cr shielding anisotropy, Ω , for the chromate anion, CrO_4^{2-} .

importance of specific, isolated structural distortions on the Cr EFG and shielding tensors, the results cannot be taken too literally. For the results to be more meaningful, cumulative effects from multiple structural distortions would have to be considered.

6.3.4. Comparison of NMR Results for the Chromate and Molybdate Salts

In the solid-state ^{53}Cr NMR study carried out by Bryce and Wasylshen,³²⁷ the ^{53}Cr NMR results for $\text{Cr}(\text{CO})_6$ were found to match the ^{95}Mo NMR results for $\text{Mo}(\text{CO})_6$ ²⁴⁷ remarkably well; in fact, the magnitude of the Cr and Mo shielding anisotropies, Ω , and the relative orientation of the Cr shielding and EFG tensors were identical within experimental error. The ratio of the measured quadrupolar coupling constants, $C_Q(^{53}\text{Cr})/C_Q(^{95}\text{Mo}) = 1.75$, was found to be reduced from the expected, 'theoretical' value; *i.e.*, the ratio of their quadrupole moments, $Q(^{53}\text{Cr})/Q(^{95}\text{Mo}) = 6.8$. To compare EFG and shielding parameters between different compounds, the compounds must be isomorphous. Of all the molybdate and chromate salts investigated, only the Cs salt maintains the same structure (orthorhombic $Pnma$) in both the molybdate and chromate salts. The measured EFG and shielding parameters for Cs_2MoO_4 and Cs_2CrO_4

Table 6.3: Comparison of Cr and Mo Quadrupolar and Shielding Parameters for Isomorphous Cs_2MoO_4 and Cs_2CrO_4 .

| | Cs_2MoO_4 | Cs_2CrO_4 |
|-----------------------------|---------------------------|---------------------------|
| δ_{iso} / ppm | 1832* | 1778 |
| C_Q / MHz | 0.34 | 1.23 |
| η_Q | 0.45 | 0.23 |
| Ω / ppm | 30 | 28 |
| κ | -0.50 | -0.95 |
| α, β, γ / ° | 0, 90, 0 | 90, 8 ± 3 , 0 |

* The δ_{iso} value for Cs_2MoO_4 given here is with respect to solid $\text{Mo}(\text{CO})_6$, *i.e.*, $[\delta_{\text{iso}}(\text{Cs}_2\text{MoO}_4) - \delta_{\text{iso}}(\text{Mo}(\text{CO})_6)]$ where $\delta_{\text{iso}}(\text{Mo}(\text{CO})_6) = -1854$ ppm and $\delta_{\text{iso}}(\text{Cs}_2\text{MoO}_4) = -22.0$ ppm (see Chapter 5); this allows more meaningful comparison between the chemical shift values for isomorphous Cs_2CrO_4 and Cs_2MoO_4 , due to their different respective primary NMR reference compounds.

are summarized in Table 6.3. Although the shielding anisotropy is comparable for the two systems, the skew of the shielding tensors and the relative orientation of the EFG and shielding tensors differ; nevertheless, the NMR results for both Cs_2CrO_4 and Cs_2MoO_4 are consistent with the symmetry requirements imposed by the $Pnma$ Space Group. The ratio of the C_Q values observed for Cs_2CrO_4 and Cs_2MoO_4 , $C_Q(^{53}\text{Cr})/C_Q(^{95}\text{Mo}) = 3.62$, is less than the theoretical value of 6.8, similar to the result found for $\text{Cr}(\text{CO})_6$ and $\text{Mo}(\text{CO})_6$. Given the structural differences in the chromate and molybdate salts, such as variation in bond lengths and bond angles, this is not surprising since even subtle structural changes are reflected in the Cr and Mo EFG tensors and, hence, their C_Q values. These results demonstrate that the chromium quadrupole moment significantly amplifies the EFGs for $\text{Cr}(\text{CO})_6$ and Cs_2CrO_4 .

In *Chapter 5*, ^{95}Mo NMR results for molybdate salts were presented and it was shown that the Mo shielding anisotropy was significant and had a comparable effect on the ^{95}Mo NMR lineshapes as the quadrupolar interaction. The current ^{53}Cr NMR study indicates that the Cr shielding anisotropies are small, but non-negligible, for the A(I) chromate salts, and negligible for the A(II) chromates and chromate hydrates. The smaller $C_Q(^{53}\text{Cr})$ values observed for the A(I) chromates balance the discrepancy in magnitude between the quadrupolar and shielding interactions and allow small shielding anisotropies to be measured. Alternatively, the measured $C_Q(^{53}\text{Cr})$ values are significantly larger for the A(II) chromate salts, thus diminishing the importance of the anisotropic Cr shielding interaction. Overall, these results demonstrate the sensitivity of the Cr quadrupolar interaction, which is a consequence of the large Cr quadrupole moment compared to that of ^{95}Mo ; this is explicitly demonstrated in a survey of observed C_Q values for the A(I) and A(II) chromate and molybdate salts, shown in Figure 6.8.

From Figure 6.8, two generalizations can be made: first, C_Q values for the chromates are consistently larger than those for the molybdates, as expected, based on the much larger value of the chromium quadrupole moment relative to that of molybdenum. This resulted in broad ^{53}Cr NMR lineshapes and generally precluded the study of MAS samples, due to spinning speeds that were insufficient compared to the ^{53}Cr quadrupolar interaction; for stationary samples, use of the QCPMG pulse sequence in combination with the stepped-frequency technique was often necessary. In contrast, ^{95}Mo NMR

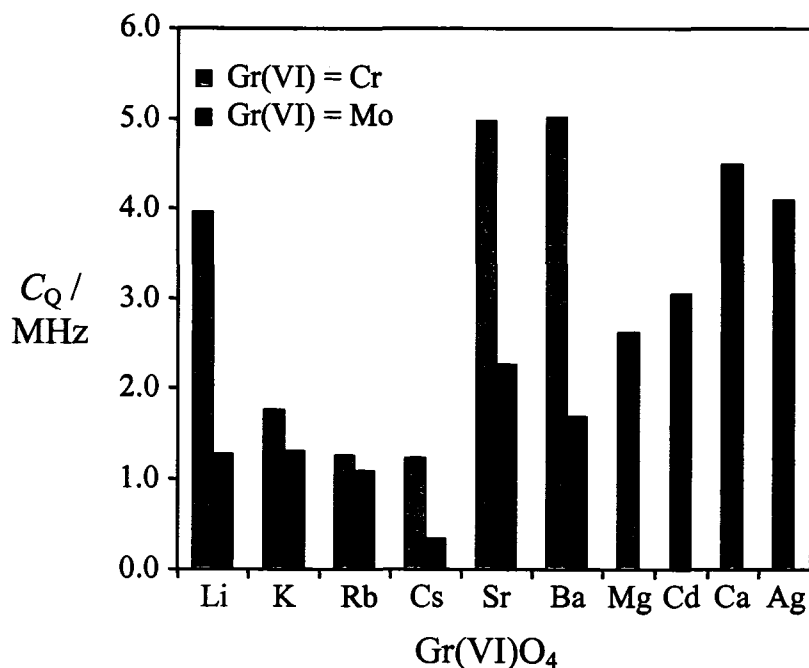


Figure 6.8: Survey of experimentally-determined ^{53}Cr and ^{95}Mo quadrupolar coupling constants for selected A(I) and A(II) chromate and molybdate salts.

spectra were acquired for MAS and stationary samples using single experiments and conventional one-pulse or spin-echo pulse sequences.

The second point to note from the plot in Figure 6.8 is that the C_Q values for both the A(II) chromate and A(II) molybdate salts are significantly greater than those for the analogous A(I) salts. The calculated structural distortion parameters, Δr and σ^2 , for the A(II) chromates and molybdates are consistently larger than those for the A(I) chromates (*Appendix 6.2*). Attempts to correlate the observed $C_Q(^{53}\text{Cr})$ and $C_Q(^{95}\text{Mo})$ values with Δr and σ^2 for the chromate and molybdate salts are contradictory: for Mo, the results suggest a correlation between C_Q and σ^2 ; however, several anomalies in the analysis reduce the assurance of this result. For Cr, the results weakly suggest a relationship between C_Q and σ^2 . Unfortunately, the incomplete list of reliable structural data for the chromate and molybdate salts prevents further conclusions to be drawn.

6.3.5. Solid-State ^{53}Cr NMR Studies of Dichromate Salts

Success of the ^{53}Cr NMR experiments for the A(I) and A(II) chromate salts encouraged examination of a more challenging system - the dichromate anion, $\text{Cr}_2\text{O}_7^{2-}$.

In a dichromate anion, the two Cr atoms are linked via a bridging oxygen ligand. Although the dichromate anion is structurally simple, distortions from tetrahedral symmetry about each Cr atom add a level of difficulty to ^{53}Cr NMR experiments that surpasses that for the chromates. Terminal Cr, O bond lengths for the chromate salts are approximately $1.65 \pm 0.03 \text{ \AA}$, while bridging Cr, O bond lengths are significantly longer, $1.77 \pm 0.03 \text{ \AA}$, and the angle involving the bridging oxygen ligand and the two Cr atoms, Cr, O_{bridge}, Cr, is widened considerably, $\sim 124^\circ$,³³⁸ relative to the ideal tetrahedral value of 109.47° . These structural differences are expected to induce large EFGs at Cr and test the boundaries of solid-state ^{53}Cr NMR studies.

Here, two dichromate salts, $\text{Cs}_2\text{Cr}_2\text{O}_7$ and $\text{K}_2\text{Cr}_2\text{O}_7$, have been examined using solid-state ^{53}Cr NMR at a single applied magnetic field, 18.8 T. The dichromate anion adopts a staggered conformation in $\text{Cs}_2\text{Cr}_2\text{O}_7$, which is triclinic; the presence of an inversion center requires the two Cr atoms to be magnetically equivalent. For potassium dichromate, two polymorphs with monoclinic and triclinic structures have been reported. The former, $\beta\text{-K}_2\text{Cr}_2\text{O}_7$,³⁴³ has a formal C_2 -axis, forcing the two Cr atoms to be crystallographically equivalent; however, the absence of an inversion center for the eclipsed configuration renders the two Cr atoms magnetically non-equivalent. The latter, $\alpha\text{-K}_2\text{Cr}_2\text{O}_7$,³³⁸ has a near C_2 -axis; hence, the two Cr atoms are both crystallographically and magnetically non-equivalent. The monoclinic polymorph, $\beta\text{-K}_2\text{Cr}_2\text{O}_7$, is metastable at room temperature and converts to the triclinic form when the sample is physically ground.³⁴⁴ For K dichromate, the polymorph investigated herein is triclinic $\alpha\text{-K}_2\text{Cr}_2\text{O}_7$.

QCPMG ^{53}Cr NMR spectra of stationary samples of $\text{Cs}_2\text{Cr}_2\text{O}_7$ and $\alpha\text{-K}_2\text{Cr}_2\text{O}_7$ have been acquired at 18.8 T using the stepped-frequency technique and are shown in Figure 6.9. For $\text{Cs}_2\text{Cr}_2\text{O}_7$, five sub-spectra were required to obtain the whole ^{53}Cr NMR spectrum, the breadth of which is approximately 210 kHz. The ^{53}Cr NMR spectrum for $\alpha\text{-K}_2\text{Cr}_2\text{O}_7$ is somewhat broader, 250 kHz, and is comprised of six sub-spectra. Given the excessive breadths of the ^{53}Cr NMR lineshapes, the quality of the spectra and the required experiment times, 11.4 hrs and 7.3 hrs for $\text{Cs}_2\text{Cr}_2\text{O}_7$ and $\alpha\text{-K}_2\text{Cr}_2\text{O}_7$, respectively, are impressive. In analyzing the ^{53}Cr NMR spectra of Cs and K dichromate, the Cr shielding anisotropy was neglected. For $\alpha\text{-K}_2\text{Cr}_2\text{O}_7$, two Cr sites were included in the simulation, each with different chemical shifts and quadrupolar parameters: $\delta_{\text{iso}}(1) =$

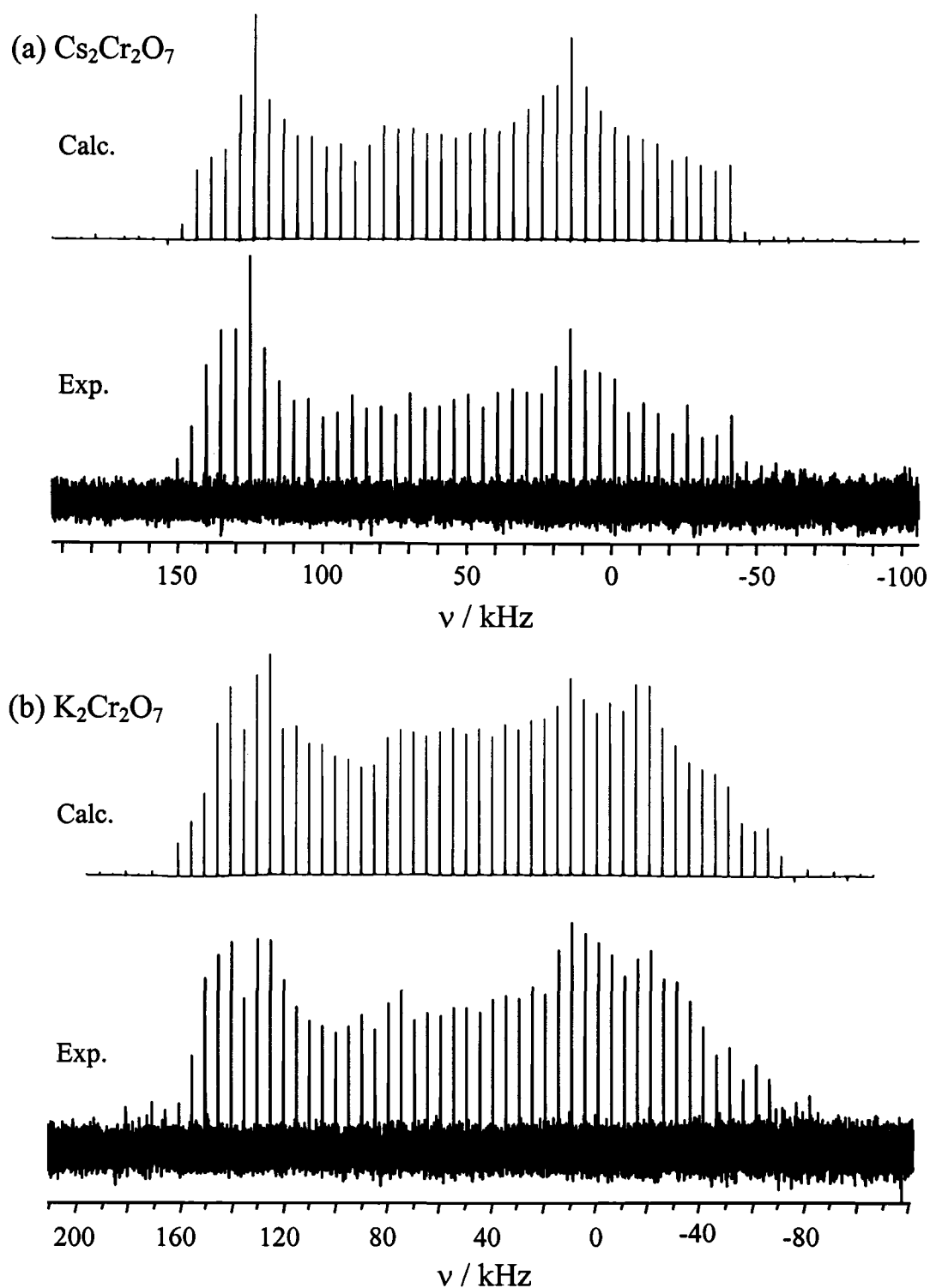


Figure 6.9: Simulated (top) and experimental (bottom) solid-state ^{53}Cr NMR spectra of stationary samples of (a) $\text{Cs}_2\text{Cr}_2\text{O}_7$ and (b) $\alpha\text{-K}_2\text{Cr}_2\text{O}_7$ acquired using the stepped-frequency QCPMG experiment with $\nu_{\text{QCPMG}} = 5$ kHz and $B_0 = 18.8$ T. The best-fit simulated parameters are given in the text and in Table 6.2.

1775 ± 50 ppm, $C_Q(1) = 7.48 \pm 0.10$ MHz, $\eta_Q(1) = 0.30 \pm 0.05$; $\delta_{\text{iso}}(2) = 1730 \pm 50$ ppm, $C_Q(2) = 8.28 \pm 0.10$ MHz, $\eta_Q(2) = 0.21 \pm 0.05$, while only one site was required for $\text{Cs}_2\text{Cr}_2\text{O}_7$: $\delta_{\text{iso}} = 1780 \pm 30$ ppm, $C_Q = 7.25 \pm 0.10$ MHz, $\eta_Q = 0.30 \pm 0.05$. Fortuitously, the isotropic Cr chemical shift, quadrupolar coupling constant and asymmetry parameter for *site 1* (Table 6.2) in $\alpha\text{-K}_2\text{Cr}_2\text{O}_7$ are similar to those for $\text{Cs}_2\text{Cr}_2\text{O}_7$ (Table 6.2). The absence of a three-fold, or higher, principal rotation axis does not impose symmetry restrictions on the Cr EFG tensors for $\text{Cs}_2\text{Cr}_2\text{O}_7$ and $\alpha\text{-K}_2\text{Cr}_2\text{O}_7$, resulting in their significant deviations from axial symmetry.

To investigate the role of structural distortions on the dichromate anion, $\text{Cr}_2\text{O}_7^{2-}$, ZORA DFT calculations of the Cr EFG and shielding tensors were performed and the results are summarized in the graphs shown in Figure 6.10. The reference structure for the dichromate anion was given an eclipsed, idealized structure that obeyed the C_{2v} point group symmetry. Structural manipulations involved varying $\angle(\text{Cr}, \text{O}_{\text{bridge}}, \text{Cr})$ while monitoring the effects on the ^{53}Cr quadrupolar coupling constant, quadrupolar asymmetry parameter, and shielding anisotropy. According to the crystal structure for $\alpha\text{-K}_2\text{Cr}_2\text{O}_7$, $\angle(\text{Cr}, \text{O}_{\text{bridge}}, \text{Cr}) = 124^\circ$; referring to the graphs in Figure 6.10, this particular angle corresponds to calculated values of: $C_Q(^{53}\text{Cr}) \sim -12$ MHz, $\eta_Q \sim 0.25$, and $\Omega \sim 170$ ppm. Compared to the measured $C_Q(^{53}\text{Cr})$ values for $\text{Cs}_2\text{Cr}_2\text{O}_7$ and $\alpha\text{-K}_2\text{Cr}_2\text{O}_7$ (Table 6.2), the ZORA DFT calculations correctly predict η_Q , but overestimate $C_Q(^{53}\text{Cr})$. In our experimental analysis of ^{53}Cr NMR spectra of $\text{Cs}_2\text{Cr}_2\text{O}_7$ and $\alpha\text{-K}_2\text{Cr}_2\text{O}_7$, the Cr shielding anisotropy, Ω , was neglected; however, inclusion of $\Omega \leq 200$ ppm was found to have no apparent effect on the observed ^{53}Cr NMR lineshapes.

From Figure 6.10, the ZORA DFT calculations consistently overestimate $C_Q(^{53}\text{Cr})$ relative to the experimentally-determined $C_Q(^{53}\text{Cr})$ values obtained for $\text{Cs}_2\text{Cr}_2\text{O}_7$ and $\alpha\text{-K}_2\text{Cr}_2\text{O}_7$. Upon widening $\angle(\text{Cr}, \text{O}_{\text{bridge}}, \text{Cr})$, $C_Q(^{53}\text{Cr})$ increases considerably and η_Q steadily decreases until an axially-symmetric EFG tensor is obtained for the linear geometry, *i.e.*, $\angle(\text{Cr}, \text{O}_{\text{bridge}}, \text{Cr}) = 180^\circ$. Lastly, variation of $\angle(\text{Cr}, \text{O}_{\text{bridge}}, \text{Cr})$ has a more pronounced effect on the Cr shielding anisotropy, which covers a substantial range of ~ 160 ppm for the angles investigated herein.

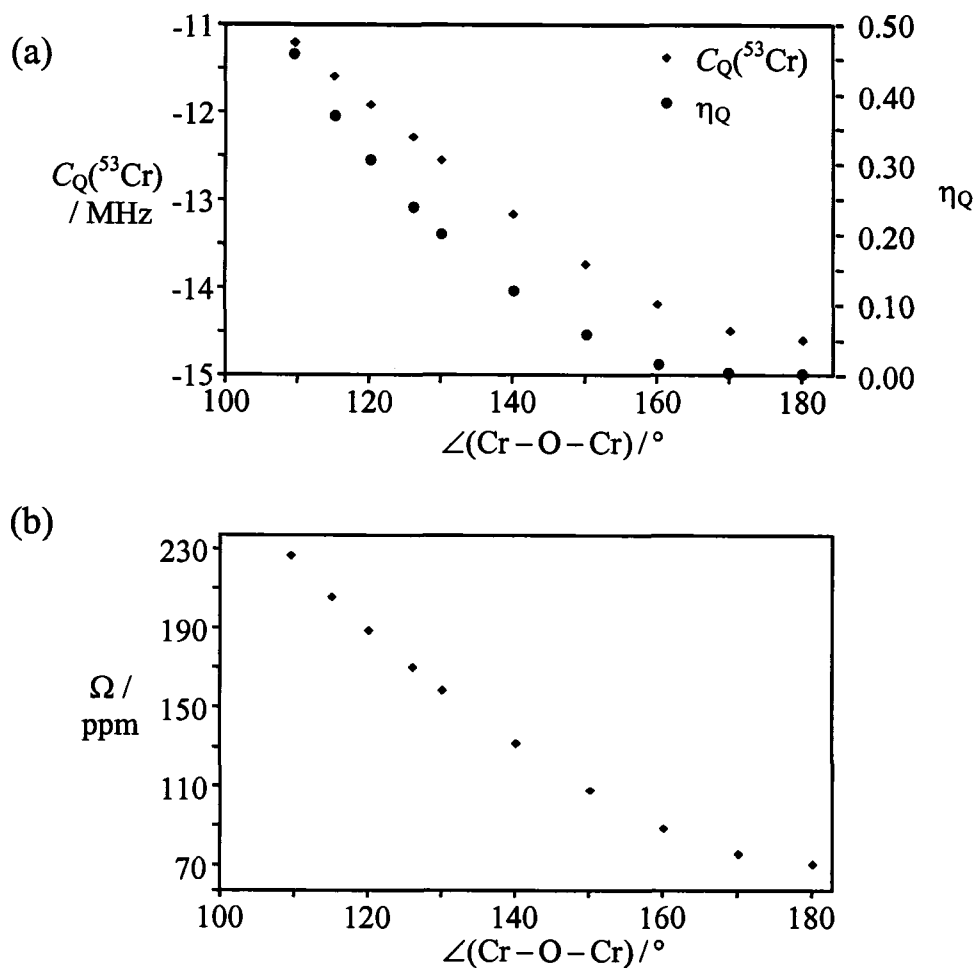


Figure 6.10: ZORA DFT results for Cr EFG and shielding tensors for the dichromate anion, summarizing the effects of $\angle(\text{Cr}, \text{O}_{\text{bridge}}, \text{Cr})$ on: (a) $C_Q(^{53}\text{Cr})$ and η_Q , and (b) the Cr shielding anisotropy, Ω . Note the dual y-axes in (a), which correspond to $C_Q(^{53}\text{Cr})$ (left) and η_Q (right).

6.4. Conclusions

Solid-state central transition ^{53}Cr NMR spectra have been acquired for a series of A(I) and A(II) chromate and A(I) dichromate salts at moderate, 11.75 T, and/or high, 18.8 T, magnetic fields. The QCPMG pulse sequence was utilized to collect all ^{53}Cr NMR data for stationary chromate and dichromate samples and, in many cases, the stepped-frequency technique was required to obtain the entire central transition spectrum due to the broad ^{53}Cr NMR lineshapes. Together, the QCPMG, stepped-frequency technique, and high magnetic fields played a critical role in this study; had conventional

pulse sequences and low magnetic fields been used, data collection would have been extremely time-consuming, if not impossible. By acquiring the ^{53}Cr NMR spectra in a piecewise fashion and by appropriately varying the QCPMG spikelet spacing, ^{53}Cr NMR powder patterns, with breadths ranging from 20 kHz to 250 kHz, were successfully obtained. Despite the broad powder patterns, most ^{53}Cr NMR spectra were collected in reasonable times; for example, experiments carried out at 18.8 T required durations of 20 minutes to 30 hours.

Acquiring ^{53}Cr NMR spectra of MAS samples was generally not feasible due to rotor spinning speeds that are insufficiently fast with respect to the ^{53}Cr second-order quadrupolar interaction; exceptions apply to Rb_2CrO_4 and Cs_2CrO_4 , for which ^{53}Cr NMR spectra have been obtained at 18.8 T and 11.75 T, respectively. Likewise, carrying out variable-temperature ^{53}Cr NMR experiments to investigate motion of the CrO_4^{2-} anions for the various A(I) and A(II) chromate salts was not practical given the lengthy experiment times required for conducting such experiments.

The success of the QCPMG experiment is partially attributed to the ^{53}Cr spin-spin relaxation times, T_2 , which are generally long relative to the acquisition times employed; *i.e.*, ≤ 30 ms, for the chromate and dichromate salts. The long T_2 values give rise to ^{53}Cr FIDs that decay slowly, allowing the loop of π -pulses in the QCPMG experiment to be applied repeatedly in a single scan. Significantly shorter T_2 values were found for the chromate hydrates, thereby reducing the number of echoes that could be applied; however, in general, the chromate salts are particularly well-suited for the QCPMG experiment. In addition, the ^{53}Cr spin-lattice relaxation times, T_1 , were found to be short, allowing pulse delays ranging from 1 to 5 seconds to be employed. The short T_1 values are a consequence of the large ^{53}Cr quadrupole moment, which causes efficient relaxation.

Solid-state ^{53}Cr NMR spectra for the chromate and dichromate salts are dominated by the Cr quadrupolar interaction, as reflected in their characteristic lineshapes. Variations in the breadth and shape of the observed ^{53}Cr NMR spectra are a consequence of the small structural changes in the individual chromate and dichromate salts, which are amplified by the large ^{53}Cr quadrupole moment and reflected in the experimentally-measured $C_Q(^{53}\text{Cr})$ values. In contrast, the anisotropic Cr shielding

interaction has generally been found to be small or negligible; exceptions include some A(I) chromates, for which inclusion of Cr shielding anisotropy was necessary in the spectral analyses. In general, small shielding anisotropies are expected for d^0 -complexes due to the lack of low-lying d -dominated molecular orbitals. The large difference in shielding anisotropies for d^0 - versus d^n -type compounds was observed for the d^0 -monomolybdate and d^2 -octacyanomolybdate(IV) salts in *Chapter 5*, where the anisotropic Mo shielding interaction was an order of magnitude larger for the d^2 -system due to mixing of low-lying d -dominated molecular orbitals (*vide supra*).

Analyses of ^{53}Cr NMR results for the chromate salts indicate that significantly larger $C_Q(^{53}\text{Cr})$ values and smaller shielding anisotropies are found compared to the analogous ^{95}Mo NMR results for the molybdate salts, presented in *Chapter 5*. For both the chromate and molybdate salts, the A(II) cations cause greater structural distortions than the A(I) cations, which are reflected in the generally larger observed C_Q values. No definite correlation has been established between the angle of distortion from T_d symmetry and the observed $C_Q(^{53}\text{Cr})$ values for the chromate salts. Finally, ZORA DFT calculations of the Cr EFG and shielding tensors are in qualitative agreement with experimental measurements; however, more accurate values would require consideration of the A(I) and A(II) cations and long-range contributions from the extended lattice; this could be achieved using the DFT-based program, WIEN2k,³⁴² which has capabilities of computing EFGs for extended lattice systems.

The success of this ^{53}Cr NMR study is accredited to the combined use of high magnetic fields and the stepped-frequency QCPMG experiment, particularly for the A(II) chromate and A(I) dichromate salts. These results have laid the groundwork for future solid-state ^{53}Cr NMR studies on more complex systems and have proved that not only are such studies feasible, but high-quality results are achievable.

Chapter 7: Concluding Remarks

This *Thesis* focuses on solid-state NMR investigations of "traditionally difficult" nuclei. Most of the nuclei examined are half-integer spin quadrupolar nuclei with low magnetic moments and significant quadrupole moments; however, the spin-1/2 nucleus, ^{129}Xe , was also investigated. The relatively high receptivity of ^{129}Xe permitted NMR experiments to be carried out at a low applied magnetic field, 4.7 T, to investigate the linear molecule, XeF_2 . In this study, use of a low B_0 was desirable since the Xe shielding interaction was found to be highly anisotropic, $\Omega = 4245 \pm 20$ ppm; use of higher fields would lead to an unfavorable scaling of the breadth of the ^{129}Xe NMR signal. This study also provided the first experimental demonstration that relativistic effects play an important role in determining the nuclear magnetic shielding for linear molecules containing heavy atoms. Specifically, the parallel component of the experimentally-determined xenon chemical shift tensor, δ_{\parallel} , was found to be deshielded with respect to the free Xe atom value, $\delta(\text{free atom})$; in contrast, non-relativistic theory predicts δ_{\parallel} and $\delta(\text{free atom})$ to be coincident. These experimental results were corroborated by non-relativistic and spin-orbit relativistic ZORA DFT calculations of Xe shielding tensors for XeF_2 , which indicate that relativity may significantly influence shielding tensors for linear molecules.

The remaining studies examined ^{131}Xe , ^{95}Mo and ^{53}Cr in model compounds. The systems investigated were specifically selected for their high molecular symmetries, which result in reduced EFGs. First, two forms of sodium perxenate, $\text{Na}_4\text{XeO}_6 \cdot 2\text{H}_2\text{O}$ and Na_4XeO_6 , were investigated by probing the two magnetically-active Xe isotopes, ^{129}Xe and ^{131}Xe . The different spin properties of the two nuclei, ^{131}Xe ($I = 3/2$) and ^{129}Xe ($I = 1/2$) allowed the Xe σ and EFG tensors to be effectively separated and characterized at a single magnetic field, 11.75 T. The Xe shielding and quadrupolar interactions proved to be extremely sensitive to changes in the local Xe environment for the two forms of sodium perxenates; however, the large Xe quadrupole moment had a detrimental effect on the observed ^{131}Xe NMR lineshape for $\text{Na}_4\text{XeO}_6 \cdot 2\text{H}_2\text{O}$, resulting in an exceedingly broad signal that spanned several hundred kilohertz. That three weeks of spectrometer time was required to obtain a spectrum for a pseudo-octahedral molecule suggests that

^{131}Xe NMR studies are not practical. On the contrary, the feasibility and practicality of ^{129}Xe NMR experiments have been demonstrated, allowing pertinent information concerning the molecular structure to be obtained and in reasonable experiment times.

Preliminary ^{95}Mo NMR studies involved characterization of the Mo σ and quadrupolar interactions for a series of A(I) and A(II) molybdate salts. Contributions from the anisotropic Mo shielding to the observed ^{95}Mo NMR lineshapes were found to be significant and comparable to the ^{95}Mo quadrupolar interaction. This is a consequence of the small Mo quadrupole moment, which reduces the magnitude of the quadrupolar interaction and allows the effects from the anisotropic Mo shielding to be observed in the molybdate salts. The success of these experiments encouraged the study of two symmetry forms, D_{2d} and D_{4d} , of the octacyanomolybdate anion, $\text{Mo}(\text{CN})_8^{4-}$. Based on the PCA, these two forms should be easily distinguishable since the EFG is predicted to be non-zero for D_{2d} symmetry, but exactly zero for D_{4d} symmetry. Using a combined experimental and computational approach, the PCA was shown to break down for the case of ideal square antiprismatic symmetry. The use of ZORA DFT and RHF computations was of critical importance in rationalizing the origin of the EFG for systems possessing D_{4d} symmetry.

Finally, the feasibility of ^{53}Cr NMR studies of chromate and dichromate salts was demonstrated. Similar to ^{131}Xe , the large Cr quadrupole moment generally resulted in broad ^{53}Cr NMR lineshapes that are dominated by the quadrupolar interaction. Some exceptions, in which the observed $C_Q(^{53}\text{Cr})$ values are small, *i.e.*, less than 2 MHz, allowed characterization of the Cr σ tensor.

Until recently, solid-state NMR studies of ^{131}Xe , ^{95}Mo and ^{53}Cr were severely hampered due to the lack of adequate resources, such as high-field super-conducting magnets and robust pulse sequences. Fortunately, overwhelming interest from the scientific community to utilize NMR as a research tool has triggered many advances in NMR technology. The use of moderate and high applied magnetic field strengths (11.75 T, 17.63 T, 18.8 T, and 21.15 T), often in combination with the quadrupolar Carr-Purcell Meiboom-Gill and stepped-frequency techniques, has ultimately led to the success of the NMR investigations presented herein. With the on-going demands to produce super-conducting magnets of "ever-increasing field strength" and to construct new and

improved signal-to-noise and sensitivity-enhancement techniques, continued progress in the area of difficult nuclei is expected. It is hoped that the research presented in this *Thesis* will stimulate future interest in this area so that the study of challenging nuclei in model systems may evolve to similarly-challenging nuclei in more complex systems.

Appendices

Appendix 3.1: Sample input file for calculation of QCPMG NMR spectrum using SIMPSON.

```
# Static QCPMG: simulation parameters are from spin orbit relativistic calc
# using QZ4P basis sets on all nuclei; calculation performed on plethora.
# Mo-95
# Sample: K4Mo(CN)8.2H2O
```

```
spinsys {
  channels 95Mo
  nuclei 95Mo 13C
  shift 1 165p 665.452p 0.055 0.0 0.0 0.0
  quadrupole 1 2 -7.32123e6 0.02573 0 0 0
}
```

```
par {
  spin_rate 0
  sw 80000
  crystal_file zcw4180
  start_operator I1z
  detect_operator I1p
  verbose 1101
  proton_frequency 500.3038086e6
  variable rf 40064
  variable N 21
  variable R 30
}
```

```
proc pulseseq {} {
  global par

  set tsw [expr 1.0e6/$par(sw)]
  set t90 2.08
  set t180 4.16

  set t1 100.0
  set t2 100.0
  set t3 100.0
  set t4 100.0

  matrix set 1 totalcoherence {-1 1}

  reset
```

```

delay $tsw
store 1

reset
pulse $t90 $par(rf) x
filter 1
delay $t1
pulse $t180 $par(rf) y
filter 1
delay $t2
acq $par(N) 1
prop 1
delay $t3
pulse $t180 $par(rf) y
filter 1
delay $t4
acq [expr 2*$par(N)] 1
}

proc main {} {
global par

set par(np) [expr 2*$par(N)*(1+$par(R))+$par(N)]
set f [fsimpson]

set N2 [expr 2*$par(N)]

for {set i 1} {$i <= $N2} {incr i} {
set c [findex $f [expr $i + $par(N)]]
set re [lindex $c 0]
set im [lindex $c 1]
for {set j 1} {$j <= $par(R)} {incr j} {
fsetindex $f [expr $i+$j*$N2+$par(N)] $re $im
}
}
fsave $f $par(name).fid
fzerofill $f 16384
faddlb $f 20 0
fft $f
fphase $f -rp 92
fsave $f $par(name).spe
fsave [fssbint $f 1000 0 1000] $par(name)-int.spe
}

```

Appendix 4.1: Non-Relativistic and Spin-Orbit Relativistic ZORA DFT Plots of σ_{iso} for free atoms; TZ2P basis sets were employed.

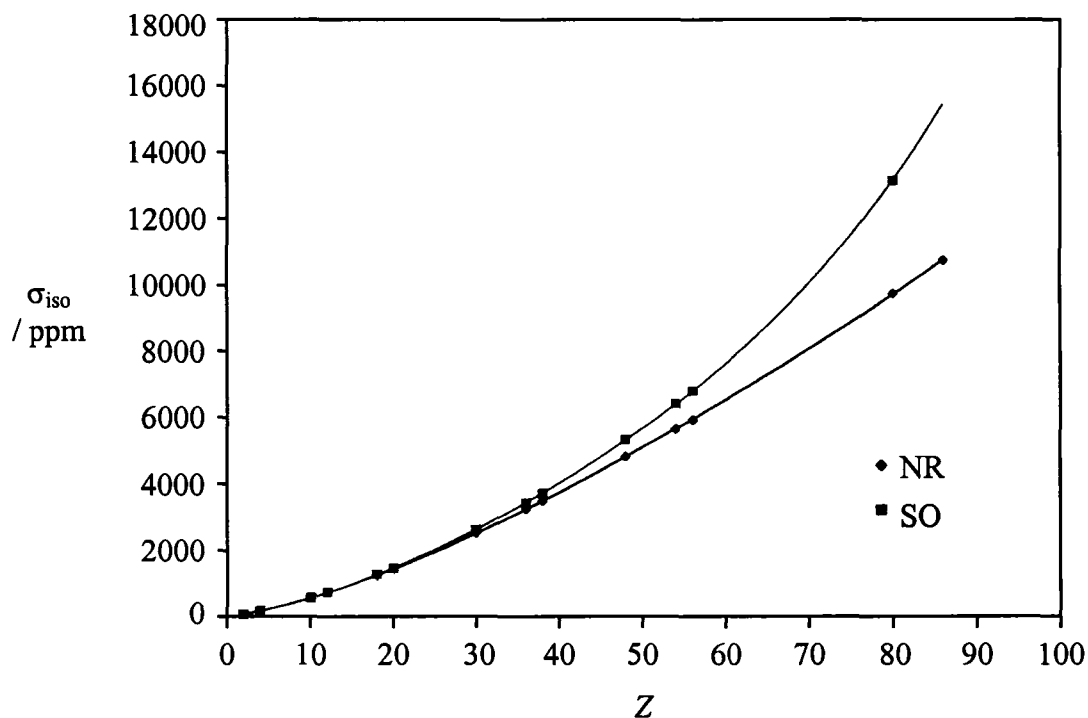


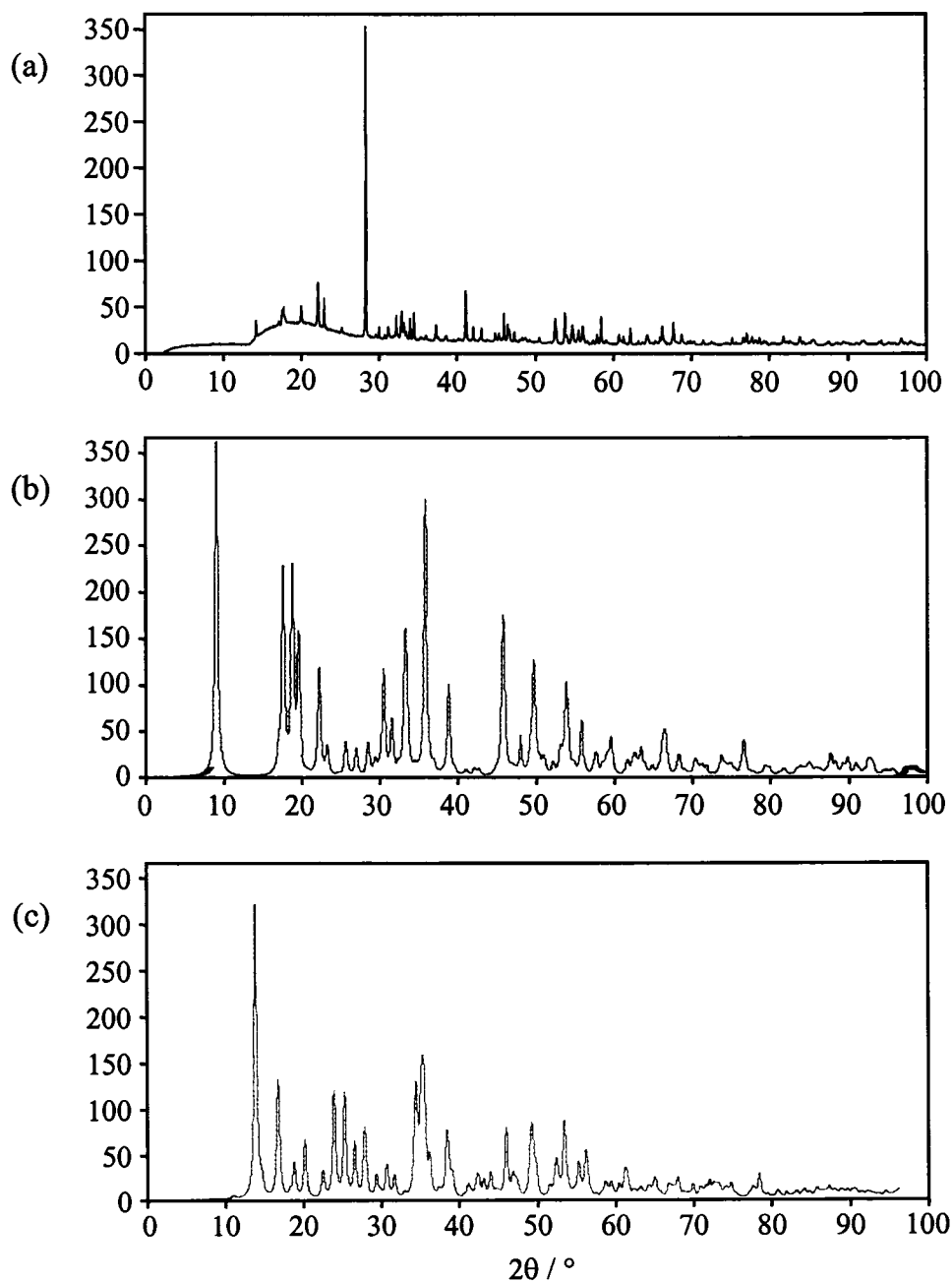
Figure A4.1: Plot of calculated isotropic magnetic shielding constants, σ_{iso} , as a function of atomic number, Z . Calculations were carried out for isolated, closed-shell atoms using non-relativistic (NR) and spin-orbit relativistic (SO) ZORA DFT. The data were fit to polynomial functions (given below), allowing σ_{iso} values for open-shell atoms to be determined through interpolation.

The data were fit to the following polynomial functions:

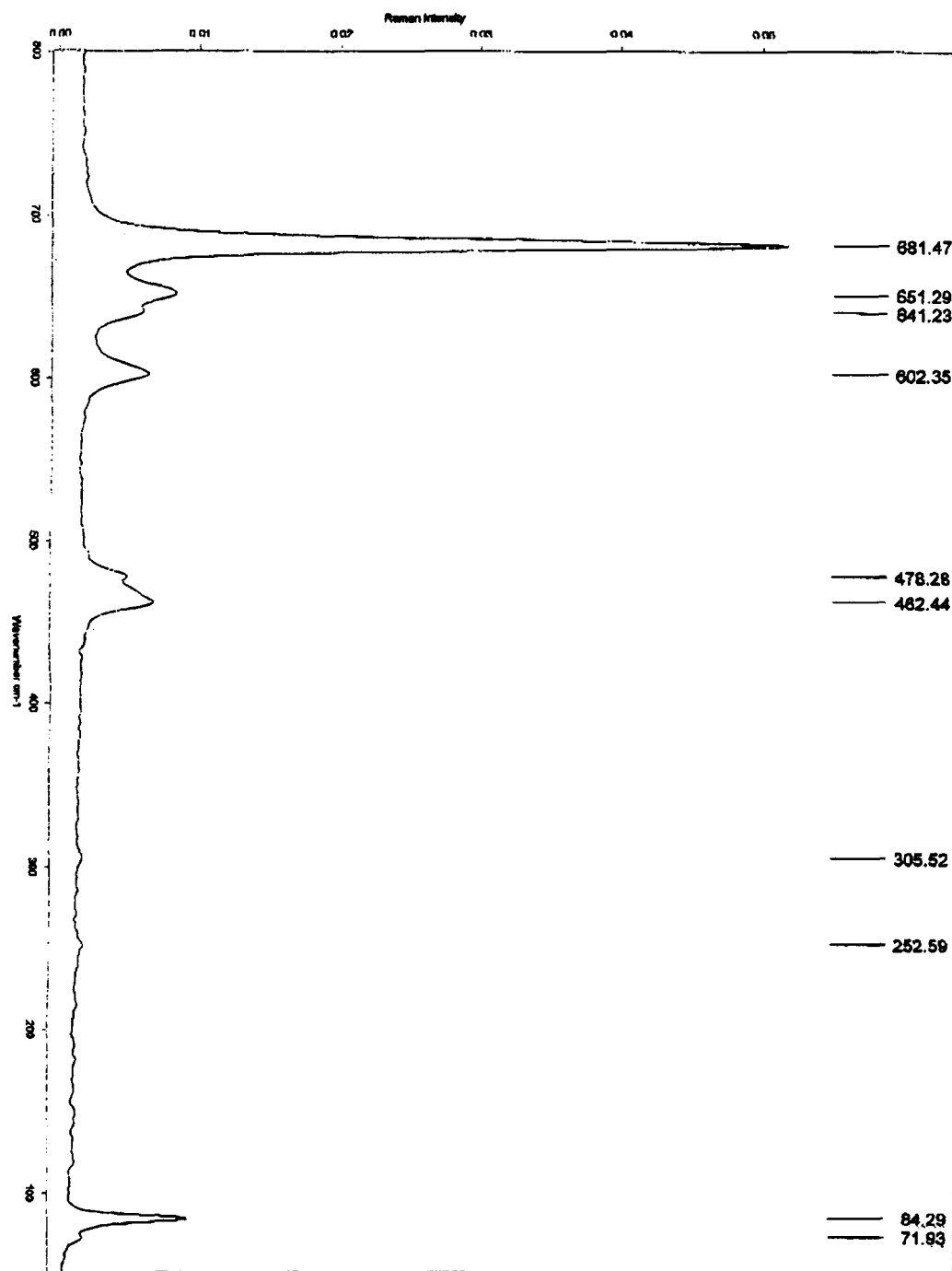
$$\sigma_{\text{iso}}(\text{so}) = 0.0002 Z^4 - 0.0294 Z^3 + 2.4531 Z^2 + 34.529 Z - 17.134$$

$$\sigma_{\text{iso}}(\text{nr}) = 7 \times 10^{-5} Z^4 - 0.015 Z^3 + 1.7545 Z^2 + 44.453 Z - 48.443$$

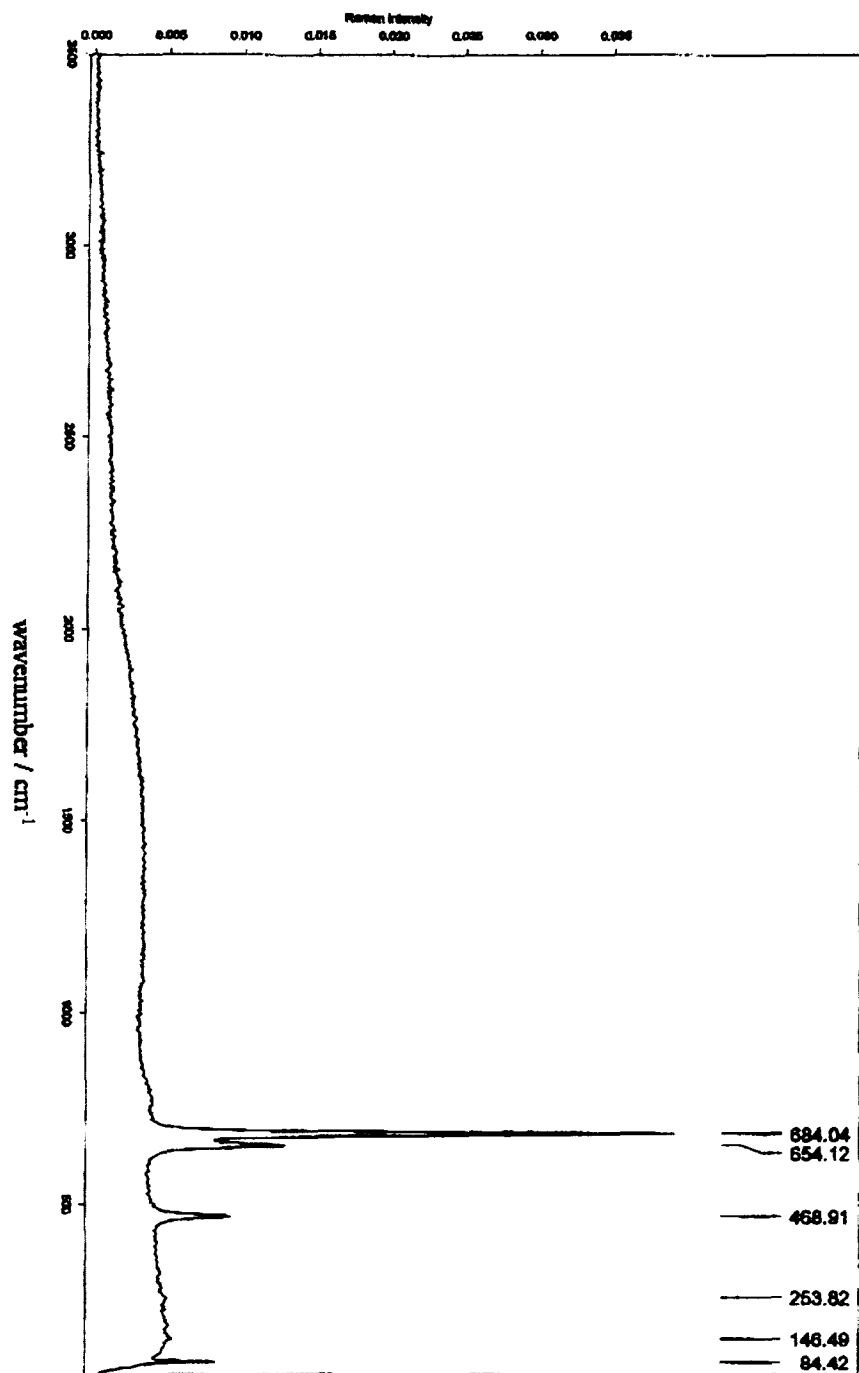
Appendix 4.2: X-Ray Diffraction Patterns of Various Hydrates of Sodium Perxenate: (a) $\text{Na}_4\text{XeO}_6 \cdot x\text{H}_2\text{O}$ (experimental; this work), (b) $\text{Na}_4\text{XeO}_6 \cdot 6\text{H}_2\text{O}$ (calculated from known cell parameters given in Ref. 206), (c) $\text{Na}_4\text{XeO}_6 \cdot 8\text{H}_2\text{O}$ (calculated from known cell parameters given in Ref. 207).



Appendix 4.3: Raman Spectrum of Solid $\text{Na}_4\text{XeO}_6 \cdot 2\text{H}_2\text{O}$



Appendix 4.4: Raman Spectrum of Solid Na₄XeO₆



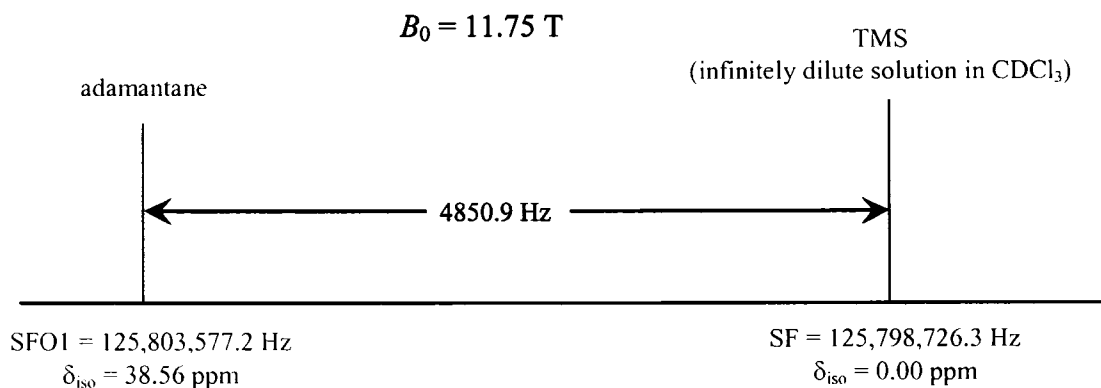
Appendix 4.5: NMR Referencing by Absolute Frequency Method

The goal of the absolute frequency method is to establish a unified scale for reporting the NMR chemical shifts of all nuclei relative to the ^1H resonance of tetramethylsilane (TMS). This method is designed to provide a precise ratio, \mathcal{Z} , of the resonance frequency of a given nuclide to that of the primary reference, the ^1H resonance of TMS in dilute solution (volume fraction $< 1\%$) in chloroform at **exactly** 100.000000 MHz. Referring to the IUPAC nomenclature manuscript by Harris *et al.*,³⁷ a list of absolute frequencies, \mathcal{Z} , for 69 of the most commonly-studied nuclides is provided.

The absolute frequency method is employed when a suitable NMR reference sample is unavailable. For example, the primary ^{129}Xe NMR reference, XeOF_4 (neat liquid, 24 °C), is not easily accessible. A second ^{129}Xe NMR reference is $\text{Xe}(g)$, but its chemical shift is both temperature- and pressure-dependent.

The following steps outline the procedure for determining NMR chemical shifts using the absolute frequency method. As an example, the isotropic ^{129}Xe chemical shift will be determined for $\text{Na}_4\text{XeO}_6 \cdot 2\text{H}_2\text{O}$.

1. Determine the absolute frequency of the isotropic ^{129}Xe NMR signal for the sample of interest, $\text{Na}_4\text{XeO}_6 \cdot 2\text{H}_2\text{O}$, on your spectrometer.
2. Find the accepted literature value of \mathcal{Z} for the primary reference, XeOF_4 (neat liquid, 24 °C), of the nucleus of interest, ^{129}Xe ; this value is fixed: $\mathcal{Z}(^{129}\text{Xe})\text{XeOF}_4$ (neat liquid, 24 °C) = 27.810 186 MHz.³⁷
3. Resort to another nucleus; *e.g.*, ^{13}C NMR resonance of adamantane. Adamantane is a convenient and well-studied sample. In addition, the NMR frequencies of ^{13}C and ^{129}Xe are relatively close: 25.145 020 MHz and 27.810 186 MHz, respectively. Values of interest are: $\mathcal{Z}(^{13}\text{C})\text{TMS} = 25.145\ 020\ \text{MHz}$ and $\mathcal{Z}(^1\text{H})\text{TMS} = 100.000000\ \text{MHz}$.
4. Measure ^{13}C NMR spectrum of adamantane on your spectrometer and determine the frequency difference between TMS and the ^{13}C NMR signal from adamantane at $\delta_{\text{iso}} = 38.56\ \text{ppm}$.



5. Next, determine the ^1H frequency of TMS on our spectrometer using the ratio:

$$\frac{^{13}\text{C}(\text{our spectrometer})}{\Xi(^{13}\text{C})} = \frac{^1\text{H}(\text{our spectrometer})}{\Xi(^1\text{H})}$$

$$\frac{125,798,726.3}{25,145,020} = \frac{^1\text{H}(\text{our spectrometer})}{100,000,000}$$

This gives: $\nu(^1\text{H})_{\text{our spectrometer}} = 500,292,806.7 \text{ Hz}$.

6. Now calculate the absolute frequency of the ^{129}Xe reference, XeOF_4 (neat liquid, 24°C) on our spectrometer.

$$\frac{^1\text{H}(\text{our spectrometer})}{\Xi(^1\text{H})} = \frac{^{129}\text{Xe}(\text{our spectrometer})_{\text{XeOF}_4}}{\Xi(^{129}\text{Xe})}$$

$$\frac{500,292,806.7}{100,000,000} = \frac{^{129}\text{Xe}(\text{our spectrometer})_{\text{XeOF}_4}}{27,810,186}$$

We obtain: $\nu(^{129}\text{Xe})_{\text{our spectrometer}, \text{XeOF}_4} = 139.1323601 \text{ MHz}$.

7. Finally, calculate the chemical shift of Na_4XeO_6 with respect to the primary ^{129}Xe NMR reference, XeOF_4 (neat liquid, 24°C):

$$\delta_{\text{iso}}(^{129}\text{Xe})_{\text{sample}} = \left[\frac{\nu(\text{sample}) - \nu(\text{ref})}{\nu(\text{ref})} \right] \times 10^6$$

$$\delta_{\text{iso}}(^{129}\text{Xe})_{\text{Na}_4\text{XeO}_6 \cdot x\text{H}_2\text{O}} = \left[\frac{139.0314077 - 139.1323601}{139.1323601} \right] \times 10^6$$

$$\delta_{\text{iso}}(^{129}\text{Xe})_{\text{Na}_4\text{XeO}_6 \cdot x\text{H}_2\text{O}} = -725.58 \text{ ppm}$$

Appendix 5.1: Structures of (a) K_2MoO_4 and Rb_2MoO_4 , (b) Li_2MoO_4 , (c) Cs_2MoO_4 , and (d) $CaMoO_4$, $SrMoO_4$, $CdMoO_4$, $BaMoO_4$, and $PbMoO_4$, with views along the indicated crystallographic axes. Mo is yellow, O is red, and A(I) and A(II) cations are other.

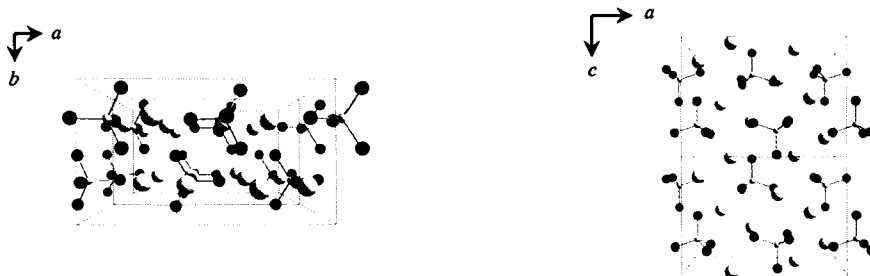
(a) Monoclinic, $C2/m$: K_2MoO_4 and Rb_2MoO_4



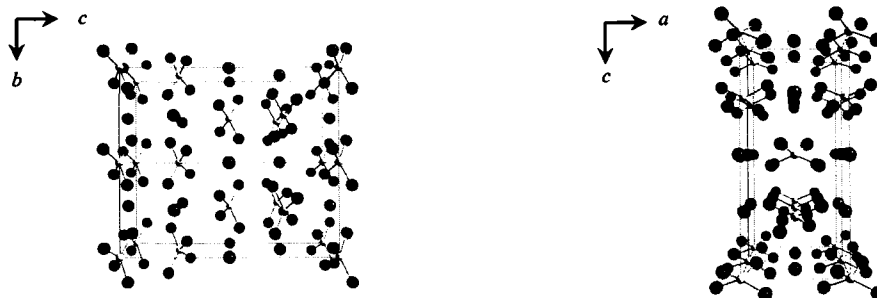
(b) Rhombohedral, $R\bar{3}$: Li_2MoO_4



(c) Orthorhombic, $Pnma$: Cs_2MoO_4



(d) Tetragonal, $I4_1/a$: $CaMoO_4$, $SrMoO_4$, $CdMoO_4$, $BaMoO_4$, $PbMoO_4$



Appendix 5.2: Acquisition Parameters for Solid-State ^{95}Mo NMR Spectra of Stationary Samples of A(I) and A(II) Molybdate Salts

Figure 5.4: (i) The ^{95}Mo NMR spectrum of a stationary sample of K_2MoO_4 acquired at 11.75 T was obtained using a one-pulse experiment with a 10 s pulse delay and is the sum of 2199 scans; a Gaussian linebroadening function of 100 Hz was applied to the FID prior to Fourier transformation. The spectrum acquired at 17.63 T was obtained using a QCPMG experiment with $M = 72$, $\nu_{\text{QCPMG}} = 200$ Hz, a 10 s pulse delay and is the sum of 800 scans; a Gaussian linebroadening function of 2 Hz was applied to the FID prior to Fourier transformation. (ii) The ^{95}Mo NMR spectrum of a stationary sample of Rb_2MoO_4 acquired at 11.75 T was obtained using a one-pulse experiment with a 10 s pulse delay and is the sum of 5622 scans; a Gaussian linebroadening function of 50 Hz was applied to the FID prior to Fourier transformation. The spectrum acquired at 17.63 T was obtained using a QCPMG experiment with $M = 32$, $\nu_{\text{QCPMG}} = 250$ Hz, a 10 s pulse delay and is the sum of 1024 scans; a Gaussian linebroadening function of 2 Hz was applied to the FID prior to Fourier transformation.

Figure 5.5: The ^{95}Mo NMR spectrum of a stationary sample of Cs_2MoO_4 acquired at 11.75 T is the sum of 2414 scans and was obtained using a pulse delay of 10 s; the FID was processed after applying a Gaussian linebroadening function of 30 Hz.

Figure 5.6: (i) The ^{95}Mo NMR spectrum of a stationary sample of BaMoO_4 acquired at 11.75 T was obtained using a one-pulse experiment with a 15 s pulse delay and is the sum of 3476 scans; a Gaussian linebroadening function of 50 Hz was applied to the FID prior to Fourier transformation. The spectrum acquired at 17.63 T was obtained using a QCPMG experiment with $M = 72$, $\nu_{\text{QCPMG}} = 200$ Hz, a 15 s pulse delay and is the sum of 448 scans; a Gaussian linebroadening function of 2 Hz was applied to the FID prior to Fourier transformation. (ii) The ^{95}Mo NMR spectrum of a stationary sample of SrMoO_4 acquired at 11.75 T was obtained using a one-pulse experiment with a 20 s pulse delay and is the sum of 4031 scans; a Gaussian linebroadening function of 30 Hz was applied to the FID prior to Fourier transformation. The experimental spectra acquired at 17.63 T (a) were obtained using a QCPMG (a, bottom) and spin-echo (a, top) experiment using a 20 s pulse delay. The QCPMG spectrum is the sum of 8 scans and was acquired with $M = 64$ and $\nu_{\text{QCPMG}} = 250$ Hz. The spin-echo spectrum (a, top) is the sum of 544 scans and a Gaussian linebroadening function of 20 Hz was applied to the FID prior to Fourier transformation. (iii) The ^{95}Mo NMR spectrum of a stationary sample of CdMoO_4 acquired at 11.75 T was obtained using a one-pulse experiment with a 10 s pulse delay and is the sum of 7416 scans; a Gaussian linebroadening function of 100 Hz was applied to the FID prior to Fourier transformation.

Appendix 5.3: Cartesian coordinates (Å) employed for RHF and ZORA/DFT electric field gradient calculations of D_{2d} , D_{4d} and O_h $\text{Mo}(\text{CN})_8^{4-}$ and of the hypothetical $\text{Zr}(\text{CN})_8^{4-}$ and MoF_8^{4-} square antiprismatic anions.

Dodecahedral (D_{2d}) $\text{Mo}(\text{CN})_8^{4-}$

| | | | |
|----|----------|----------|----------|
| Mo | 0.00000 | 0.00000 | 0.00000 |
| C1 | 0.00000 | -1.27250 | 1.75152 |
| C1 | 0.00000 | 1.27250 | 1.75152 |
| C1 | -1.27250 | 0.00000 | -1.75152 |
| C1 | 1.27250 | 0.00000 | -1.75152 |
| C2 | 0.00000 | -2.06642 | -0.63572 |
| C2 | 0.00000 | 2.06642 | -0.63572 |
| C2 | -2.06642 | 0.00000 | 0.63572 |
| C2 | 2.06642 | 0.00000 | 0.63572 |
| N | 0.00000 | -1.94792 | 2.68108 |
| N | 0.00000 | 1.94792 | 2.68108 |
| N | -1.94792 | 0.00000 | -2.68108 |
| N | 1.94792 | 0.00000 | -2.68108 |
| N | 0.00000 | -3.16845 | -0.97474 |
| N | 0.00000 | 3.16845 | -0.97474 |
| N | -3.16845 | 0.00000 | 0.97474 |
| N | 3.16845 | 0.00000 | 0.97474 |

Square Antiprism (D_{4d}) $\text{Mo}(\text{CN})_8^{4-}$

| | | | |
|----|----------|----------|----------|
| Mo | 0.00000 | 0.00000 | 0.00000 |
| C | 0.00000 | 1.76780 | 1.24980 |
| C | 0.00000 | -1.76780 | 1.24980 |
| C | 1.76780 | 0.00000 | 1.24980 |
| C | -1.76780 | 0.00000 | 1.24980 |
| C | 1.25000 | 1.25000 | -1.24980 |
| C | 1.25000 | -1.25000 | -1.24980 |
| C | -1.25000 | 1.25000 | -1.24980 |
| C | -1.25000 | -1.25000 | -1.24980 |
| N | 0.00000 | 2.70600 | 1.91313 |
| N | 0.00000 | -2.70600 | 1.91313 |
| N | 2.70600 | 0.00000 | 1.91313 |
| N | -2.70600 | 0.00000 | 1.91313 |
| N | 1.91340 | 1.91340 | -1.91313 |
| N | 1.91340 | -1.91340 | -1.91313 |
| N | -1.91340 | 1.91340 | -1.91313 |
| N | -1.91340 | -1.91340 | -1.91313 |

Cubic (O_h) $\text{Mo}(\text{CN})_8^{4-}$

| | | | |
|----|----------|----------|----------|
| Mo | 0.00000 | 0.00000 | 0.00000 |
| C | 0.00000 | 1.76780 | -1.24980 |
| C | 0.00000 | -1.76780 | -1.24980 |
| C | 1.76780 | 0.00000 | -1.24980 |
| C | -1.76780 | 0.00000 | -1.24980 |
| C | 0.00000 | 1.76780 | 1.24980 |
| C | 0.00000 | -1.76780 | 1.24980 |
| C | 1.76780 | 0.00000 | 1.24980 |
| C | -1.76780 | 0.00000 | 1.24980 |
| N | 0.00000 | 2.70600 | 1.91313 |
| N | 0.00000 | -2.70600 | 1.91313 |
| N | 2.70600 | 0.00000 | 1.91313 |
| N | -2.70600 | 0.00000 | 1.91313 |
| N | 0.00000 | 2.70600 | -1.91313 |
| N | 0.00000 | -2.70600 | -1.91313 |
| N | 2.70600 | 0.00000 | -1.91313 |
| N | -2.70600 | 0.00000 | -1.91313 |

Square Antiprismatic (D_{4d}) $\text{Zr}(\text{CN})_8^{4-}$

| | | | |
|----|----------|----------|----------|
| Zr | 0.00000 | 0.00000 | 0.00000 |
| C | 0.00000 | 1.76780 | 1.24980 |
| C | 0.00000 | -1.76780 | 1.24980 |
| C | 1.76780 | 0.00000 | 1.24980 |
| C | -1.76780 | 0.00000 | 1.24980 |
| C | 1.25000 | 1.25000 | -1.24980 |
| C | 1.25000 | -1.25000 | -1.24980 |
| C | -1.25000 | 1.25000 | -1.24980 |
| C | -1.25000 | -1.25000 | -1.24980 |
| N | 0.00000 | 2.70600 | 1.91313 |
| N | 0.00000 | -2.70600 | 1.91313 |
| N | 2.70600 | 0.00000 | 1.91313 |
| N | -2.70600 | 0.00000 | 1.91313 |
| N | 1.91340 | 1.91340 | -1.91313 |
| N | 1.91340 | -1.91340 | -1.91313 |
| N | -1.91340 | 1.91340 | -1.91313 |
| N | -1.91340 | -1.91340 | -1.91313 |

Square Antiprismatic (D_{4d}) MoF_8^{4-}

| | | | |
|----|----------|----------|----------|
| Mo | 0.00000 | 0.00000 | 0.00000 |
| F | 0.00000 | 1.76780 | 1.24980 |
| F | 0.00000 | -1.76780 | 1.24980 |
| F | 1.76780 | 0.00000 | 1.24980 |
| F | -1.76780 | 0.00000 | 1.24980 |
| F | 1.25000 | 1.25000 | -1.24980 |
| F | 1.25000 | -1.25000 | -1.24980 |
| F | -1.25000 | 1.25000 | -1.24980 |
| F | -1.25000 | -1.25000 | -1.24980 |

Appendix 6.1: Summary of Stepped-Frequency ^{53}Cr QCPMG Experiments for A(I) and A(II) Chromate and A(I) Dichromate Salts.

| Compound | $B_0 = 11.75 \text{ T}$ | $B_0 = 18.8 \text{ T}$ | | |
|---|-------------------------|------------------------|----------------------------------|-----------------------|
| | # of Steps | # of Steps | $\nu_{\text{QCPMG}} / \text{Hz}$ | Total Exp. Time / hr. |
| Cs_2CrO_4 | 1 | 1 | 200 | 0.6 |
| Rb_2CrO_4 | 1 | 1 | 250 | 1.4 |
| K_2CrO_4 | 1 | 1 | 400 | 0.3 |
| $\text{Mg}_2\text{CrO}_4 \cdot x\text{H}_2\text{O}$ | 1 | 1 | 2000 | 3.9 |
| $\text{Na}_2\text{CrO}_4 \cdot x\text{H}_2\text{O}$ | 1 | 1 | 2000 | 3.6 |
| $\text{Li}_2\text{CrO}_4 \cdot x\text{H}_2\text{O}$ | 3 | 2 | 2000 | 5.7 |
| Ag_2CrO_4 | 3 | 1 | 2000 | 4.6 |
| PbCrO_4 | ----- | 3 | 3000 | 30.3 |
| CaCrO_4 | 3 | 1 | 3000 | 2.9 |
| SrCrO_4 | 4 | 2 | 4000 | 5.6 |
| BaCrO_4 | 3 | 2 | 4000 | 5.7 |
| $\text{Cs}_2\text{Cr}_2\text{O}_7$ | ----- | 5 | 5000 | 11.4 |
| $\text{K}_2\text{Cr}_2\text{O}_7$ | ----- | 6 | 5000 | 7.3 |

Appendix 6.2: Summary of Structural Parameters, Δr and σ^2 , and NMR Parameters, δ_{iso} , $C_Q(^{53}\text{Cr})$, and η_Q , for A(I) and A(II) Chromate and A(I) Dichromate Salts; see Equations 6.1 and 6.2 for Δr and σ^2 .

| | $\Delta r / \times 10^{-5}$ Å | $r(\text{Cr, O})_{\text{avg}}$ / Å | $\delta_{\text{iso}} / \text{ppm}$ | $\sigma^2 / \text{°}$ | $C_Q(^{53}\text{Cr}) /$ MHz | η_Q |
|-----------------------------------|----------------------------------|---------------------------------------|------------------------------------|-----------------------|--------------------------------|----------|
| K_2CrO_4 | 5.8 | 1.6466 | 1762 | 0.39 | 1.76 | 0.43 |
| Rb_2CrO_4 | 8.3 | 1.6024 | 1773 | 3.3 | 1.255 | 0.80 |
| Cs_2CrO_4 | 0.8 | 1.6501 | 1778.5 | 0.1 | 1.234 | 0.23 |
| Ag_2CrO_4 | 25.2 | 1.6545 | 1985 | 3.3 | 4.095 | 0.28 |
| Li_2CrO_4 | 7.3 | 1.6448 | 1735 | 0.8 | 3.96 | 0.30 |
| MgCrO_4 | 5.1 | 1.6717 | 1730 | 10.1 | 2.62 | 0.38 |
| CaCrO_4 | 0 | 1.6466 | 1680 | 13.44 | 4.49 | 0.00 |
| SrCrO_4 | 29 | 1.6478 | 1770 | 8.5 | 4.98 | 0.68 |
| BaCrO_4 | 1.2 | 1.6330 | 1750 | 17.0 | 5.01 | 0.14 |
| PbCrO_4 | 10 | 1.6838 | 1865 | 10.5 | 4.35 | 0.85 |
| $\text{K}_2\text{Cr}_2\text{O}_7$ | 176 | 1.6560 | 1730 | 3.64 | 8.28 | 0.30 |
| $\text{K}_2\text{Cr}_2\text{O}_7$ | 210 | 1.6563 | 1775 | 0.79 | 7.48 | 0.21 |

References and Notes

1. See, for example, *Encyclopedia of Nuclear Magnetic Resonance*, Grant, D. M., Harris, R. K., Eds.; John Wiley & Sons: Chichester, 1996, Vol. 1.
2. (a) Pauli, W. Jr. *Z. Phys.* **1927**, *43*, 601-623; (b) Darwin, C. G. *Proc. R. Soc. London, Ser. A* **1927**, *115*, 1-19.
3. (a) Estermann, I.; Stern, O. *Z. Phys.* **1933**, *85*, 17-24.; (b) Frisch, R.; Stern, O. *Z. Phys.* **1933**, *85*, 4-16; (c) Estermann, I.; Simpson, O. C.; Stern, O. *Phys. Rev.* **1937**, *52*, 535-545. Note, the famous Stern-Gerlach experiment was carried out in 1921: Gerlach, W.; Stern, O. *Z. Phys.* **1921**, *8*, 110-111.
4. Larmor, J. *Philos. Mag.* **1897**, *44*, 503.
5. Gorter, C. J. *Physica (The Hague)* **1936**, *3*, 995-998.
6. Rabi, I. I.; Zacharias, J. R.; Millman, S.; Kusch, P. *Phys. Rev.* **1938**, *53*, 318.
7. Purcell, E. M.; Torrey, H. C.; Pound, R. V. *Phys. Rev.* **1946**, *69*, 37-38.
8. Bloch, F.; Hansen, W. W.; Packard, M. *Phys. Rev.* **1946**, *69*, 127.
9. Bloembergen, N.; Purcell, E. M.; Pound, R. V. *Phys. Rev.* **1948**, *73*, 679-712.
10. Pake, G. E. *J. Chem. Phys.* **1948**, *16*, 327-336.
11. (a) Proctor, W. G.; Yu, F. C. *Phys. Rev.* **1950**, *77*, 717; (b) Dickinson, W. C., *Phys. Rev.* **1950**, *77*, 736-737; (c) Arnold, J. T.; Dharmatii, S. S.; Packard, M. E. *J. Chem. Phys.* **1951**, *19*, 507.
12. (a) Andrew, E. R.; Bradbury, A.; Eades, R. G. *Nature* **1959**, *183*, 1802-1803; (b) Lowe, I. J. *Phys. Rev. Lett.* **1959**, *2*, 285-287.
13. (a) Abragam, A.; Proctor, W. G. *Phys. Rev.* **1957**, *106*, 160-161; (b) Hartmann, S. R.; Hahn, E. L. *Phys. Rev.* **1962**, *128*, 2042-2053; (c) Lurie, F. M.; Slichter, C. P. *Phys. Rev. A* **1964**, *133*, 1108-1122; (d) Pines, A.; Gibby, M. G.; Waugh, J. S. *J. Chem. Phys.* **1972**, *56*, 1776-1777; (e) **1973**, *59*, 569-590; (f) Pines, A.; Waugh, J. S. *J. Magn. Reson.* **1972**, *8*, 354-365.
14. Hahn, E. L. *Phys. Rev.* **1950**, *77*, 297-298; *80*, 580-594.

-
15. (a) Proctor, W. G.; Yu, F. C. *Phys. Rev.* **1951**, *81*, 20-30; (b) Andrew, E. R. *Phys. Rev.* **1951**, *82*, 443-444; (c) Gutowsky, H. S.; McCall, D. W. *Phys. Rev.* **1951**, *82*, 748-749; (d) Gutowsky, H. S.; McCall, D. W.; Slichter, C. P. *Phys. Rev.* **1951**, *84*, 589-590; (e) Hahn, E. L.; Maxwell, D. E. *Phys. Rev.* **1951**, *84*, 1246-1247; **1952**, *88*, 1070-1084; (f) Ramsey, N. F.; Purcell, E. M. *Phys. Rev.* **1952**, *85*, 143-144; (g) Ramsey, N. F. *Phys. Rev.* **1953**, *91*, 303-307.
 16. Fourier, J. B. J. *Théorie Analytique de la Chaleur*, Didot: Paris, 1822.
 17. Ernst, R. R.; Anderson, W. A. *Rev. Sci. Instrum.* **1966**, *37*, 93-102.
 18. Mehring, M. *Principles of High Resolution NMR in Solids*, 2nd ed.; Springer-Verlag: Berlin, 1983.
 19. Zeeman, P. *Philos. Mag.* **1897**, *43*, 226.
 20. Mehring M.; Weberruß, V. A. *Object-Oriented Magnetic Resonance: Classes and Objects, Calculations and Computations*, Academic Press: San Diego, 2001, Ch. 7.
 21. (a) Chu, P. J.; Gerstein, B. C. *J. Chem. Phys.* **1989**, *91*, 2081-2101; (b) Cheng, J. T.; Edwards, J. C.; Ellis, P. D. *J. Phys. Chem.* **1990**, *94*, 553-561; (c) Koons, J. M.; Hughes, E.; Cho, H. M.; Ellis, P. D. *J. Magn. Reson., Ser. A* **1995**, *114*, 12-23; (d) Bryce, D. L.; Eichele, K.; Wasylshen, R. E. *Inorg. Chem.* **2003**, *42*, 5085-5096; (e) Power, W. P.; Wasylshen, R. E.; Mooibroek, S.; Pettitt, B. A.; Danchura, W. *J. Phys. Chem.* **1990**, *94*, 591-598.
 22. Rose, M. E. *Elementary Theory of Angular Momentum*, John Wiley & Sons: New York, 1957, Ch. IV.
 23. Duer, M. J. *Introduction to Solid State NMR Spectroscopy*, Blackwell: Oxford, 2004, Ch. 1.
 24. (a) Haeberlen, U. In *Advances in Magnetic Resonance*, Waugh, J. S., Ed.; Academic Press: New York, 1976, Supplement 1, Ch. VI; (b) Anet, F. A. L.; O'Leary, D. J. *Conc. Magn. Reson.* **1991**, *3*, 193-214; (c) **1992**, *4*, 35-52.
 25. Veeman, W. S. *Prog. Nucl. Magn. Reson. Spectrosc.* **1984**, *16*, 193-235.

-
26. Facelli, J. C.; Grant, D. M. *Top. Stereochem.* **1989**, *19*, 1-61.
 27. Schmidt-Rohr, K.; Spiess, H. W. *Multidimensional Solid-State NMR and Polymers*, Academic Press: London, 1994.
 28. Buckingham, A. D.; Malm, S. M. *Mol. Phys.* **1971**, *22*, 1127-1130.
 29. For example, see: Wasylshen, R. E.; Bryce, D. L. *J. Chem. Phys.* **2002**, *117*, 10061-10066.
 30. Mason, J. *Solid State Nucl. Magn. Reson.* **1993**, *2*, 285-288.
 31. Jameson, C. J. In *Multinuclear NMR*, Mason, J., Ed.; Plenum Press: New York, 1987, Chapter 4.
 32. Spiess, H. W. In *NMR, Basic Principles and Progress*; Diehl, P., Fluck, E., Günther, H., Kosfeld, R., Eds.; Springer-Verlag: Berlin, 1978, Vol. 15, pp 55-214.
 33. (a) Ramsey, N. F. *Molecular Beams*, Oxford University Press: London, 1956; (b) *Phys. Rev.* **1950**, *78*, 699-703; (c) Ramsey, N. F. *Phys. Rev.* **1950**, *77*, 567.
 34. Pyykkö, P. *Theor. Chem. Acc.* **2000**, *103*, 214-216.
 35. Jameson, C. J.; Mason, J. In *Multinuclear NMR*, Mason, J., Ed.; Plenum Press: New York, 1987; Chapter 3.
 36. Abragam, A. *Principles of Nuclear Magnetism*, Adair, R. K., Elliott, R. J., Marshall, W. C., Wilkinson, D. H., Eds.; Clarendon Press: Oxford, 1961.
 37. Harris, R. K.; Becker, E. D.; Cabral de Menezes, S. M.; Goodfellow, R.; Granger, P. *Pure Appl. Chem.* **2001**, *73*, 1795.
 38. Baugher, J. F.; Taylor, P. C.; Oja, T.; Bray, P. J. *J. Chem. Phys.* **1969**, *50*, 4914-4925.
 39. Jones, W. H., Jr.; Graham, T. P.; Barnes, R. G. *Phys. Rev.* **1963**, *132*, 1898-1909.
 40. Bain, A. D.; Khasawneh, M. *Conc. Magn. Reson., Part A* **2004**, *22*, 69-78.

-
41. Amoureux, J. P.; Fernandez, C.; Granger, P. In *Multinuclear Magnetic Resonance in Liquids and Solids – Chemical Applications*, Granger, P., Harris, R. K., Eds.; Kluwer Academic Publishers: Dordrecht, 1990; Ch. XXII.
 42. Samoson, A. *Chem. Phys. Lett.* **1985**, *119*, 29-32.
 43. Slichter, C. P. *Principles of Magnetic Resonance*, 3rd ed., Cardona, M., Fulde, P., von Klitzing, K., Queisser, H.-J., Eds.; Springer-Verlag: Berlin, 1990.
 44. Han, O. H.; Oldfield, E. *Inorg. Chem.* **1990**, *29*, 3666-3669.
 45. Bryce, D. L.; Wasylishen, R. E. *Phys. Chem. Chem. Phys.* **2002**, *4*, 3591-3600.
 46. Akitt, J. W.; McDonald, W. S. *J. Magn. Reson.* **1984**, *58*, 401-412.
 47. Ooms, K. J.; Wasylishen, R. E. *J. Am. Chem. Soc.* **2004**, *126*, 10972-10980.
 48. Segel, S. L. *J. Chem. Phys.* **1969**, *51*, 848-850.
 49. Mooberry, E. S.; Spiess, H. W.; Sheline, R. K. *J. Chem. Phys.* **1972**, *57*, 813-821.
 50. Rehder, D.; Paulsen, K.; Basler, W. *J. Magn. Reson.* **1983**, *53*, 500-502.
 51. Sternheimer, R. M. *Phys. Rev.* **1951**, *84*, 244-253; **1952**, *86*, 316-324; **1954**, *95*, 736-750.
 52. *Calculation of NMR and EPR Parameters: Theory and Applications*, Kaupp, M., Bühl, M., Malkin, V. G., Eds.; Wiley-VCH: Weinheim, 2004.
 53. Wasylishen, R. E. In *Encyclopedia of Nuclear Magnetic Resonance*; Grant, D. M., Harris, R. K., Eds.; John Wiley & Sons: Chichester, 1996, Vol. 3. pp 1685-1695.
 54. Forgeron, M. A. M.; Gee, M.; Wasylishen, R. E. *J. Phys. Chem. A* **2004**, *108*, 4895-4908.
 55. Buckingham, A. D.; Love, I. *J. Magn. Reson.* **1970**, *2*, 338-351.
 56. Malleier, R.; Kopacka, H.; Schuh, W.; Wurst, K.; Peringer, P. *Chem. Commun.* **2001**, 51-52.
 57. Dusold, S.; Sebald, A. *Annu. Rep. NMR. Spectrosc.* **2000**, *41*, 185-264.

-
58. Vaara, J.; Jokisaari, J.; Wasylishen, R. E.; Bryce, D. L. *Prog. Nucl. Magn. Reson. Spectrosc.* **2002**, *41*, 233-304.
 59. Wasylishen, R. E. In *Encyclopedia of Nuclear Magnetic Resonance*, Grant, D. M., Harris, R. K., Eds.; Wiley: Chichester, 2002, Vol. 9, pp 274-282.
 60. Gee, M.; Wasylishen, R. E.; Ragogna, P. J.; Burford, N.; McDonald, R. *Can. J. Chem.* **2002**, *80*, 1488-1500.
 61. Stejskal, E. O.; Memory, J. D. *High Resolution NMR in the Solid State*, Oxford University Press: New York, 1994.
 62. Levitt, M. H. *Spin-Dynamics: Basics of Nuclear Magnetic Resonance*, John Wiley & Sons: Chichester, 2001.
 63. Emsley, J. W.; Lindon, J. C. *NMR Spectroscopy Using Liquid Crystal Solvents*, Pergamon Press: Oxford, 1975.
 64. Lounila, J.; Jokisaari, J. *Prog. Nucl. Magn. Reson. Spectrosc.* **1982**, *15*, 249-290.
 65. Kaski, J.; Vaara, J.; Jokisaari, J. *J. Am. Chem. Soc.* **1996**, *118*, 8879-8886.
 66. Kaski, J.; Lantto, P.; Vaara, J.; Jokisaari, J. *J. Am. Chem. Soc.* **1998**, *120*, 3993-4005.
 67. Vaara, J.; Kaski, J.; Jokisaari, J. *J. Phys. Chem. A.* **1999**, *103*, 5675-5684.
 68. Bryce, D. L.; Wasylishen, R. E. *J. Am. Chem. Soc.* **2000**, *122*, 3197-3205.
 69. Dyke, T. R.; Muentzer, J. S. In *Physical Chemistry Series Two: Molecular Structure and Properties*, Buckingham, A. D., Ed.; Butterworths: London, 1975, Vol. 2.
 70. Bryce, D. L.; Wasylishen, R. E. *Acc. Chem. Res.* **2003**, *36*, 327-334.
 71. Herzfeld, J.; Berger, A. E. *J. Chem. Phys.* **1980**, *73*, 6021-6030.
 72. (a) Dixon, W. T.; Schaefer, J.; Sefcik, M. D.; Stejskal, E. O.; McKay, R. A. *J. Magn. Reson.* **1982**, *49*, 341-345; (b) Dixon, W. T. *J. Chem. Phys.* **1982**, *77*,

-
- 1800-1809; (c) Nielsen, N. Chr.; Bildsøe, H.; Jakobsen, H. J. *J. Magn. Reson.* **1988**, *80*, 149-154.
73. Dixon, W. T. *J. Magn. Reson.* **1981**, *44*, 220-223.
74. Massiot, D.; Montouillout, V.; Fayon, F.; Florian, P.; Bessada, C. *Chem. Phys. Lett.* **1997**, *272*, 295-300.
75. Geen, H.; Levitt, M. H.; Bodenhausen, G. *Chem. Phys. Lett.* **1992**, *200*, 350-356; (b) Song, Z.; Antzutkin, O. N.; Feng, X.; Levitt, M. H. *Solid State Nucl. Magn. Reson.* **1993**, *2*, 143-146; (c) Hong, J.; Harbison, G. S.; *J. Magn. Reson., Ser. A* **1993**, *105*, 128-136; (d) Geen, H.; Bodenhausen, G. *J. Am. Chem. Soc.* **1993**, *115*, 1579-1580.
76. Bennett, A. E.; Rienstra, C. M.; Auger, M.; Lakshmi, K. V.; Griffin, R. G. *J. Chem. Phys.* **1995**, *103*, 6951-6958.
77. Waugh, J. S.; Huber, L. M.; Haeberlen, U. *Phys. Rev. Lett.* **1968**, *20*, 180-182.
78. Mansfield, P.; Orchard, M. J.; Stalker, D. C.; Richards, K. H. B. *Phys. Rev. B* **1973**, *7*, 90-105.
79. Burum, D. P.; Rhim, W. -K. *J. Chem. Phys.* **1979**, *71*, 944-956.
80. Lee, M.; Goldberg, W. I. *Phys. Rev. A* **1965**, *140*, 1261.
81. Bielecki, A.; Kolbert, A. C.; Levitt, M. H. *Chem. Phys. Lett.* **1989**, *155*, 341-346.
82. VanderHart, D. L.; Campbell, G. C. *J. Magn. Reson.* **1998**, *134*, 88-112.
83. Gan, Z.; Ernst, R. R. *Solid State Nucl. Magn. Reson.* **1997**, *8*, 153-159.
84. Tekely, P.; Palmas, P.; Canet, D. *J. Magn. Reson. Ser. A* **1994**, *107*, 129-133.
85. Peersen, O. B.; Wu, X.; Kustanovich, I.; Smith, S. O. *J. Magn. Reson., Ser. A* **1993**, *104*, 334-339.
86. Metz, G.; Wu, X.; Smith, S. O. *J. Magn. Reson., Ser. A* **1994**, *110*, 219-227.
87. Forgeron, M. A. M.; Bryce, D. L.; Wasylishen, R. E.; Rösler, R. *J. Phys. Chem. A* **2003**, *107*, 726-735.

-
88. MacKenzie, K. J. D.; Smith, M. E. *Multinuclear Solid-State NMR of Inorganic Materials*, Cahn, R. W., Ed.; Pergamon Press: Amsterdam, 2002; Vol. 6, Ch. 8.
 89. (a) Cheng, J. T.; Ellis, P. D. *J. Phys. Chem.* **1989**, *93*, 2549-2555; (b) Larsen, F. H.; Skibsted, J.; Jakobsen, H. J.; Nielsen, N. Chr. *J. Am. Chem. Soc.* **2000**, *122*, 7080-7086.
 90. Carr, H. Y.; Purcell, E. M. *Phys. Rev.* **1954**, *94*, 630-638.
 91. Meiboom, S.; Gill, D. *Rev. Sci. Instrum.* **1958**, *29*, 688-691.
 92. Larsen, F. H.; Jakobsen, H. J.; Ellis, P. D.; Nielsen, N. Chr. *J. Phys. Chem. A* **1997**, *101*, 8597-8606.
 93. Lefort, R.; Wiench, J. W.; Pruski, M.; Amoureux, J. -P. *J. Chem. Phys.* **2002**, *116*, 2493-2501.
 94. (a) Siegel, R.; Nakashima, T. T.; Wasylishen, R. E. *Conc. Magn. Reson., Ser. A* **2005**, *26*, 62-77; (b) Hung, I.; Rossini, A. J.; Schurko, R. W. *J. Phys. Chem. A* **2004**, *108*, 7112-7120.
 95. Man, P. P.; Klinowski, J.; Trokiner, A.; Zanni, H.; Papon, P. *Chem. Phys. Lett.* **1988**, *151*, 143-150.
 96. Vega, A. J. In *Encyclopedia of Nuclear Magnetic Resonance*, Grant, D. M., Harris, R. K., Eds.; Wiley: Chichester, 1996, Vol. 6, pp 3869-3889.
 97. Kennedy, M. A.; Vold, R. L.; Vold, R.R. *J. Magn. Reson.* **1991**, *92*, 320-331.
 98. Massiot, D.; Farnan, I.; Gautier, N.; Trumeau, D.; Trokiner, A.; Coutures, J. P. *Solid State Nucl. Magn. Reson.* **1995**, *4*, 241-248.
 99. (a) Nagayama, K.; Bachmann, P.; Wüthrich, K.; Ernst, R. R. *J. Magn. Reson.* **1978**, *31*, 133-148; (b) Blümich, B.; Ziessow, D. *J. Magn. Reson.* **1982**, *49*, 151-154.
 100. Granger, P. *Magn. Reson. Chem.* **1990**, *28*, 156-158.
 101. Eichele, K.; Wasylishen, R. E. *WSOLIDS NMR Simulation Package*. 2000; Version 1.17.26.

-
102. Bak, M.; Rasmussen, J. T.; Nielsen, N. C. *J. Magn. Reson.* **2000**, *147*, 296-330.
103. Alderman, D. W.; Solum, M. S.; Grant, D. M. *J. Chem. Phys.* **1986**, *84*, 3717-3725.
104. (a) Chang, C.; Pelissier, M.; Durand, P. *Phys. Scr.* **1986**, *34*, 394-404; (b) van Lenthe, E.; Baerends, E. J.; Snijders, J. G. *J. Chem. Phys.* **1993**, *99*, 4597-4610; (c) **1994**, *101*, 9783-9792; (d) van Lenthe, E.; Ehlers, A.; Baerends, E. J. *J. Chem. Phys.* **1999**, *110*, 8943-8953; (e) van Lenthe, E.; van Leeuwen, R.; Baerends, E. J.; Snijders, J. G. *Int. J. Quantum Chem.* **1996**, *57*, 281-293.
105. ADF 2000.02, 2002.99, and 2004.01, Theoretical Chemistry, Vrije Universiteit, Amsterdam, <http://www.scm.com>.
106. (a) Baerends, E. J.; Ellis, D. E.; Ros, P. *Chem. Phys.* **1973**, *2*, 41-51; (b) Versluis, L.; Ziegler, T. *J. Chem. Phys.* **1988**, *88*, 322-328; (c) te Velde, G.; Baerends, E. J. *J. Comput. Phys.* **1992**, *99*, 84-98; (d) Fonseca Guerra, C.; Snijders, J. G.; te Velde, G.; Baerends, E. J. *Theor. Chem. Acc.* **1998**, *99*, 391-403.
107. (a) Schreckenbach, G.; Ziegler, T. *Int. J. Quantum Chem.* **1997**, *61*, 899-918; (b) Wolff, S. K.; Ziegler, T. *J. Chem. Phys.* **1998**, *109*, 895-905.
108. (a) Dickson, R. M.; Ziegler, T. *J. Phys. Chem.* **1996**, *100*, 5286-5290; (b) Autschbach, J.; Ziegler, T. *J. Chem. Phys.* **2000**, *113*, 936-947; (c) 9410-9418; (d) Khandogin, J.; Ziegler, T. *Spectrochim. Acta, Part A* **1999**, *55*, 607-624.
109. van Lenthe, E.; Baerends, E. J. *J. Chem. Phys.* **2000**, *112*, 8279-8292.
110. Vosko, S. H.; Wilk, L.; Nusair, M. *Can. J. Phys.* **1980**, *58*, 1200-1211.
111. Becke, A. D. *Phys. Rev. A* **1988**, *38*, 3098-3100.
112. Perdew, J. P. *Phys. Rev. B* **1986**, *33*, 8822-8824; **1986**, *34*, 7406.
113. (a) Grigoleit, S.; Bühl, M. *Chem. Eur. J.* **2004**, *10*, 5541-5552; (b) *J. Chem. Theory Comput.* **2005**, *1*, 181-193.
114. Narath, A. *Phys. Rev.* **1967**, *163*, 232-237.

-
115. Phillips, B. L.; Houston, J. R.; Feng, J.; Casey, W. H. *J. Am. Chem. Soc.* **2006**, *128*, 3912-3913.
116. Mann, B. E. *Annu. Rep. NMR Spectrosc.* **1991**, *23*, 141-207.
117. Ernsting, J. M.; Gaemers, S.; Elsevier, C. J. *Magn. Reson. Chem.* **2004**, *42*, 721-736.
118. Khriachtchev, L.; Pettersson, M.; Runeberg, N.; Lundell, J.; Räsänen, M. *Nature* **2000**, *406*, 874-877.
119. Pettersson, M.; Khriachtchev, L.; Lignell, A.; Räsänen, M.; Bihary, Z.; Gerber, R. *B. J. Chem. Phys.* **2002**, *116*, 2508-2515.
120. Frenking, G.; Cremer, D. *Struct. Bonding* **1990**, *73*, 17-95.
121. Khriachtchev, L.; Tanskanen, H.; Cohen, A.; Gerber, R. B.; Lundell, J.; Pettersson, M.; Kiljunen, H.; Räsänen, M. *J. Am. Chem. Soc.* **2003**, *125*, 6876-6877.
122. Feldman, V. I.; Sukhov, F. F.; Orlov, A. Y.; Tyulpina I. V. *J. Am. Chem. Soc.* **2003**, *125*, 4698-4699.
123. Stein, L. *Nature* **1973**, *243*, 30-32.
124. Holloway, J. H.; Hope, E. G. *Adv. Inorg. Chem.* **1998**, *46*, 51-100.
125. Gerken, M.; Schrobilgen, G. J. *Coord. Chem. Rev.* **2000**, *197*, 335-395.
126. Gillespie, R. J. *Molecular Geometry*, Van Nostrand Reinhold: New York, 1972.
127. (a) Dixon, D. A.; de Jong, W. A.; Peterson, K. A.; Christe, K. O.; Schrobilgen, G. *J. Am. Chem. Soc.* **2005**, *127*, 8627-8634; (b) Pilmé, J.; Robinson, E. A.; Gillespie, R. J. *Inorg. Chem.* **2006**, *45*, 6198-6204; (c) Antušek, A.; Pecul, M.; Sadlej, J. *Chem. Phys. Lett.* **2006**, *427*, 281-288.
128. (a) Bartell, L. S.; Gavon, R. M., Jr. *J. Chem. Phys.* **1968**, *48*, 2466-2483; (b) Claassen, H. H.; Goodman, G. L.; Kim, H. *J. Chem. Phys.* **1972**, *56*, 5042-5053; (c) Pitzer, K. S.; Bernstein, L. S. *J. Chem. Phys.* **1975**, *63*, 3849-3856; (d) Cutler,

-
- J. N.; Bancroft, G. M.; Bozek, J. D.; Tan, K. H.; Schrobilgen, G. J. *J. Am. Chem. Soc.* **1991**, *113*, 9125-9131.
129. Barrie, P. J., Klinowski, J. *Prog. Nucl. Magn. Reson. Spectrosc.* **1992**, *24*, 91-108.
130. Ratcliffe, C. I. *Annu. Rep. Nucl. Magn. Reson. Spectrosc.* **1998**, *36*, 123-221.
131. (a) Jokisaari, J. *Prog. Nucl. Magn. Reson. Spectrosc.* **1994**, *26*, 1-26; (b) In *Encyclopedia of Spectroscopy and Spectrometry*; Lindon, J. C., Tranter, G. E., Holmes, J. L., Eds.; Academic Press: San Diego, 1999, Vol. 3, 2435-2446.
132. Raftery, D.; Chmelka, B. F. In *NMR, Basic Principles and Progress*, Diehl, P., Fluck, E., Günther, H., Kosfeld, R., Seelig, J., Eds.; Springer-Verlag: Berlin, 1994; Vol. 30, 112-158.
133. Jameson, C. J. In *Multinuclear NMR*, Mason, J., Ed.; Plenum Press: New York, 1987, Chapter 18.
134. Schrobilgen, G. J., In *Encyclopedia of Nuclear Magnetic Resonance*, Grant, D. M., Harris, R. K., Eds.; John Wiley & Sons: Chichester, 1996, Vol. 5, 3251-3262.
135. Berger, S.; Braun, S.; Kalinowski, H.-O. *NMR Spectroscopy of the Non-Metallic Elements*, John Wiley & Sons: Chichester, 1997.
136. Forgeron, M. A. M.; Wasylshen, R. E.; Penner, G. H. *J. Phys. Chem. A* **2004**, *108*, 4751-4758.
137. Gerken, M.; Hazendonk, P.; Nieboer, J.; Schrobilgen, G. J. *J. Fluorine Chem.* **2004**, *125*, 1163-1168.
138. Ball, G. E.; Darwish, T. A.; Geftakis, S.; George, M. W.; Lawes, D. J.; Portius, P.; Rourke, J. P. *Proc. Natl. Acad. Sci. U.S.A.* **2005**, *102*, 1853-1858.
139. Syvret, R. G.; Mitchell, K. M.; Sanders, J. C. P.; Schrobilgen, G. J. *Inorg. Chem.* **1992**, *31*, 3381-3385.
140. Schrobilgen, G. J.; Holloway, J. H.; Granger, P.; Brevard, C. *Inorg. Chem.* **1978**, *17*, 980-987.
141. Gerken, M.; Schrobilgen, G. J. *Inorg. Chem.* **2002**, *41*, 198-204.

-
142. Moudrakovski, I. L.; Ratcliffe, C. I.; Ripmeester, J. A. *J. Am. Chem. Soc.* **2001**, *123*, 2066-2067.
 143. Luhmer, M.; Reisse, J. *J. Magn. Reson., Ser. A* **1995**, *115*, 197-205.
 144. Meersmann, T.; Deschamps, M.; Bodenhausen, G. *J. Am. Chem. Soc.* **2001**, *123*, 941-945.
 145. Reisse, J. *Nouv. J. Chim.* **1986**, *10*, 665-672.
 146. Warren, W. W., Jr.; Norberg, R. E. *Phys. Rev.* **1966**, *148*, 402-412.
 147. Cowgill, D. F.; Norberg, R. E. *Phys. Rev. B* **1972**, *6*, 1636-1638.
 148. Brinkmann, D. *Helv. Phys. Acta* **1968**, *41*, 367-384.
 149. Jameson, C. J.; Gutowsky, H. S. *J. Chem. Phys.* **1964**, *40*, 2285-2293.
 150. Jameson, C. J. In *Nuclear Magnetic Resonance: A Specialist Report*, Webb, G. A., Ed.; Royal Society of Chemistry: Cambridge, 1996, Vol. 25, Chapter 2.
 151. Liao, M.-S., Zhang, Q.-E. *J. Phys. Chem. A* **1998**, *102*, 10647-10654.
 152. Buth, C.; Santra, R.; Cederbaum, L. S. *J. Chem. Phys.* **2003**, *119*, 7763-7771.
 153. Styszyński, J.; Cao, X.; Malli, G. L. *J. Comput. Chem.* **1997**, *18*, 601-608.
 154. Bagus, P. S.; Liu, B.; Liskow, D. H.; Schaefer H. F., III *J. Am. Chem. Soc.* **1975**, *97*, 7216-7219.
 155. Malli, G. L.; Styszyński, J.; Da Silva, A. B. F. *Int. J. Quant. Chem.* **1995**, *55*, 213-225.
 156. Bryce, D. L.; Wasylshen, R. E. *Inorg. Chem.* **2002**, *41*, 3091-3101.
 157. Bagno, A.; Saielli, G. *Chem. Eur. J.* **2003**, *9*, 1486-1495.
 158. (a) Smith, D. F. *J. Chem. Phys.* **1963**, *38*, 270-271; Tsao, P.; Cobb, C. C.; (b) Claassen, H. H. *J. Chem. Phys.* **1971**, *54*, 5247-5253.
 159. Siegel, S.; Gerbert, E. *J. Am. Chem. Soc.* **1963**, *85*, 240.
 160. Levy, H. A.; Agron, P. A. *J. Am. Chem. Soc.* **1963**, *85*, 241-242.

-
161. Brassington, N. J.; Edwards, H. G. M.; Long, D. A. *J. Chem. Soc., Faraday Trans. 2* **1978**, *74*, 1208-1213.
162. Bürger, H.; Ma, S. *J. Mol. Spectrosc.* **1993**, *157*, 536-539.
163. Hindermann, D. K.; Falconer, W. E. *J. Chem. Phys.* **1969**, *50*, 1203-1205.
164. Jokisaari, J. P.; Ingman, L. P.; Schrobilgen, G. J.; Sanders, J. C. P. *Magn. Reson. Chem.* **1994**, *32*, 242-247.
165. Ingman, L. P.; Jokisaari, J.; Oikarinen, K.; Seydoux, R. *J. Magn. Reson., Ser. A* **1994**, *111*, 155-160.
166. Cutler, J. N.; Bancroft, G. M.; Bozek, J. D.; Tan, K. H.; Schrobilgen, G. J. *J. Am. Chem. Soc.* **1991**, *113*, 9125-9131.
167. Bürger, H.; Kuna, R.; Ma, S.; Breidung, J.; Thiel, W. *J. Chem. Phys.* **1994**, *101*, 1-14.
168. Lounila, J.; Oikarinen, K.; Ingman, P.; Jokisaari, J. *J. Magn. Reson., Ser. A* **1996**, *118*, 50-54.
169. Mills, I.; Cvitaš, T.; Homann, K.; Kallay, N.; Kuchitsu, K. *Quantities, Units and Symbols in Physical Chemistry*, 2nd ed.; Blackwell Science: Oxford, 1993.
170. Seppelt, K.; Rupp, H. H. *Z. Anorg. Allg. Chem.* **1974**, *409*, 331-337.
171. Flygare, W. H.; Goodisman, J. *J. Chem. Phys.* **1968**, *49*, 3122-3125.
172. Beeler, A. J.; Orendt, A. M.; Grant, D. M.; Cutts, P. W.; Michl, J.; Zilm, K. W.; Downing, J. W.; Facelli, J. C.; Schindler, M. S.; Kutzelnigg, W. *J. Am. Chem. Soc.* **1984**, *106*, 7672-7676.
173. Dickson, R. M.; McKinnon, M. S.; Britten, J. F.; Wasylshen, R. E. *Can. J. Chem.* **1987**, *65*, 941-946.
174. Jameson, C. J. In *Encyclopedia of Nuclear Magnetic Resonance*, Grant, D. M., Harris, R. K., Eds.; John Wiley & Sons: Chichester, 1996, Vol. 2.

-
175. Pyykkö P., In *Calculation of NMR and EPR Parameters: Theory and Applications*, Kaupp, M., Bühl, M., Malkin, V. G., Eds.; Wiley-VCH: Weinheim, 2004.
176. Vaara, J.; Malkina, O. L.; Stoll, H.; Malkin, V. G.; Kaupp, M. *J. Chem. Phys.* **2001**, *114*, 61-71.
177. Manninen, P.; Lantto, P.; Vaara, J.; Ruud, K. *J. Chem. Phys.* **2003**, *119*, 2623-2637.
178. Autschbach, J.; Ziegler, T. In *Encyclopedia of Nuclear Magnetic Resonance*, Grant, D. M., Harris, R. K., Eds.; Wiley: Chichester, 2002, Vol. 9, 306-323.
179. Pyykkö P.; Görling, A.; Rösch, N. *Mol. Phys.* **1987**, *61*, 195-205.
180. Pyykkö P. *Chem. Phys.* **1983**, *74*, 1-7.
181. (a) Pyper, N. C. *Chem. Phys. Lett.* **1983**, *96*, 204-210; (b) 211-217.
182. Malli, G.; Froese, C. *Int. J. Quantum Chem.* **1967**, *1*, 95-98.
183. Kolb, D.; Johnson, W. R.; Shorer, P. *Phys. Rev. A* **1982**, *26*, 19-31.
184. Kutzelnigg, W. *J. Comput. Chem.* **1999**, *20*, 1199-1219.
185. Fukui, H.; Baba, T. *J. Chem. Phys.* **2002**, *117*, 7836-7844.
186. Siegel, R.; Hirschinger, J.; Carlier, D.; Matar, S.; Ménétrier, M.; Delmas, C. *J. Phys. Chem. B* **2001**, *105*, 4166-4174.
187. Bürger, H.; Ma, S.; Breidung, J.; Thiel, W. *J. Chem. Phys.* **1996**, *104*, 4945-4953.
188. Vaara, J.; Pyykkö, P. *J. Chem. Phys.* **2003**, *118*, 2973-2976.
189. (a) Jameson, C. J.; Jameson, K. A.; Burrell, P. M. *J. Chem. Phys.* **1980**, *73*, 6013-6020; (b) Jameson, C. J.; Jameson, K. A.; Honarbakhsh, J. *J. Chem. Phys.* **1984**, *81*, 5266-5267.
190. Spiess, H. W.; Schweitzer, D.; Haeberlen, U.; Hausser, K. H. *J. Magn. Reson.* **1971**, *5*, 101-108.

-
191. (a) Bai, H.; Harris, R. K. *J. Magn. Reson.* **1992**, *96*, 24-30; (b) Cherryman, J. C.; Harris, R. K. *J. Magn. Reson.* **1997**, *128*, 21-29.
192. VanderHart, D. L.; Gutowsky, H. S. *J. Chem. Phys.* **1968**, *49*, 261-271.
193. Penner, G. H.; Power, W. P.; Wasylshen, R. E. *Can. J. Chem.* **1988**, *66*, 1821-1823.
194. (a) Kessemeier, H.; Norberg, R. E. *Phys. Rev.* **1967**, *155*, 321; (b) Reinheimer, P.; Hirschinger, J.; Gilard, P.; Goetz, N. *Magn. Reson. Chem.* **1997**, *35*, 757-764.
195. Blinc, R.; Zupančič, I.; Maričič, S.; Veksli, Z. *J. Chem. Phys.* **1963**, *39*, 2109-2110.
196. Hindermann, D. K.; Falconer, W. E. *J. Chem. Phys.* **1970**, *52*, 6198-6202.
197. Garg, S. K.; Ripmeester, J. A.; Davidson, D. W. *J. Magn. Reson.* **1980**, *39*, 317-323.
198. Autschbach, J.; le Guennic, B. *J. Am. Chem. Soc.* **2003**, *125*, 13585-13593.
199. Wells, A. F. *Structural Inorganic Chemistry, 5th ed.*, Clarendon Press: Oxford, 1984.
200. Burbank, R. D. Jones, G. R. *J. Am. Chem. Soc.* **1974**, *96*, 43-48
201. Zalkin, A.; Ward, D. L.; Biagioni, R. N.; Templeton, D. H.; Bartlett, N. *Inorg. Chem.* **1978**, *17*, 1318-1322.
202. Gerken, M.; Hazendonk, P.; unpublished results.
203. Walker, N. R.; Hui, J. K.-H.; Gerry, M. C. L. *J. Phys. Chem. A* **2002**, *106*, 5803-5808.
204. Evans, C. J.; Gerry, M. C. L. *J. Phys. Chem. A* **2001**, *105*, 9659-9663.
205. Hauck, J. Z. *Naturforsch., B: Chem. Sci.* **1970**, *25*, 224-225.
206. (a) Zalkin, A.; Forrester, J. D.; Templeton, D. H.; Williamson, S. M.; Koch, C. W. *Science* **1963**, *142*, 501-502; (b) Zalkin, A.; Forrester, J. D.; Templeton, D. H. *Inorg. Chem.* **1964**, *3*, 1417-1421.

-
207. (a) Hamilton, W. C.; Ibers, J. A.; MacKenzie, D. R. *Science* **1963**, *141*, 532-534;
(b) Ibers, J. A.; Hamilton, W. C.; MacKenzie, D. R. *Inorg. Chem.* **1964**, *3*, 1412-1416.
208. Zalkin, A.; Forrester, J. D.; Templeton, D. H.; Williamson, S. M.; Koch, C. W. *J. Am. Chem. Soc.* **1964**, *86*, 3569-3571.
209. Shustov, L. D.; Tolmacheva, N. S.; Nabiev, Sh. Sh.; Il'in, E. K.; Klimov, V. D.; Ushakov, V. P. *Zh. Neorg. Khim.* **1989**, *34*, 1673-1676.
210. Isupov, V. K.; Kirin, I. S.; Aleinikov, N. N.; Korsunskii, B. L. *Zh. Neorg. Khim.* **1977**, *22*, 1297-1300.
211. Gusev, Yu. K.; Mishin, V. Ya.; Rubtsov, E. M.; Kirin, I. S. *Zh. Neorg. Khim.* **1976**, *21*, 2546-2549.
212. Malm, J. G.; Bane, R. W.; Holt, B. D. *Proceedings of Conference on Noble Gas Compounds*, University of Chicago Press: Chicago, 1963.
213. Siegel, S.; Gebert, E. *Proceedings of Conference on Noble Gas Compounds*, University of Chicago Press: Chicago, 1963.
214. Corte, A. E., *U. S. Army Cold Regions Research and Engineering Laboratory*, Corps of Engineers, Research Rept., *85*, part I, **1961**, part II, **1962**; also, *Highway Res. Board. Bull.*, No. 317, **1962**, pp. 9-34; No. 331, **1962**, pp. 46-66.
215. Mishin, V. Ya.; Kirin, I. S.; Isupov, V. K.; Gusev, Yu. K. *Zh. Neorg. Khim.* **1971**, *16*, 51-55.
216. (a) Jaselskis, B.; Splitter, T. M.; Huston, J. L. *J. Am. Chem. Soc.* **1966**, *88*, 2149-2150; (b) Appelman, E. H. *Inorg. Syn.* **1968**, *11*, 210-213.
217. Schrobilgen, G. J.; unpublished results.
218. Sears, D. N.; unpublished results.
219. The demo version of the non-linear regression program is available at:
www.nlreg.com.
220. Freeman, R.; Hill, H. D. W. *J. Chem. Phys.* **1971**, *54*, 3367-3377.

-
221. Nakamoto, K. *Infrared and Raman Spectra of Inorganic and Coordination Compounds, Part A: Theory and Applications in Inorganic Chemistry*, 5th ed., John Wiley & Sons: New York, 1997, Section II-8, p. 214.
222. Wilson, E. B., Jr.; Decius, J. C.; Cross, P. C. *Molecular Vibrations: The Theory of Infrared and Raman Vibrational Spectra*, McGraw-Hill: New York, 1955, Ch. 10.
223. Peterson, J. L.; Claassen, H. H.; Appelman, E. H. *Inorg. Chem.* **1970**, *9*, 619-621.
224. Gruen, D. M. *Noble Gas Compounds*, H. H. Hyman, Ed.; University of Chicago Press: Chicago, 1963.
225. Clayden, N. J.; Dobson, C. M.; Lian, L.-Y.; Smith, D. J. *J. Magn. Reson.* **1986**, *69*, 476-487.
226. Demco, D. E.; Tegenfeldt, J.; Waugh, J. S. *Phys. Rev. B* **1975**, *11*, 4133-4151.
227. Alemany, L. B.; Grant, D. M.; Pugmire, R. J.; Alger, T. D.; Zilm, K. W. *J. Am. Chem. Soc.* **1983**, *105*, 2133-2141.
228. Alemany, L. B.; Grant, D. M.; Pugmire, R. J.; Alger, T. D.; Zilm, K. W. *J. Am. Chem. Soc.* **1983**, *105*, 2142-2147.
229. Martin, M. L.; Delpuech, J.-J.; Martin, G. J. *Practical NMR Spectroscopy*, Heyden: London, 1980; p. 250.
230. Cooke, S. A.; Gerry, M. C. L. *Phys. Chem. Chem. Phys.* **2004**, *6*, 3248-3256.
231. Jäger, W.; Xu, Y.; Gerry, M. C. L. *J. Chem. Phys.* **1993**, *99*, 919-927.
232. Keenan, M. R.; Buxton, L. W.; Campbell, E. J.; Balle, T. J.; Flygare, W. H. *J. Chem. Phys.* **1980**, *73*, 3523-3529.
233. Baiocchi, F. A.; Dixon, T. A.; Joyner, C. H.; Klemperer, W. *J. Chem. Phys.* **1981**, *75*, 2041-2046.
234. Cooke, S. A.; Gerry, M. C. L. *J. Am. Chem. Soc.* **2004**, *126*, 17000-17008.

-
235. Peterson, K. A.; Petrmichl, R. H.; McClain, R. L.; Woods, R. C. *J. Chem. Phys.* **1991**, *95*, 2352-2360.
236. Voet, D. V.; Voet, J. G.; Pratt, C. W. *Fundamentals of Biochemistry*; John Wiley & Sons: Toronto, 1999.
237. Cotton, F. A.; Wilkinson, G.; Murillo, C. A.; Bochmann, M. *Advanced Inorganic Chemistry*, 6th ed., Interscience Publishers: New York, 1999.
238. (a) Lent, C. S. *Science* **2000**, *288*, 1597-1599; (b) Lei, X.; Wolf, E. E.; Fehlner, T. P. *Eur. J. Inorg. Chem.* **1998**, *12*, 1835-1846.
239. (a) Seman, M.; Kondo, J. N.; Domen, K.; Reed, C.; Oyama, S. T. *J. Phys. Chem. B* **2004**, *108*, 3231-3239; (b) Liu, H.; Cheung, P.; Iglesia, E. *J. Phys. Chem. B* **2003**, *107*, 4118-4127; (c) Okamoto, Y.; Oshima, N.; Kobayashi, Y.; Terasaki, O.; Kodaira, T.; Kubota, T. *Phys. Chem. Chem. Phys.* **2002**, *4*, 2852-2862.
240. Bastow, T. J. *Solid State Nucl. Magn. Reson.* **1998**, *12*, 191-199.
241. Malito, J. *Annu. Rep. Nucl. Magn. Reson. Spectrosc.* **1997**, *33*, 151-206.
242. Nolle, A. Z. *Phys. A* **1977**, *280*, 231-234.
243. Lynch, G. F.; Segel, S. L. *Can. J. Phys.* **1972**, *50*, 567-572.
244. Bank, S.; Liu, S.; Shaikh, S. N.; Sun, X.; Zubieta, J.; Ellis, P. D. *Inorg. Chem.* **1988**, *27*, 3535-3543.
245. Mastikhin, V. M.; Lapina, O. B.; Maximovskaya, R. I. *Chem. Phys. Lett.* **1988**, *148*, 413-416.
246. Edwards, J. C.; Adams, R. D.; Ellis, P. D. *J. Am. Chem. Soc.* **1990**, *112*, 8349-8364.
247. Eichele, K.; Wasylishen, R. E.; Nelson, J. H. *J. Phys. Chem. A* **1997**, *101*, 5463-5468.
248. Edwards, J. C.; Zubieta, J.; Shaikh, S. N.; Chen, Q.; Bank, S.; Ellis, P. D. *Inorg. Chem.* **1990**, *29*, 3381-3393.

-
249. Edwards, J. C.; Ellis, P. D. *Langmuir* **1991**, *7*, 2117-2134.
250. Forgeron, M. A. M.; Wasylshen, R. E. *J. Am. Chem. Soc.* **2006**, *128*, 7817-7827.
251. d'Espinose de Lacaillerie, J.-B.; Barberon, F.; Romanenko, K. V.; Lapina, O. B.; Le Pollès, L.; Gautier, R.; Gan, Z. *J. Phys. Chem. B* **2005**, *109*, 14033-14042.
252. Abraham, Y.; Holzwarth, N. A. W.; Williams, R. T. *Phys. Rev. B* **2000**, *62*, 1733-1741.
253. *Natl. Bur. Stand. (U.S.) Monogr.* **1962**, *25*, 23.
254. *Natl. Bur. Stand. (U.S.) Monogr.* **1978**, *25*, 53.
255. *Acta Crystallogr. B* **1974**, *26*, 26.
256. Gürmen, E.; Daniels, E.; King, J. S. *J. Chem. Phys.* **1971**, *55*, 1093-1097.
257. *Natl. Bur. Stand. (U.S.) Circ.* **1957**, *539*, 50.
258. *Natl. Bur. Stand. (U.S.) Circ.* **1957**, *539*, 21.
259. *Natl. Bur. Stand. (U.S.) Circ.* **1957**, *539*, 7.
260. Leciejewicz, J. Z. *Kristallogr.* **1965**, *121*, 158-64.
261. Schurko, R. W.; Wi, S.; Frydman, L. *J. Phys. Chem. A* **2002**, *106*, 51-62.
262. Dunbar, K. R.; Heintz, R. bA. *Prog. Inorg. Chem.* **1997**, *45*, 283-391.
263. Withers, J. R.; Ruschmann, C.; Bojang, P.; Parkin, S.; Holmes, S. M. *Inorg. Chem.* **2005**, *44*, 352-358.
264. Sokol, J. J.; Hee, A. G.; Long, J. R. *J. Am. Chem. Soc.* **2002**, *124*, 7656-7657.
265. Hendrickx, M. F. A.; Clima, S.; Chibotaru, L. F.; Ceulemans, A. *J. Phys. Chem. A* **2005**, *109*, 8857-8864.
266. Chibotaru, L. F.; Hendrickx, M. F. A.; Clima, S.; Larionova, J.; Ceulemans, A. *J. Phys. Chem. A* **2005**, *109*, 7251-7257.
267. Bennett, M. V.; Long, J. R. *J. Am. Chem. Soc.* **2003**, *125*, 2394-2395.

-
268. Huheey, J. E.; Keiter, E. A.; Keiter, R. L. *Inorganic Chemistry – Principles of Structure and Reactivity*, 4th ed., Harper Collins: New York, 1993.
269. Rosenheim, A. Z. *Anorg. Chem.* **1907**, *54*, 97-103.
270. Leipoldt, J. G.; Basson, S. S.; Roodt, A. *Adv. Inorg. Chem.* **1994**, *40*, 241-322.
271. Muetterties, E. L.; Guggenberger, L. J. *J. Am. Chem. Soc.* **1974**, *96*, 1748-1756.
272. Hoard, J. L.; Nordsieck, H. H. *J. Am. Chem. Soc.* **1939**, *61*, 2853-2863.
273. Hoard, J. L.; Hamor, T. A.; Glick, M. D. *J. Am. Chem. Soc.* **1968**, *90*, 3177-3184.
274. Mak, T. C. W.; Zhou, G.-D. *Crystallography in Modern Chemistry: A Resource Book of Crystal Structures*, John Wiley & Sons: USA, 1992.
275. Meske, W.; Babel, D. *J. Alloys Compd.* **1992**, *183*, 158-167.
276. Hendrickx, M. F. A.; Mironov, V. S.; Chibotaru, L. F. Ceulemans, A. *Inorg. Chem.* **2004**, *43*, 3142-3150.
277. Greenwood, N. N.; Earnshaw, A. *Chemistry of the Elements*, Pergamon Press: Oxford, 1984, Ch. 19.
278. Perumareddi, J. R.; Liehr, A. D.; Adamson, A. W. *J. Am. Chem. Soc.* **1963**, *85*, 249-259.
279. Parish, R. V.; Simms, P. G.; Wells, M. A.; Woodward, L. A. *J. Chem. Soc. A* **1968**, 2882-2886.
280. Koenig, E. *Theor. Chim. Acta* **1962**, *1*, 23-35.
281. Stammreich, H.; Sala, O. *Z. Elektro. Angewandte Phys. Chemie* **1961**, *65*, 149-150.
282. Hartman, K. O.; Miller, F. A. *Spectrochim. Acta, Part A* **1968**, *24*, 669-684.
283. Kettle, S. F. A.; Parish, R. V. *Spectrochim. Acta* **1965**, *21*, 1087-1093.
284. Muetterties, E. L. *Inorg. Chem.* **1965**, *4*, 769-771.
285. Muetterties, E. L. *Inorg. Chem.* **1973**, *12*, 1963-1966.

-
286. Lutz, O.; Nolle, A.; Kroneck, P. *Z. Naturforsch., A: Phys. Sci.* **1976**, *31*, 454-456.
287. Brownlee, R. T. C.; Shehan, B. P.; Wedd, A. G. *Inorg. Chem.* **1987**, *26*, 2022-2024.
288. Burdett, J. K.; Hoffmann, R.; Fay, R. C. *Inorg. Chem.* **1978**, *17*, 2553-2568.
289. Gołębiewski, A.; Kowalski, H. *Theor. Chim. Acta* **1969**, *12*, 293-306.
290. Gołębiewski, A.; Nalewajski, R. *Z. Naturforsch., A: Phys. Sci.* **1972**, *27*, 1672-1677.
291. Hendrickx, M. F. A.; Chibotaru, L. F.; Ceulemans, A. *Inorg. Chem.* **2003**, *42*, 590-597.
292. Isci, H.; Mason, W. R. *Inorg. Chim. Acta* **2004**, *357*, 4065-4072.
293. (a) Yeow, E. K. L.; Slep, L. D.; Chibisov, A. K.; Braslavsky, S. E. *J. Phys. Chem. A* **2003**, *107*, 439-446; (b) 2118.
294. Schröder, U.; Scholz, F. *Inorg. Chem.* **2000**, *39*, 1006-1015.
295. Ohkoshi, S.-I.; Tokoro, H.; Hozumi, T.; Zhang, Y.; Hashimoto, K.; Mathonière, C.; Bord, I.; Rombaut, G.; Verelst, M.; Cartier dit Moulin, C.; Villain, F. *J. Am. Chem. Soc.* **2006**, *128*, 270-277.
296. Rombaut, G.; Verelst, M.; Golhen, S.; Ouahab, L.; Mathonière, C.; Kahn, O. *Inorg. Chem.* **2001**, *40*, 1151-1159.
297. Mathonière, C.; Podgajny, R.; Guionneau, P.; Labrugere, C.; Sieklucka, B. *Chem. Mater.* **2005**, *17*, 442-449.
298. Przychodzeń, P.; Lewiński, K.; Bałanda, M.; Pelka, R.; Rams, M.; Wasiutyński, T.; Guyard-Duhayon, C.; Sieklucka, B. *Inorg. Chem.* **2004**, *43*, 2967-2974.
299. Sharpe, A. G. *The Chemistry of Cyano Complexes of the Transition Metals*, Maitlis, P. M., Stone, F. G. A., West, R., Eds.; Academic Press: London, 1976, p. 57.

-
300. Murgich, J.; Bonalde, I.; Díaz, A.; Abanero, J. A. *J. Magn. Reson.* **1991**, *93*, 47-53.
301. Murgich, J.; Oja, T. *J. Chem. Soc., Dalton Trans.* **1987**, 1637-1640.
302. (a) Haase, J.; Conradi, M. S. *Chem. Phys. Lett.* **1993**, *209*, 287-291; (b) Iuga, D.; Schäfer, H.; Verhagen, R.; Kentgens, A. P. M. *J. Magn. Reson.* **2000**, *147*, 192-209.
303. Leipoldt, J. G.; Bok, L. D. C.; Cilliers, P. J. *Z. Anorg. Allg. Chem.* **1974**, *407*, 350-352.
304. Matsumoto, K; Kobayashi, A.; Sasaki, Y. *Bull. Chem. Soc. Jpn.* **1975**, *48*, 1009-1013.
305. Kanatzidis, M. G.; Coucouvanis, D. *Acta Crystallogr., Sect. C* **1983**, *39*, 835-838.
306. O'Neal, S. C.; Kolis, J. W. *J. Am. Chem. Soc.* **1988**, *110*, 1971-1973.
307. Mak, T. C. W. *Z. Kristallogr.* **1984**, *166*, 277-281.
308. Schreckenbach, G.; Ziegler, T. *J. Phys. Chem.* **1995**, *99*, 606-611.
309. PQS Version 2.5, Parallel Quantum Solutions, Fayetteville, AK; <http://www.pqs-chem.com>. sales@pqs-chem.com
310. MOLPRO, a package of *ab initio* programs designed by H.-J. Werner, P.J. Knowles, R. Lindh, M. Schütz and others; Version 2002.6100.
311. Lutz, O.; Nolle, A.; Kroneck, P. *Z. Naturforsch., A: Phys. Sci.* **1977**, *32*, 505-506.
312. Calculations were performed with Mo at the origin and the formal C₂-axis aligned parallel to the z-axis.
313. Golding, R. M. *Applied Wave Mechanics*, DVN: London, 1969.
314. Corden, B. J.; Cunningham, J. A.; Eisenberg, R. *Inorg. Chem.* **1970**, *9*, 356-362.
315. Golding, R. M.; Carrington, A. *Mol. Phys.* **1962**, *5*, 377-385.
316. Jameson, C. J.; Gutowsky, H. S. *J. Chem. Phys.* **1964**, *40*, 1714-1724.

-
317. This value for $\sigma_{\text{iso}}(\text{Mo})$, 4317 ppm, was extrapolated from a plot of $\sigma_{\text{iso}}(\text{calc.})$ vs. atomic number for all closed-shell atoms. Calculations were performed using spin-orbit relativistic ZORA DFT. This extrapolation method was employed as the program ADF does not yet permit shielding calculations on open-shell systems.
318. Hayes, R. G. *J. Chem. Phys.* **1966**, *44*, 2210-2212.
319. McGarvey, B. R. *Inorg. Chem.* **1966**, *5*, 476-479.
320. Brevard, C.; Pregosin, P. S.; Thouvenot, R. In *Transition Metal Nuclear Magnetic Resonance*; Pregosin, P. S., Ed.; Elsevier: Amsterdam, 1991, pp 67-81.
321. (a) Avalos, M.; Babiano, R.; Cintas, P.; Jiménez, J. L.; Palacios, J. C. *Chem. Soc. Rev.* **1999**, *28*, 169-177; (b) Dötz, K. H.; Tomuschat, P. *Chem. Soc. Rev.* **1999**, *28*, 187-198.
322. Bolm, C.; Muñiz, K. *Chem. Soc. Rev.* **1999**, *28*, 51-59.
323. (a) Snowling, D. C. H.; Grovenor, C. R. M. *J. Mater. Chem.* **1993**, *3*, 473-478; (b) Letouzé, F.; Martin, C.; Hervieu, M.; Maignan, A.; Daturi, M.; Michel, C.; Raveau, B. *Physica C* **1997**, *292*, 32-38.
324. Smith, M. E. *Annu. Rep. NMR Spectrosc.* **2000**, *43*, 121.
325. Berger, S. B.; Burch, T. J.; Budnick, J. I.; Darcy, L. *J. Appl. Phys.* **1971**, *42*, 1309-1310.
326. Le Dang, K.; Veillet, P. *Comptes Rendus des Seances de l'Academie des Sciences, Serie D: Sciences Naturelles* **1967**, *264B*, 1154-1157.
327. Bryce, D. L.; Wasylishen, R. E. *Phys. Chem. Chem. Phys.* **2001**, *3*, 5154-5157.
328. Bryce, D. L.; Gee, M.; Wasylishen, R. E. *J. Phys. Chem. A* **2001**, *105*, 10413-10421.
329. Barlage, H.; Jacobs, H. Z. *Anorg. Allg. Chem.* **1996**, *622*, 721-723.
330. Toriumi, K.; Saito, Y. *Acta Crystallogr., Sect. B* **1978**, *34*, 3149-3156.

-
331. Smith, H. W.; Colby, M. Y. *Z. Kristallogr.* **1941**, *103*, 90-95.
332. Hackert, M. L.; Jacobson, R. A. *J. Solid State Chem.* **1971**, *3*, 364-368.
333. Morris, A. J.; Kennard, C. H. L.; Moore, F. H.; Smith, G.; Montgomery, H. *Cryst. Struct. Commun.* **1981**, *10*, 529-532.
334. Muller, O.; White W. B.; Roy R. *Z. Kristallogr.* **1969**, *130*, 112-120.
335. Lentz, A.; Buechele, W.; Schoellhorn, H. *Cryst. Res. Technol.* **1986**, *21*, 827-833.
336. Weber, G.; Range K.-J. *Z. Naturforsch., B: Chem. Sci.* **1996**, *51*, 751-753.
337. Effenberger, H.; Pertlik, F. *Z. Kristallogr.* **1986**, *176*, 75-83.
338. Brandon, J. K.; Brown, I. D. *Can. J. Chem.* **1968**, *46*, 933-941.
339. Carter, R. L.; Bricker, C. E. *Spectrosc. Lett.* **1969**, *2*, 321-326.
340. Martin, C.; Durif, A. *Bull. Soc. Franc. Mineral. Crist.* **1964**, *87*, 280.
341. Smith, J. V.; Blackwell, C. S. *Nature* **1983**, *303*, 223-225.
342. Blaha, P.; Schwarz, K.; Madsen, G. K. H.; Kvasnicka, D.; Luitz, J. *WIEN2k, An Augmented Plane Wave Plus Local Orbitals Program for Calculating Crystal Properties*; Vienna University of Technology: Austria.
343. Krivovichev, S. V.; Kir'yanova, E. V.; Filatov, S. K.; Burns, P. C. *Acta Crystallogr., Sect. C* **2000**, *56*, 629-630.
344. Carter, R. L.; Bricker, C. E. *Spectrochim. Acta, Part A* **1973**, *29*, 253-262.